General Disclaimer

One or more of the Following Statements may affect this Document

- This document has been reproduced from the best copy furnished by the organizational source. It is being released in the interest of making available as much information as possible.

- This document may contain data, which exceeds the sheet parameters. It was furnished in this condition by the organizational source and is the best copy available.

- This document may contain tone-on-tone or color graphs, charts and/or pictures, which have been reproduced in black and white.

- This document is paginated as submitted by the original source.

- Portions of this document are not fully legible due to the historical nature of some of the material. However, it is the best reproduction available from the original submission.

SQT

DOE/NASA 0017/3
NASA CR-165494
DDA EDR 10672

CERAMIC APPLICATIONS IN TURBINE ENGINES

Progress Report for 1 July 1980 to 31 December 1980

Joseph A. Byrd
Michael A. Janovicz
Samuel R. Thrasher

Detroit Diesel Allison Division
General Motors Corporation

September 1981

Prepared for
NATIONAL AERONAUTICS AND SPACE ADMINISTRATION
Lewis Research Center
Under Contract DEN 3-17

for

U. S. DEPARTMENT OF ENERGY
Assistant Secretary for Conservation & Solar Applications
Office of Transportation Programs

1. Report No.	2. Government Accession No.	3. Recipient's Catalog No.
CR-165494		

4. Title and Subtitle

CERAMIC APPLICATIONS IN TURBINE ENGINES
Progress Report for 1 July to 31 December 1980

5. Report Date
September 1981

6. Performing Organization Code

7. Author(s)

Joseph A. Byrd, Michael A. Janovicz, Sammuel R. Thrasher

8. Performing Organization Report No.
EDR 10672

10. Work Unit No.

9. Performing Organization Name and Address

Detroit Diesel Allison
Division of General Motors Corporation
P.O. Box 894
Indianapolis, Indiana 46206

11. Contract or Grant No.
DEN 3-17

13. Type of Report and Period Covered
Contractor report

12. Sponsoring Agency Name and Address

U.S. Department of Energy
Office of Transportation Programs
Washington, D.C. 20545

14. Sponsoring Agency Code

15. Supplementary Notes

Semiannual Report. Prepared under Interagency Agreement EC-77-A-31-1040. Project Manager T. J. Miller, Transportation Propulsion Division, NASA Lewis Research Center, Cleveland, Ohio 44135.

16. Abstract

This report describes Detroit Diesel Allison's continued activities in ceramic material development, ceramic turbine component and regenerator disk testing at 36°C (65°F) above the baseline engine TIT, and other design analysis, fabrication, and development activities taking place between 1 July and 31 December 1980. Developmental testing activities on the 1900°F-configuration ceramic parts were completed, 2070°F-configuration ceramic component rig and engine testing was initiated, and the conceptual design for the 2265°F-configuration engine was identified. Fabrication of the 2070°F-configuration ceramic parts continued, along with burner rig development testing of the 2070°F-configuration metal combustor in preparation for 1132°C (2070°F) qualification test conditions. Shakedown testing of the hot engine simulator (HES) rig was also completed in preparation for testing of a spin rig-qualified ceramic-bladed rotor assembly at 1132°C (2070°F) test conditions. Concurrently, ceramics from new sources and alternate materials continued to be evaluated, and fabrication of 2070°F-configuration ceramic components from these new sources continued. Cold spin testing of the critical 2070°F-configuration blade continued in the spin test rig to qualify a set of ceramic blades at 117% engine speed for the gasifier turbine rotor. Rig testing of the ceramic-bladed gasifier turbine rotor assembly at 108% engine speed was also performed, which resulted in the failure of one blade. The new three-piece hot seal with the nickel oxide/calcium flouride wearface composition was qualified in the regenerator rig and introduced to engine operation with marginal success. Ceramic regenerator seal development continued with high temperature and friction/wear testing of the wearface material. Engine testing was performed on two engines (C-1 and C-4), which included demonstration of the I_6 microprocessor, 2070°F-configuration insulation material, and engine block cooling design; durability testing of the 2070°F-configuration ceramic gasifier turbine nozzle assembly; and development of the abradable gasifier turbine tip seal material. The ceramic suppliers continue to make progress toward improving strength, minimizing variability, and further developing nondestructive evaluation techniques; however, development of properties to their full capability in fabricated shapes will require continuing effort throughout the project.

17. Key Words (Suggested by Author(s))	18. Distribution Statement
Ceramic components Process development Proof testing Ceramic material characterization	Unclassified--unlimited STAR category 85 DOE category UC-96

19. Security Classif. (of this report)	20. Security Classif. (of this page)	21. No. of Pages	22. Price*
Unclassified	Unclassified		

*For sale by the National Technical Information Service, Springfield, Virginia 22151

TABLE OF CONTENTS

LIST OF ILLUSTRATIONS

LIST OF TABLES

I. INTRODUCTION AND SUMMARY

This report relates progress made from 1 July 1980 to 31 December 1980 on National Aeronautics and Space Administration (NASA) Contract DEN3-17, funded by the Department of Energy (DOE) to apply ceramic materials to an existing Detroit Diesel Allison (DDA) 404 industrial gas turbine engine. Excellent progress has been made in building a ceramic materials design data base, establishing design approaches for ceramic components in turbine engines, involving the ceramics industry in the fabrication of high-technology ceramic components, and defining the true structural, thermal, and chemical environment for ceramic components in turbine engines by rig and engine testing. These elements are essential to application of gas turbines to highway vehicles. High-temperature ceramic materials allow higher engine-operating temperatures in gas turbine engines than do metal components. This increased temperature capability yields a more efficient engine that may reduce fuel usage per mile by more than 20%. Furthermore, ceramic components may ultimately be less expensive than metal parts and may help to make feasible a mass-production vehicular (truck, bus, or passenger car) gas turbine.

DDA's 404/505/605 series industrial gas turbine (IGT) engines presented a unique means for exploring specific fuel consumption (SFC) improvement, since it is a highly developed gas turbine engine with near-term production potential for introduction into truck, bus, and generator set markets. These markets use approximately 21% of transportation petroleum products. Consequently, using this engine as a test bed for ceramic application is a logical first step to introducing changes on the broad automotive marketplace. Technology developed in this program is readily transferred to vehicular gas turbine engines.

Contract activities were initiated to demonstrate ceramic components in a DDA 404-4 industrial gas turbine in 1976. In initial work, a study of the parametric sensitivities of the 404-4 engine were defined and the candidate components for ceramic application and efficiency improvement identified. The initial activity also included fabrication and testing of selected ceramic components, ceramic material characterization and qualification, and conversion of two contractor-owned engines to an initial ceramic configuration capable of operating at 1038°C (1900°F).

The analysis and studies explored operating temperatures from 1002°C (1835°F) turbine inlet temperature (TIT) (baseline IGT) to 1371°C (2500°F) TIT. These studies indicated that a configuration at 1241°C (2265°F) with component efficiency improvements would be best. Ceramics would be required for the following components: gasifier turbine nozzle vanes, gasifier turbine tip shroud, gasifier turbine blades, power turbine nozzle vanes, inlet plenum, combustor, and regenerator disks. Improvements in component efficiency would be made in the compressor, plenum flow, power turbine (two-stage), gasifier turbine nozzle and tip shroud, and gasifier turbine tip and wall losses. These components would be introduced at three discrete TIT steps--the 1038°C (1900°F), 1132°C (2070°F), and 1241°C (2265°F) configurations. The project plan, which was published in DOE/NASA Report CONS0064-1 in May 1977, included ceramic material testing and characterization, rig testing, engine performance and durability, and vehicle demonstration at each temperature level. Subsequently, this plan became the basis for the project now in progress at DDA.

DOE/NASA Reports DDA EDR 9519, DDA EDR 9722, DDA EDR 9951, DDA EDR 10156, and DDA EDR 10383, previously issued, cover the ceramic materials characterization, component design, rig test, and engine test activities of the project from January 1978 through December 1980. Through that period, 6439 hr of engine operation to truck and bus operating cycles were accomplished on initial ceramic parts at a turbine inlet temperature of 1038°C (1900°F), some 36°C (65°F) above that of the all-metal baseline engine. These initial tests of ceramic parts indicated the chemical and structural stability of silicon carbide nozzle vanes, sintered silicon nitride and silicon carbide turbine tip shrouds, and alumina silicate regenerator disks. In addition, reaction-bonded silicon carbide nozzle vanes and alumina silicate regenerator disks have successfully withstood 10,500 km (6,533 miles) of over-the-road engine use in a turbine-powered truck, including exposure to rigorous road hazard test courses. This truck experience has demonstrated the utility and durability of ceramic parts operating in a turbine engine under actual vehicle operating conditions. During this time, activities were conducted to characterize ceramic material candidates, to improve the realized strength of ceramics in part configurations, to define ceramic design methodology, to explore nondestructive evaluation (NDE) techniques applicable to ceramic materials, to qualify parts with rigs simulating critical engine conditions, and to design a configuration to operate at 1132°C (2070°F). The data, experience, and methodology obtained can be effectively applied to the fabrication and process development that lead to an initial complement of 2070°F-configuration ceramic components.

This reporting period marked the completion of testing of the initial 1900°F-configuration ceramic parts, the beginning of the 2070°F-configuration ceramic part rig and engine development testing, and continuation of the design and analysis of the final engine in the project (2265°F-configuration). The reporting period is summarized in the project plan shown in Figure 1. This plan has been revised from that previously presented, reflecting a delay in initiation of 2265°F-configuration testing due to funding limitations imposed over FY 81 and FY 82. Project completion is still targeted for mid-1984.

With the conclusion of the 1900°F-configuration testing, a very meaningful milestone has been achieved in the use of ceramic parts in turbine engines. In testing, the 1900°F-configuration has accumulated 6,533 hr of engine experience with the three ceramic components shown in Figure 2, indicating that the components are viable in operating engines. Alumina silicate regenerator disks and reaction-bonded silicon carbide gasifier nozzle vanes have also been successfully operated in a truck for 10,500 km (6,533 miles) on the road and over special truck durability test courses which attests to their applicability in the vehicular environment. The development of these parts has advanced ceramic material technology process, evaluation of candidate ceramic materials and sources, NDE technology, ceramic materials design data base, and ceramic part rig qualification test equipment and procedures.

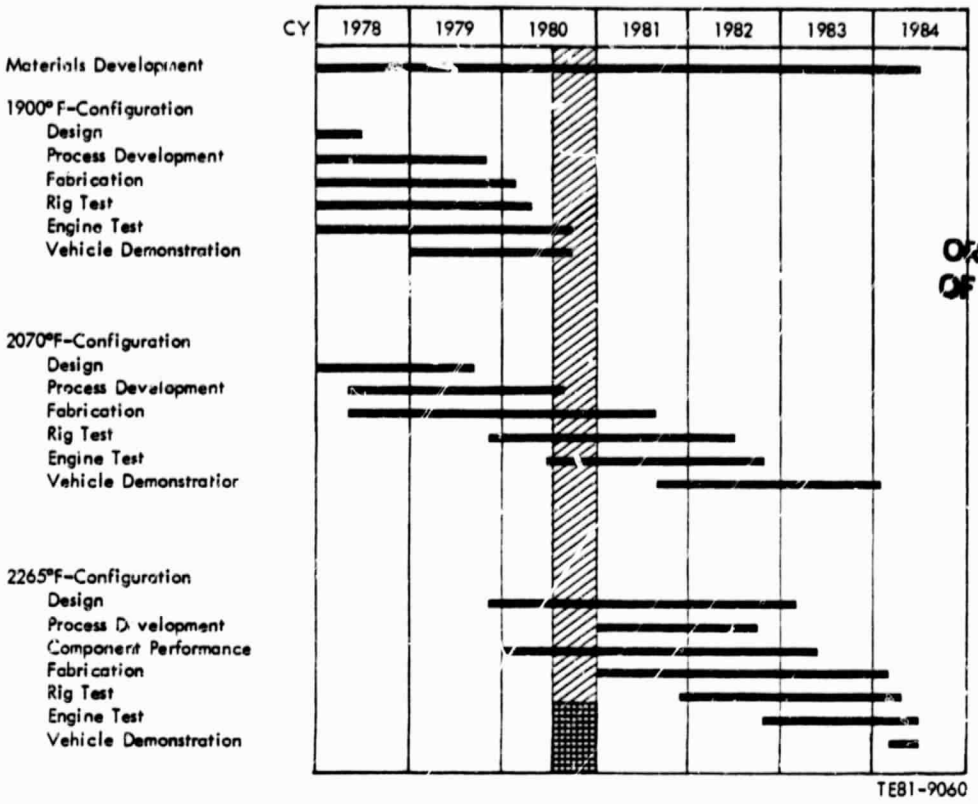

Figure 1. CATE project master plan.

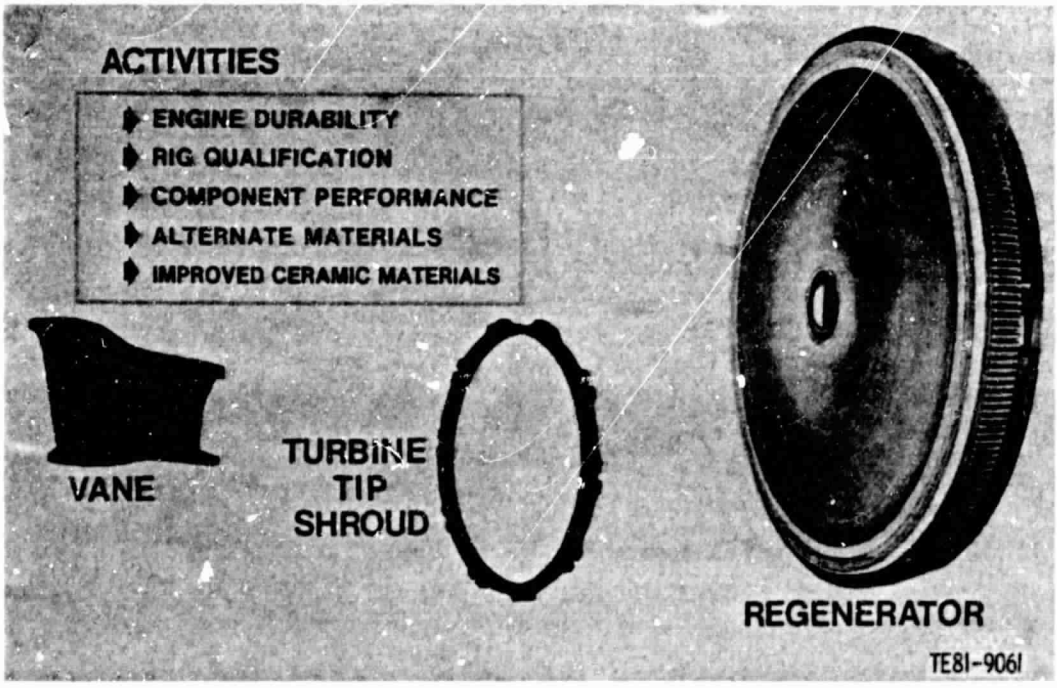

Figure 2. Initial engine configuration.

The emphasis in this report period has been directed at development activities leading to operation of the 2070°F-configuration engine. Significant progress has been made, but engine operation at 1132°C (2070°F) TIT will be delayed because development of the ceramic blade is requiring more time than expected. Progress has been made with other ceramic components, but 1132°C (2070°F) TIT cannot be attained until a ceramic bladed rotor is operational.

In terms of 2070°F-configuration development, Table I indicates the status of each activity that must be completed before full 2070°F-configuration engine testing begins. Three elements remain before engine operation at 1132°C (2070°F) is possible: qualification of a ceramic-bladed rotor, qualification of a ceramic nozzle/turbine tip shroud assembly at 1132°C (2070°F), and qualification of the ceramic plenum. Current plans project accomplishment of these steps and engine operation in the second quarter of 1981. The following paragraphs describe the development activities involved with 2070°F-configuration engine operation.

Three rigs have been brought on line to test the ceramic parts at the increased temperatures of the advanced configuration. The thermal shock rig has already been used for combustor development and 2070°F-configuration nozzle and tip shroud testing. The regenerator rig has demonstrated ability to operate at 927°C (1800°F), the maximum for the Ceramic Applications in Turbine Engines (CATE) project, with a regenerator assembly test of 50 hr. The simulator is a gas producer configured engine in which the 2070°F-configuration gasifier section is used to subject the ceramic-bladed rotor to various speeds and temperatures without downstream components, such as the power turbine and regenerators, that could be damaged in the event of blade failure. The simulator has been operated with a metal rotor and is ready to test the first qualified ceramic-bladed rotor (Figure 3).

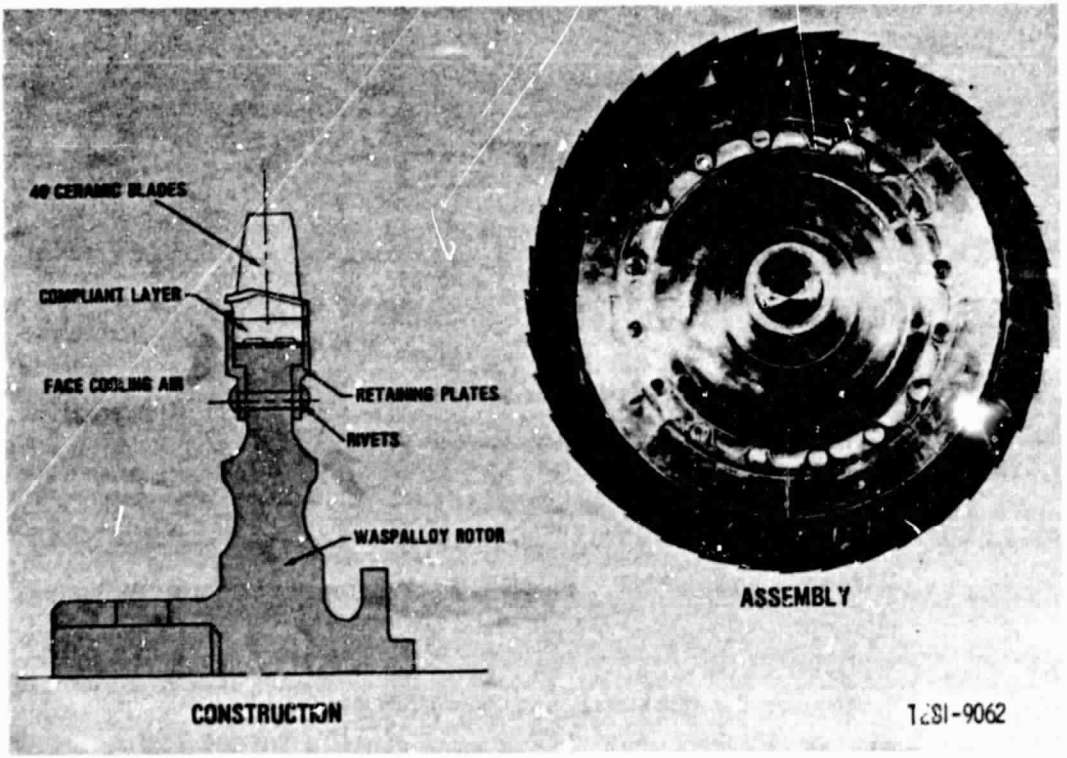

Figure 3. Ceramic bladed turbine rotor.

TABLE I. 2070°F-CONFIGURATION DEVELOPMENT ACTIVITIES

Task	Engine incorporation: Yes	Engine incorporation: No	Status
Basic engine features			
o New engine (C-4)	Mar 80 (9-79)	-	o Operating
o Block cooling and insulation	Oct 80	-	o Baseline test completed--operating/evaluating
o T_6 microprocessor control	Nov 80	-	o Engine demonstrated--working on remaining unit qualification and environmental test
o Combustor	Jan 80	-	o Available--requires 2070°F-configuration rig trial
Ceramic parts			
o Plenum (2)	-	X	o Initial parts available--requires rig qualification
o Nozzle assembly (32)	Jul 80	-	o 1900°F-configuration TIT engine test at 580 hr o Requires 2070°F-configuration rig qualification
o Turbine tip shroud (1)	Jul 80	-	o 1900°F-configuration TIT engine test at 580 hr o Requires 2070°F-configuration rig qualification
o Turbine blades (40)	-	X	o 48 blades qualified at 117% speed--proceeding with rotor qualification, hot engine simulator, and development tests
o Regenerator			
o Disk ass'y (2)	Aug 79	-	o 1900°F-configuration TIT engine test at 1320 hr o Rig qualifying with mechanical design features
o Hot seal (2)	Dec 80		o Rig qualified o 1900°F-configuration TIT engine test at 35 hr
Test rigs			
o Thermal shock	-	-	o Operational--updating for more realistic secondary cooling flow
o Regenerator	-	-	o In place and operational
o Simulator (blades)	-	-	o Operational

The engine is being prepared to accept the 2070°F-configuration parts, engine C-4 has been modified for high-temperature operation with improved block insulation and block air cooling. An engine control system is now operational that senses power turbine exit gas temperature as the control parameter, instead of gasifier inlet temperature, since the 2070°F- and higher-configuration engines operate at too high a turbine inlet temperature for thermocouple sensors. A Lamilloy (transpiration cooled) combustor has been rig tested, and only a checkout test with a ceramic nozzle at full engine conditions is required. A second new engine (C-6) is being built, awaiting a complement of qualified ceramic parts to become the primary 2070°F-configuration test stand durability engine. More will be said about these engine features when engine test activities are discussed.

The ceramic blade has always been considered critical since it is the only rotating ceramic part in the project. With limited blade assets and known material strengths below design goals, 52 sintered alpha silicon carbide

blades were individually spin tested to 110% engine speed, with 42 (81%) passing. From these a rotor was assembled and tested to 93% engine speed, when one blade fractured, causing minor secondary damage to several others. Some of the observations made regarding this test included failure upon retest at lesser load; known lower part strength than bar strength; failure in the stalk (above attachment), which is only a secondary stress level area; and the appearance of a glassy layer on the blade surface after preoxidation to recover strength loss realized with machining. Because of these results, numerous material evaluations, special mechanical tests, examination of the failure surface of many blades and test bars, examination of the finite element analysis, and a statistical examination of the test sequence were initiated. It has been shown that the variations in the attachment method (compliant layers, dovetail slots, system friction, etc.) can produce a significant failure probability upon retest, even at reduced speeds. Sixty-two blades have now been spin tested to 117% rotor speed, with 48 being qualified. These will undergo a second 117% spin early in the next report period, followed by a rotor spin test at 108% speed to yield a rotor with a high probability of survival upon engine operation at 100% speed.

Many activities will carry over in the first quarter of 1981, but current part inventories with the test procedure described above should yield a rotor for engine operation despite the lower than anticipated strength of the parts and variability of attachment parameters. Efforts are also continuing to raise material strength levels simultaneously to eliminate the need for extensive qualification tests and attendant part losses.

The ceramic gasifier nozzle and tip shroud assembly shown in Figure 4 has produced mixed results. During the previous report period, a ceramic nozzle and tip shroud assembly had been thermal shock qualification tested to 1038°C (1900°F) with the original thermal shock rig facility. This assembly has now been operated in engine C-4 for 616 hr without incident to 1038°C (1900°F). The nozzle in the engine includes reaction-bonded and sintered alpha silicon carbide vanes; reaction-bonded silicon carbide inner support, outer support, and tip shroud; and Refel silicon carbide strut shells and retaining ring (see Figure 5). In all, 36 individual ceramic parts have operated in concert with their supporting metal structure.

During this report period a second nozzle-tip shroud assembly was thermal shock tested to conditions of the 1900°F-configuration preparatory to increasing the temperature to 1132°C (2070°F). Multiple fractures were sustained to the reaction-bonded silicon carbide inner support, outer support, and turbine tip shroud when the assembly was subjected to five thermal shock cycles. Extensive failure surface examination, visual examination of the metal parts, dimensional checks, and stress studies using the finite element models have been initiated to determine the causes and established corrective actions required. Testing should resume early in the next reporting period. The rig is being modified to more closely simulate engine air cooling of the metal parts and the thermal shock cycle used. A circumferential gas stream thermal gradient resulting from leakage around the strut interfaces with the plenum and inner annulus is being corrected by sealing at the interfaces.

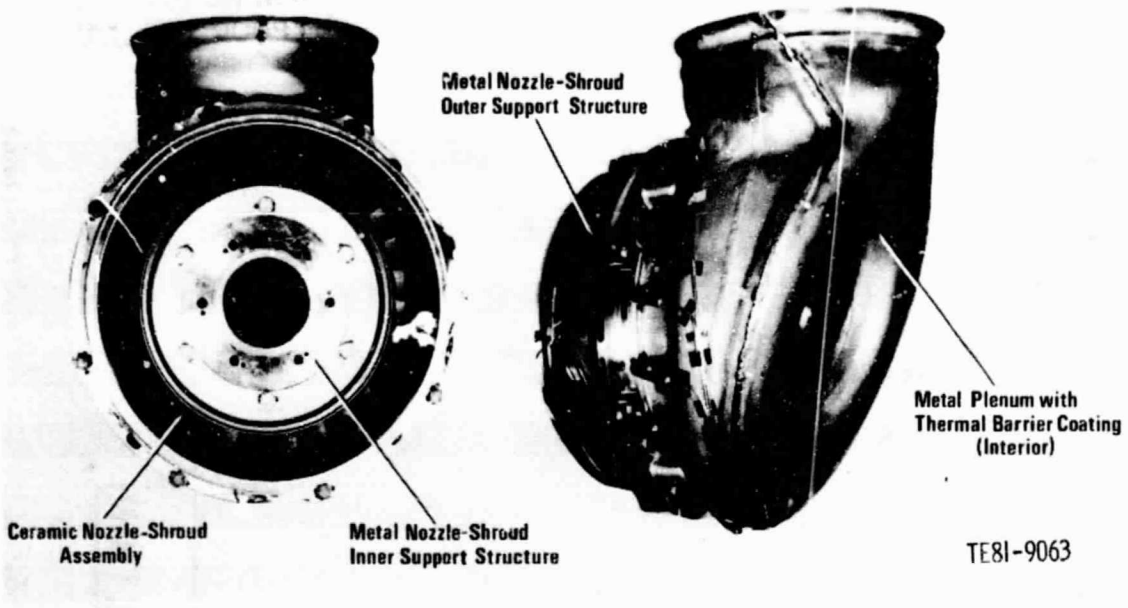

Figure 4. Initial 2070°F-configuration development test.

Modifications are being made to metal parts to provide more clearance with the ceramic parts where mechanical pinching was established. Finally, the outer support is being slotted to accommodate the thermal shock stresses. Each of these corrective actions is in process to permit resumption of testing leading to 1132°C (2070°F) qualification with current ceramic part inventories.

The plenum and inner annulus shown in Figure 6 are available for rig testing. They must await resumption of ceramic nozzle testing to permit testing to 1132°C (2070°F). Metal plenums such as those shown in Figure 4 are available and can be used in place of the ceramic plenum assembly.

The final component in the 2070°F-configuration is the regenerator system, the disk assembly of which is shown in Figure 6. The disk assembly closely resembles that of the previous 1900°F-configuration. The disk core material is a 1100°C (2012°F) alumina silicate of the triangular matrix construction. Six disks have been operating in the engines for 1320 hr at 788°C (1450°F) inlet temperature. Meanwhile, disks have been run with their companion seals for 16- and 50-hr runs at 927°C (1800°F), the anticipated worst case for the 2070°F and 2265°F engine configurations. Rig testing of a new hot seal system has led to introduction of the first set of seals to the engine. Leakage has approached that with the best initial configuration seals. The nickel oxide/calcium fluoride hot seal wearface composition has been evaluated at 927°C (1800°F) without material degradation or excessive friction when placed against the 1100°C (2012°F) rated alumina silicate disk. This seal is unique because its mechanical construction is designed to avoid buckling of the metal substrates, which would cause excessive leakage, and because the back side is air cooled to preserve the life of the leaf seal material. At this time the seals are in use in engine C-4, and it appears that a suitable regenerator system is now available for 2070°F-configuration operation.

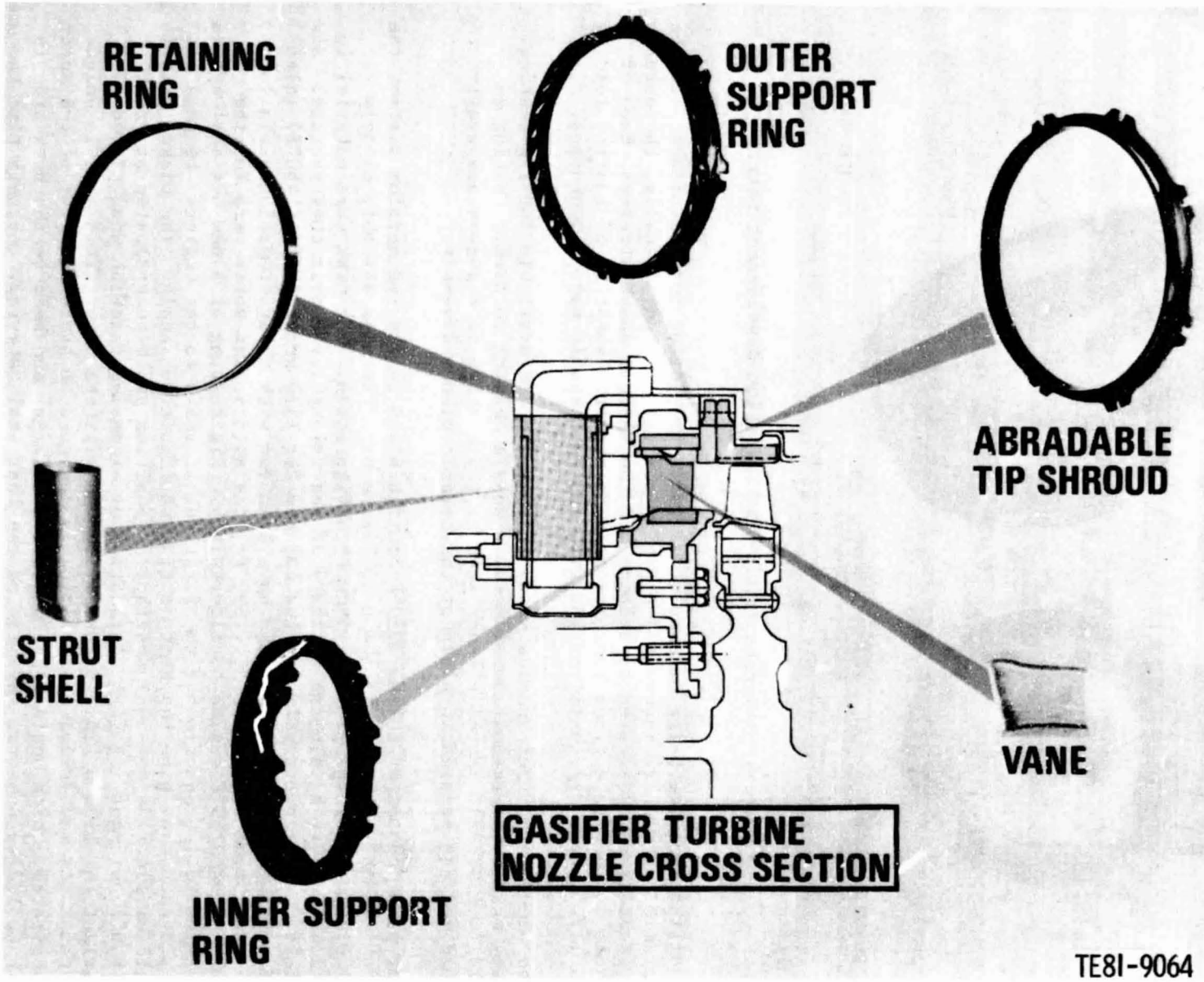

Figure 5. 2070°F-configuration engine nozzle.

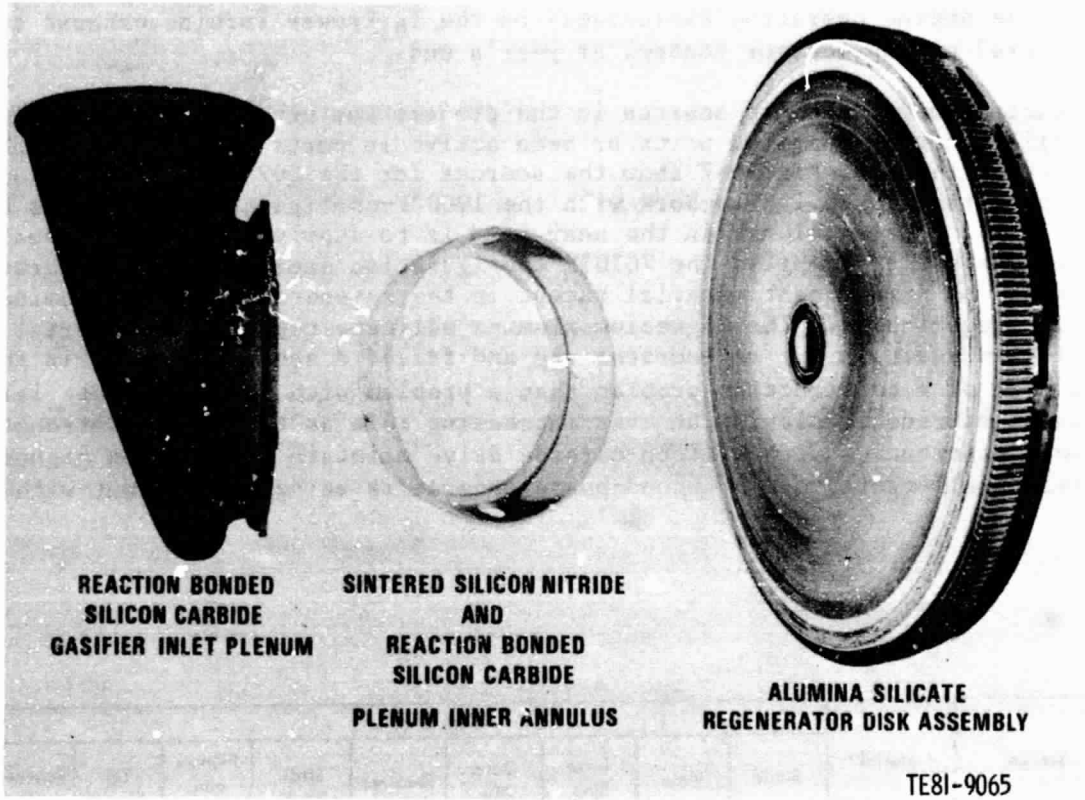

Figure 6. Large ceramic components.

In summary, the development tasks leading to the 2070°F-configuration are on course after the two disruptive failures, which led only to delay of full 2070°F-configuration engine operation. The experience has been valuable and the progress steady in the application of ceramic parts to the gas turbine engine.

During the reporting period, engines C-1 and C-4 accumulated 665 operating hr, bringing the project total to 7084. Engine C-1 was used to complete the development test and qualify three microprocessor control systems for 2070°F-configuration engine use. Two significant experiments were carried out on the 1900°F-configuration parts in the nozzle assembly as testing of the control proceeded. An abradable coating of eccospheres filled with yttrium-stablized zirconia was applied to the metal shroud of the gasifier section. Examination after 50 hr of operation showed that the coating was intact, and there was little sign of erosion. There has been a tip rub, and the performance of the coating appeared far superior to that for any abradable coating tested in this project. The vanes of this nozzle assembly had thermocouple approaches for

ceramic parts attached. Again after 50 operating hr, they were found structurally sound and adhering to the ceramic parts. This suggests that ceramics can be instrumented as the need arises. Engine C-4 was primarily used to run the durability hours accumulated on the 2070°F-configuration nozzle/tip shroud assembly. Three T_6 microprocessor controls were qualified on engine C-4, with the engine operating exclusively on the T_6 (power turbine exhaust temperature) microprocessor control at year's end.

Participation of ceramic sources in the project has been encouraging, with ten suppliers having supplied parts or been active in parts fabrication. The shaded portions of Figure 7 show the sources for the 2070°F-configuration ceramic parts through 1981. Work with the 1900°F-configuration parts has been completed. The challenge in the near term is to supply the 80 individual ceramic parts that comprise the 2070°F-configuration engine. Silicon carbide remains the predominant material except in the regenerator, where alumina silicate predominates. The magnesium alumina silicate regenerator material was evaluated again in the regenerator rig and failed a second time; again this was more of a construction problem than a problem with the basic material. Silicon nitride is playing an ever increasing role as the current strength level deficiencies with silicon carbide drive maintain interest in higher-strength alternatives. A second-phase program is being carried out with the

Source	Material*	Component								
		Blade	Vane	Inner Ring	Outer Ring	Retainer	Strut Shell	Plenum and Annulus	Tip Shroud	Regenerator Disk
Carborundum	SiC	▨	▨	▨	▨	▨	▨	▨	▨	
GTE Labs	Si_3N_4	▨			▨					
Norton	SiC							▨		
Pure/BNF	SiC		▨		▨	▨	▨		▨	
Kyocera	SiC			▨						
NGK	Si_3N_4			▨			▨	▨		
NGK	MAS									▨
Corning	AS									▨

*SiC—silicon carbide, Si_3N_4—silicon nitride, MAS—magnesium alumina silicate, AS—alumina silicate.

TE81-9066

Figure 7. 2070°F-configuration ceramic source summary.

Carborundum Company to continue development of selected parts. These include plenum and inner annulus dimensional ring structures, alternative abradable tip shroud concepts, and blade yield improvement. GTE laboratories are nearing completion on process development of the sintered silicon nitride blade. Initial parts were anticipated in the first quarter of 1981. As indicated in Figure 7, each part now is covered or will be covered upon parts receipt from fabrication in process by either an alternative material or source. Follow-on procurement has been initiated, covering parts requirements through the fall of 1981. As a result of the ceramic machining technology development activities, DDA has now machined at least one of each ceramic component. Of particular note is qualification of creep feed grinding of the ceramic blade attachment and subsequent completion of an initial lot of blades. In addition, the particularly delicate plenum machining has been completed, yielding the first plenum for test. With the initial engine complement of ceramic parts available, a significant challenge has been met, as ceramic parts have been fabricated to the complex shape and dimensional requirements for turbine engine application.

The two primary activities in the ceramic materials development are (1) the task of assessing the structural quality of 2070°F-configuration parts being received and (2) the failure site and material investigations surrounding the blade and nozzle/tip shroud rig failures. Abradability activity centered upon DDA approaches to coatings, with eccospheres filled with yttrium-stabilized zirconia and zirconia fabric tape systems. Both are showing promise during rig tests. A ceramic-bladed rotor is now in use for valuating abradability. To date, no ceramic blade breakage has been experienced in the tests, which were conducted at room temperature. Other activities that continued during this report period are advanced NDE technology development, scanning laser acoustic microscopy (SLAM) in the dark field, and scanning photoacoustic spectroscopy (SPAS). SPAS evaluation with metal specimens has progressed from surface to subsurface flaws, leading to experiments on ceramic specimens in the next reporting period. Equipment adapters are being fabricated to permit use of SPAS on the ceramic blades. This will mark the first direct application of this advanced technology to the project's parts. Past regenerator core matrix strength/structure relationship and NDE technology are now being applied to parts, with both X-ray inspection and process modifications being made to ensure proper core matrix structure. Strength testing continues to indicate that the 1100°C (2012°F) matrix is superior to the previous 1000°C (1832°F) matrix. Using existing high-time engine disk samples, a study of ion migration (nickel, calcium and fluorine) and its impact on regenerator core matrix strength is in progress, due for completion in early 1981.

Design activities are progressing on the 2265°F-configuration engine. The combustor with six ceramic parts has been detached, with award of process development or initial parts to be made early in 1981. The power turbine design is proceeding, with only the first of two stages incorporating a ceramic nozzle and tip shroud. This decision was made to adapt to FY 81 and FY 82 funding limits. The second-stage nozzle would not contribute new ceramic technology, since it represents a resized version of the first-stage. With a metal second-stage nozzle assembly, the operating life of the 2265°F-configuration engine is shortened. It is within limits that will permit structural testing, with periodic parts replacement as a precaution, and a limited over-the-road fuel consumption run in the truck as planned. The ceramic parts

drawings of the first-stage power turbine nozzle and tip shroud will be available early in the second quarter of 1981 to permit initial part fabrication. Associated metal part design and ceramic part analysis will continue through 1981, leading to engine testing in late 1982.

The overall results of design, analysis, ceramic process development, and ceramic component testing continue to reflect favorable progress, leading to operation of the second-generation ceramic gas turbine engine at 1132°C (2070°F) in the next report period. Although development problems were encountered with ceramic parts, these have been analyzed and corrective action is in process at the close of the report period. This period was marked by completion of fabrication of the initial 2070°F-configuration ceramic parts, accumulation of significant engine time on the 2070°F-configuration nozzle and tip shroud assembly plus the advanced regenerator system, qualification spin testing of a complement of ceramic rotor blades at a 79% yield, successful completion of the 1900°F-configuration engine development, and successful development testing of a very promising abradable tip shroud material for application with ceramic or metal rotor blades. Further reports on this project will be issued semiannually.

SUMMARY

The test activities that occurred during the reporting period were conducted on both the 1900°F-configuration and 2070°F-configuration ceramic components. These components are first proof tested in rigs and then tested in engines. The engines used to evaluate the ceramic components were C-1 and C-4, which are IGT 404-4 models modified to accept ceramic parts rated at 1038°C (1900°F) gasifier rotor inlet temperature.

The engine test hours during the reporting period are plotted in Figure 8. Both 1900°F-configuration and 2070°F-configuration ceramic components were engine tested. The 1900°F-configuration ceramic component test activities are plotted in Figure 9 (gasifier turbine vanes and shroud), the 2070°F-configuration ceramic component test activities in Figure 10 (gasifier nozzle), and the ceramic regenerator test activities in Figure 11. Table II summarizes the engine test hours accumulated on all ceramic components since the start of testing.

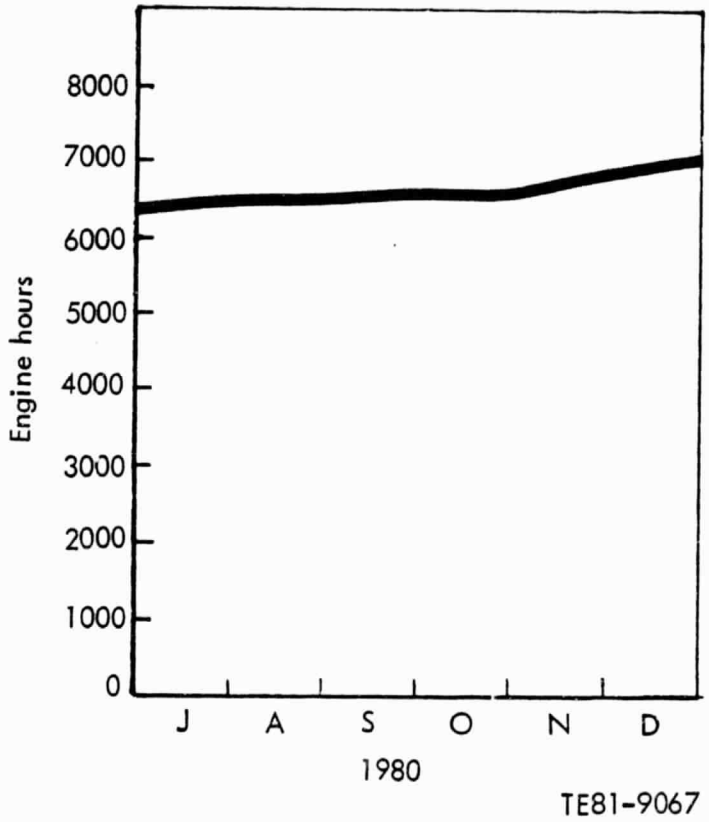

Figure 8. Engine test hour summary.

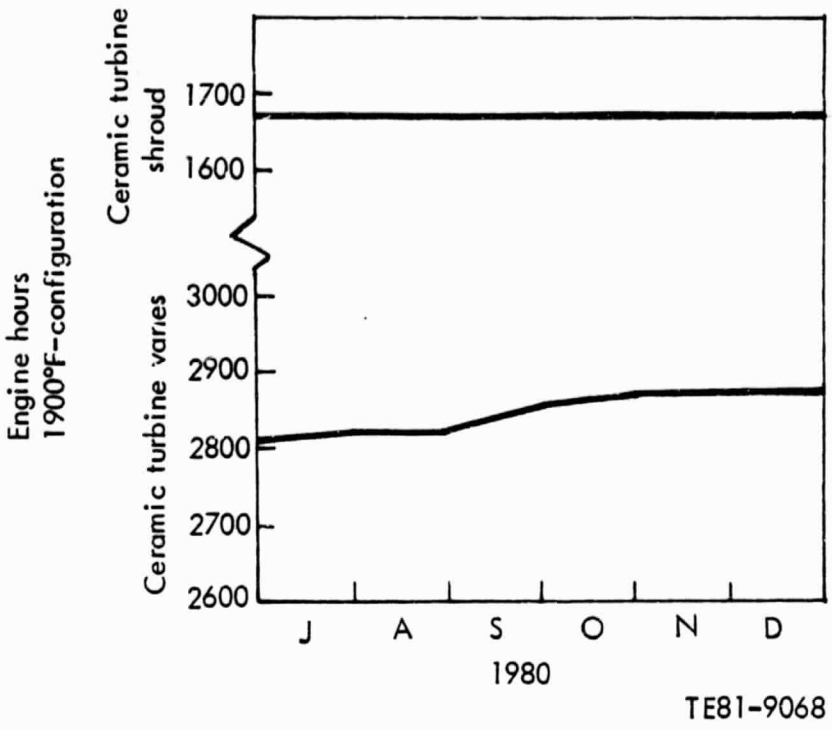

Figure 9. 1900°F-configuration gasifier turbine vane and shroud engine hours.

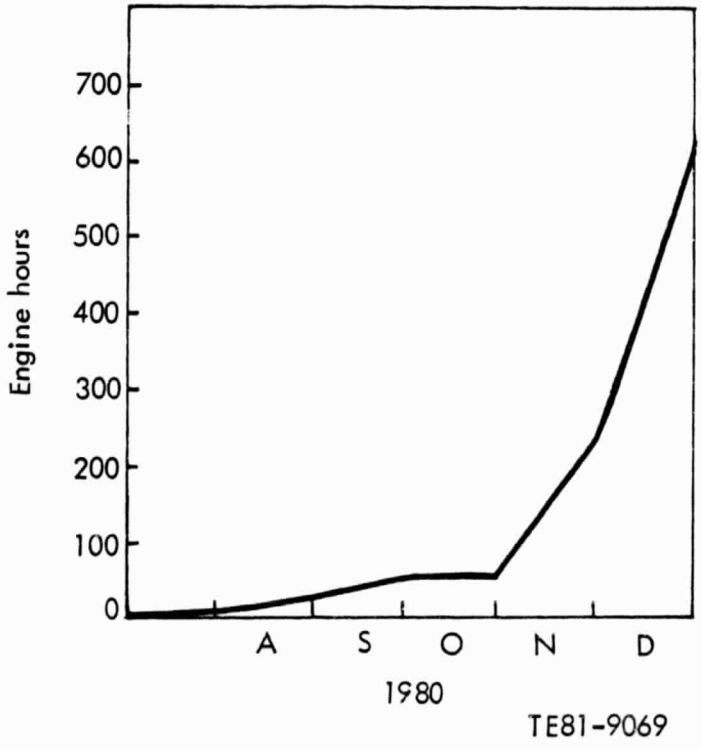

Figure 10. 2070°F-configuration gasifier turbine nozzle engine hours.

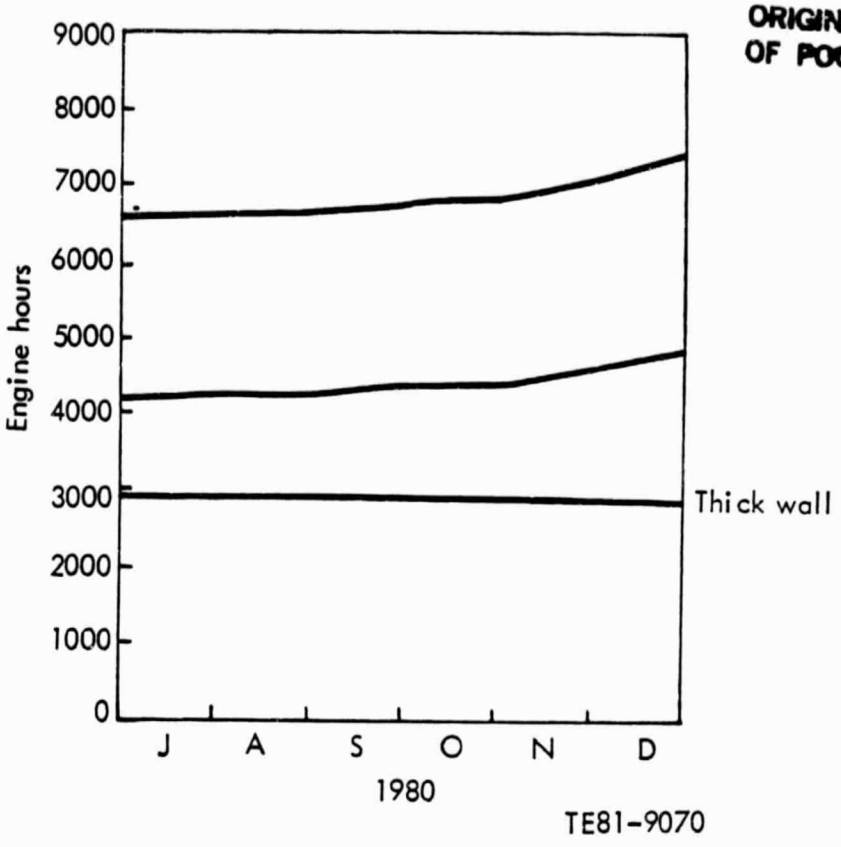

Figure 11. Ceramic regenerator engine hours.

TABLE II. ENGINE DURABILITY HOURS OF CERAMIC COMPONENTS

Component	Maximum hours for one component	Total durability (hours)
Thick-wall regenerators	1808	2833
Thin-wall regenerators		
1000°C (1832°F) rated	3050	3938
1100°C (2012°F) rated	1059	1314
1900°F-configuration		
Gasifier turbine vanes		
Silicon carbide (Carborundum)	1512	2791
Silicon carbide (Pure)	435	435
Silicon nitride (AiResearch)	81	81
Gasifier turbine shroud		
Silicon carbide (Carborundum)	985	1546
Silicon nitride (GTE Sylvania)	113	113
LAS (Corning)	11	11
2070°F-configuration		
Gasifier turbine nozzle assembly	616	616

Rig development and qualification testing of the three-piece 2070°F-configuration inboard regenerator seal continued during this reporting period. The initial engine test with a three-piece seal was completed. Development testing of the 2070°F-configuration gasifier nozzle in the thermal shock rig continued, while durability testing of a previously qualified nozzle was conducted in engine C-4.

Table III lists the 2070°F-configuration ceramic gasifier nozzle components tested and those that qualified for engine testing. The hot engine simulator rig was assembled and operated with a metal gasifier turbine rotor and metal substitutes for the 2070°F-configuration gasifier nozzle ceramic components. The hot engine simulator rig is ready to qualify ceramic blades for engine testing.

TABLE III. SUMMARY OF 2070°F-CONFIGURATION GASIFIER NOZZLE COMPONENT RIG TESTING

Ceramic component	Number rig tested	Number qualified for engine test
Vanes		
Reaction-bonded SiC	52	48
Alpha SiC	9	9
Shroud		
Reaction-bonded SiC	3	1
Outer vane support ring Reaction-bonded SiC	2	1
Inner vane support ring Reaction-bonded SiC	3	1
Vane retaining ring Purebide Refel SiC	3	3
Strut shells		
Purebide Refel SiC	6	6
Alpha SiC	6	4

ASSEMBLY AND LABORATORY TEST ACTIVITIES

Objectives

The primary objectives of the engine test activities during the reporting period were to conduct durability testing of the 2070°F-configuration ceramic gasifier turbine nozzle and to continue development of and qualify for 2070°F-configuration engine testing of both the T_6 microprocessor control system and the improved engine block cooling configuration.

Discussion

Engine C-1

Engine C-1 accumulated 84 hr of testing, for a total test time of 3354 hr. Reaction-bonded silicon carbide (SiC) 1900°F-configuration gasifier turbine vanes from Carborundum were tested. The ceramic regenerators tested were thin-wall alumina silicate (AS) material rated at 1100°C (2012°F). The inboard regenerator seals were 1900°F-configuration single piece seals with crossarm wearface material of 70% NiO/30% CaF_2. The primary engine test activity consisted of development and successful qualification of the T_6 microprocessor control system for use in the 2070°F-configuration engine test program. During control development testing, a secondary test activity was performed. An abradable plasma-sprayed coating was applied to the gasifier tip shroud area of the nozzle. This coating was a dual-density zirconia coating that demonstrated abradability without measurable performance loss during the testing conducted in this reporting period. No visual inspection was permitted because of the control development activity. Early in the next reporting period a nozzle inspection is planned.

Engine C-4

Engine C-4 accumulated 616 hr during the reporting period, for a total test time of 657 hr. The testing was entirely devoted to durability evaluation of the first rig-qualified 2070°F-configuration ceramic gasifier nozzle assembly. Two ceramic regenerators tested were thin-wall alumina silicate (AS) material rated at 1100°C (2012°F). The inboard regenerator seals were 1900°F-configuration single piece seals with crossarm wearface material of 70% NiO/30% CaF_2. Late in the reporting period the first 2070°F-configuration three-piece inboard seal was tested for 25 hr. The crossarm wearface material was 90% NiO/10% CaF_2 and the seal leaf structure has air-cooling provisions that are required for 982°C (1800°F) regenerator inlet temperature operation.

The engine block was the ambient air-cooled 2070°F-configuration, which resulted from previous development testing of a prototype air-cooled block in engine C-2 (Ref. 1). The block in engine C-4 is the 2070°F-configuration design, which has been successfully qualified for 1132°C (2070°F) operation. In addition to air cooling, the block featured improved "wet blanket"-type insulation, which is formed to intimately fit the block during installation, then cured to harden into a rigid layer.

Periodic inspections during the durability test were conducted. No nozzle or regenerator problems were evident and no significent engine performance deterioration was measurable. Late in the reporting period the T_6 microprocessor control was used during automatically controlled durability testing with no problem. Just prior to the end of the reporting period, the 2070°F-configuration three-piece inboard regenerator seal was installed and tested for 25 hr. The testing scheduled for early in the next report period includes block cooling and regenerator system performance at 871°C (1600°F) regenerator inlet temperature.

III. STRUCTURAL CERAMIC MATERIALS DEVELOPMENT

CERAMIC COMPONENT CHARACTERIZATION

Summary

During this reporting period, efforts were concentrated on the evaluation of components made from new candidate ceramic materials. Component materials evaluated included a reaction-sintered silicon carbide (Annawerk CS 600, 1900°F-configuration vane), a sintered silicon carbide (NGK-Locke, 1900°F vane), a sintered silicon nitride (NGK-Locke, 1900°F-configuration vane and 2070°F-configuration plenum), and a sintered silicon carbide (Kyocera International, 2070°F-configuration inner support ring). The room-temperature fast-fracture strength (modulus of rupture) and microstructure of these new materials were of primary concern. Particular attention was also paid to determining the nature of strength-controlling flaws through fracture surface analysis.

Objective

The primary objective of this task was to establish appropriate material characteristics to support the design, development, and testing of hot-section components for the 2070°F- and 2265°F-configuration engines. A secondary objective was to evalute new candidate materials and compositions and to assess which if any should be used in specific component development efforts. Work undertaken in this reporting period focused on the evaluation of such new materials.

Discussion

Annawerk Reaction-Sintered Silicon Carbide (SiC), CS-600--1900°F-Configuration Vane

Annawerk CS-600 is a slip-cast, reaction-sintered silicon carbide material. It has an average density of 3.064 g/cm^3. The microstructure is coarse, consisting of very large (20-50 μm in diameter) and small (1-3 μm) SiC grains with free silicon occupying the remaining porosity (Figure 12). A small quantity of large graphite particles (10-30 μm) are also present.

The average room temperature MOR (four-point loading) strength for the as-fired surface condition was 182.10 MPa (26.41 ksi), with a standard deviation of 12.41 MPa (1.80 ksi). The MOR strength of machined bars was 291.95 MPa (42.34 ksi), with a standard deviation of 36.78 MPa (5.33 ksi). All specimens failed from surface sites in both as-fired and machined materials. A typical fractograph of a failure origin is shown in Figure 13.

NGK-Locke Sintered SiC--1900°F-Configuration Vane

This material, a pressureless sintered SiC, was reported previously to have a low density (2.57 g/cm^3) and low strength (219.4 MPa [31.82 ksi]). During this reporting period, testing at 1050°C (1922°F) was completed. The measured MOR strength at 1050°C (1922°F) was 203.55 MPa (29.52 ksi), with a standard deviation of 19.26 MPa (2.79 ksi). This is essentially unchanged from the room temperature strength measured earlier. All specimen failures seemed to originate at surface pores.

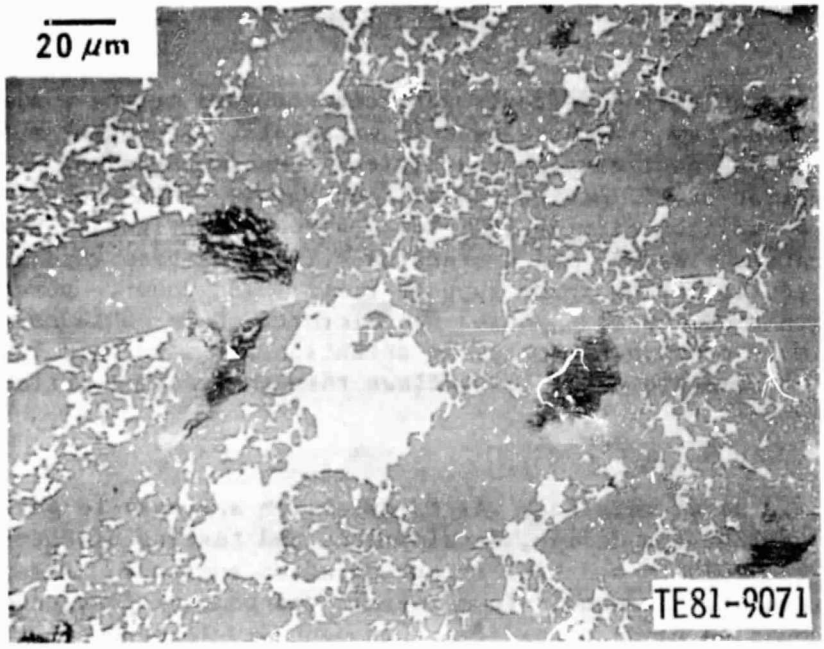

Figure 12. Optical micrograph of a polished Annawerk reaction-sintered SiC (CS-600), 1900°F-configuration vane qualification bar. Gray phase SiC, white phase free silicon, dark phase graphite.

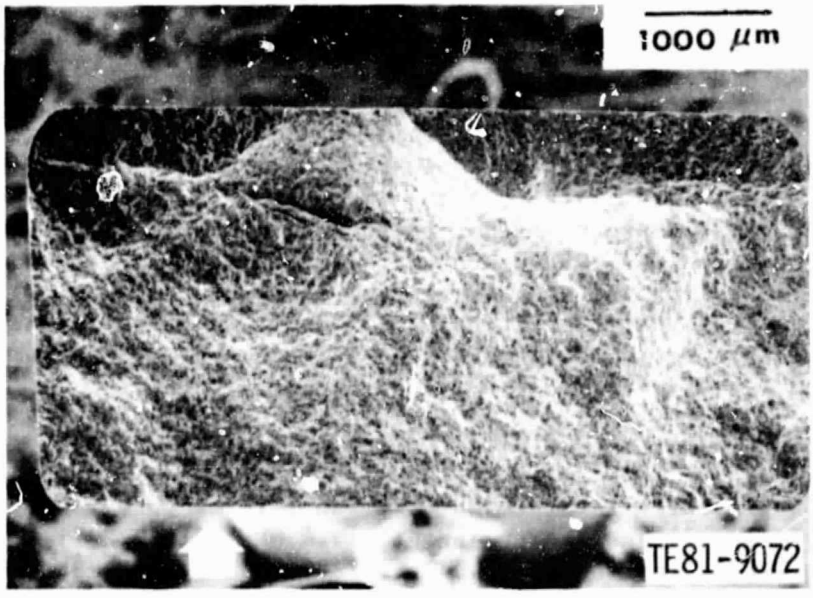

Figure 13. Scanning electron microscope (SEM) fractograph of an Annawerk reaction-sintered SiC (CS-600), 1900°F-configuration vane qualification test bar. Failure probably started at surface side indicated by white arrow.

NGK-Locke Sintered Silicon Nitride (Si_3N_4)--1900°F-Configuration Vane

The pressureless sintered Si_3N_4 from NGK-Locke had an average density of 2.90 g/cm^3, very large interconnected pores, and an MOR strength at room temperature of 355.94 MPa (52.63 ksi). Tests at 1050°C (1922°F) showed a decrease in strength from the room temperature value. The average strength at 1050°C (1922°F) was only 252.33 MPa (36.60 ksi), with a standard deviation of 19.09 MPa (2.77 ksi). All failures of the specimens originated in surface sites. A typical example is shown in Figure 14.

NGK-Locke Sintered Si_3N_4--2070°F-Configuration Plenum

The most recently received NGK-Locke sintered silicon nitride material for a 2070°F-configuration plenum has a higher density (3.042 g/cm^3) than earlier versions. Large pores are still present throughout the microstructure, however. X-ray analysis indicates both magnesium and cerium are present in this material. Previous analysis of the 1900°F-configuration vane material revealed only the presence of MgO.

The average room-temperature MOR strength in the machined condition is 368.28 MPa (53.41 ksi), with a standard deviation of 22.47 MPa (3.26 ksi). Internal pores and a large ball-type inclusion about 100 μm in diameter were found to be the strength-controlling defects. The ball inclusion, shown in Figure 15, is of the same composition as its surrounding matrix but is poorly bound to the matrix.

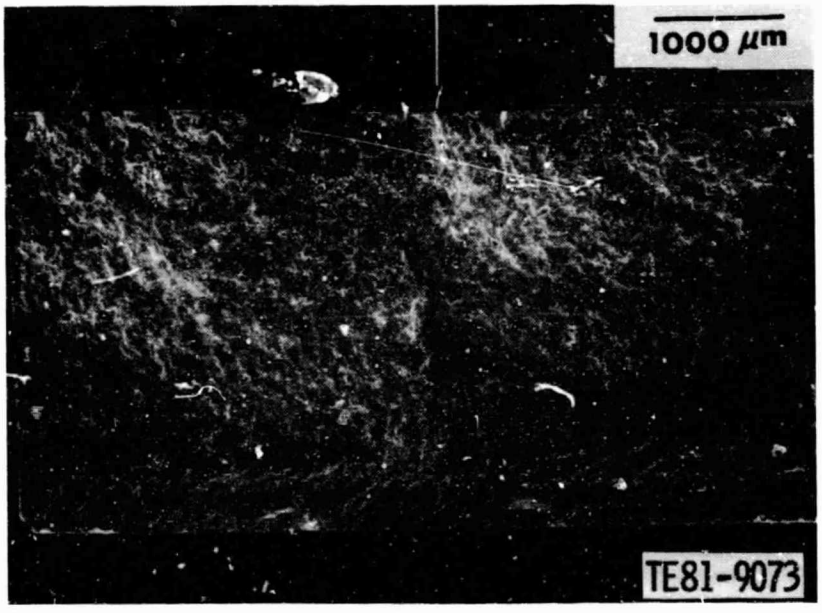

Figure 14. SEM fractograph of an NGK-Locke sintered Si_3N_4, 1900°F-configuration vane qualification test bar tested at 1050°C (1922°F).

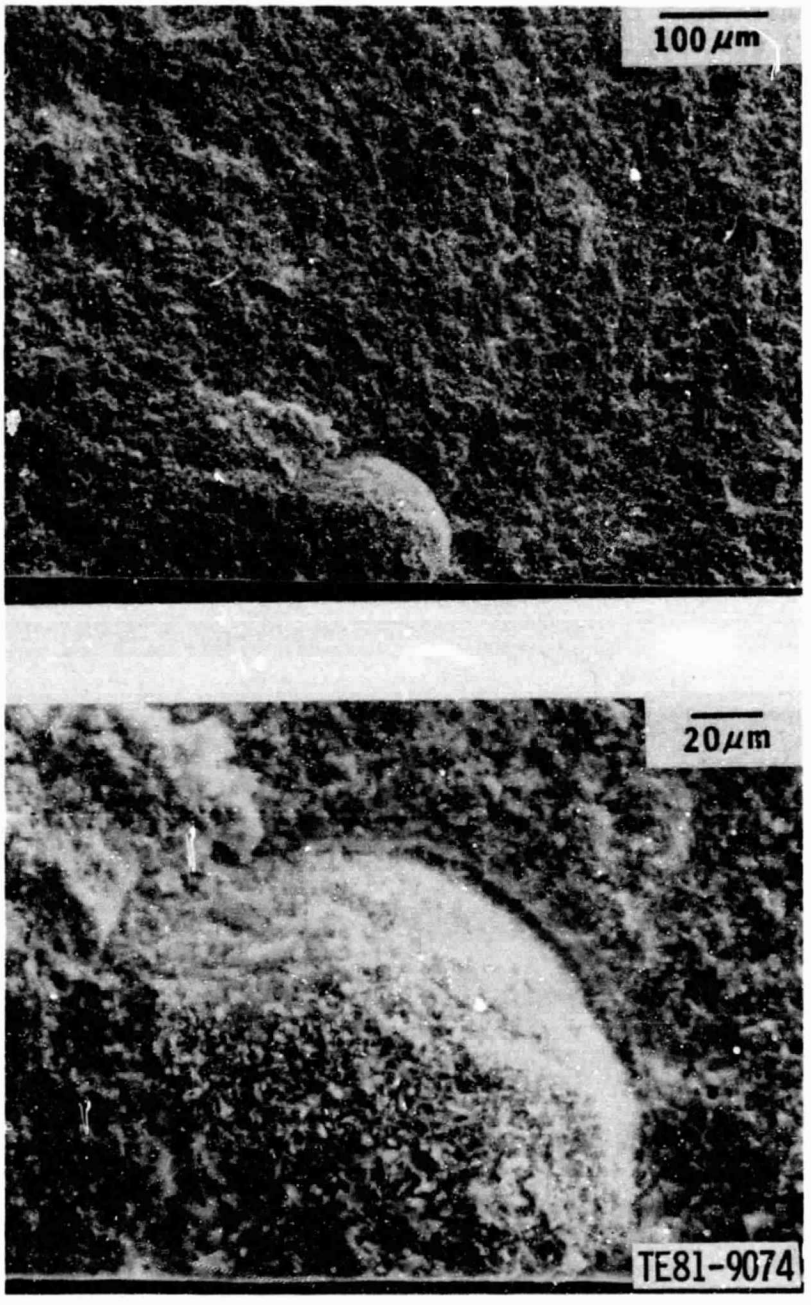

Figure 15. SEM fractographs of an NGK-Locke sintered Si_3N_4, 2070°F-configuration plenum inner annulus test bar. The initial flaw is a large ball-type inclusion.

Kyocera Sintered SiC--2070°F-Configuration Inner Support Ring

Kyocera sintered silicon carbide was previously reported to be a fine-grained (grain diameter 2.5 μm) and dense (3.13 g/cm^3) material. Its room temperature MOR strength was 410.12 MPa (59.49 ksi). The recently received 2070°F-configuration inner support ring was isopressed, machined, and sintered. The density of this material is 3.135 g/cm^3 and the average grain diameter is 4 μm (Figure 16).

Specimens of this material tested in the machined condition at room temperature produced an average MOR strength of 357.61 MPa (51.87 ksi), with a standard deviation of 46.84 MPa (6.79 ksi). The strength-controlling flaws were primarily surface flaws and surface pores.

TIP SHROUD ABRADABILITY

Summary

This task is directed toward the development of abradable seal materials compatible with metal and ceramic turbine blading.

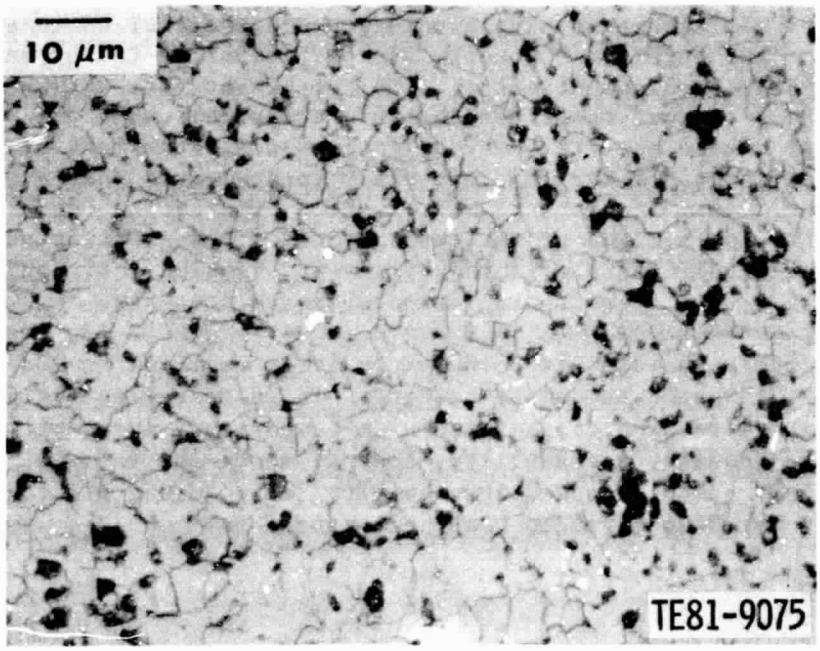

Figure 16. Optical micrograph of a polished Kyocera sintered SiC, 2070°F-configuration inner support ring test bar.

Preliminary abradability and erosion testing of a plasma-sprayed zirconia/eccosphere system has resulted in a performance level with silicon carbide blading significantly greater than has been possible with metallic blading. Further, a laminated zirconia fabric material has been developed that has exhibited excellent abradability characteristics against a metal blade tip, along with moderate erosion resistance. There appears to be significant potential for further improvement in this system, particularly with respect to ceramic blading.

Studies have been initiated to deposit abrasive materials on turbine blade tips as a means of improving materials system abradability. Both metallic and ceramic blading are included in the studies.

Objective

The goal of this effort is to develop ceramic-based abradable materials with associated processing specifications compatible with metallic-bladed turbines operating at temperatures of 1038°C (1900°F) and with ceramic-bladed turbines operating at temperatures of 1240°C (2265°F). In addition to abradability, these seal materials must also demonstrate a high degree of resistance to hot gas and particulate erosion. Resistance to thermal shock, fatigue, and oxidation is also essential for success.

To achieve this goal, a dual-path approach has been taken to increase the probability of reaching a viable solution. Commercial sources of ceramic materials for the turbine components are participating to varying degrees in the abradable seal development effort. To complement this external effort, DDA is investigating ceramic materials that are compatible with the ceramic engine structures. These materials investigations are extensions of DDA's basic work in areas of abradable seal and materials technology. They are directed towards the identification and modification of existing ceramic materials in an effort to improve the properties that offer the greatest potential for satisfying the requirements of abradability and erosion resistance. These materials include both freestanding structures and coatings.

All candidate materials are to be extensively examined in a series of laboratory test rigs prior to engine testing. These test rigs include low-speed abradability screening, high-speed/high-temperature abradability, aerodynamic/particulate erosion, permeability, thermal shock and fatigue, and oxidation. Both the low- and high-speed abradability rigs can use silicon carbide blading as well as Mar-M246 stylized blade elements.

Discussion

Materials Screening

Materials screening studies were continued, with the major emphasis placed on in-house efforts to develop abradable systems composed of mineral compacts, zirconia-filled laminates, and zirconia/eccosphere plasma-sprayed materials.

Two mineral compact compositions previously described in DDA EDR 10383 (Ref. 1) were fabricated and tested for abradability against a metal blade tip. The current compositions differ from those discussed earlier in that they were fired at a higher temperature to improve erosion resistance. Figure 17 shows

a. 1121°C (2050°F) Bake-out condition

TE81-9076

b. 1177°C (2150°F) Bake-out condition

Figure 17. Mineral compact, low-speed abradability, metal blade tip (X5).

the results of the abradability tests. Both samples were subjected to infeed rates of 0.025 mm/sec (0.001 in./sec) on the low-speed screening rig. Metal transfer was evident almost immediately upon contact, as can be seen in the figure. Erosion resistance was very good, as was expected, and results are shown in Figure 18. Additional samples, not yet tested, have been fabricated to reduce the extreme hardness encountered in the previous test specimens.

Several improved zirconia (Z_rO_2)-filled fabric tape systems were investigated for abradability and erosion characteristics. These improved tapes differed from previously fabricated samples in the type and size of the cloth weave pattern. Results of abradability testing with metal blade tips were encouraging, with at least one of the samples warranting further study.

Four basic zirconia fabrics were investigated:

- o 0.76 mm (0.030 in.) satin weave
- o 0.38 mm (0.015 in.) square weave
- o 0.38 mm (0.015 in.) knit
- o Zircar-supplied 0.76 mm (0.030 in.) satin weave, 65% reduction in volume.

Fabrication techniques for the layups of the zirconia fabric tapes were similar and involved impregnating the tapes with a zirconia cement, followed by several intermediate- and high-temperature thermal treatments.

The Zircar-supplied material was fabricated with a hydraulic press technique, while the other three materials were made by a vacuum bagging process.

Each sample was subjected to low-speed room-temperature abradability tests using a Mar-M246 bladed wheel operating at a tip speed of 27.4 m/sec (90 ft/sec). An incursion rate of 0.025 mm (0.001 in./sec) was used to feed the sample into the rotating blades. Erosion testing was performed at a 45° impingement angle for 30 min using coarse Arizona road dust as the erosive medium.

Figures 19 to 26 show the results of the abradability and erosion tests. In Figure 19, the blade tip rubbed to a depth of 0.64 mm (0.025 in.) with no distress to the tip or the abradable coating. Passage of the blade tip through the material was very smooth. The coarse satin weave pattern can be seen at the base of the rub. Figure 20 shows a 0.25 mm (0.010 in.) deep rub in the 0.38 mm (0.015 in.) square weave laminate. This material is harder than the coarse satin weave laminate and penetration was slightly more difficult than in the previous sample. Some of the weave does not appear to be completely filled in, as can be seen at the base of the rub. Figure 21 shows a 0.51 mm (0.020 in.) deep rub in the 0.38 mm (0.015 in.) knit laminate. The hardness of this laminate falls between that of the previously discussed materials. As can be seen, the rub signature is quite clean and well defined. Figure 22 is a view of the rub signature in the 0.76 mm (0.030 in) satin weave laminate, which had a 65% reduction in layup height. The resultant hardness was significantly greater than in any of the previous samples R15Y = 69, as compared to 14 for the 0.38 mm (0.015 in.) square weave pattern) and the abradability was the poorest of the group. A 0.13 mm (0.005 in.) rub was effected in this material with some difficulty, and both the inlet and exit rub areas had traces of metallic debris.

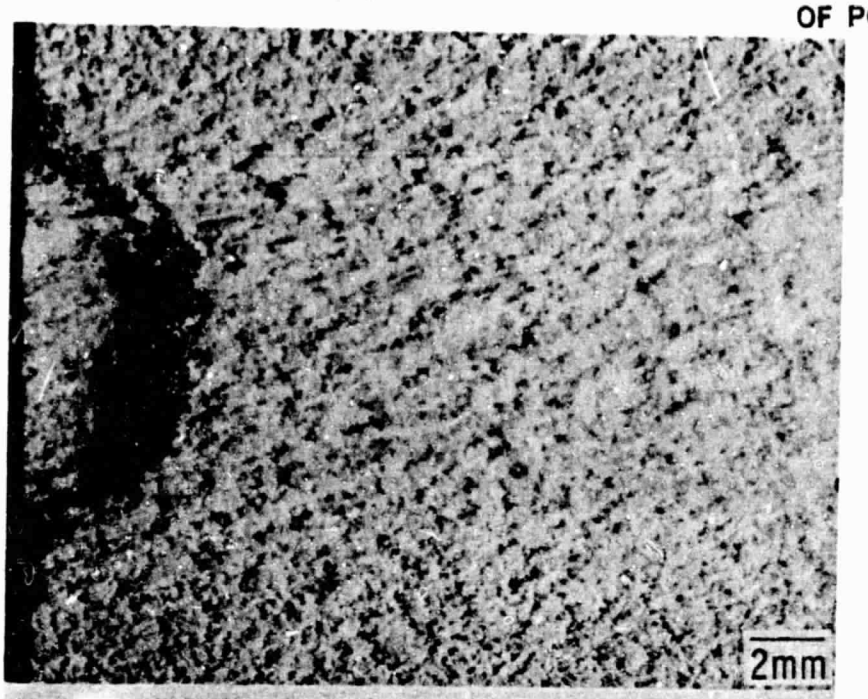

a. 1121°C (2050°F) Bake-out condition, direction of flow ——————→

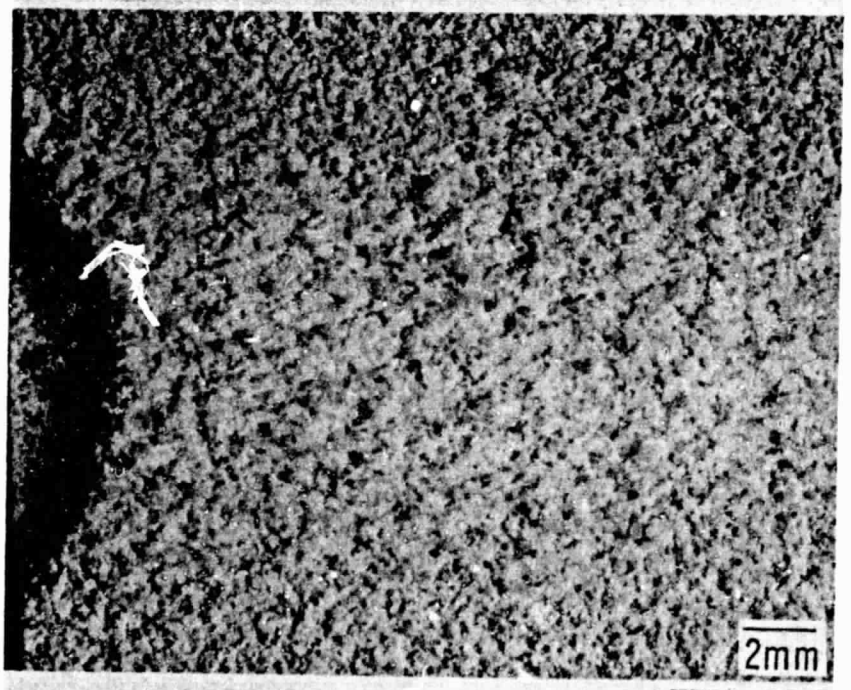

TE81-9077

b. 1177°C (2150°F) Bake-out condition, direction of flow ——————→

Figure 18. Mineral compact, erosion 15° 30 min (X5).

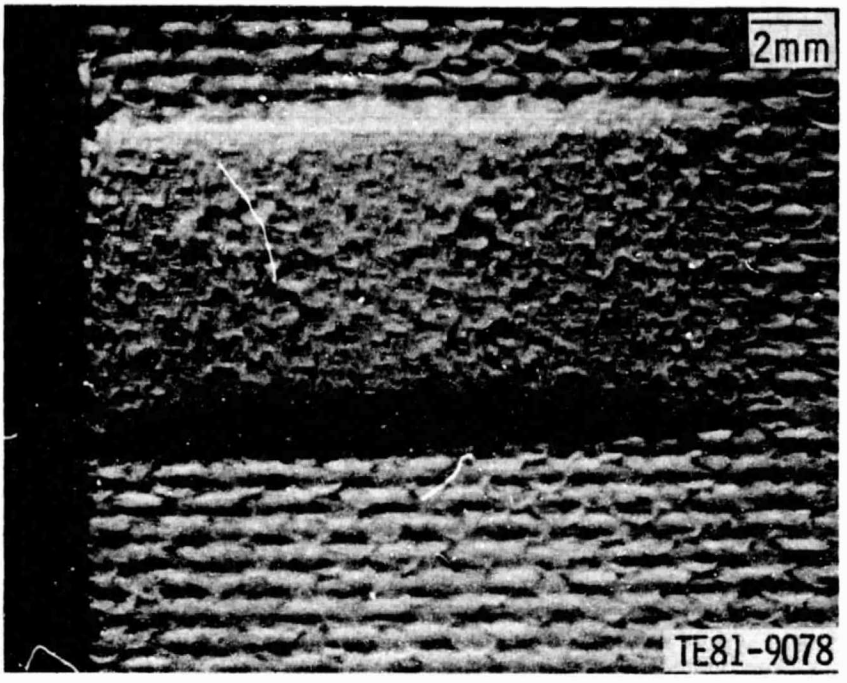

Figure 19. 0.76 mm (0.030 in.) satin weave ZrO_2 laminate, six layers--abradability test 0.64 mm (0.025 in.) deep (X5).

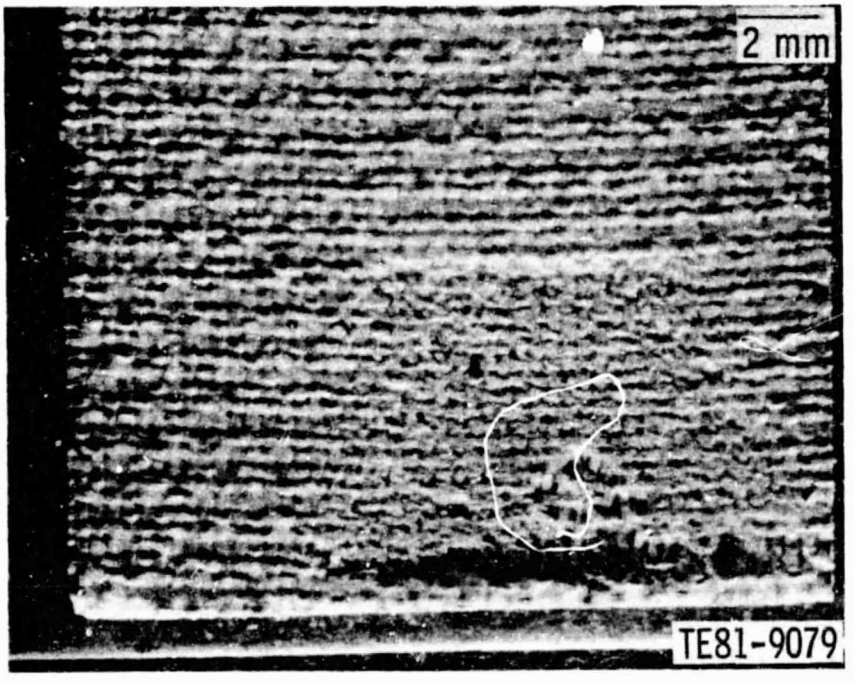

Figure 20. 0.38 mm (0.015 in.) square weave ZrO_2 laminate, 12 layers--abradability test 0.25 mm (0.010 in.) deep (X5).

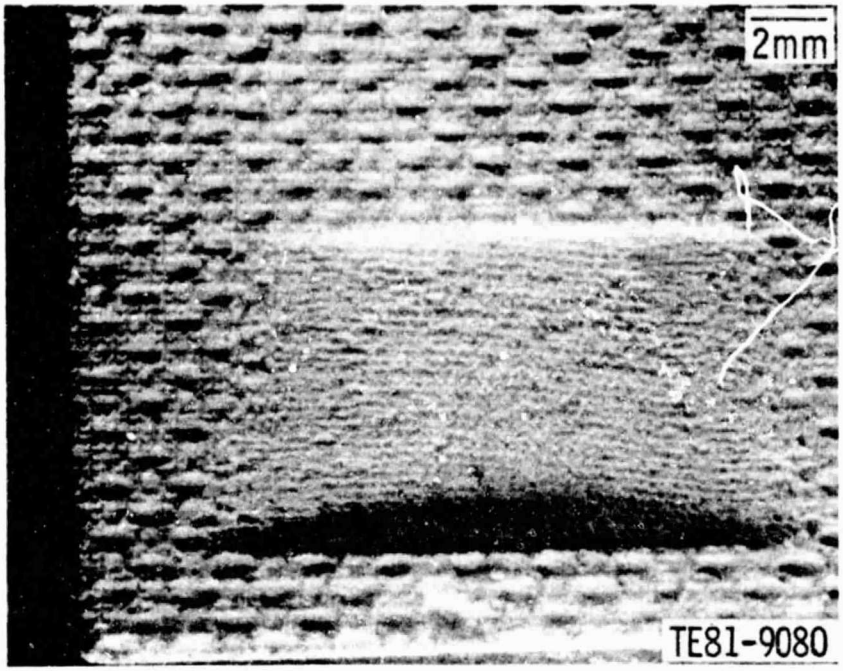

Figure 21. 0.38 mm (0.015 in.) ZrO_2 laminate, 12 layers--abradability test 0.51 mm (0.020 in.) deep (X5).

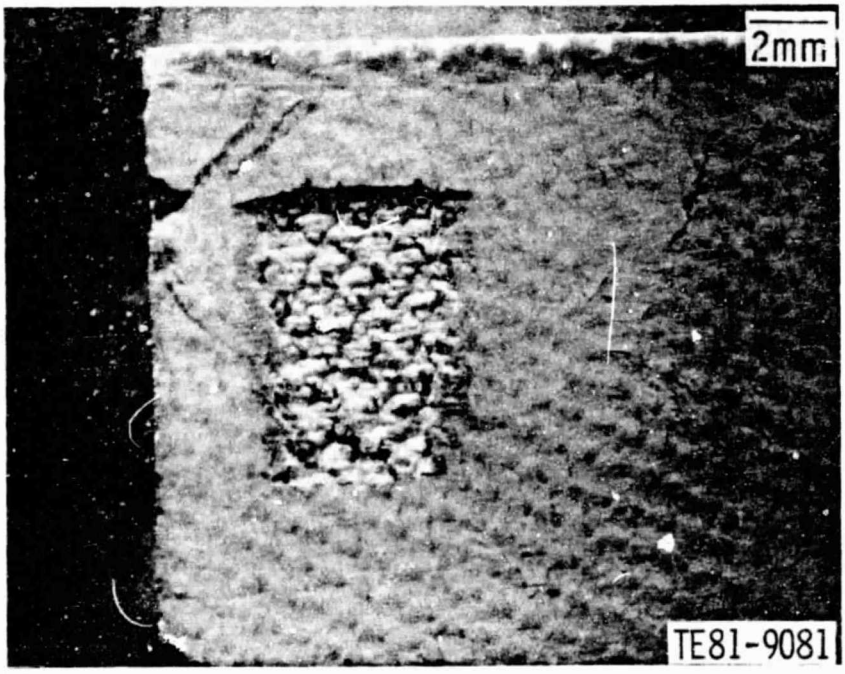

Figure 22. Zircar 0.76 mm (0.030 in.) satin weave ZrO_2 laminate--65% lay-up reduction, abradability test 0.13 mm (0.005 in.) deep (X5).

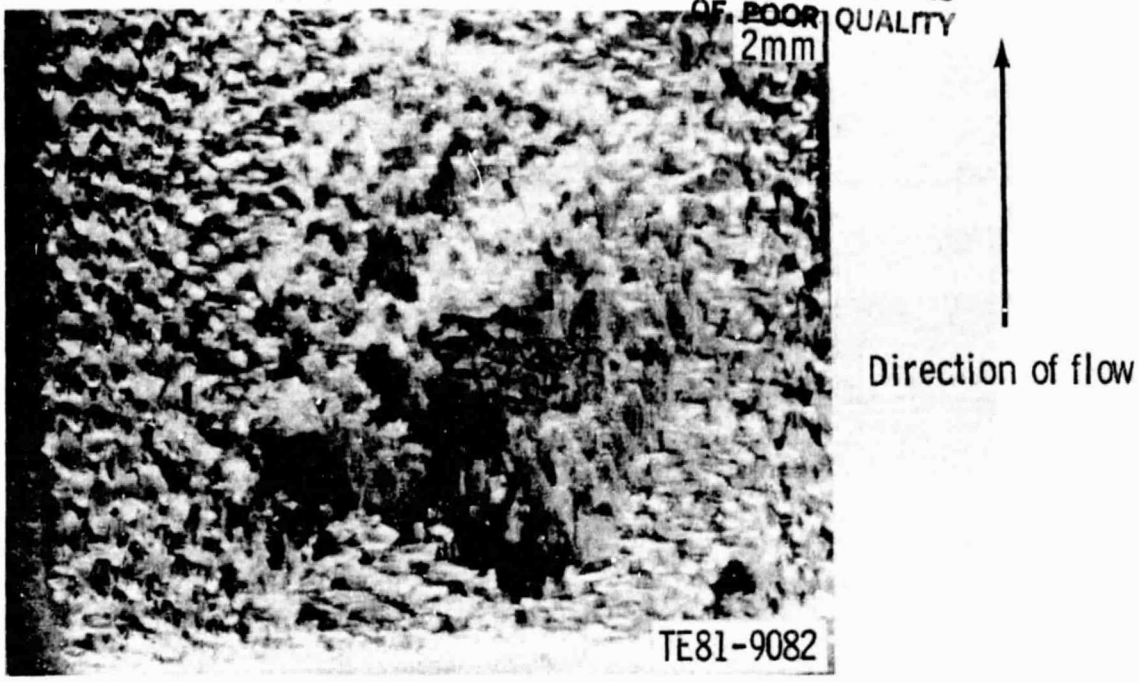

Figure 23. 0.76 mm (0.030 in.) satin weave--severe erosion, 30 min, 45° angle (X5).

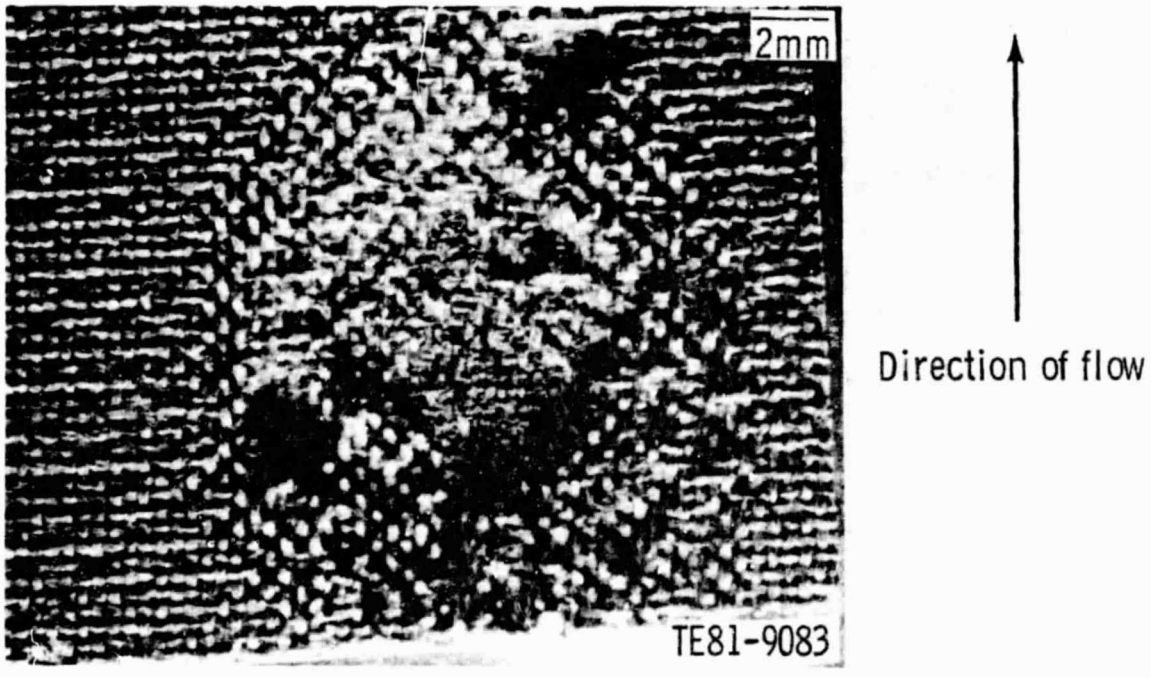

Figure 24. 0.38 mm (0.015 in.) square weave--moderate erosion, 30 min, 45° angle (X5).

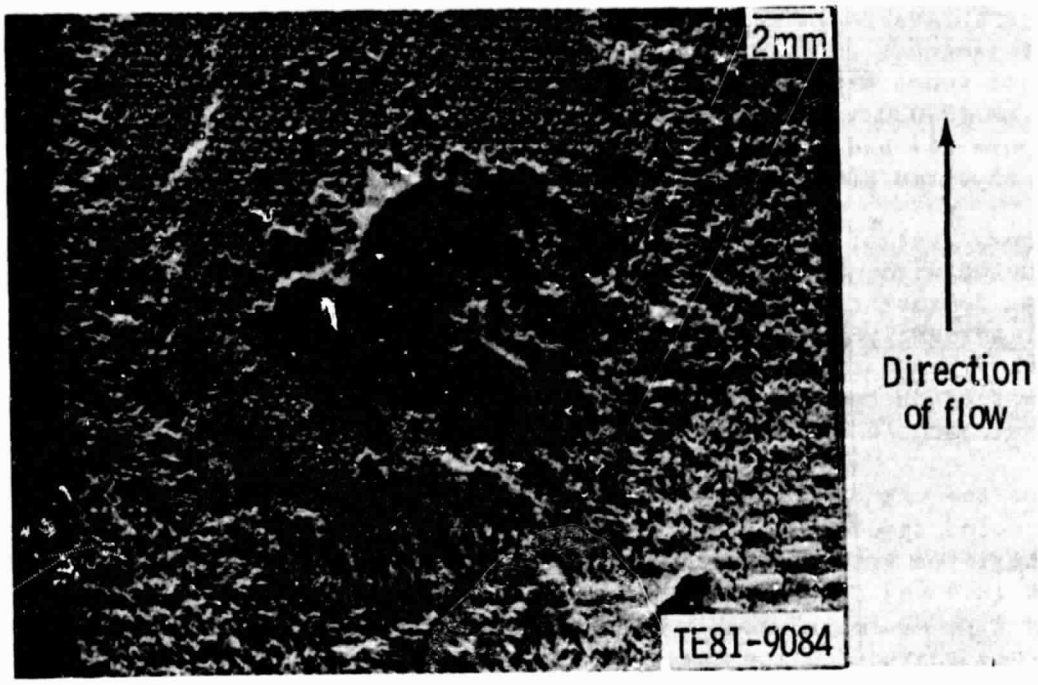

Figure 25. 0.38 mm (0.015 in.) knit--severe erosion, 30 min, 45° angle (X5).

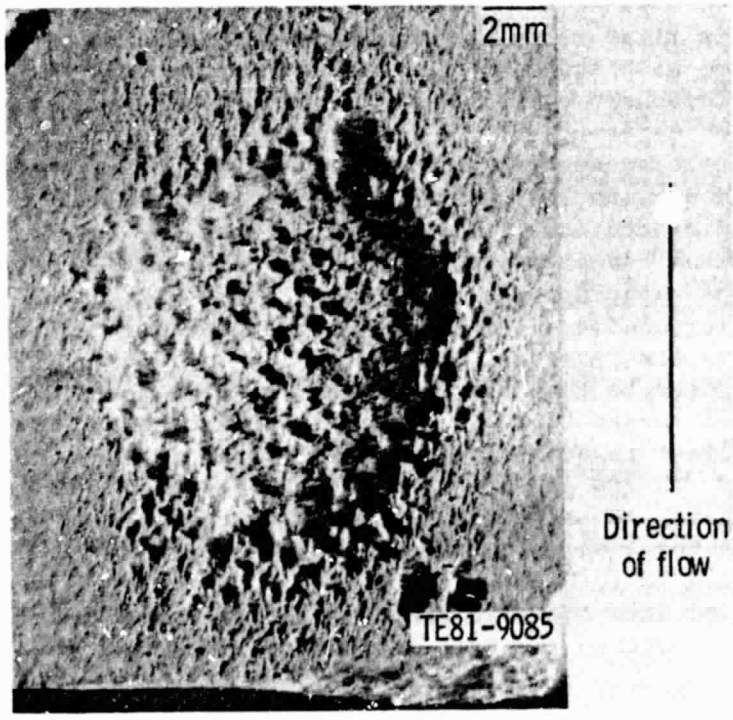

Figure 26. Zircar 0.76 mm (0.030 in.) satin weave--moderate erosion, 30 min, 45° angle (X5).

The erosion rate for the 0.38 mm (0.015 in.) square weave laminate (Figure 24) was essentially equal to that of the 65% reduced material seen in Figure 26 (0.0167 gm abradable/gm sand, as compared with 0.0154). This is surprising, since the laminate in Figure 24 is significantly softer. The orientation and the type of weave may have an influence on the laminate erosion resistance. The 0.76 mm (0.030 in.) satin laminate and the 0.38 mm (0.015 in.) knit laminate (Figure 25) had measurably greater erosion than the other samples, but this was expected since they were significantly softer.

A laboratory test of silicon carbide blades in an intentional rub situation was conducted with no damage to the blade tips or distress to the abradable material. Because the reactions involved in this rub situation were unpredictable, a readily available abradable material comprised of 100% eccospheres was selected, even though the erosion resistance is known to be inferior. Testing was conducted at room temperature with a blade tip speed of 83.2 m/sec (273 ft/sec) and an incursion rate of 0.025 mm/sec (0.001 in./sec).

Because of the unknown nature of the rub, a preliminary test was conducted at half the noted speed to get a better "feel" for the severity of the interaction. The rotor prior to testing is shown in Figure 27. A rub depth of 0.15 mm (0.006 in.) was developed in the initial test with no resultant distress to the blade tips or the abradable material. Following this initial rub, the specimen was re-indexed and the test repeated with a higher tip speed of 83.2 m/sec (273 ft/sec). As shown in Figure 28, the rub path of the second run was superimposed on that of the first run. The measured rub depth was 0.33 mm (0.013 in.). Again no distress was noted on the blade tips or the abradable material.

The success of this first rub with silicon carbide blading provided incentive for further testing with modified zirconia/eccosphere structures. As noted above, the 100% eccosphere system has very poor erosion resistance. To increase the erosion resistance of the coating system, yttria-stabilized zirconia (YSZ) powder is added to the system. The zirconia provides high-temperature strength and erosion resistance, while the eccospheres create closed-pore voids in the ceramic structure, thereby maintaining the required abradability characteristics. Dual-density structures were fabricated that were comprised of abradable layers superimposed on layers of 100% YSZ typical of NASA-developed thermal barrier coatings. The volume of zirconia in the abradable layer of these structures was increased from 0% to 35% in 5% intervals. Each composition was subjected to the test conditions of 83.2 m/sec (273 ft/sec) blade tip speed and 0.025 mm/sec (0.001 in./sec) incursion rate. Abradability performance was excellent in each case and only in the case of the higher zirconia volume percentages (30/70% and 35/65% zirconia/eccosphere system) did glazing of the surface appear. No significant damage to the silicon carbide blade tip was evident except for a slight adherence of glaze material. The maximum rub depth recorded, 0.40 mm (0.016 in.), occurred in the 30/70% specimen. Seven tests were conducted with the same blading system; reconditioning of the blade tips by grinding to restore the original condition was not required.

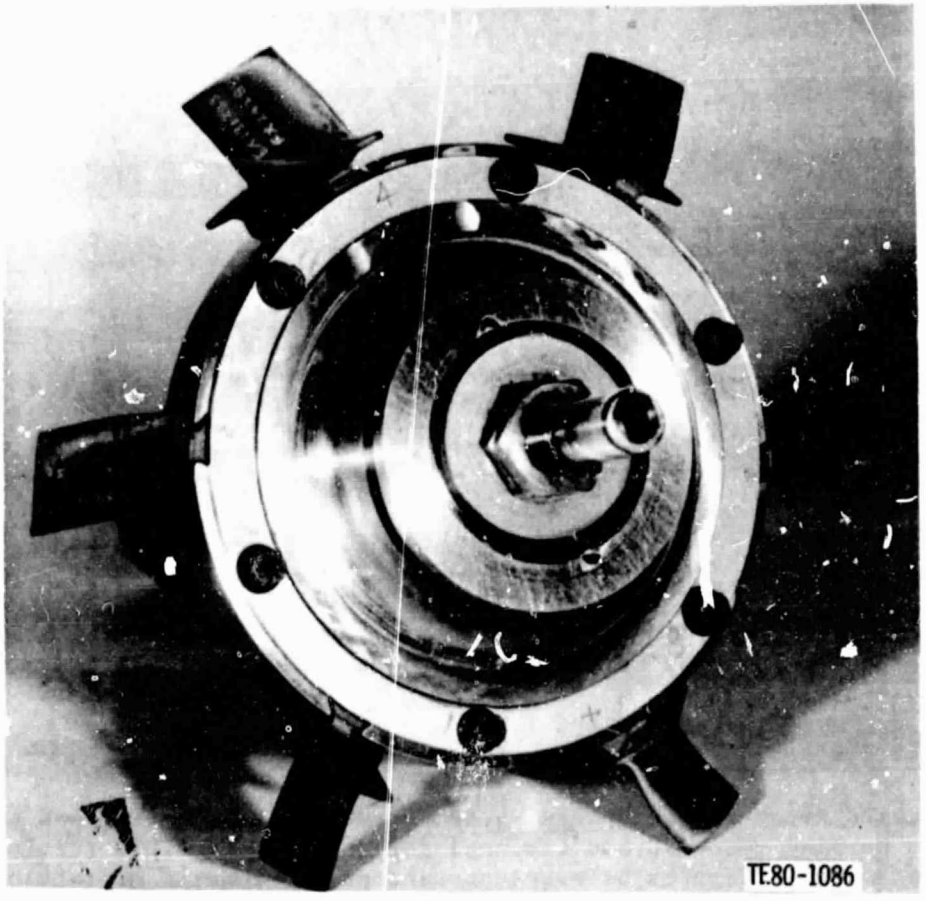

Figure 27. SiC-bladed rotor prior to testing.

Figures 29 and 30 show the rub tracks of the SiC blading in three successively harder zirconia/eccosphere systems. A clean, distinct rub path can be seen in the 25/75% system (Figure 29A), while a slight glazing can be seen in the rub track of the 30/70% composition (Figure 29B). A view of a silicon carbide blade tip with a slight adherence of glaze material resulting from the 30/70% composition rub is seen in Figure 31. A more significant degree of glazing has occurred in the 35/65% composition (Figure 30).

Significant differences in the erosion resistance can be seen by comparing Figures 32A and 32B. Both are 30-min duration tests and the 35/65% composition is more erosion resistant than the former material by a factor of 2.6. The 120-min sample of the 35/65% composition shown in Figure 33 appears virtually the same as the 30-min 30/70% specimen seen in Figure 32A.

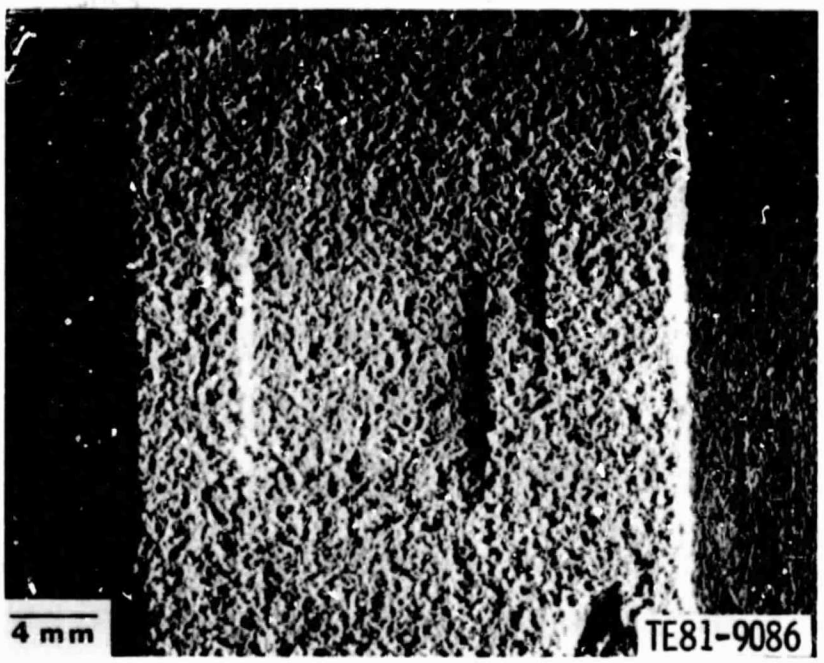

Figure 28. Plasma-sprayed 100% eccosphere system rub path of SiC blade tip 0.33 mm (0.013 in.) deep (X3).

Engine Test Evaluation

A plasma-sprayed zirconia/eccosphere system of 14/86% composition was used as an abradable turbine rotor shroud tip seal for engine C-1. This turbine was a metal-bladed system. Results of rig tests and engine running of this composition are shown in Figures 34 and 35. Formation of a slight glaze can be seen in the rig abradability coupon (Figure 34). Engine test results after approximately 40 hr of testing show moderate glazing and metal transfer resulting from shroud-to-rotor interference, as seen in Figure 35. Slight erosion effects were becoming noticeable at this time. The depth of rub was 0.25 mm (0.010 in.), with a comparable amount removed from the blade tips.

This result was not totally unexpected. At the 1093°C (2000°F) temperatures the blades are experiencing the tips are relatively soft compared to the ceramic/eccosphere shroud seal, and the tendency for metal transfer is markedly increased. This composition appears to be the practical limit for use with a metal blade.

The foregoing results make clear that the abradability of ceramic-bladed systems is promising compared to that of metal-bladed systems. The ceramic-bladed system has shown a marked improvement in abradability performance over previously run metal blades and can be expected to follow suit in actual engine testing. However, it is apparent that the limit has been reached in terms of achieving a high-density abradable seal material within the current metal rotor system. This is because in that composition, which uses a relatively high content of eccospheres (up to approximately 80% by volume), mate-

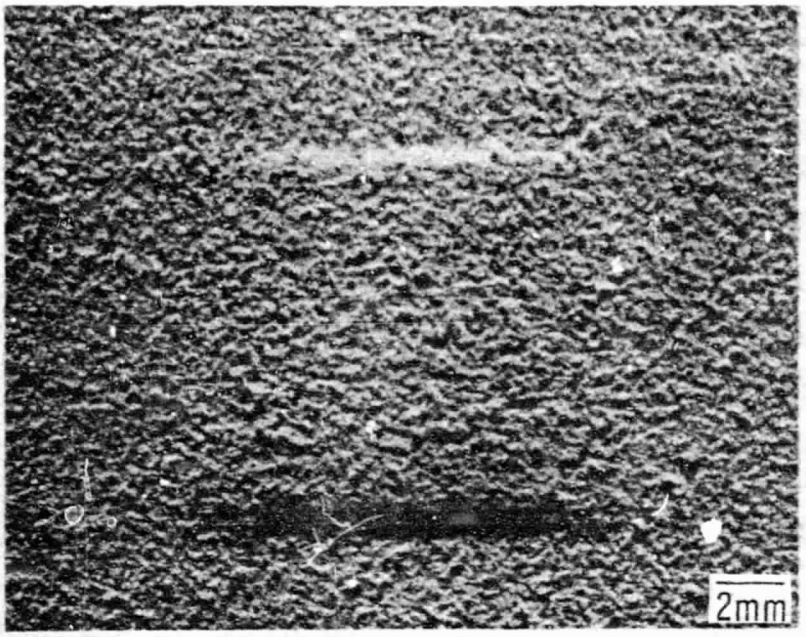

A. 25/75% composition
10000 rpm rub-SiC blade tip 0.35 mm (0.014 in.) deep

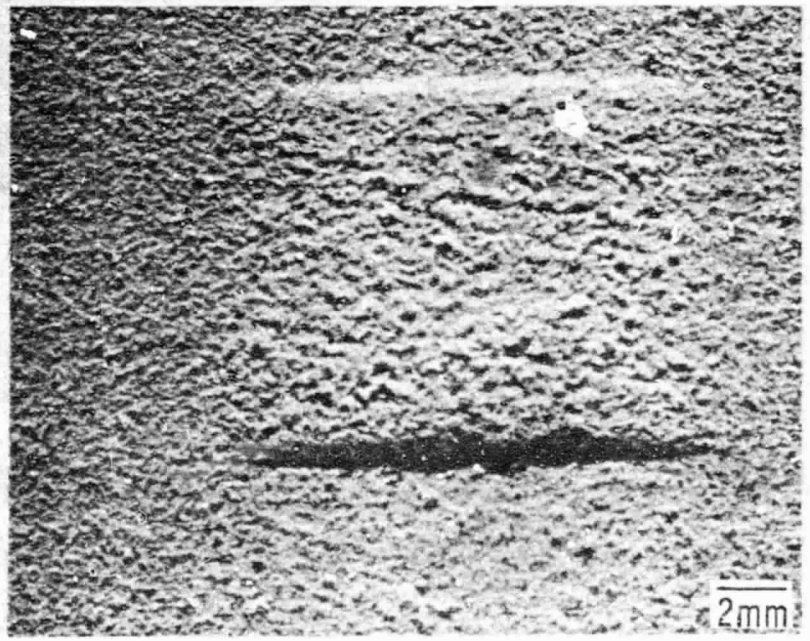

TE81-9087

B. 30/70% composition
10000 rpm rub-SiC blade tip 0.40 mm (0.016 in.) deep

Figure 29. Plasma-sprayed zirconia/eccosphere system (X5).

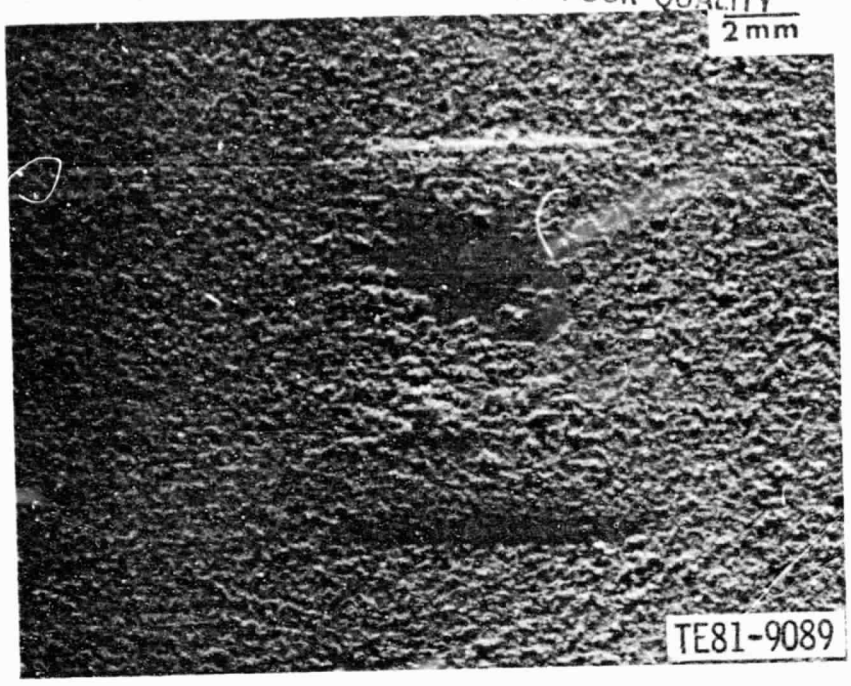

Figure 30. Plasma-sprayed zirconia/eccosphere system, 35/65% composition, 10,000 rpm rub--SiC blading 0.125 mm (0.005 in.) (X5).

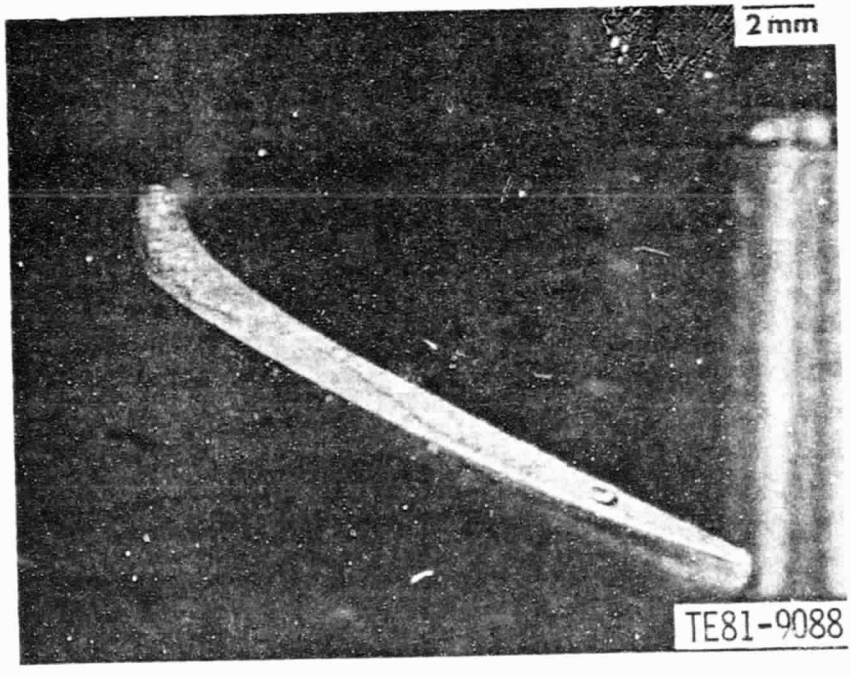

Figure 31. SiC blade tip after 10,000 rpm rub with 30/70% zirconia/eccosphere system (X5).

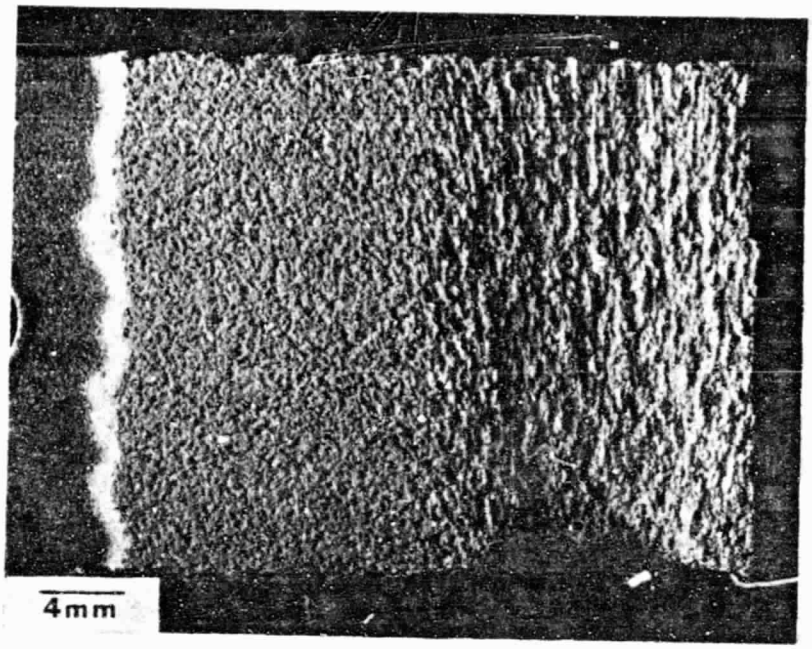

Direction of flow

A. 30/70% composition

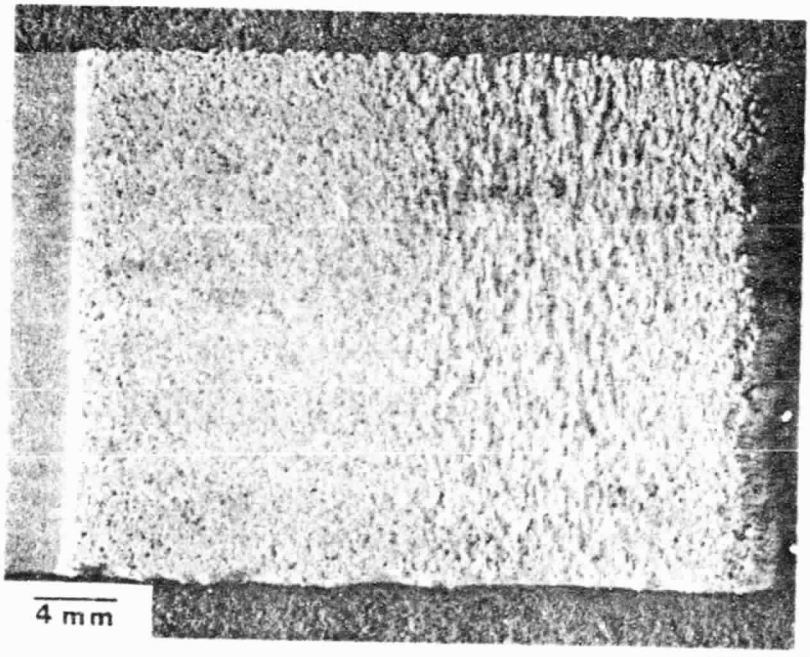

Direction of flow

TE81-9090

B. 35/65% composition
Plasma-sprayed zirconia/eccosphere system

Figure 32. Plasma-sprayed zirconia/eccosphere system, 30-min erosion test (X3).

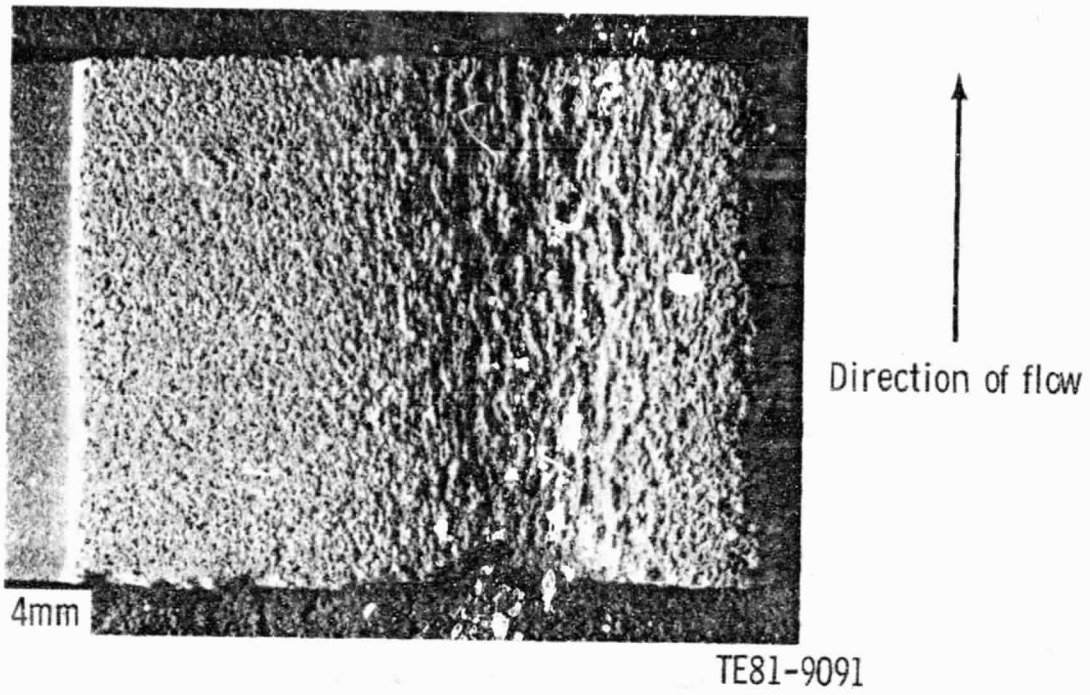

Figure 33. Plasma-sprayed zirconia/eccosphere system, 120-min erosion test, 35/65% composition (X3).

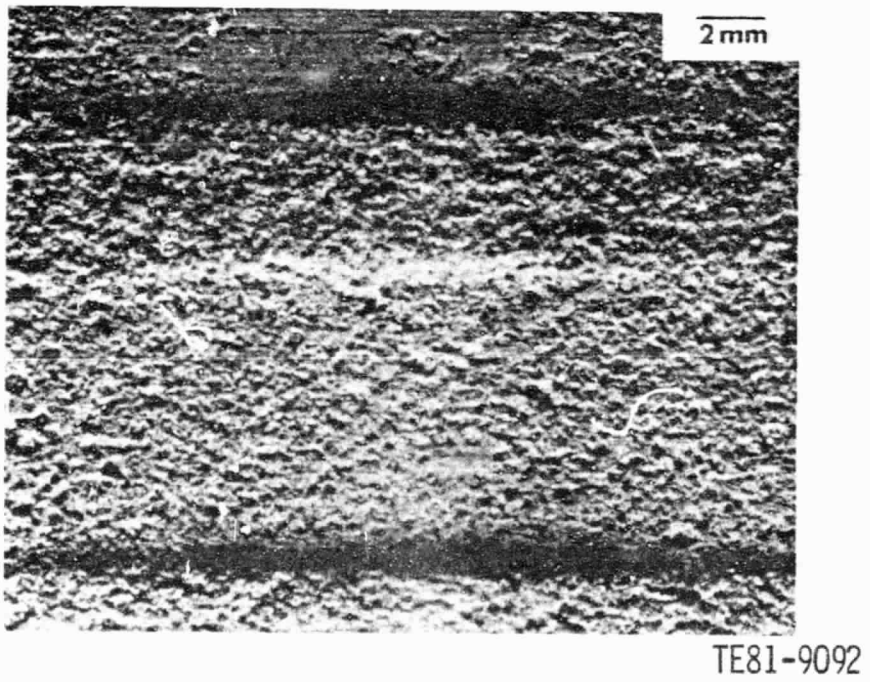

Figure 34. Plasma-sprayed zirconia/eccosphere system, 14/86% composition rig test coupon rub. Mar-M247 blade tip rub 0.5 mm (0.020 in.) deep (X5).

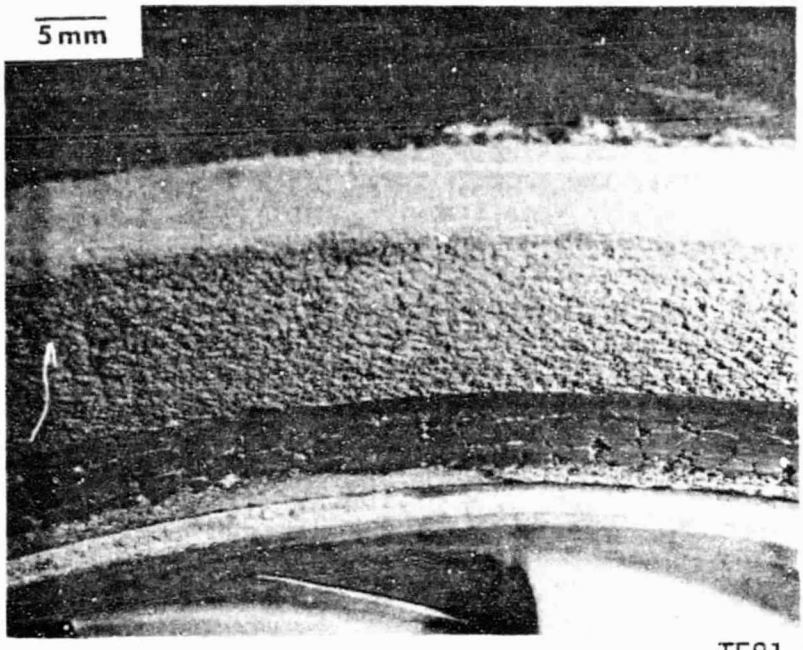

TE81-9093

Figure 35. Plasma-sprayed zirconia/eccosphere system, engine C-1 nozzle shroud rub, Mar-M247 blade tip (X2).

rial appears to be removed by a crushing action. In this type of action the rotating blade tip crushes the zirconia/eccosphere mixture and the resultant debris is flushed out of the rub path. Densification at the surface also occurs as part of the crushing action. As the proportion of zirconia in the mixture increases, the void percentage decreases and the material tends to densify under the moving blade tip. Under these conditions a glaze similar to the scar seen in Figure 30 for a ceramic-blade tip appears. The glaze may be acccompanied by metal transfer, as shown in Figure 35, for a metal-blade tip. It should be noted that the compositions of the two systems are vastly different, the ceramic-blade system having a significantly higher percentage of zirconia. If it follows that engine testing will result in poorer performance than the rig tests indicate, as was the case for the metalbladed system, then improvement is needed for the ceramic system as well as for the metal one. Recent developments in the field of rub energetics have led to a new understanding of the fundamentals of the rub mechanism, and possibly explain the phenomena observed in the foregoing tests.

Blade Tip Rub Phenomena and Treatments

The development of a viable abradable materials system (in which the blade tip and the abradable material are considered a mutually dependent pair of components) hinges on the manner in which the blade tip removes the abradable seal material (i.e., the rub mechanics). Simply stated, the mechanism must be compatible with the seal structure. Crushing mechanisms must be avoided in nonfriable systems because they lead to densification of the material and a smeared surface at the interface of the rub, thereby promoting adverse interactions, such as metal transfer, between the blade tip and the abradable ma-

terial. For material to be removed by chip formation and to avoid smearing or densification, the blade tip "cutting edge" must have a radius smaller than the depth of cut of each individual blade tip as it enters the abradable. The depth of cut is determined by the radial incursion rate of the rotor, the rotor speed, and the number of blades. This value is typically about 10^{-6} mm (4×10^{-8} in.). Since the cutting edge radius of practical systems is many times larger than this, the contact force is always directed down into the abradable material, causing densification, which then results in greater forces, etc. Unless the abradable structure can fracture and break away, gross smearing will occur as a result of the shearing actions taking place. Since it is improbable that the cutting edge will ever be smaller than the depth of cut, the alternative is to ensure that the material is always friable or to assist the blade tip in its cutting function. Friability, or the property of being crushed and flushed out of the blade path, is usually achieved at the expense of erosion resistance. As the structure is made harder or denser to improve erosion resistance, a limit of acceptable abradability is reached prior to achieving satisfactory erosion performance. Beyond this point, the blade tips require assistance. One approach is to provide the tip with many sharp, randomly oriented minisurfaces, much like a grinding wheel surface, that will serve as more efficient cutting edges than a single blade tip.

To investigate this concept further with a silicon carbide blade tip, work has been initiated at San Fernando Labs, Pacoima, Los Angeles, California, to supply DDA with a number of silicon carbide turbine blades upon which granular silicon carbide has been chemically vapor deposited. This should improve the cutting ability of the blade tip and permit the use of a denser, more erosion-resistant abradable material than has heretofore been possible.

It is evident that the formation of material smearing at the blade tip/abradable interface cannot be avoided with a bare blade tip, regardless of whether it is metal or ceramic. The use of "unassisted" blade tips will be discontinued, and all future abradability tests will use a modified structure.

NDE DEVELOPMENT AND EVALUATION

Summary

Three techniques--Scanning Photoacoustic Spectroscopy (SPAS), Scanning Laser Acoustic Microscopy (SLAM), and high-frequency ultrasonics--are currently under investigation to determine their applicability for characterizing ceramic materials. Recent efforts have concentrated on the SPAS and SLAM techniques.

The SPAS experimental arrangement was improved during this reporting period. Subsurface flaws in metals and ceramics were readily detected with the new SPAS system.

Simulated surface-drilled holes and cracks (Knoop indents) were easily detected in the dark field mode. Good correlation was found between acoustic microscopy-predicted failure sites and actual fracture locations in alpha silicon carbide.

Objective

The objective of this task is to develop one or more NDE techniques capable of detecting and characterizing critical fracture-controlling flaws in silicon-based structural ceramic materials. Effective flaw detection can improve process control by eliminating the strength-limiting defects and helping to establish probable accept/reject criteria for the qualification of ceramic components.

Scanning Photoacoustic Spectroscopy (SPAS)

Scanning photoacoustic spectroscopy has been proven to be effective in detecting surface and subsurface flaws in metal and ceramic materials. Early development efforts focused on establishing the feasibility of detecting surface flaws (Ref. 2). Subsequently, an in-house laboratory was established to perform systematic parametric studies to measure the limits of detectibility for a variety of surface and subsurface flaw types. Initial in-house studies established that simulated tight surface cracks such as Knoop indentations and naturally occurring pores are readily detectible in silicon-base ceramic materials (Ref. 1). During the present reporting period, work has been initiated to determine the depth of detection of subsurface defects in a wide variety of metallic and ceramic materials. Two metals--aluminum (6061-T6) and carbon steel (1018)--and three ceramic materials--alpha silicon carbide (α-SiC), reaction-bonded silicon carbide (RB-SiC), and sintered silicon nitride (SNW-1000)--were investigated.

Plate specimens with side drilled holes (SDH) were produced for both metals and all three ceramic materials. The size, shape, and location of the simulated defects in metallic and ceramic specimens are shown in Figures 36 and 37, respectively.

The basic experimental arrangement has been described in Ref. 1. Modifications and improvements made during this reporting period are as follows:

- The photoacoustic cell was modified to operate at lower frequencies and to eliminate contribution of spurious signals to the SPAS signal. By decreasing the operating chopping frequency, thermal diffusion length is increased and hence detectibility of subsurface flaws is improved.
- A programmable microprocessor-based controller synchronizing all the motions (direction, speed, distance, increment, etc.) of a two-dimensional stage and x-y recorder was added to the system. The front panel of the scanner control consists of a eight-function knob, nine programmable keys, and a manual speed override. The location of the servo-controlled stages (X and Y) is continuously displayed as front panel digital readout, as well as analog voltage for the x-y recorder. The SPAS signal is electronically mixed with the y-axis signal to provide an isometric presentation of the specimen. Scanning speed can be varied from 2.0 μm/sec to about 30 mm/sec. Finally, the minimum increment is 2.0 μm for each axis. Figure 38 shows the present experimental arrangement.

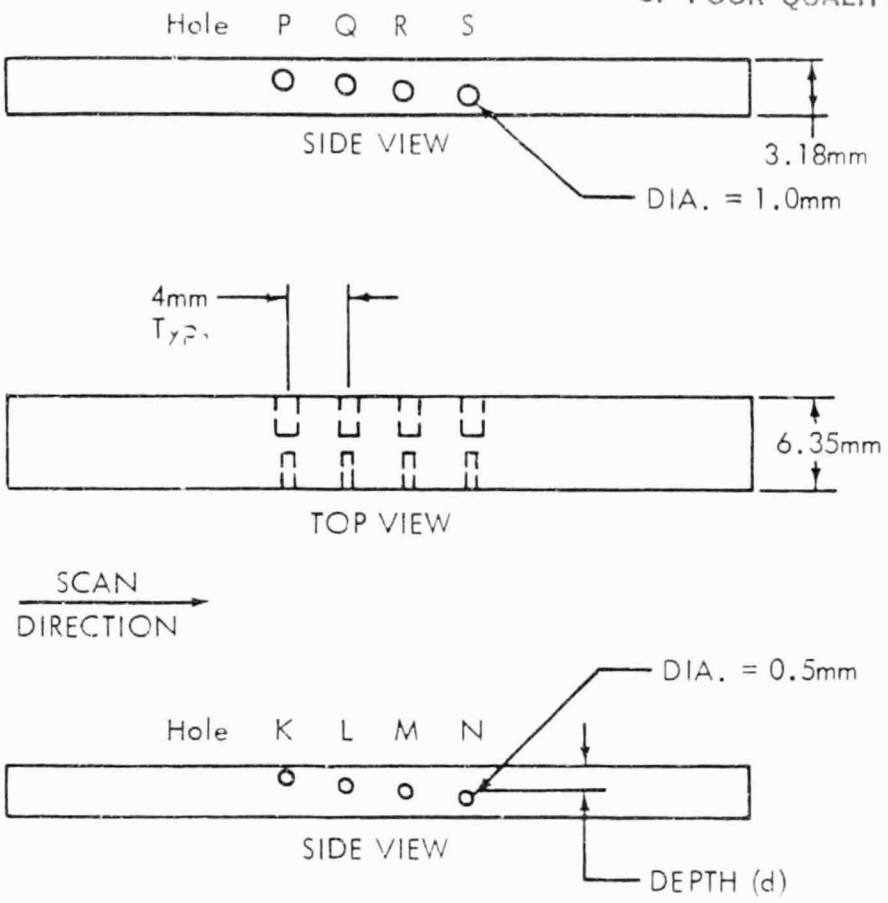

	Hole Depth (d), μm.							
	K	L	M	N	P	Q	R	S
Aluminum (6061-T6)	10	230	550	900	0	10	250	520
Carbon Steel (1018)	10	200	520	840	230	560	800	900

361771
TE81-9094

Figure 36. Schematic and measured dimensions of metal specimens with side drilled holes for subsurface flaw detection by SPAS.

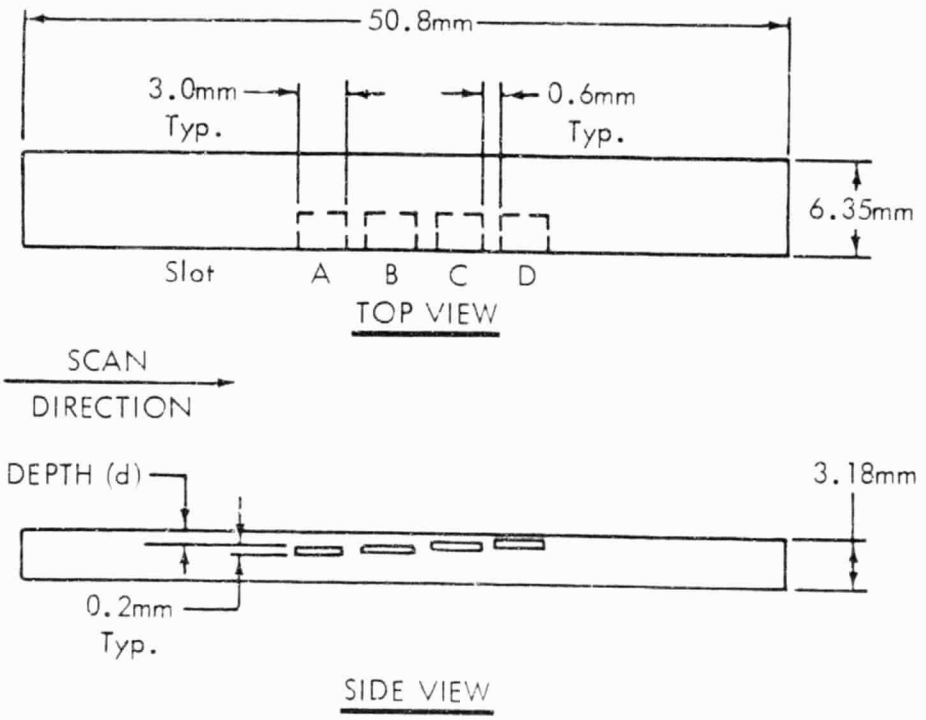

Material	Slot Depth (d), μm			
	A	B	C	D
α - SiC	680	590	500	400
RB-SiC	400	300	220	170
SNW-1000 (Si_3N_4)	450	390	330	250

TE81-9095
361772

Figure 37. Schematic and measured dimensions of ceramic specimens with slots for subsurface flaw detection by SPAS.

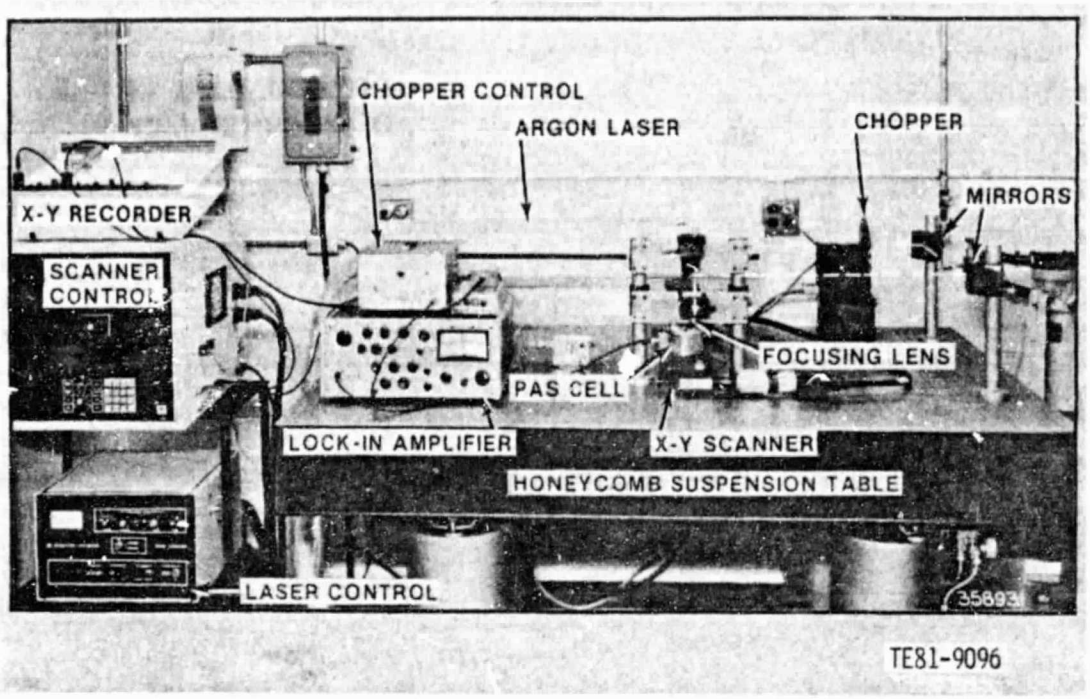

Figure 38. Improved experimental setup at DDA for flaw detection in ceramics by SPAS.

Test parameters were held constant as follows: laser power--0.4 w, time constant--300 msec, and scan speed--250 μm/sec. In all this work we are measuring only the magnitude of the SPAS signal, not the phase. Each specimen was evaluated at a number of chopping frequencies until the deepest flaw could not be discerned from the background. To further improve the discernibility of flaws from the random background signal, a threshold circuit was designed and built at DDA and incorporated into the system.

Figures 39 and 40 show the results of initial efforts to detect subsurface holes 0.5 mm (0.02 in.) in diameter (SDH) in aluminum and steel, respectively. Three holes were detected in each specimen. The depth of the deepest detected holes was 550 μm in aluminum and 520 μm in steel. This size hole was detected and resolved up to 120 hz in aluminum and 30 hz in steel. Hole N (not shown), the deepest hole, could not be distinguished from the background signal in the aluminum specimen at 20 hz, even though its mean depth (900 μm) was less than one thermal diffusion length of 1011 μm at this frequency. Obviously, there is a critical depth up to which holes 0.5 mm (0.02 in.) in diameter can be detected under these experimental conditions. It may be possible, however, to detect smaller flaws by decreasing the scan speed, increasing the laser power, or measuring the phase of the SPAS signal.

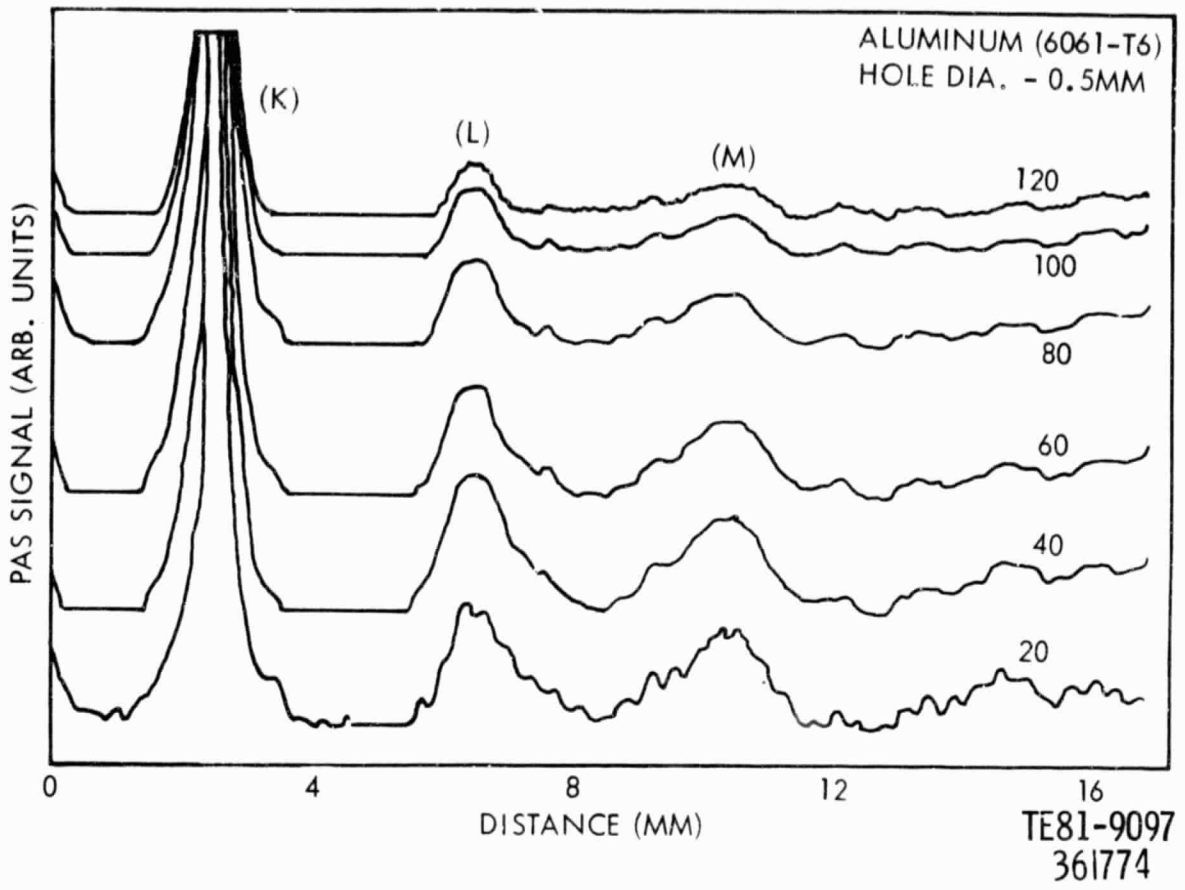

Figure 39. Photoacoustical signal as a function of chopping frequency f_c (hz) and holes K, L, and M at various depths (D) in aluminum. Values of f_c are shown for each trace.

Figure 41 shows SPAS signals from slots in the ceramic specimens. All of the slots in both materials were easily detected. The deepest detected planar flaw in all the specimens was slot A. The depth of this slot was 680 μm in alpha silicon carbide, 400 μm in reaction-bonded silicon carbide, and 450 μm in sintered silicon nitride. The corresponding maximum frequencies of detection were 100 hz in α-SiC, 450 hz in RB-SiC, and 40 hz in SNW-1000.

Figure 39 shows that the magnitude of the SPAS signal decreases as the depth of a flaw increases. This is expected because heat diffuses exponentially in solid materials, with similar decreases in the surface temperature of the specimen in the SPAS cell. The SPAS signal from hole M (Figure 39) and hole S (Figure 42) is larger when detected from 20 to 60 hz than from 80 to 120 hz. Up to 60 hz, the depth of the flaw is lower than the thermal diffusion length (μ_s). This represents the thermally thin condition. Conversely, from 80 hz and up, the depth of the flaw is greater than the thermal diffusion length (μ_s). This is the thermally thick condition. Therefore, the SPAS signal is larger when detected under thermally thin conditions than under thermally thick conditions. This is consistent with the published results of Refs. 3 and 4.

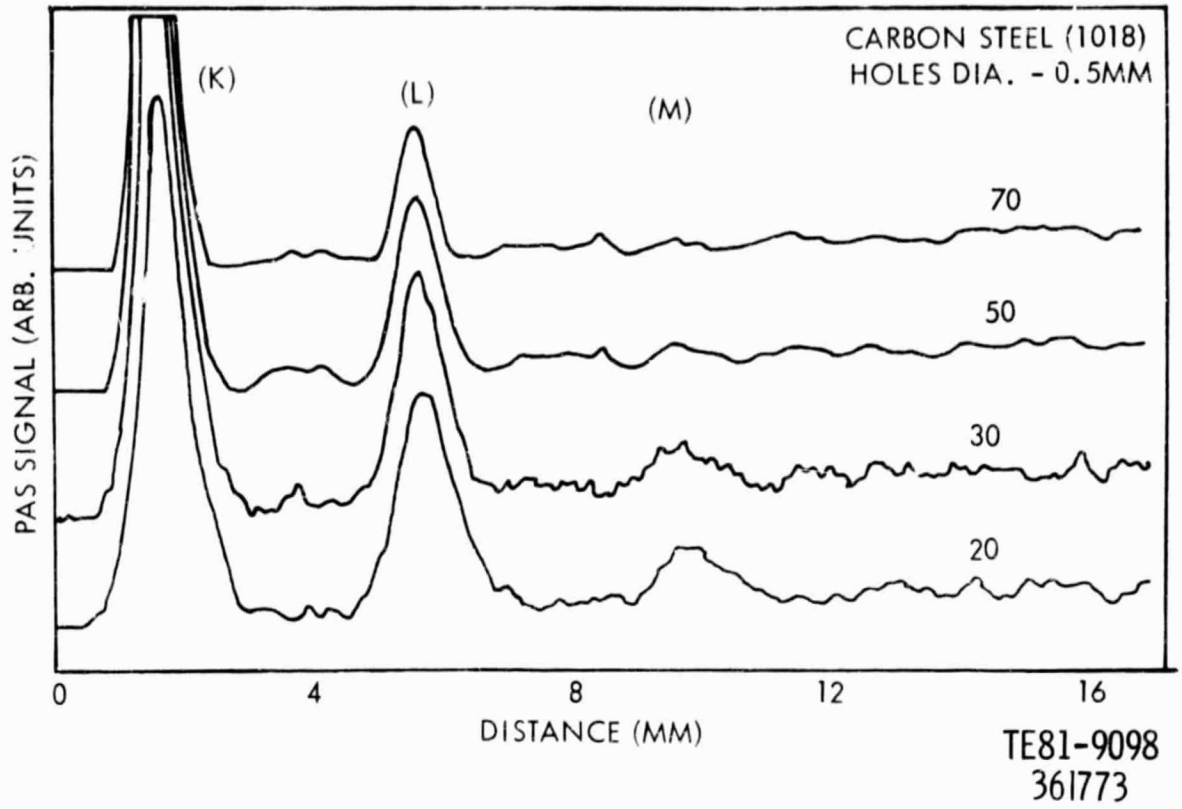

Figure 40. Photoacoustic signal as a function of f_c (hz) and holes K, L, and M at various depths (D) in carbon steel. Values of f_c are shown for each trace.

Since holes K and S are at about the same depth as holes L and M, respectively, the larger SPAS signals from them (Figure 41) can only be related to their difference in sizes. The larger the flaw the higher the SPAS signal, and vice versa. This is analogous to the size dependence of the signal from a spherical flaw in ultrasonics.

Table IV gives the effective depth (t_{eff}) to which the simulated flaws examined here could be detected in each of the five materials investigated. The results clearly show that 0.50-mm holes in both aluminum and steel can be distinguished from the background signal at depths greater than one thermal diffusion length. The holes 1.0 mm in diameter in aluminum were detected up to a similar depth. These experimentally measured depths are about 30% higher than those reported by Thomas et al. (Ref. 4) for slotted wedged specimens. Those authors showed that flaws up to one thermal diffusion length (μs) could be detected. The slots in the ceramic specimens were detected up to (1.35 to 2.0) x μs depth. This is 35-100% more than reported by Ref. 4. Therefore, the subsurface depth to which defects could be detected depends on the characteristics of the flaw, because changes in the thermal resistance parameter may affect the surface temperature of the specimen in the cell and hence the SPAS signal.

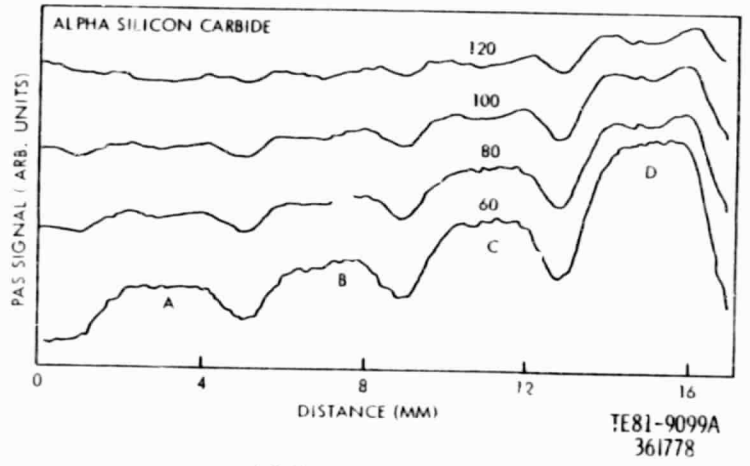

(a) Alpha silicon carbide

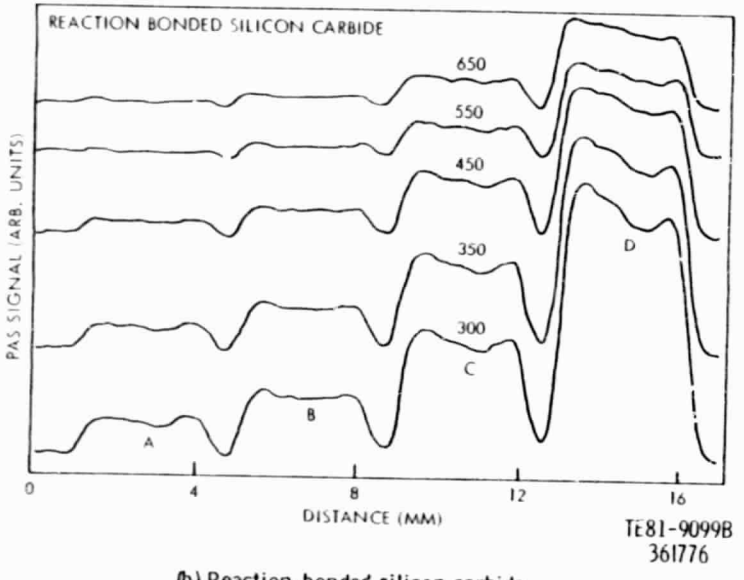

(b) Reaction-bonded silicon carbide

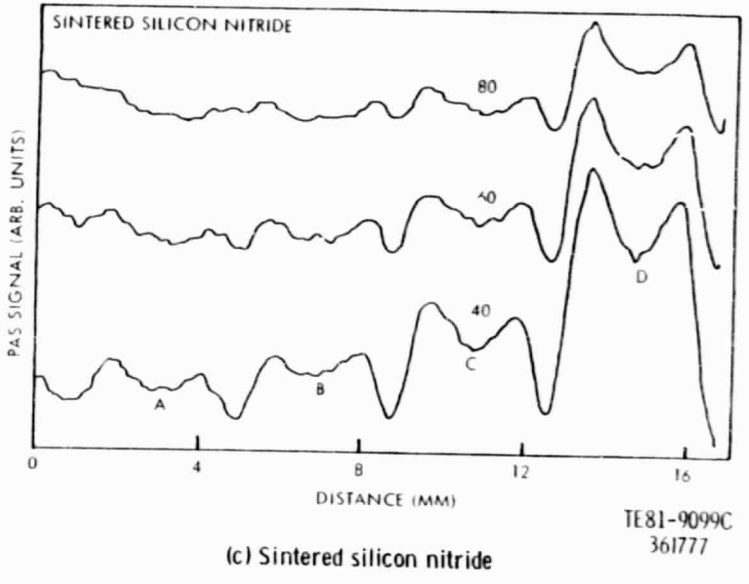

(c) Sintered silicon nitride

Figure 41. Photoacoustic signal as a function of f_c (hz) and slots A, B, C, and D at various depths (D) in (a) alpha silicon carbide, (b) reaction-bonded silicon carbide, and (c) sintered silicon nitride. Values of f_c are shown for each trace.

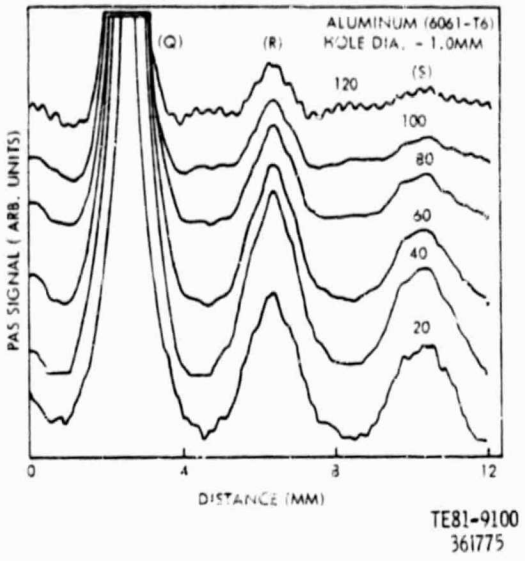

Figure 42. Photoacoustic signal as a function of f_c (hz) and holes Q, R, and S at various depths (D) in aluminum. Values of f_c are shown for each trace.

TABLE IV. EFFECTIVE DEPTH (t_{eff}) OF FLAW DETECTION IN METALS AND CERAMICS

Materials	Depth of detected flaw (d)--μm	Maximum frequency of detection --f_c, hz	Thermal diffusion length (μs)* at max frequencies--μm	Effective depth of detection t_{eff} = (d/μs)
Aluminum (6061-T6)				
Hole M	550	120	413	1.33
Hole S	520	120	413	1.26
1018 steel				
Hole M	520	30	408	1.27
α-SiC				
Slot A	680	100	459	1.48
RB-SiC				
Slot A	400	450	197	2.03
SNW-1000				
Slot A	450	40	334	1.35

*$\mu s = \sqrt{(\alpha/\pi f_c)}$ 1/2 where α = thermal diffusivity (cm^2/sec).

Thermal diffusivity used--aluminum, 0.643; steel, 0.157; α-SiC, 0.663; RB-SiC, 0.55; SNW-1000, 0.14.

Further work is planned to determine the effect of flaw characteristics on the SPAS signal in a wide variety of metal and ceramic structural materials. Also, the lock-in-amplifier will be modified to provide a dc output proportional to the phase of the complex SPAS signal. Phase detection is expected to increase the depth of flaw detection.

Scanning Laser Acoustic Microscopy (SLAM)

Scanning laser acoustic microscopy has shown potential for detecting both surface and subsurface flaws in structural ceramic materials. Present efforts have concentrated on applying this technique to the study of surface flaws. During the previous reporting period (Ref. 1) it was established that the dark field imaging mode is the most sensitive in detecting tight surface cracks (Knoop indentations). Consequently, the current effort has emphasized the use of this mode. The operating principle of this technique is described in Ref. 1 and will be be repeated here.

Two types of specimens/defects have been examined:

- o Radiographic step penetrameters of α-SiC and RB-SiC with surface drilled holes
- o MOR specimens of α-SiC with tight surface cracks (Knoop indentations)

Evaluation of Step Penetrameters

Two step penetrameters, one each of alpha silicon carbide (α -SiC) and reaction-bonded silicon carbide (RB-SiC), were designed according to the general guidelines of ASTM procedure E142-77. The planned level of inspection was 2-1T, 2-2T, and 2-4T. The penetrameters were fabricated (cold pressed, sintered, and machined) by the Carborundum Company. The density of the α-SiC penetrameter was determined to be 3.11 gm/cc and that of the RB-SiC penetrameter 2.99 gm/cc. The latter corresponds to a free silicon content of 25% by volume in RB-SiC. Holes were ultrasonically drilled by Bullen Ultrasonics. Figure 43 shows the penetrameter geometry, along with the location and size of each hole. The thickness and dimension of each step and hole were measured by a micrometer and an optical microscope at 200X, respectively. The holes were numbered 1 to 9 and steps 1 to 8. Holes in RB-SiC are identified as RB1 through RB9, while in α-SiC they are designated as α1 through α9.

Both the penetrameters were examined with the acoustic microscope at Sonoscan, Inc. Several different imaging modes are available in the commercial acoustic microscope. Two modes--acoustic amplitude (bright and dark field) and dark field interferogram (forward and backscatter)--were employed in this initial study.

The results are summarized in Table V. All the holes in both penetrameters were detected. The discernibility in the present case was primarily affected by the surface condition. Microscopic examination of each penetrameter revealed varying degrees of surface pitting. This was particularly true of the α-SiC penetrameter. Less pitting was observed in the RB-SiC penetrameter. The size of the some of the pits was on the same order as the smaller holes and hence their acoustic scattering characteristics were quite similar.

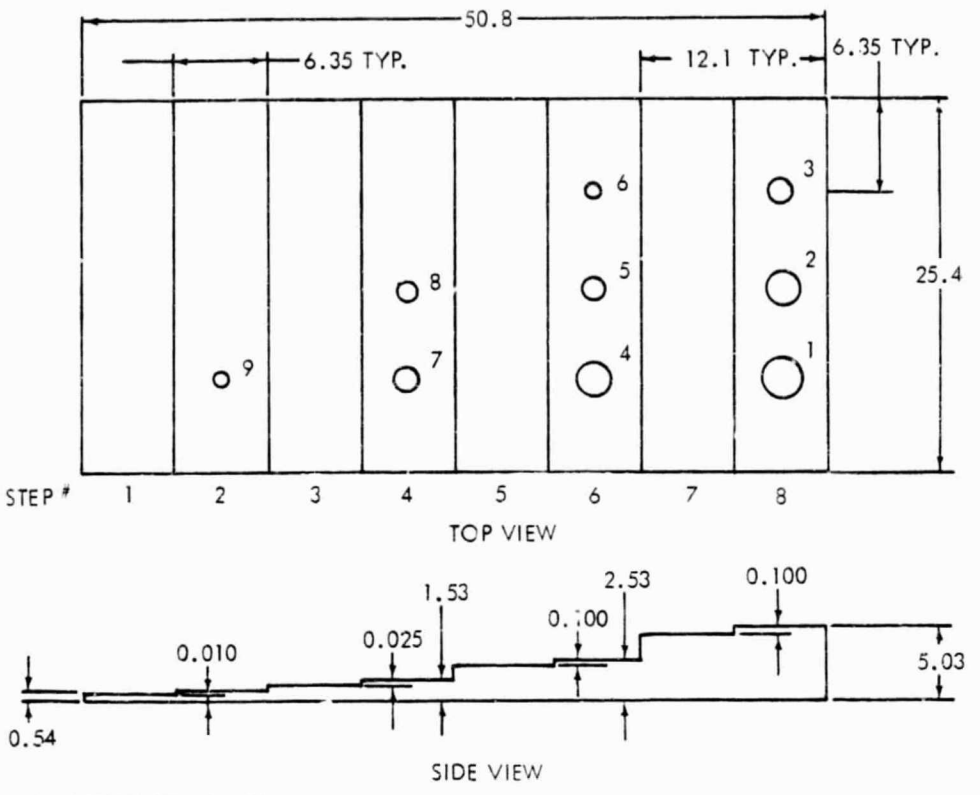

REACTION BONDED SILICON CARBIDE

STEP NUMBER			
2	4	6	8
HOLE DIAMETER - MICRONS			
		70	117
	102	105	210
75	102	202	500
HOLE DEPTH - MICRONS			
		60	123
	38	60	105
17	45	53	117

ALPHA SILICON CARBIDE

STEP NUMBER			
2	4	6	8
HOLE DIAMETER - MICRONS			
		52	108
	80	100	205
68	100	190	388
HOLE DEPTH - MICRONS			
		42	115
	38	55	115
25	35	55	95

361770
TE81-9101

Figure 43. Layout of radiographic penetrameters showing location of holes and measured dimensions.

TABLE V. SCANNING LASER ACOUSTIC MICROSCOPY (SLAM) OF CERAMIC PENETRAMETERS

Material	Hole No. 1	2	3	4	5	6	7	8	9
α-SiC	D, DB*	D, DB	D, NDB	D, DB	D, DB	D, NDB	D, NDB	D, NDB	D, NDB
RB-SiC	D, DB	D, DB	D, DB	D, DB	D, NDB	D, NDB	D, DB	D, DB	D, DB

*D--detected, DB--discernible with background signal, NDB--not discernible from the background signal and/or surface pits.

Figure 44 shows acoustic micrographs of detected holes RB1 and α1 in both the bright and dark field modes. The image of the holes in the bright field shows a lighter center. This is due to the sound being focused when propagating across the curved surface at the bottom of the hole. The holes also have a brighter center in the dark field mode. Again, this is a result of focusing that occurs when sound is refracted at the bottom curved surfaces of the hole.

Acoustic micrographs (Figure 45) of hole RB7 in step 4 show that it is readily detected against the background structure in both the bright and dark field modes. In the amplitude mode the hole appears as a shadow with a ring pattern emanating from it. These rings are believed to be due to interference between the bulk skimming wave (horizontal component of the incident bulk wave) along the surface of the specimen and the scattered wave from the flaw. These rings are always present, but are visible only when constructive interference occurs and contrast between the background and flaw signal is high. In the dark field mode the flaw produces a bright, cometlike tail and stands out well from the background structure. The spacing between the fringes is the wavelength at 100 Mhz for surface wave propagation in this material.

Figure 46 shows an acoustic micrograph of hole α5 in step 6 of the alpha silicon carbide penetrameter. The hole is easily detected in both modes. This hole also appeared to approach the size of the surface pits.

It is concluded from the present study that acoustic microscopy can detect fracture-controlling surface flaws such as voids (holes) in both RB-SiC and α-SiC. The size (diameter x depth) of the smallest detected hole was 75 μm x 17 μm in RB-SiC and 68 μm x 25 μm in α-SiC. While these holes were detected in the thinnest step (0.54 mm [0.021 in.]), similar size voids can probably be detected by SLAM in thicker specimens, since the bulk acoustic attentuation of both materials at 100 Mhz is quite small.

Evaluation of Knoop Indented Specimens

Because of earlier successful results (Ref. 1), a systematic study was initiated at the Indianapolis Center for Advanced Research (CFAR) to further establish the ability of dark field acoustic microscopy to detect surface cracks, to predict failure sites by observation and/or imaging of the acoustic scattering behavior of the detected flaw and to correlate fracture location with predicted site, and to determine fracture toughness from measured flaw parameters. Two types of MOR specimens of alpha silicon carbide were prepared:

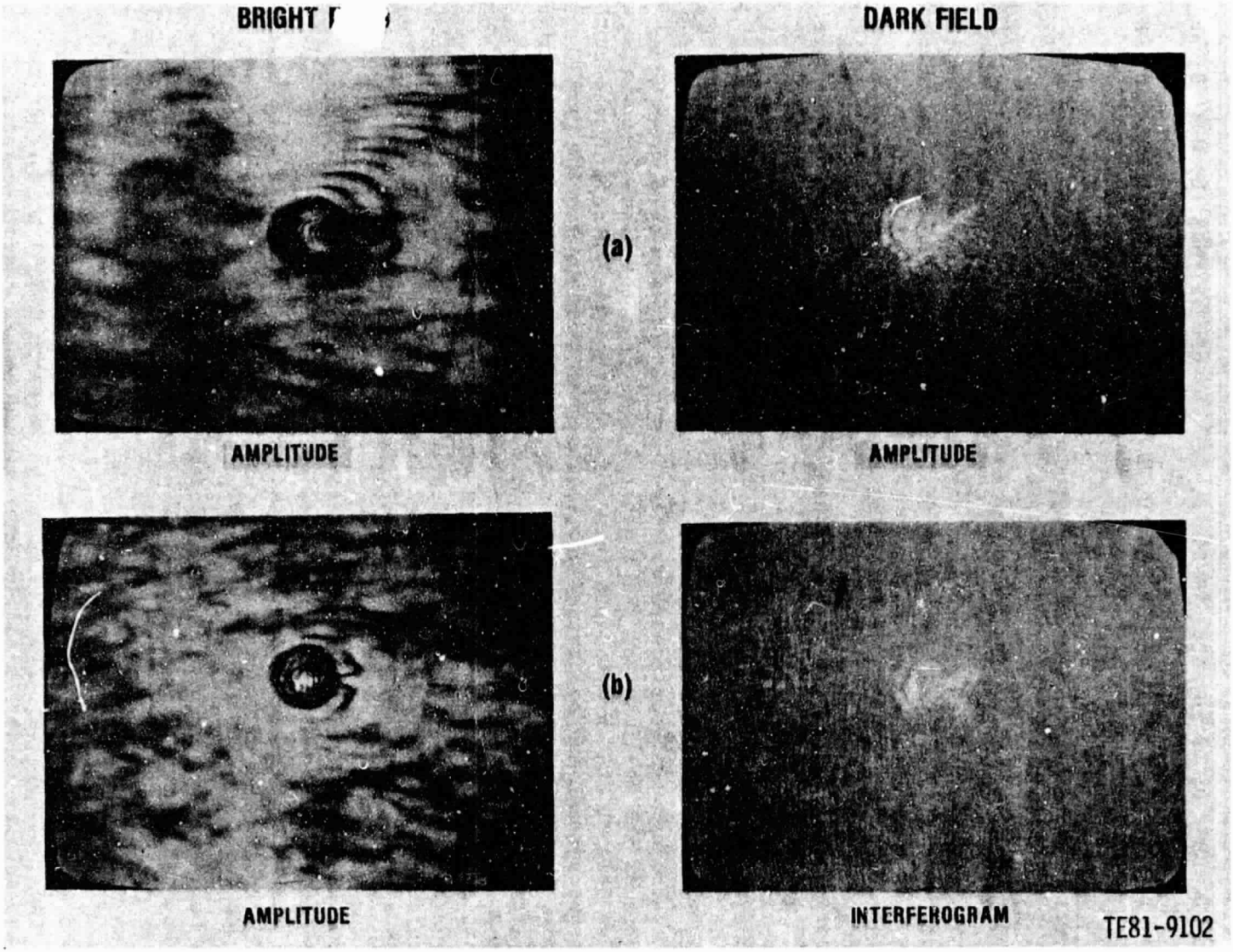

Figure 44. Acoustic micrographs of hole 1 in (a) reaction-bonded silicon carbide and (b) alpha silicon carbide penetrameters in step 1.

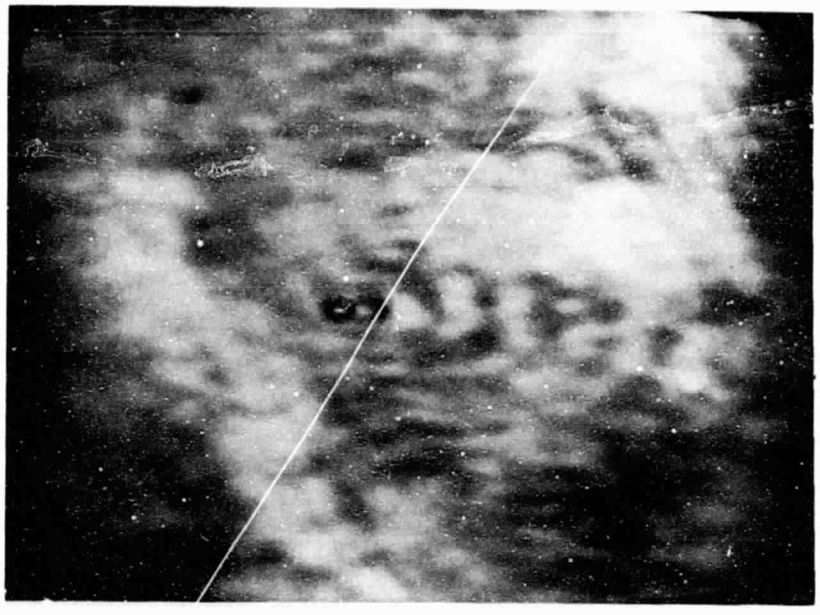

(a)

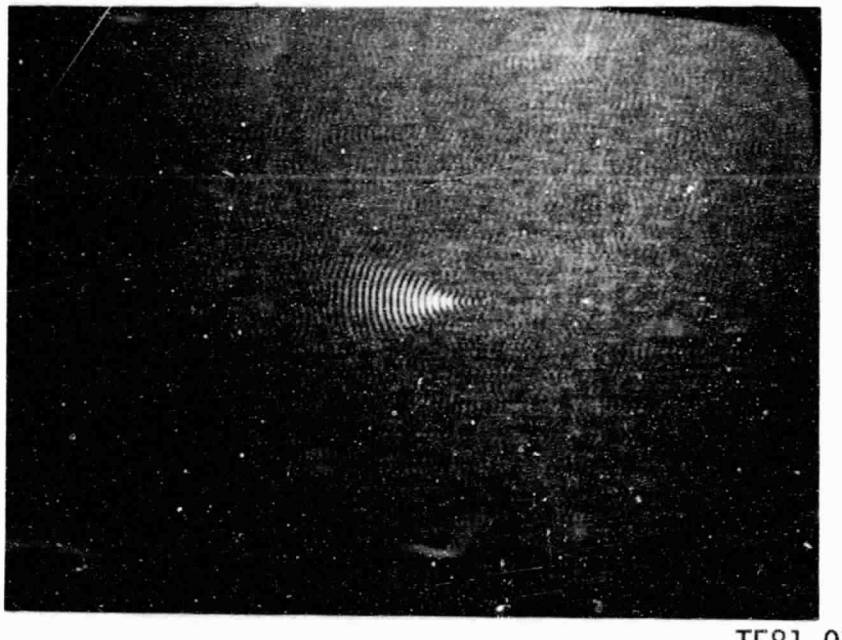

(b)

TE81-9103

Figure 45. Acoustic micrographs of hole 7 in reaction-bonded silicon carbide penetrameter in (a) bright-field amplitude and (b) dark-field interferogram mode in step 4.

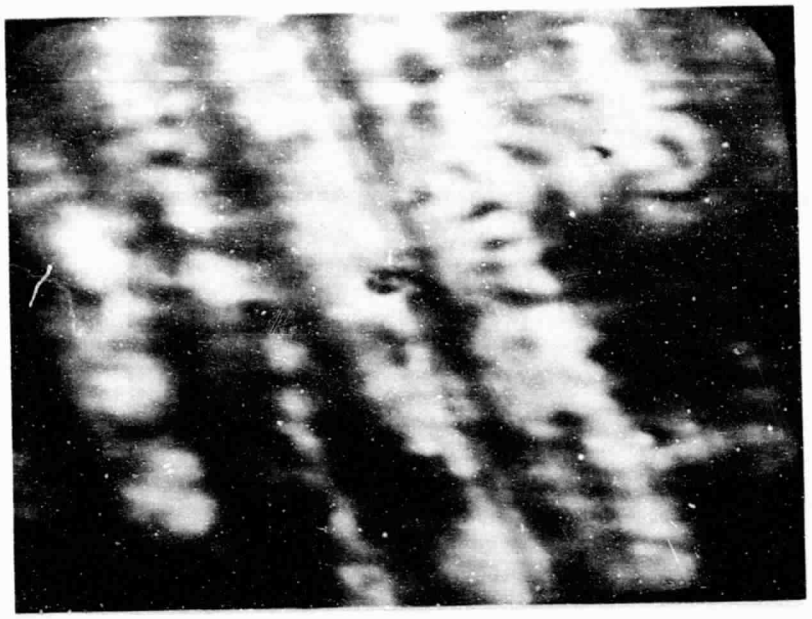

(a)

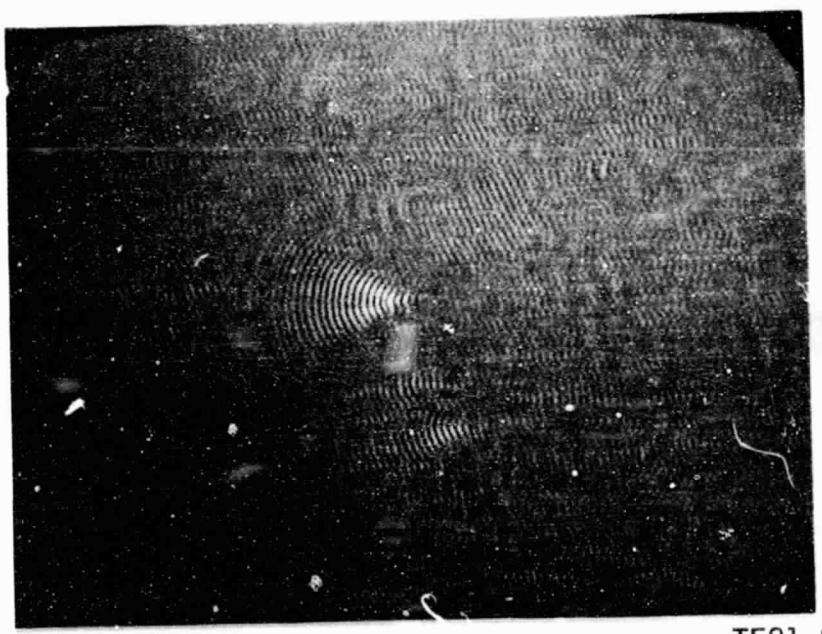

(b)

TE81-9104

Figure 46. Acoustic micrographs of hole 5 in step 6 in alpha silicon carbide penetrameter in (a) bright-field amplitude and (b) dark-field interferogram mode.

Type A: A specimen surface was polished to a 5 surface finish. Twelve Knoop indentations, three each of 23.54-, 13.73-, 4.91-, and 0.98-N (2.4-, 1.4-, 0.5-, and 0.1-kg) loads, were placed within the inner span of 19 mm (0.75 in.) of the four-point MOR bar. These indentations (Figure 47) were equally spaced to minimize any acoustic interference between scattered waves from adjacent flaws.

Type B: Three specimens of this type per indentation load (23.54, 13.73, and 4.91 N [2.4, 1.4, and 0.5 kg]) were evaluated. All the specimens were polished to a 6 surface finish. Each specimen had three indents of the same load made within the constant stress inner span or gage length (Figure 48). Therefore, all three flaws (indents) in a specimen were subjected to the same stress and acted as competing flaws during fracture testing in a quarter-point loading condition.

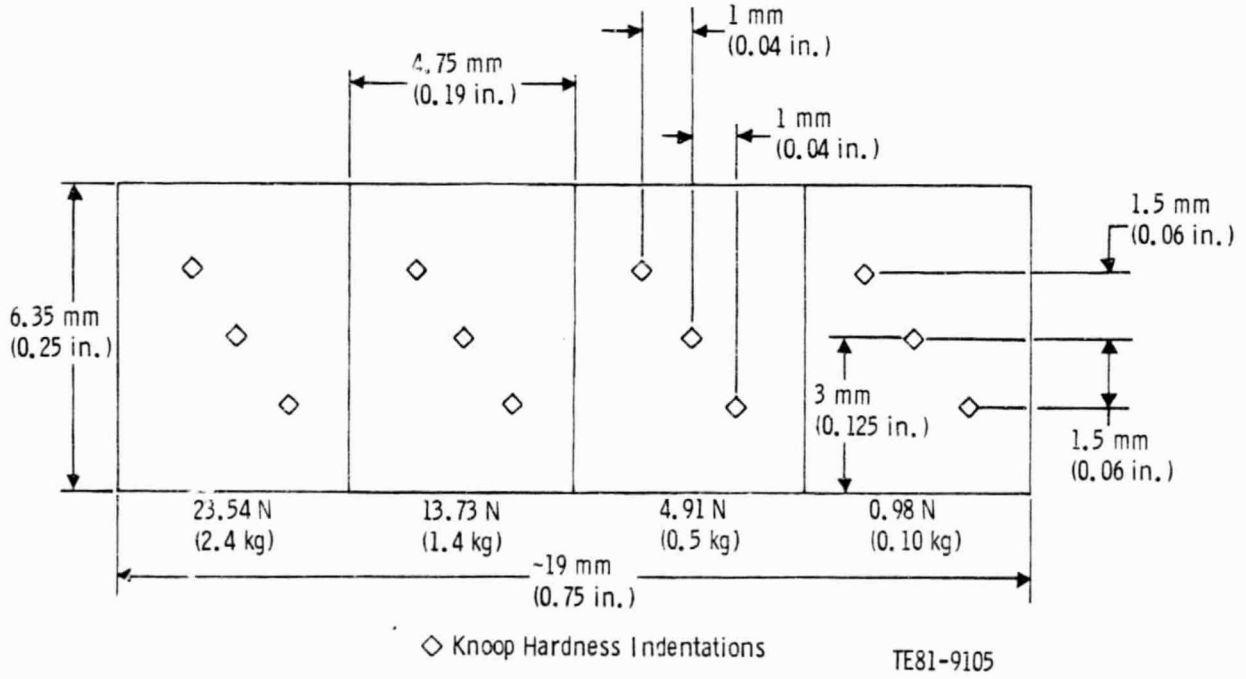

Figure 47. Layout of indentations in Type A specimen.

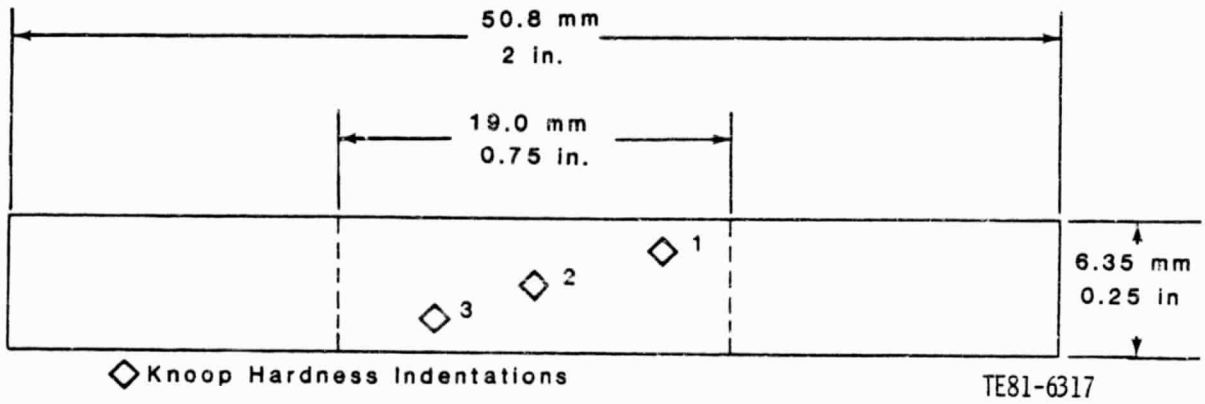

Figure 48. Layout of indentations in Type B specimen.

During the present reporting period, the first two parts of the study with Type A and B specimens have been completed and reported herein. The third part of the study on fracture toughness is in progress and will be completed during the next reporting period.

Evaluation of the Type A Specimen

All 23.54- and 13.73-N (2.4- and 1.4-kg) indentations were easily detected and imaged (Figure 49) with excellent discernibility in the dark field interference mode. The 4.91-N (0.5-kg) indentations could be detected and visualized on the TV monitor but could not be imaged on a Polaroid film with sufficient contrast. The 0.98-N (0.1-kg) indentations could not be detected. The acoustic micrographs clearly show the variability in the images of the 23.54- and 13.73-N (2.4- and 1.4-kg) indentations. Scanning electron microscopy (SEM) analysis of the indented surface of 23.54-N (2.4-kg) specimens showed variable damage around each indentation. Similar observations were made for 13.73-N (1.4-kg) load indentations. These variabilities are related to the local microstructural properties that govern both the surface and subsurface indentation-induced damage. Figure 49 also shows that the intensity of the backscattered energy is greatest in the center and least at the edge. It appears that the crack (indentation) has similar acoustic properties to a plane wave oscillator.

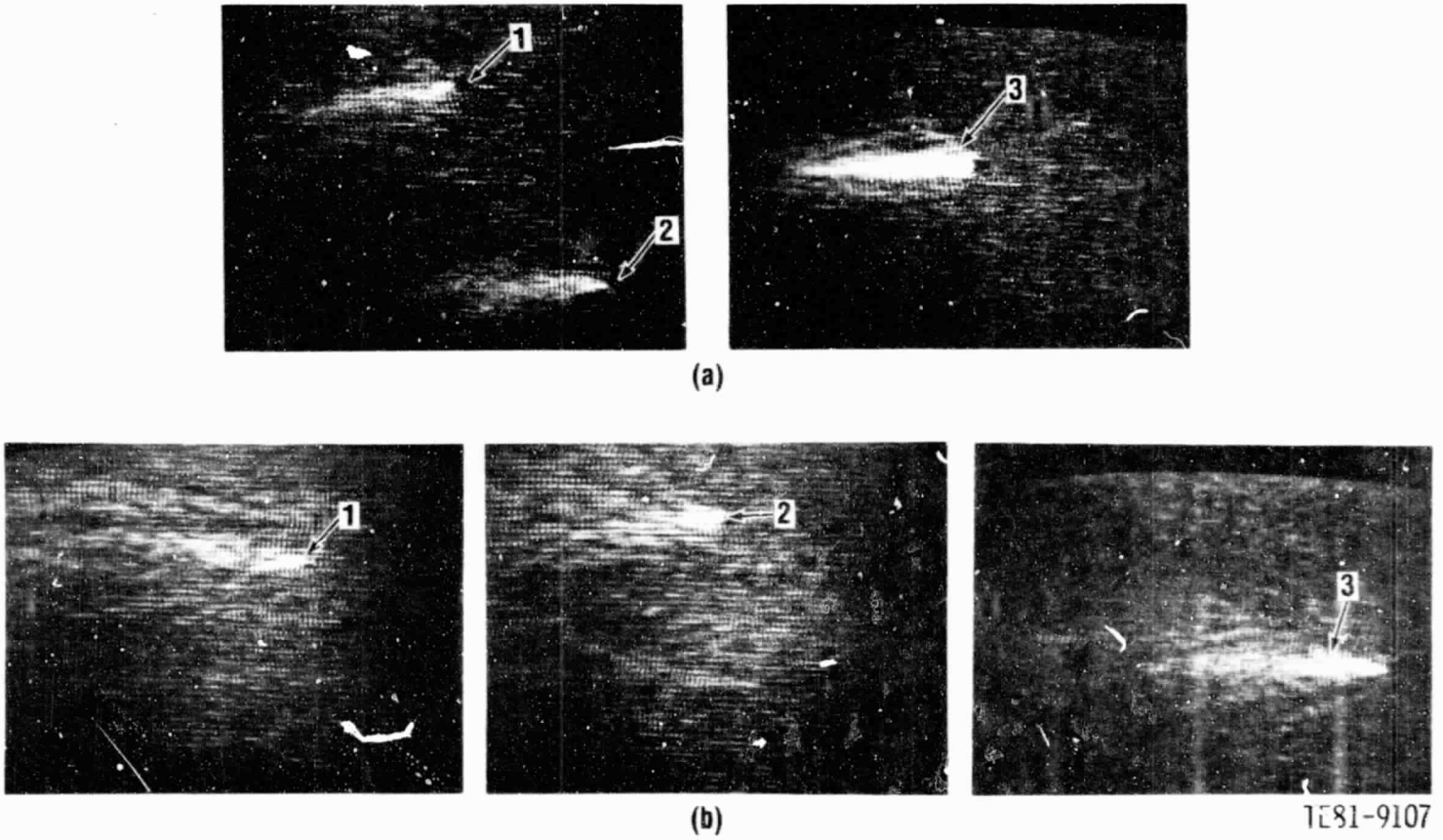

Figure 49. Dark-field acoustic interferograms of three Knoop indentations each for (a) 23.54-N (2.4-kg) and (b) 13.73-N (1.4-kg) loads in Type A specimen.

Another observable phenomenon is the regularity of the wavefronts. A perfectly planar scattered crack produces regular coaxial wavefronts. When the crack is not planar, it has been observed that mixed-mode scattering occurs, giving rise to different interference patterns with a characteristic fringe spacing and wavelength. This disturbance in the regularity of the wavefronts may be useful for predicting the shape of the scattering crack.

Evaluation of Type B Specimens

Figures 50, 51, and 52 show the dark field (backscattered) acoustic interferograms of 23.54- and 13.73-N (2.4- and 1.4-kg) indented specimens. The variation in the magnitude of the backscattered energy from indentation to indentation both within a specimen and between specimens is evident for all indentation loads. Surprisingly, however, the fringe spacing or wavelength (λ) is almost constant, suggesting that the acoustic mode conversion due to the interaction between the incident acoustic beam and flaw remains similar. It has also been found that small rotations (Figure 51) of the specimen have significant effects on the defect image. It appears, therefore, that the scattering characteristic of the two edges of the indentation may be different. Note that

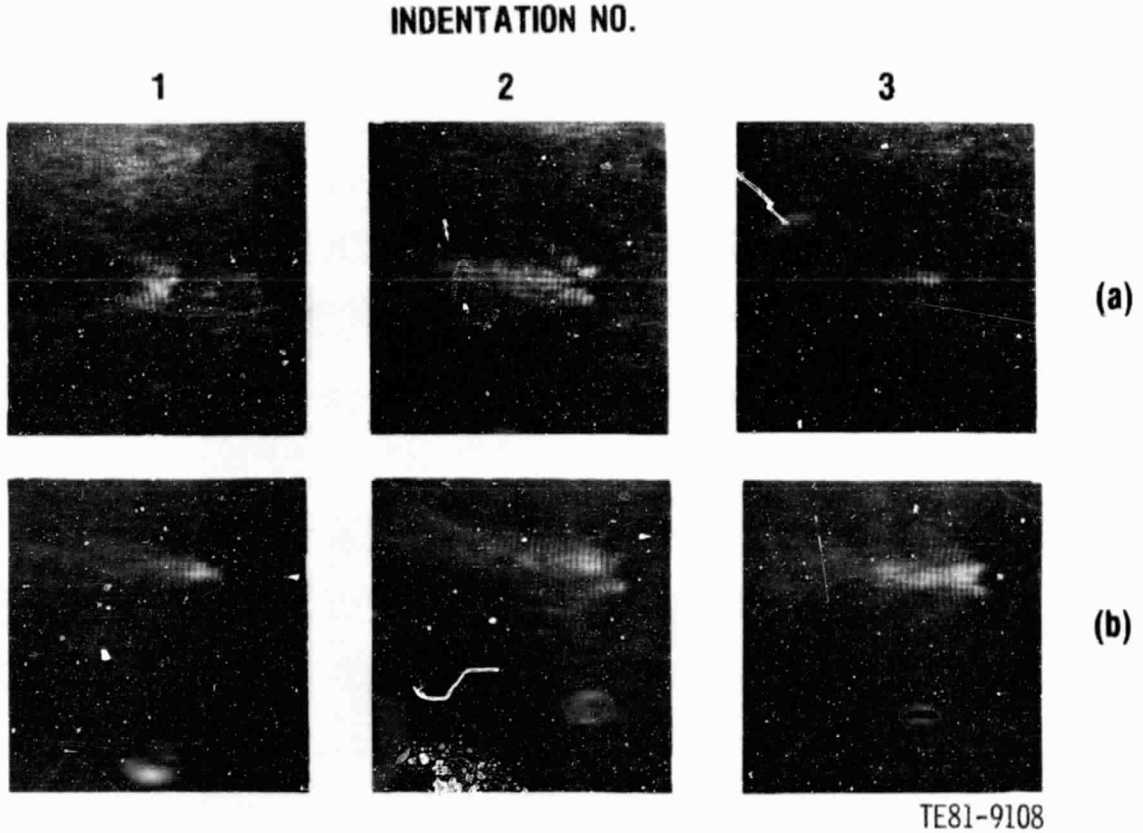

Figure 50. Dark-field interferograms of three 23.54-N (2.4-kg) load Knoop indentations in specimen 22.0369 (a) and 22.0379 (b) without removing the indentor-induced surface damage.

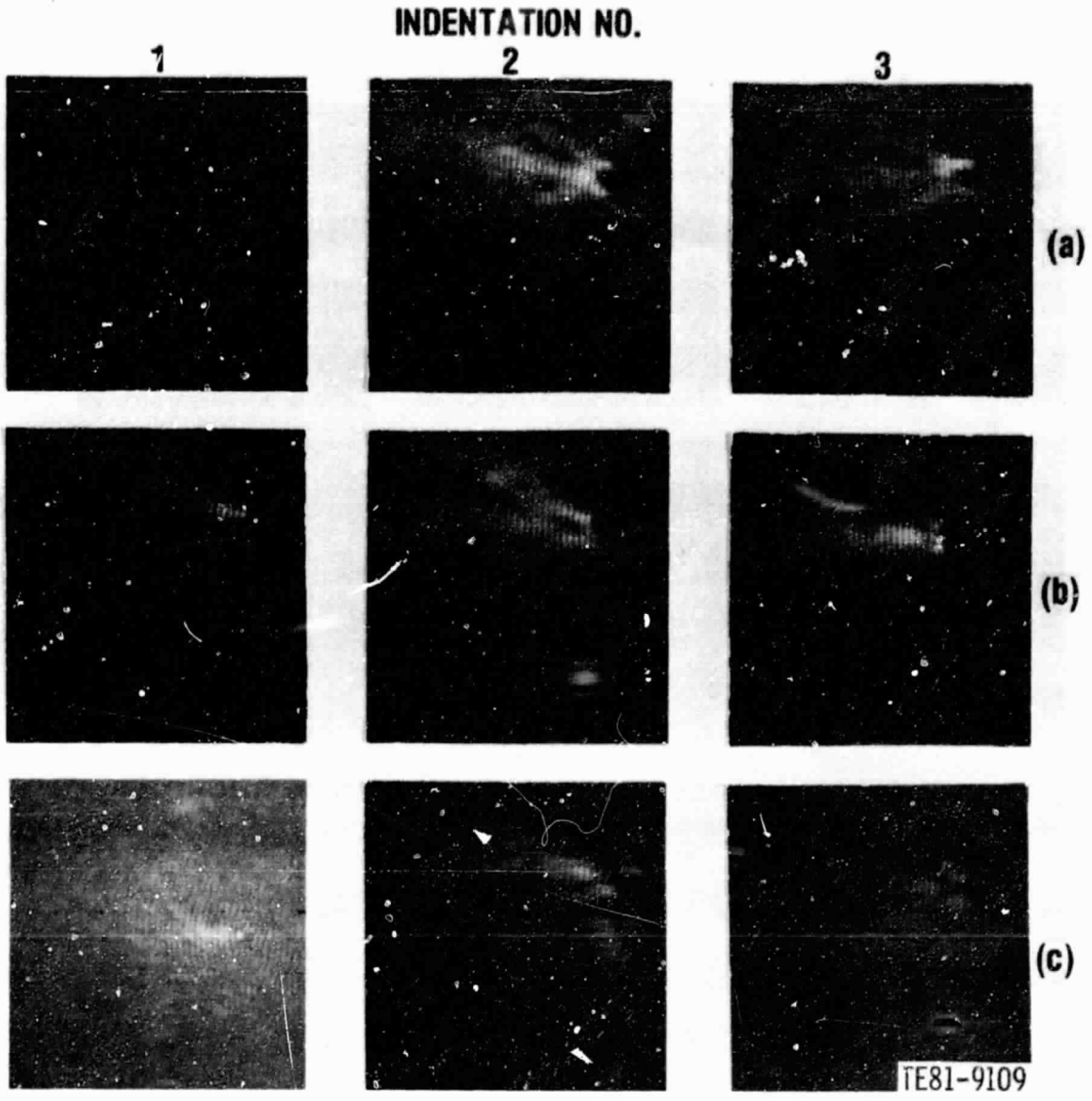

Figure 51. Dark-field interferograms of three 23.54-N (2.4-kg) load Knoop indentations in specimen 22.0383: (a) without removing surface-induced indentation damage, (b) surface as (a) except after rotating specimen 180°, and (c) after removing surface damage and oriented as (a).

the acoustic beam is insonifying a different volume of the specimen on rotation, which may also affect the intensity of the acoustic beam interacting with the flaw due to variation in attentuation.

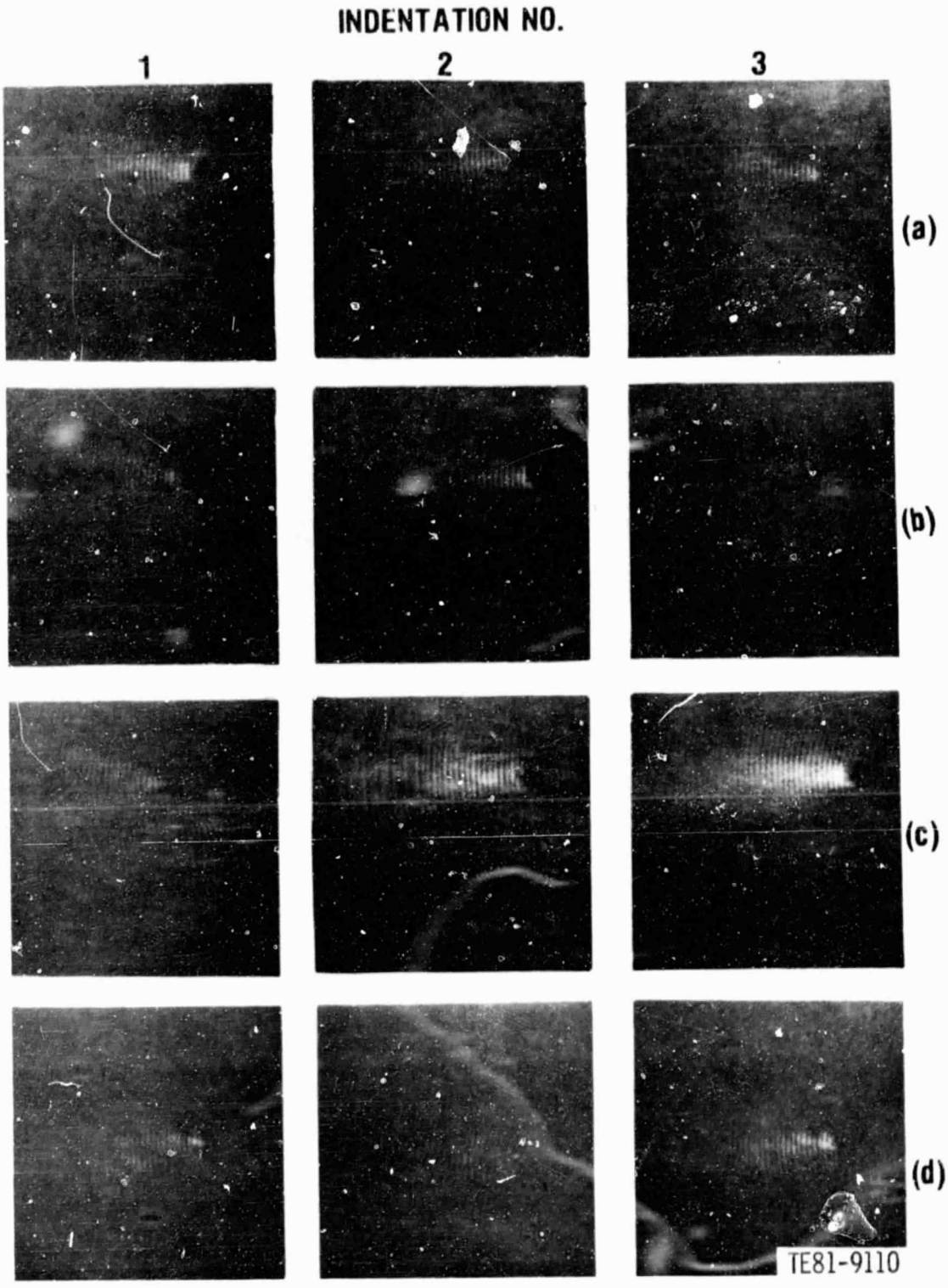

Figure 52. Dark-field interferograms of three 13.73-N (1.4-kg) load Knoop indentations each in specimen 22.0385 (a), 22.0399 (b), 22.0343 (c) without removing indentation damage, and 22.0343 (d) after removing indentation damage.

All three indentations in specimen 22.0383 were detected even after the indentor-induced surface damage was removed by diamond polishing. Both the surface and subsurface damage produced by the Knoop indentor are believed to contribute to the acoustic signal and image. Figure 52 shows a similar kind of variability in detection of the 13.73-N (1.4-kg) indentation in the dark field interferogram mode. All three indentations in specimen 22.0343 were also detected after the surface damage caused by indentation was removed. The 4.91-N (0.5-kg) indented specimens were also evaluated, and indentations along with other naturally occurring flaws were detected. However, no micrographs were possible because of poor photographic quality.

Failure locations and critical flaws for each specimen with three indentations within the inner span were observed by SLAM. The prediction was based on the intensity of the backscattered energy, its angle of divergence, and other observable features on the TV video monitor from each flaw. Specimens were subsequently tested in four-point bending. Table VI shows both the predicted and actual failure origins for all nine specimens. Seven specimens failed at predicted locations. Predictions for 23.54- and 13.73-N (2.4- and 1.4-kg) indented specimens were 100% accurate. No prediction was possible in specimen 22.0349 because the acoustic scattering characteristic of all three indentations was similar to that from the large number of naturally occurring surface flaws, resulting in no discernibility against the background structure. Specimen 22.0353 was predicted to fail at a natural flaw (SEM and optical microscopy revealed multiple flaws in the vicinity from which the acoustic microscopy signal was received), but instead failed at indentation 3. Since the size of the indentation 4.91 N (0.5 kg) in this specimen is similar to a naturally occurring flaw, the MOR test is realistic and has practical significance. The accurate prediction that specimen 22.0391 would fail at indentation 2 of the same load is remarkable The 90% accuracy (seven out of eight) for predicting failure origin by acoustic microscopy is excellent. These initial results are quite encouraging. However, substantial data with 4.91 N (0.5-kg) indentations and/or naturally occurring flaws are needed to conduct a probabilistic analysis and to develop accept/reject criteria.

TABLE VI. CORRELATION OF ACOUSTIC MICROSCOPY AND MOR TEST

	Results			
	Knoop indentation load		Indentation number at fracture	
Specimen	N	(kg)	Predicted by SLAM	Actual in four-point MOR test
22.0369	23.54	(2.4)	2	2
22.0379	23.54	(2.4)	2	2
22.0383*	23.54	(2.4)	2	2
22.0343*	13.73	(1.4)	2	2
22.0385	13.73	(1.4)	1	1
22.0399	13.73	(1.4)	2	2
22.0349	4.91	(0.5)	NDB	3
22.0353	4.91	(0.5)	NF	3
22.0391	4.91	(0.5)	2	2

*These specimens were tested in four-point bending after removal of indentation damage.

NDB--no prediction possible, no discernibility against background structure,
NF--failure predicted at a natural flaw.

CERAMIC MACHINING DEVELOPMENT

Two major goals of the ceramic machining study have been accomplished in the past six months. First, the successful machining of a ceramic plenum has been completed. Secondly, creep-feed grinding has been proven capable of machining ceramic components.

The overall goal of the study of ceramic machining techniques has been to develop methods to finish machine ceramic components in a cost-effective manner. The machining of the ceramic plenum demonstrates several facts: first, a thin-walled, irregularly shaped part can be safely affixed using a compound like Rigidax ^{R} ; secondly, conventional diamond-grinding techniques can safely machine thin wall areas; lastly, normal affixing methods are safe if the part has a ground, qualified surface for the mounting points to contact. The qualification of creep-feed grinding provides an effective method of machining close-tolerance two-dimensional contours. With the completion of the two major goals stated above, only the machining of blind and through holes for the inner vane and outer vane support rings remains. The scope of this study will now be restricted to the development of an acceptable method of producing blind and through holes.

In general, conventional machining techniques were studied and either rejected or accepted. All single-point machining methods were found unacceptable. With the exception of form grinding, conventional methods of grinding were found acceptable. The proper affixing and selection of diamond grinding wheels are essential if costs are to be held to a reasonable level. When a component could not be machined by conventional methods, nonconventional methods were examined.

The nonconventional methods examined were creep-feed grinding and ultrasonic impact grinding. Creep-feed grinding is a type of form grinding. This method uses a slow table speed of 2.5 to 100.0 cm/min (1 to 40 in./min) and cuts to the full depth in one pass.

Creep-feed grinding was used to grind the dovetail portion of the turbine blade. The actual work was done by Midwest Precision Services of Roselce, Illinois, which used a crush-dressable diamond wheel and a carbide crush roll on a Tripet grinder. The first blades that were machined by this grinding method have been spin-tested. The results have been good and indicate that no critical flaws are induced by creep-feed grinding.

IV. CERAMIC TURBINE COMPONENTS

GASIFIER TURBINE NOZZLE

Assessment of Ceramic Components at 1038°C (1900°F)

Forty-one hr of engine testing were accumulated on a 1900°F-configuration ceramic nozzle assembly in this reporting period. This time was devoted solely to engine testing to evaluate ceramic vanes, experimental instrumentation on ceramic vanes, and abradable turbine tip shrouds. The high time on the 1900°F-configuration vane currently on test in engine C-1 is 1033 hr. The overall high-time vane in the CATE program has 1512 hr. There have been no ceramic vane failures on engine test during this reporting period. Two noteworthy ceramic technology features were included in this test sequence: four ceramic vanes had experimental thermocouples attached to the airfoils, and a metal gasifier rotor shroud had a zirconia plus glass eccospheres ceramic coating sprayed on the surface shrouding the rotor blade tip.

The four instrumented ceramic vanes had fine wire thermocouples, 0.076-0.102 mm (0.003-0.004 in.) in diameter, attached to the vane airfoil with "H" cement and a "Denex-2" adhesive. These adhesives were the most promising of 14 samples evaluated. After 41 hr of testing in engine C-1, examination of the four vanes showed that on the concave (pressure) side of the airfoil both adhesives had eroded away. The adhesives on the convex (suction) surface were still in place. It is not known if the adhesive--thin-wire combination would have survived a short-term test.

A second problem identified with the thin-wire thermocouple was the lack of a satisfactory system to attach the 0.76 mm (0.030 in.) sheathed leadout thermocouple wire to the thin-wire thermocouple. All cements tried would not hold the thick leadout to the ceramic vane. Considerable work needs to be done on the thin-wire thermocouple concept before a practical system of temperature measurement can be developed.

The abradable ceramic turbine tip shroud tested on engine C-1 was a plasma-sprayed, zirconia eccosphere ceramic material applied to a standard IGT air-cooled metal shroud. This system is being developed by the DDA Materials Laboratory. The percentages of zirconia and glass eccospheres have been adjusted to produce the desired hardness and erosion resistance. The rotor assembly was built with 0.203 mm (0.008 in.) radial clearance, instead of the nominal 0.406 mm (0.016 in.). This resulted in rotor-to-shroud contact and interference during engine operation. Some metal transferred from the rotor blade tips to the abradable material (Figure 53), and some abradable material was removed from the shroud. This was not considered a successful abradable shroud.

2070°F-Configuration Gasifier Nozzle Design and Development

Summary

During this period, initial engine operation with a 2070°F-configuration nozzle assembly resulted in the successful completion of 616 hr of testing in engine C-4 at a 1038°C (1900°F) turbine inlet temperature.

Figure 53. Turbine tip rub on zirconia/eccosphere abradable coating. Rotor material is Mar-M246.

Additional testing on the thermal shock rig identified several development problems on the ceramic ring structures, and these are now under investigation. There were also design activities to define hardware development changes and follow-up activity on ceramic component process development. Continued thermal shock proof testing and engine testing to 1132°C (2070°F) are planned for the next reporting period.

Objective

The 2070°F-configuration gasifier nozzle design and development effort had two objectives. The first was to proof test ceramic nozzle components to qualify them for 2070°F-configuration engine operation. This proof test will be conducted in a thermal shock rig that simulates the most severe engine transient temperature conditions. The second objective is to use the qualified ceramic components for engine test evaluation. This will be accomplished by running a vehicle durability schedule on the test stand. Initial running will be limited to 1038°C (1900°F) turbine inlet temperature until ceramic rotor blades and a ceramic turbine inlet plenum become available.

Discussion

Design Hardware Development Changes

The significant design changes involving the gasifier nozzle were the redesign of the block crossarm cooling system and the addition of ceramic rope packing between the vane retaining ring and the vane support ring. The previous block cooling system used compressor discharge air to cool the crossarm bulkhead, after which this air cooled the turbine containment ring and the gasifier nozzle support struts and provided gasifier turbine rotor rim cooling. Section VI in this report describes the new system's use of ambient air and a fan to force convection cool only the block crossarm bulkhead. The 2070°F-configuration gasifier nozzle system had to be reconfigured to provide cooling for the containment ring, struts, and turbine rotor rim. The ceramic rope packing was added between the vane retaining and outer support rings to act as a dampening feature and to block secondary leakage.

The ambient air cooling system for the crossarm bulkhead was required for engine operation at 1132°C (2070°F). Figure 54 shows the original compressor discharge air cooling system. This system was used to establish the ceramic component heat transfer boundary conditions for the probability of survival analysis work.

Figure 55 shows the revised cooling system, which is compatible with the ambient air block crossarm cooling system. This turbine cooling system still uses compressor discharge air to cool the nozzle assembly, but the routing of the air is significantly revised. Compressor discharge air is taken from the supply source on the gasifier front support and fed up the strut, around the containment ring, and back through the outer diameter of the ceramic nozzle support into the flow path. A second circuit takes air from the same source and introduces it ahead of the inner ceramic vane support ring to cool the gasifier turbine rotor rim.

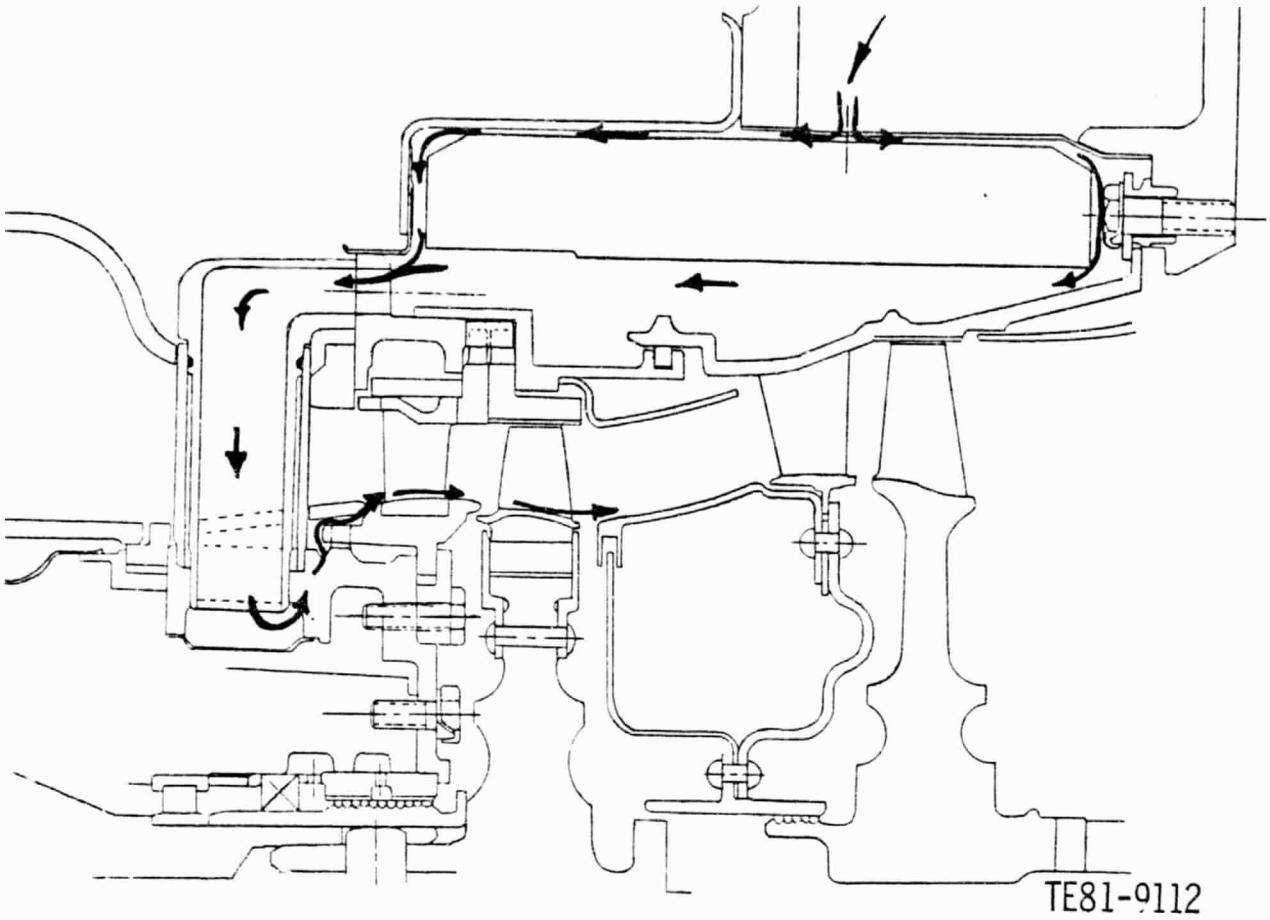

Figure 54. Original 2070°F-configuration gasifier turbine nozzle cooling system, used with compressor discharge air block cooling.

The significant effects of this revision on the ceramic components are the temperature of this cooling air and its cooling effect. The same amount of cooling air flows over the inner ceramic vane support ring as in the old system, but the air is estimated to be 278°C (500°F) cooler. This should help cool the turbine rotor rim, but its effect on the inner ceramic ring can be evaluated only by analysis.

In the previous turbine cooling system, the gas path flow recirculated over and between the vane outer support ring and the vane retaining ring. Besides affecting the heating rate of the rings, this recirculating flow was suspected to be affecting the vane passage aerodynamics. In the revised system, the strut and containment ring cooling flow enters the gas path by passing forward through the outer nozzle metal support structure and over the outer diameter of the outer ceramic rings. This flow tends to scrub the outer diameter of the shroud and the vane support ring. It could contribute to increased thermal gradients and stresses in those rings.

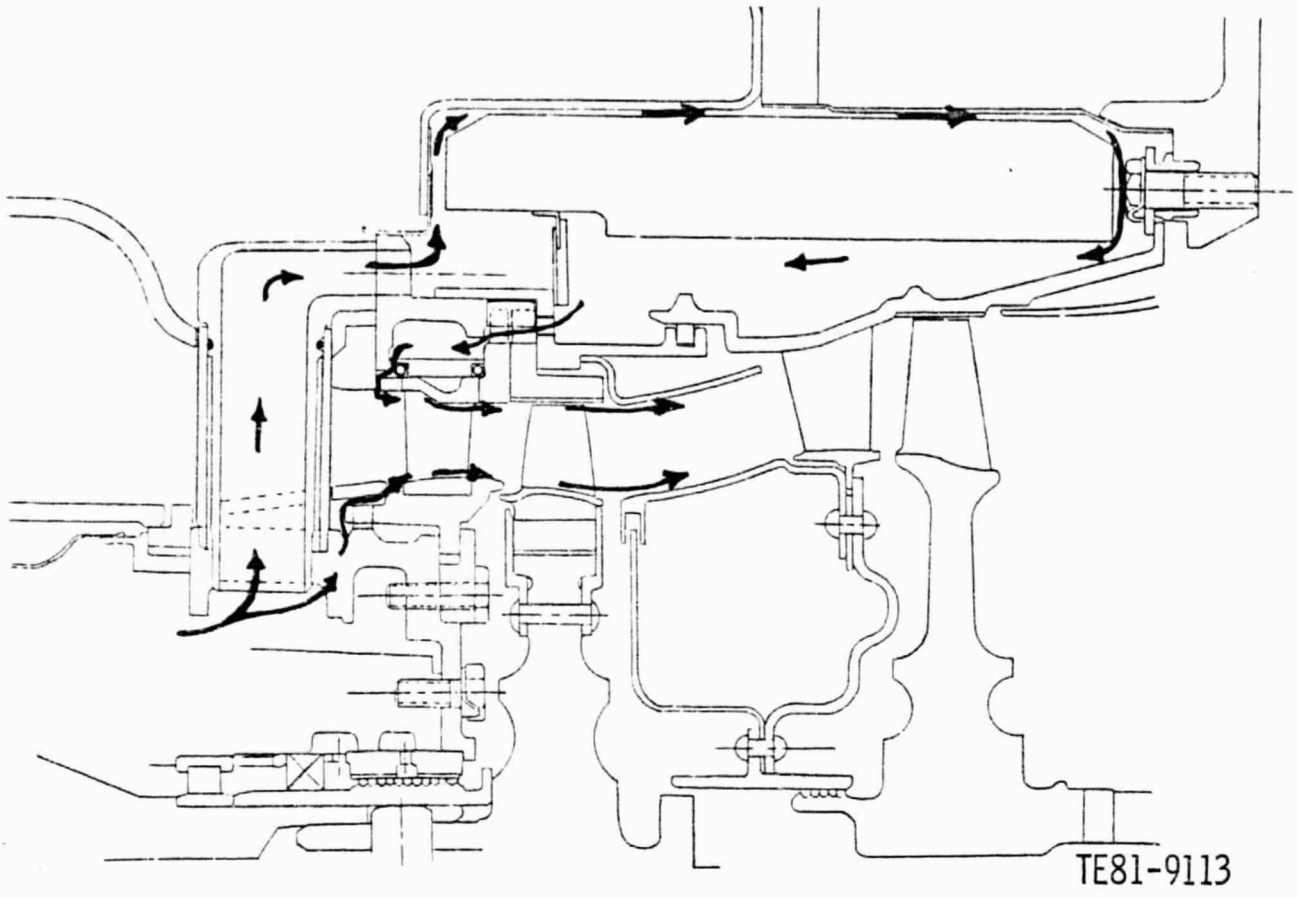

Figure 55. Revised 2070°F-configuration gasifier turbine nozzle cooling system, used with ambient air block cooling.

To reduce leakage between the vane support ring and the vane retaining ring, two pieces of ceramic rope packing were added to grooves machined in the ceramic vane retaining ring. Besides reducing leakage, this entrapped packing dampens vibrations between the free-floating retaining ring and the slotted outer vane support ring. The effect of the packing on aerodynamic performance will have to be evaluated in terms of nozzle cold flow capacity in a subsequent rig test.

Process Development

In tne previous reporting period, Carborundum completed activities on its subcontract to develop ceramic nozzle components. Concurrent with the last phases of the subcontract, follow-on orders were placed with Carborundum for additional rings and vanes made to the final specifications in the process routing. The only changes from the process routing were on the inner and outer vane support rings. In the previous progress report (Ref. 1), under Tasks IIIb and IIIc of Process Development, elimination of green body stress

cracks was discussed. Carborundum maintained that these cracks could be avoided by molding the green body to a lower green density. This processing change was included in the follow-on orders of inner and outer vane support rings. There was no evidence of this type of flaw with the follow-on order of rings.

During the subcontract development effort, incomplete siliconizing of the reaction-sintered bodies was observed. This results in porosity and severely reduced material strength. Carborundum feels that this problem is related to the size and temperature control limits of the siliconizing furnace. It is attempting to obtain a furnace with increased capability on both parameters.

The three shrouds delivered under the follow-on orders were all found to have cracks in the abradable layer, as illustrated in Figure 56. Investigation by Carborundum traced these flaws to localized variations in clamping loads on the ring during green machining. Carborundum will revise and specify the green machining clamping procedure prior to remaking these three shrouds.

There were no problems with the fabrication of the follow-on orders of the reaction-bonded or alpha silicon carbide vanes.

Three additional vendors have been fabricating 2070°F-configuration nozzle components. Pure Carbon Co. is having British Nuclear Fuels Ltd. fabricate three isopressed outer vane support rings from Refel reaction-bonded silicon carbide. These would be finish machined except for the vane pockets. Delivery is expected in the next reporting period. Kyocera made sintered silicon carbide inner vane support rings. Again the rings were finish machined except for the vane pockets. The first three rings delivered to DDA did not meet print dimensions. These were returned to Kyocera and the replacement rings have passed DDA inspection. Machining is in process on the vane pockets.

The final vendor, NGK, has proposed making unsolicited silicon nitride samples of all ceramic components in the 2070°F-configuration design. This includes all nozzle parts, plenum, and blades. Several of these components have been received and are being inspected at DDA.

Thermal Shock Rig

The previous progress report, Ref. 1, documented the results of the first three thermal shock rig proof tests on 2070°F-configuration nozzle components. Ceramic parts were subjected to a rapid thermal heat-up from 260°C to 1038°C (500°F to 1900°F) in 2 sec. The rapid cool-down transient used in the design analysis was not attempted, since design changes were still being studied to improve the low probability of survival (P_s = .76) on the outer vane support ring. This thermal shock rig proof test was compatible with initial engine testing, which would experience rapid heat-up only because engine operation was limited to the absorption dynamometer test stand.

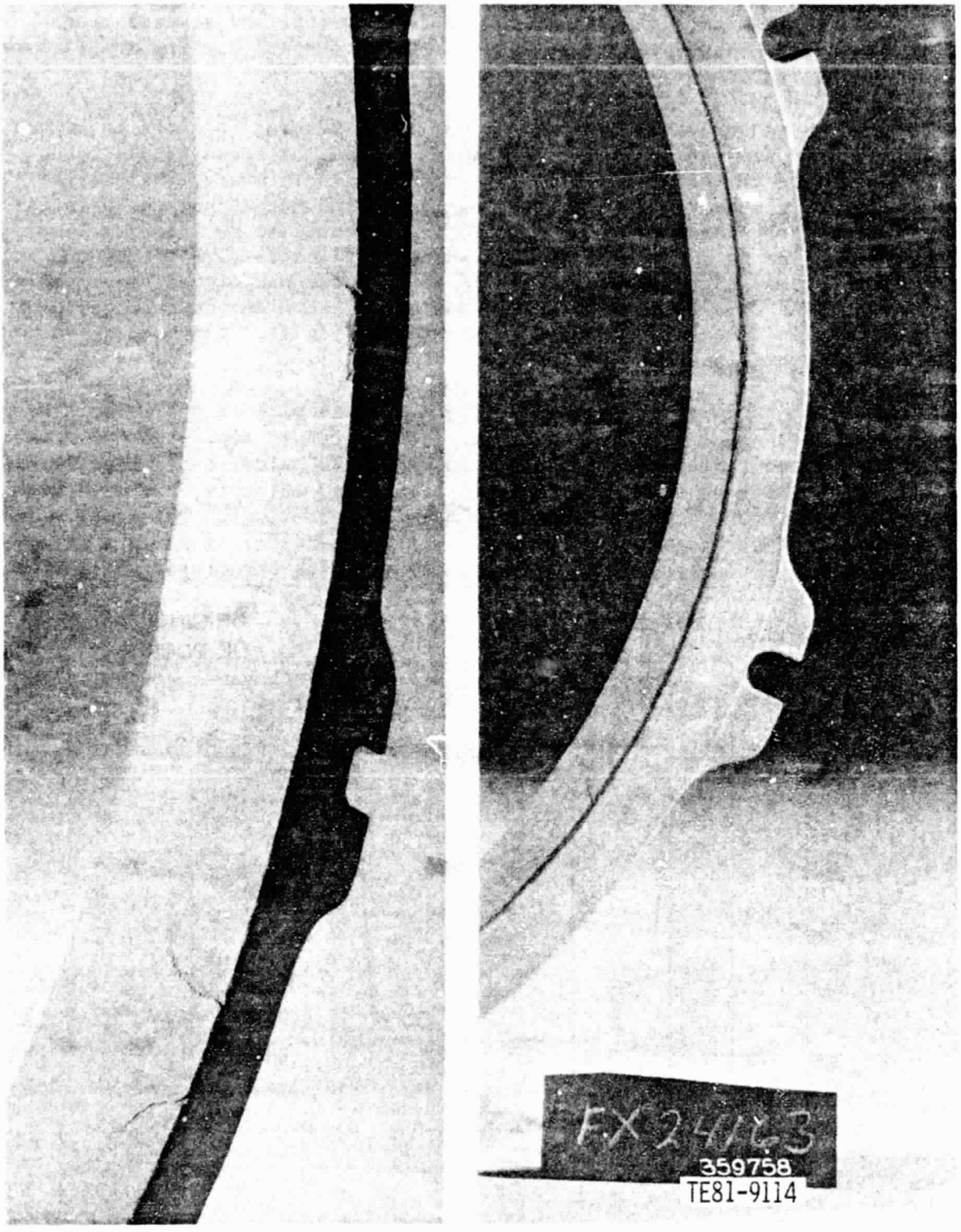

Figure 56. Shroud ring cracks due to improper clamping in green machining.

In the current reporting period a new rig with a higher temperature capability (identified as rig S/N 95) was introduced into the proof test program. The cool-down thermal transient was added to the proof test cycle, but the maximum steady-state temperature was still limited to 1038°C (1900°F). One set of ceramic nozzle hardware was proof tested in the new rig, and several rings failures resulted. This discussion will cover the current testing and failure analysis investigation.

The temperature schedule used in the thermal shock testing is shown in Figure 57. The initial test on the new rig limited the maximum steady-state rotor inlet temperature to 1038°C (1900°F). As mentioned previously, the thermal shock temperature schedule included the rapid cool-down that had not been included in the first three tests on the old rig (identified as S/N 2). The test procedure was to run five thermal transient cycles to 1038°C (1900°F) and inspect the ceramic parts for failure. If no failures were found, five thermal cycles to the 1132°C (2070°F) level were to be run. Any ceramic parts that passed Zyglo inspection after this proof test would be considered qualified for engine testing.

A set of ceramic hardware was tested in the above-described manner. This was the first test of an outer vane support ring subjected to rapid cool-down, and the probability of failure was predicted to be 23.7%. After testing to 1038°C (1900°F), inspection of the ceramic hardware revealed multiple fractures of the shroud, outer vane support, and inner vane support rings. The vanes, retaining ring, and strut shells all passed Zyglo inspection. A failure investigation was subsequently conducted on the ceramic ring structures.

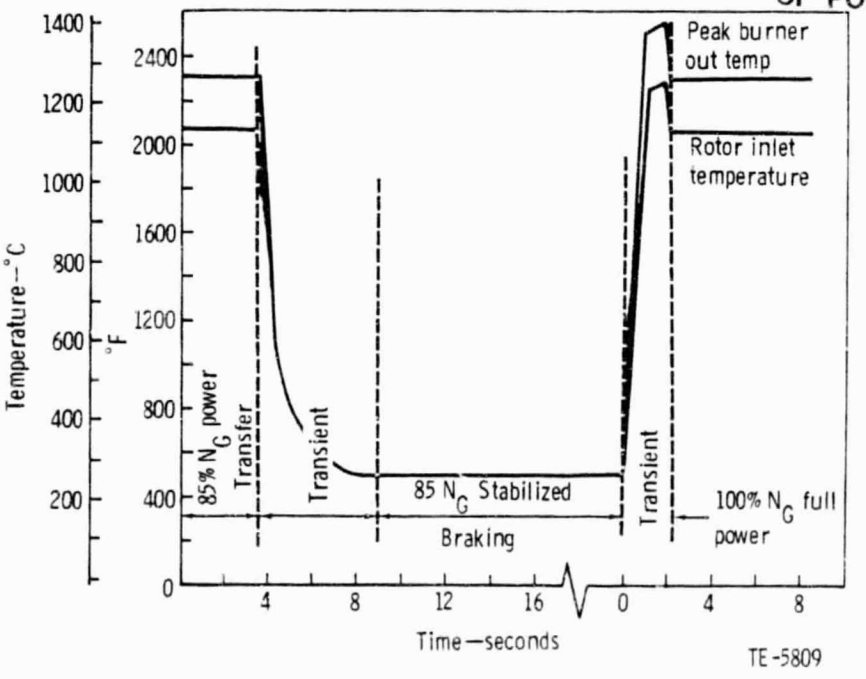

Figure 57. 2070°F-configuration engine thermal transients for transfer analysis and thermal proof testing.

Figure 58 shows the locations of the ring fractures. The inner vane support ring was fractured at 90°, as viewed from the rear. The shroud ring was fractured at 90° and 158° viewed from rear. The fracture at 90° went through a shroud centering lug that was in contact with a metal alignment peg. The outer vane support ring had multiple fractures (Figure 59). The same alignment lugs at 90° on the outer vane support and the shroud were broken. All the ceramic fractures, rig data, and component measurements were carefully examined.

Figure 60 presents nozzle exit gas temperatures measured at a burner outlet temperature (BOT) of 1027°C (1881°F). The four dips in the circumferential temperature profile are very pronounced. Examination of the test hardware revealed that this distortion was due to secondary flow through the clearance between the four ceramic strut shells and the four openings in the plenum and plenum inner annulus (Figure 61a). This gap is 1.96/1.45 mm (0.077/0.057 in.) in hot operation with a metal plenum. Calculations suggest that this clearance would allow 4.75% of the combustion air to bypass the burner. Depending on the degree of localized mixing of this bypass flow, this amount is sufficient to account for the circumferential temperature profile distortion. Figure 61b shows the revised design in which the clearance gap is blocked with ceramic rope packing held in place by a retainer. The effect of the design rework on the gas path temperature profile will be evaluated in the next reporting period.

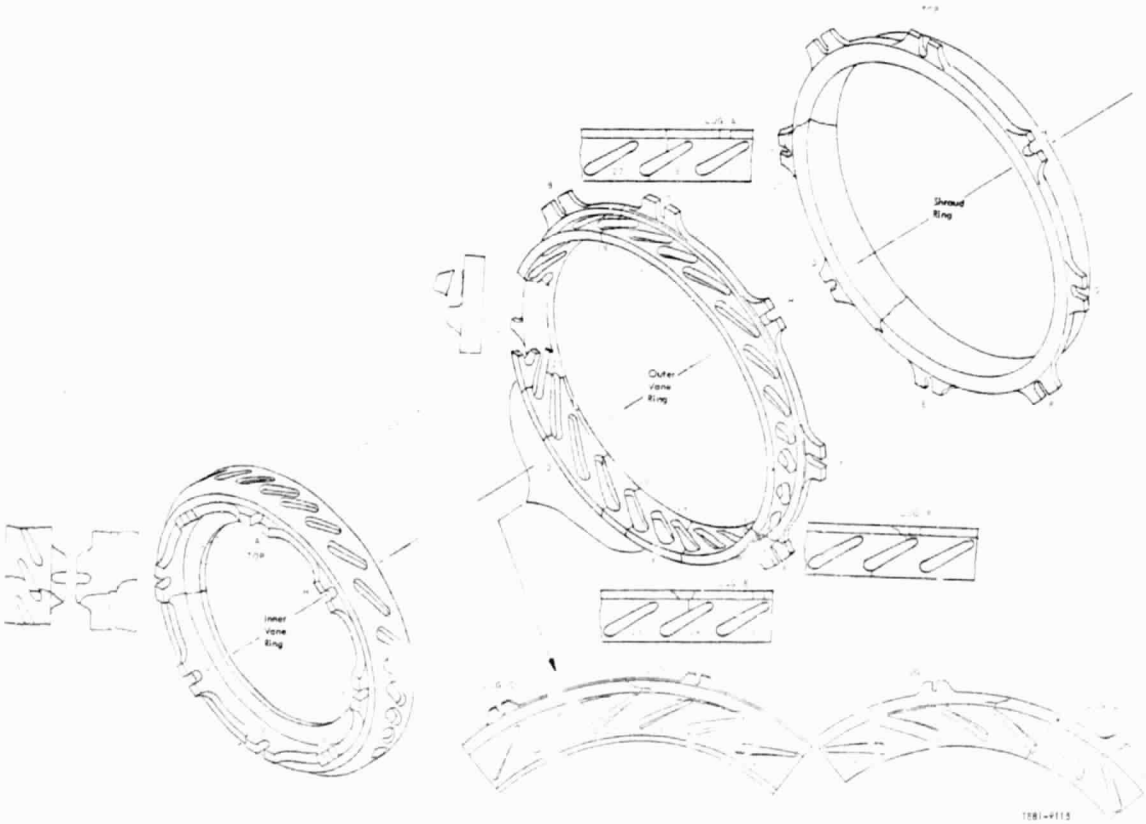

Figure 58. Thermal shock rig test failures (rig S/N 95, BU 1).

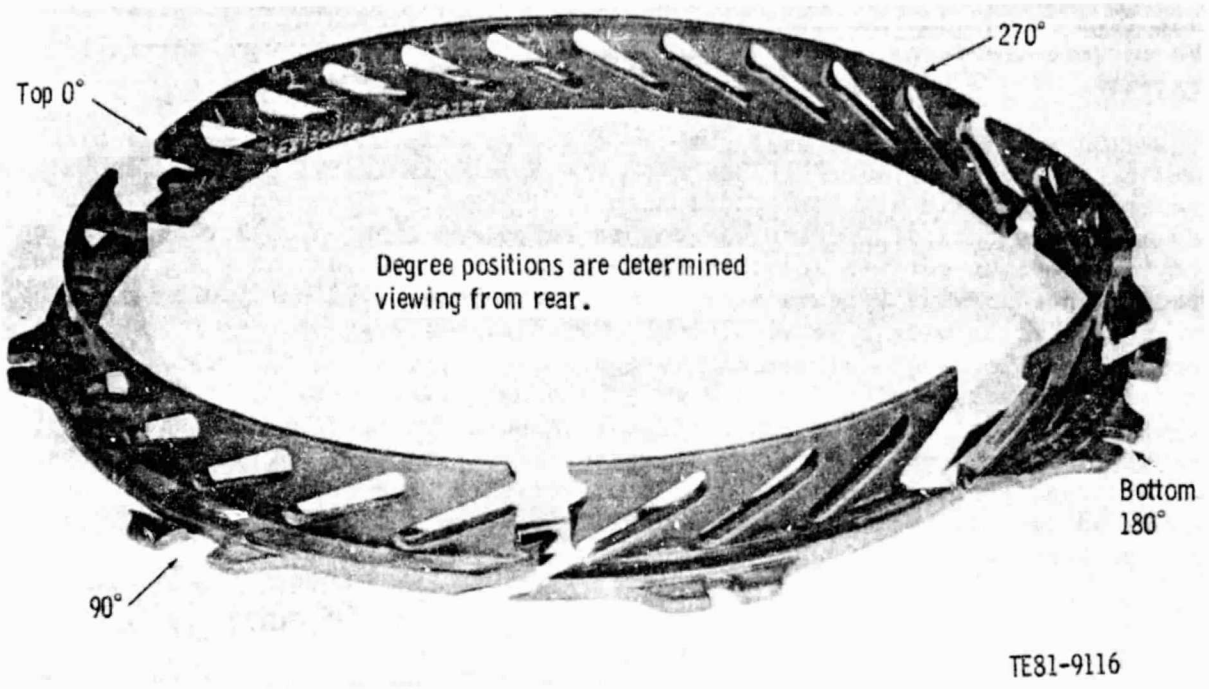

Figure 59. Failed outer vane support ring, thermal shock rig S/N-95, BU 1. Degree positions are determined by viewing from rear.

o Outer Vane Support Ring

Careful examination of the outer vane support ring showed three separate failure modes: lug fracture at one location, flange fracture at two locations, vane pocket fracture at multiple locations.

The lug fracture was identical in nature to that on the shroud ring. The same side of each alignment lug at the 90° position fractured. The common element was the metal alignment peg. Investigation revealed that the large circumferential temperature gradient in the gas path produced uneven heating of the outer metal support ring. This uneven heating resulted in nonuniform thermal expansion, with the metal alignment pegs shifting out of line with the alignment lugs on the ceramic rings. This shift was more than the part clearances could accommodate. The ceramic lugs could not restrain the thermal growth of the metal support ring. This mechanical load created stresses that exceeded the ceramic material strength, and failure resulted.

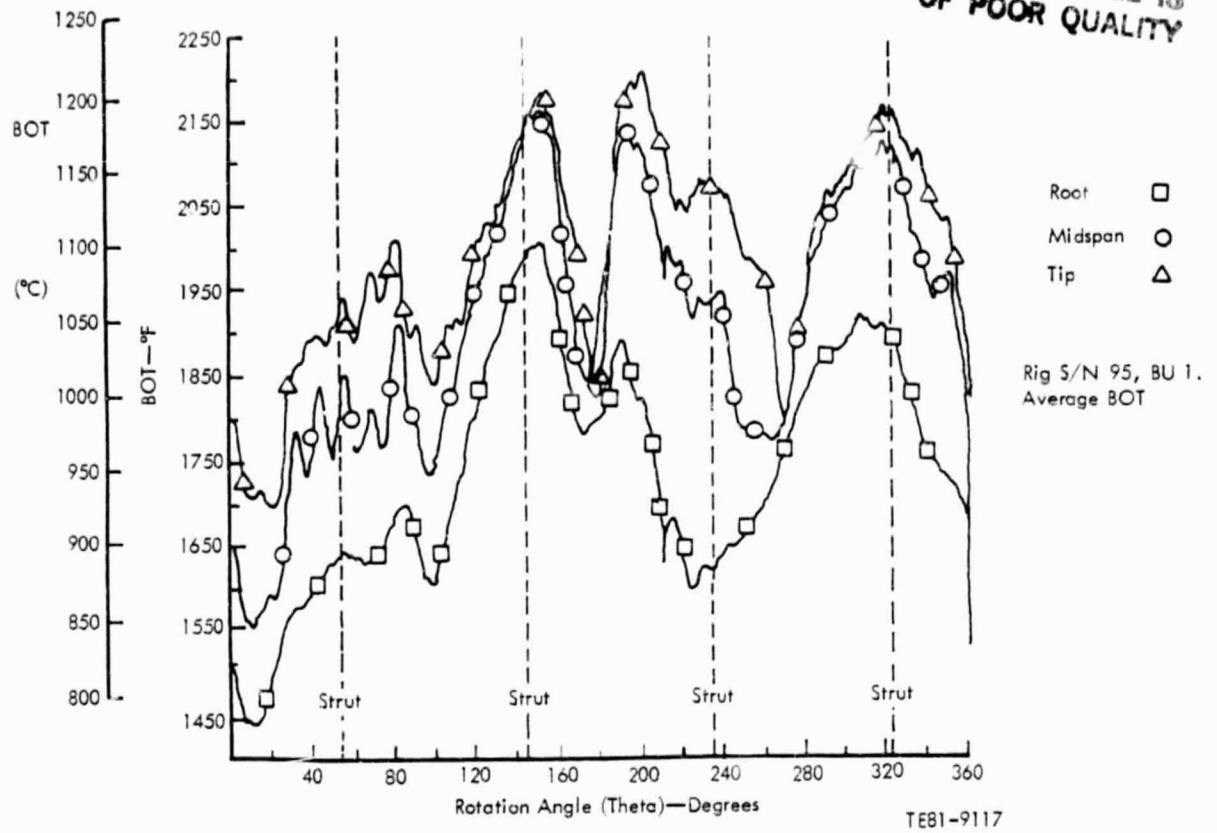

Figure 60. Survey of 2070°F-configuration gasifier nozzle exit showing circumferential temperature gradients.

Design changes were made to correct this condition. The clearance between the metal alignment peg and the ceramic alignment lug was increased to accommodate thermal distortion of the metal ring. Additionally, the block crossarm cooling circuit design changes, described in the design development section, will cause the inner and outer surfaces of the metal ring to be surrounded with cooling air. This will tend to nullify the effects of uneven heating from the gas path and reduce metal ring thermal distortion. Finally, the ceramic rope packing added to stop the plenum/strut shell leakage should improve the circumferential temperature profile and reduce the uneven heating of the metal support and thus the thermal distortion of the metal ring. These design changes are in progress and will be evaluated during the next reporting period.

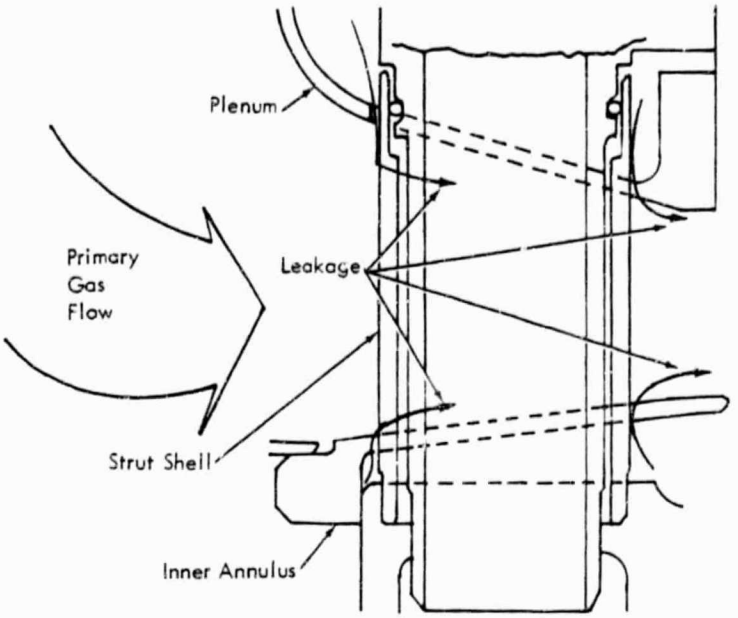

(a) Original 2070°F-Configuration Design

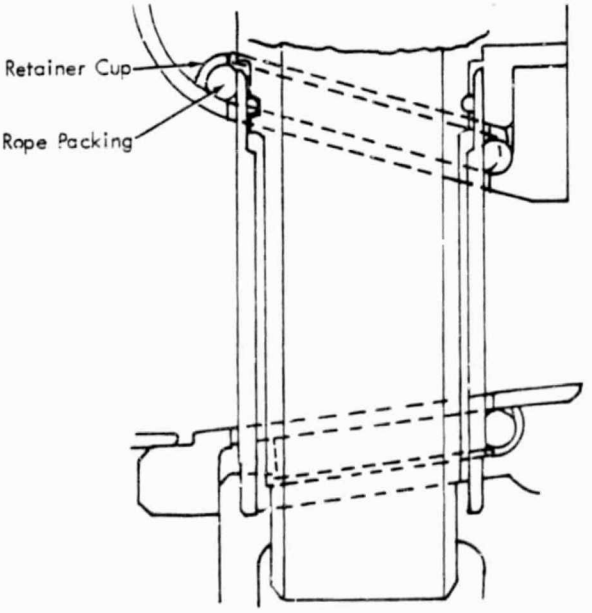

(b) Plenum/Inner Annulus Strut Leakage
Design Change

TE81-9118

Figure 61. Plenum/inner annulus/strut bypass leakage and design changes.

The flange fractures on the ceramic outer vane support ring were found to be the result of inadequate axial clearance between the metal shroud assembly and the outer metal support ring in the hot rig operating condition. The measured axial clearance was at the print minimum that would result in 0.015 mm (0.006 in.) clearance on a transient heat-up. This minimum clearance was probably consumed when the metal shroud assembly operated at the cooler temperature caused by the water-cooled structure on the thermal shock rig. The ceramic rings showed evidence of contact stress failure at the two flange failure origins. The two metal rings also had evidence of localized contact, with burnishing at the point of ceramic ring failure. Figure 62 illustrates how the outer metal shroud assembly (dimension "A") would be made smaller by cooler operation, resulting in a reduction in the minimum clearance of 0.015 mm (0.0006 in.) and a metal-to-ceramic interference. The metal shroud operating temperature has only to decrease by 20°C (68°F) for this interference to occur.

This situation was corrected as a result of the block crossarm cooling system redesign. Figure 63 shows how providing a cooling passage for the strut and containment ring cooling flow removed the axial interference. Axial positioning of the outer ceramic rings is now accomplished by the vane retaining ring

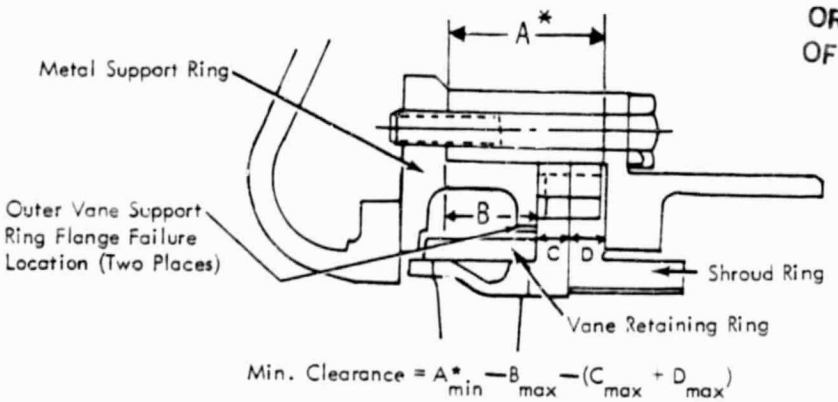

	Minimum Clearance		
	Print	Rig S/N 95 BU 1 Measured Dimensions	Rig S/N 2 BU 29 Measured Dimensions
Build	0.279 mm (0.011 in.)	0.279 mm (0.011 in.)	0.406 mm (0.016 in.)
Transient	0.015 mm (0.0006 in.)	0.015 mm (<0.0006 in.) Failure Condition	0.142 mm (0.0056 in.)
Operation	0.150 mm (0.0059 in.)	0.150 mm (<0.0059 in.)	0.277 mm (0.0109 in.)
Ring Fracture	—	Yes	No

*Dimension "A" on rig S/N 95 did not thermally grow as much as on engine or rig S/N 2 due to cooler part temperature.

TE81-9119

Figure 62. Outer vane support ring flange failure mode.

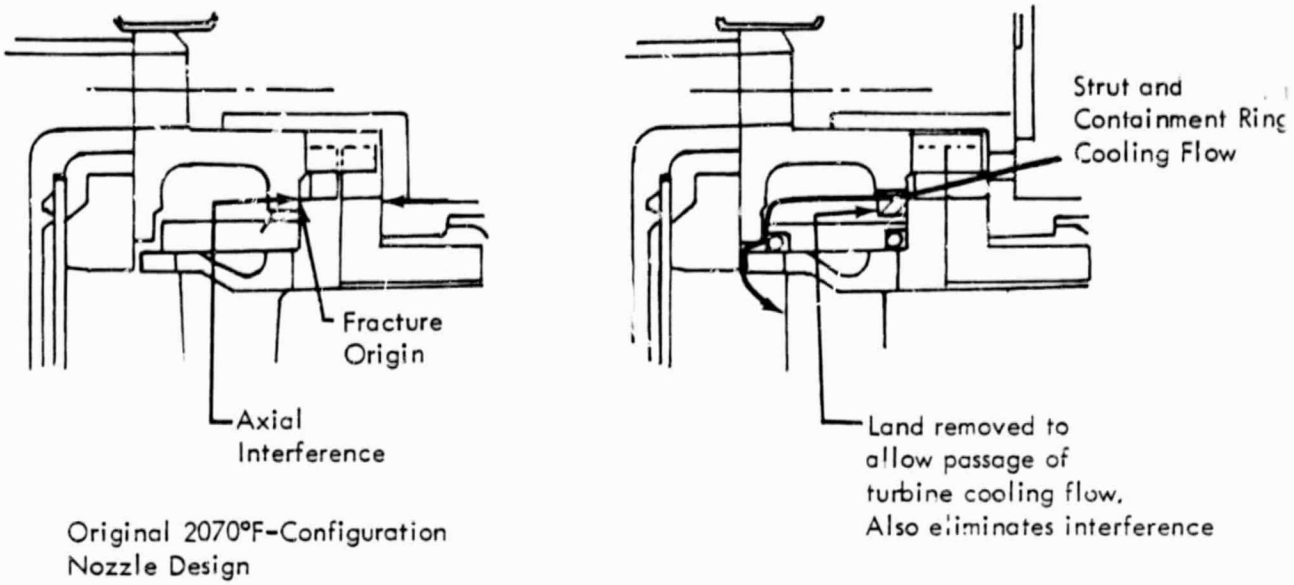

Figure 63. Design change to eliminate outer vane support ring flange failure.

bearing between the ceramic outer vane support ring and the rear axial inner lip of the outer metal support ring. There is an axial clearance gap as before, but the minimum gap has been revised to 0.30 mm (0.012 in.). This design change is currently under test evaluation in engine C-4 and will be incorporated into the thermal shock rig in the next build.

Investigation of the vane pocket failures in the outer vane support ring indicated that they were caused by thermal stresses occurring during rapid heat-up and cool-down of the gas path. Figure 64 presents the stress analysis results to support the failure analysis. Case I is the original 2070°F-configuration, which was rig tested. Analysis predicts a peak stress of 397 MPa (57.6 ksi) with P_s = 0.76317. The material strength represented in these calculations was MOR = 366.8 MPa (53.2 ksi), with M = 8.0. Two test bars cut from the failed ring had MOR = 249.9 MPa (36.1 ksi). This low material strength plus the fact that the pocket failures originated from predicted stress concentrations suggests that initial fracture occurred at either end of the vane pocket. Case II illustrates that even if a fracture were to relieve the load at a given vane pocket, there is still enough stress in adjacent pockets to lead to fracture. In summary, the outer vane support ring probably failed from both the front and rear of the vane pockets as a result of thermal stress and low material strength.

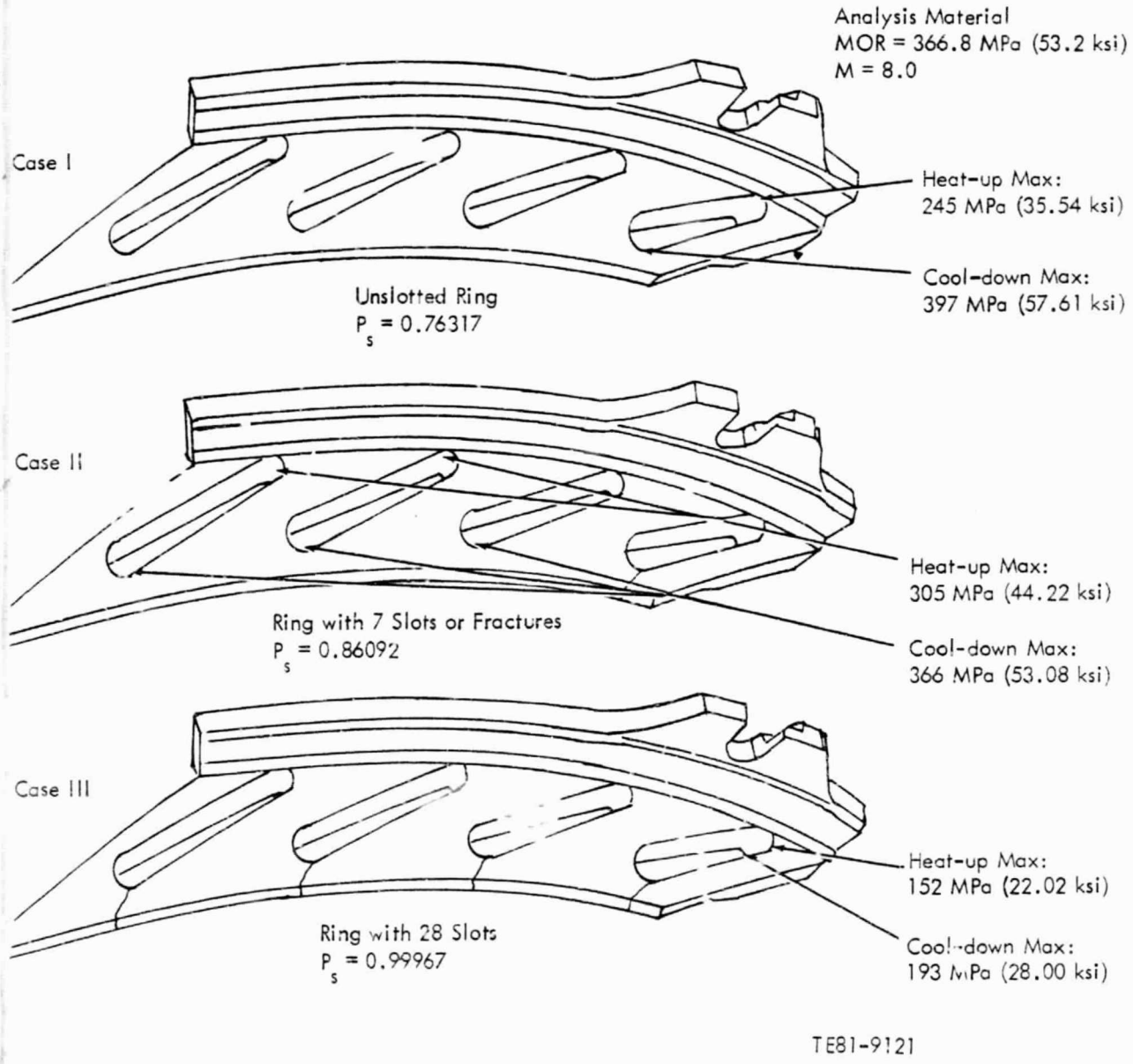

Figure 64. 2070°F-configuration ceramic nozzle outer support ring fracture analysis.

The design change made to reduce the stress in the vane pocket was to slot the front edge of all vane pockets (Case III, Figure 64). This design change reduced peak stress in the vane pockets to 193.1 MPa (28.0 ksi) and improved the P_s to 0.99967, with a material strength of MOR = 366.8 MPa (53.2 ksi), M = 8. An outer vane support ring has been modified with slots at each of the vane pockets. This ring will be evaluated on the thermal shock rig during the next reporting period.

o Turbine Tip Shroud

Two different failure modes on the ceramic turbine tip shroud were identified. The first was the alignment lug failure at the same location as the outer vane support ring alignment lug failure. The cause and corrective action for this are the same as for the outer vane support ring lug. The second was an axial split between alignment lugs. Examination of the fracture surface of the axial split showed it originated in the front edge of the abradable layer inside diameter. From this point, the fracture propagated both radially and axially, as shown in Figure 65. A review of stresses generated during a transient thermal cool-down (Figure 66) showed a stress of 41.4 MPa (6.00 ksi) in the abradable layer. MOR data, measured on test bars treated for abradability, indicated strength values ranging from 36.5 MPa (6.1 ksi) to 106.9 MPa (15.5 ksi).

Consideration was given to whether a fracture that started in the abradable layer would spread into the base material with a strength of 233.7 MPa (33.9 ksi) if the stress in the base material were only 33.2 MPa (5.1 ksi). If this were possible, then the axial split in the shroud ring occurred when the abradable layer fractured as a result of thermal stress and spread into and through the base shroud material.

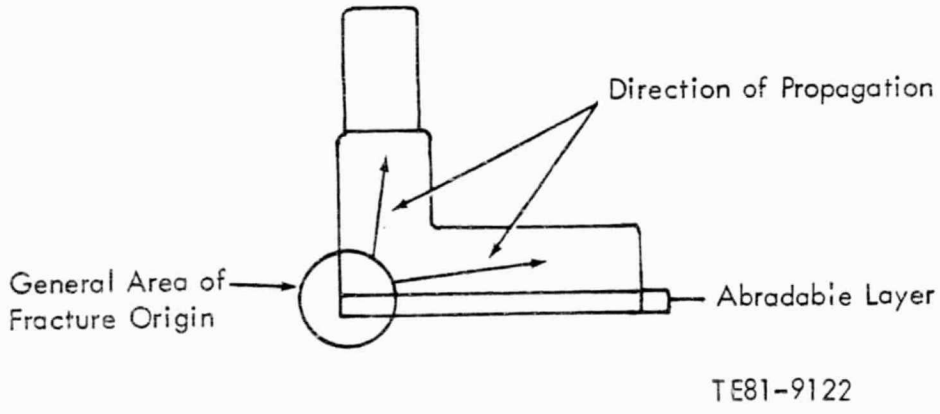

Figure 65. Axial fracture in 2070°F-configuration shroud ring.

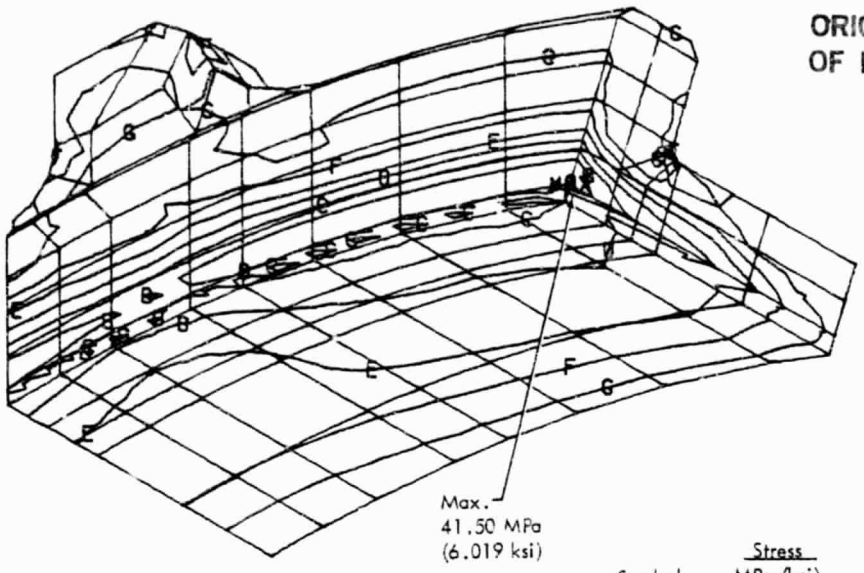

Material: Reaction-Sintered Silicon Carbide

Symbol	Stress MPa (ksi)
A	41.37 (6.00)
B	35.16 (5.10)
C	28.96 (4.20)
D	22.75 (3.30)
E	16.55 (2.40)
F	10.34 (1.50)
G	4.14 (0.60)
H	-2.07 (-0.30)

TE81-9123

Figure 66. 2070°F-configuration shroud maximum principal stress 22 sec into thermal transient (85° N_G to dynamic braking).

This points out a possible weakness in the abradable shroud system. Because of their porous nature, abradable materials tend to be weak. The thermal cool-down transients in the CATE design cycle generate tensile hoop stresses sufficient to cause a fracture in the abradable layer. For an abradable ceramic shroud to be successful, one of two conditions must exist. Either the thermal transient cool-down must be slowed to the point that the abradable material can withstand the thermal stresses or the base material must be able to arrest a fracture propagating through the abradable layer. If neither condition can be met, then the feasibility of a ceramic abradable tip shroud must be questioned.

The CATE development effort is presently looking at several alternate abradable materials and is reviewing the cool-down rates used in the design and thermal shock testing phases of the 2070°F-configuration.

o Inner Vane Support Ring

The inner vane support ring in the most recent thermal shock rig test broke in one axial fracture that originated at the trailing edge outside diameter. An inner ring in a prior rig test (BU 20) had broken in five locations, all originating in the inside diameter flange. Neither of these rig failures (Figure 67) can be attributed to a specific cause at this time. The fracture origins in each case correspond to areas of highest stress predicted by analysis. However, the predicted level of stress for these two locations was only 82.7 MPa (12 ksi) at the trailing edge o.d. and 114.0 MPa (16.5 ksi) at the i.d. flange. Both levels are considerably below the MOR test bar strength of 274 MPa (39.7 ksi) cut from the failed rings. A review of the analysis has found that the transient time increment selected for analysis may not have represented the point in time when the minimum probability of survival occurred. Additional analysis is under way to investigate the probability of survival at alternate points in time. This analysis will not improve survivability, but will more accurately predict survival rate.

To change the survival rate of the inner vane support ring, it is necessary to change either the part geometry, the heat transfer boundary conditions around the part, or the transient temperature schedule to which the part is subjected. An effort is being made to investigate each of these areas. Several part geometry changes are being considered that would make the inner ring more

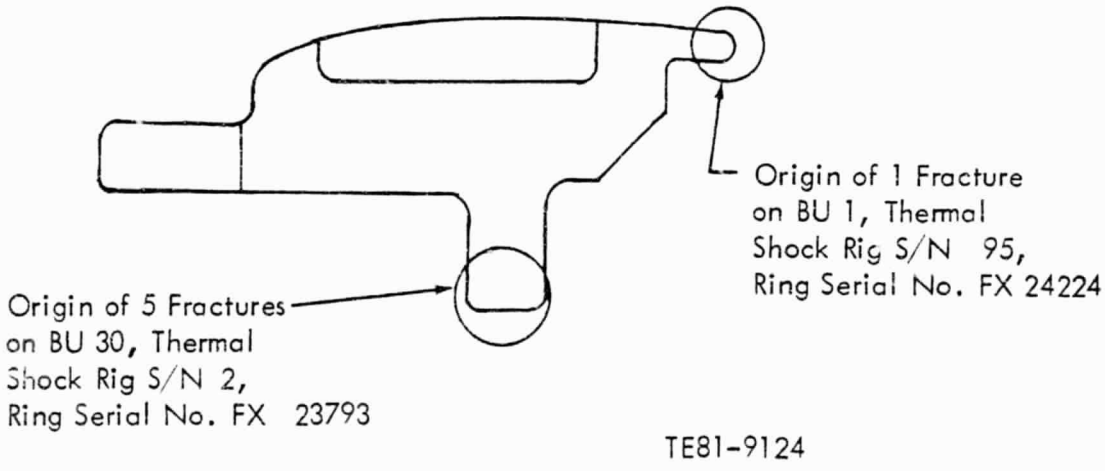

Figure 67. Fracture locations on failed inner vane support ring.

tolerant of thermal gradients. In addition, environment boundary conditions are being reviewed and reevaluated. Finally, engine C-1 will be run on the motoring dynamometer to verify the transient temperature response rates used in the CATE design and on the thermal shock rig.

Engine Test Evaluation--2070°F-Configuration Nozzle

As documented in the previous progress report, a set of 2070°F-configuration nozzle components was qualified on the thermal shock rig, the cold flow rig, and the vibration rig for engine test evaluation at 1083°C (1900°F). During the current reporting period testing was started on engine C-4, followed by durability evaluation, for a total of 616 hr of operation with no failure of ceramic components. The four builds comprising this initial engine testing were limited to 1038°C (1900°F) due to lack of a proof-tested ceramic turbine inlet plenum and ceramic-bladed rotor. This engine test temperature limit and dynamometer test stand operation are compatible with the ceramic component proof test to 1038°C (1900°F) with rapid heat-up only. Most of the testing was done with the redesigned block crossarm cooling system described earlier in this section.

The initial engine build and test of the 2070°F-configuration nozzle were run with enough gasifier turbine tip clearance to prevent a rotor-to-shroud rub--0.97 mm (0.038 in.) cold radial clearance. To improve engine starting ability, on the second build the turbine tip clearance was reduced to 0.71 mm (0.028 in.) cold radial clearance. Previous engine test experience had indicated that with this clearance the rotor would probably interfere with the shroud on transient operation. The rotor should have 0.18 mm (0.007 in.) hot steady-state radial clearance. Materials laboratory tests at room temperature had indicated that the ceramic tip shroud was abradable. Engine starting capability at this reduced radial clearance was unsuccessful, resulting in high turbine inlet temperatures on start and at idle. Subsequent inspection and engine teardown showed a heavy turbine rub with heavy metal transfer from the rotor to the shroud (Figure 68).

Teardown Zyglo inspection revealed that the ceramic components and metal support structure had absorbed the rotor shroud rub forces with no detectable damage. The shroud was not abradable as tested in the hot engine environment.

On the next build of the 2070°F-configuration nozzle, the rotor tip clearances were increased back to the initial build number of 0.97 mm (0.038 in.) radial cold clearance. The engine in this configuration is operating satisfactorily, accumulating test time at the end of this reporting period.

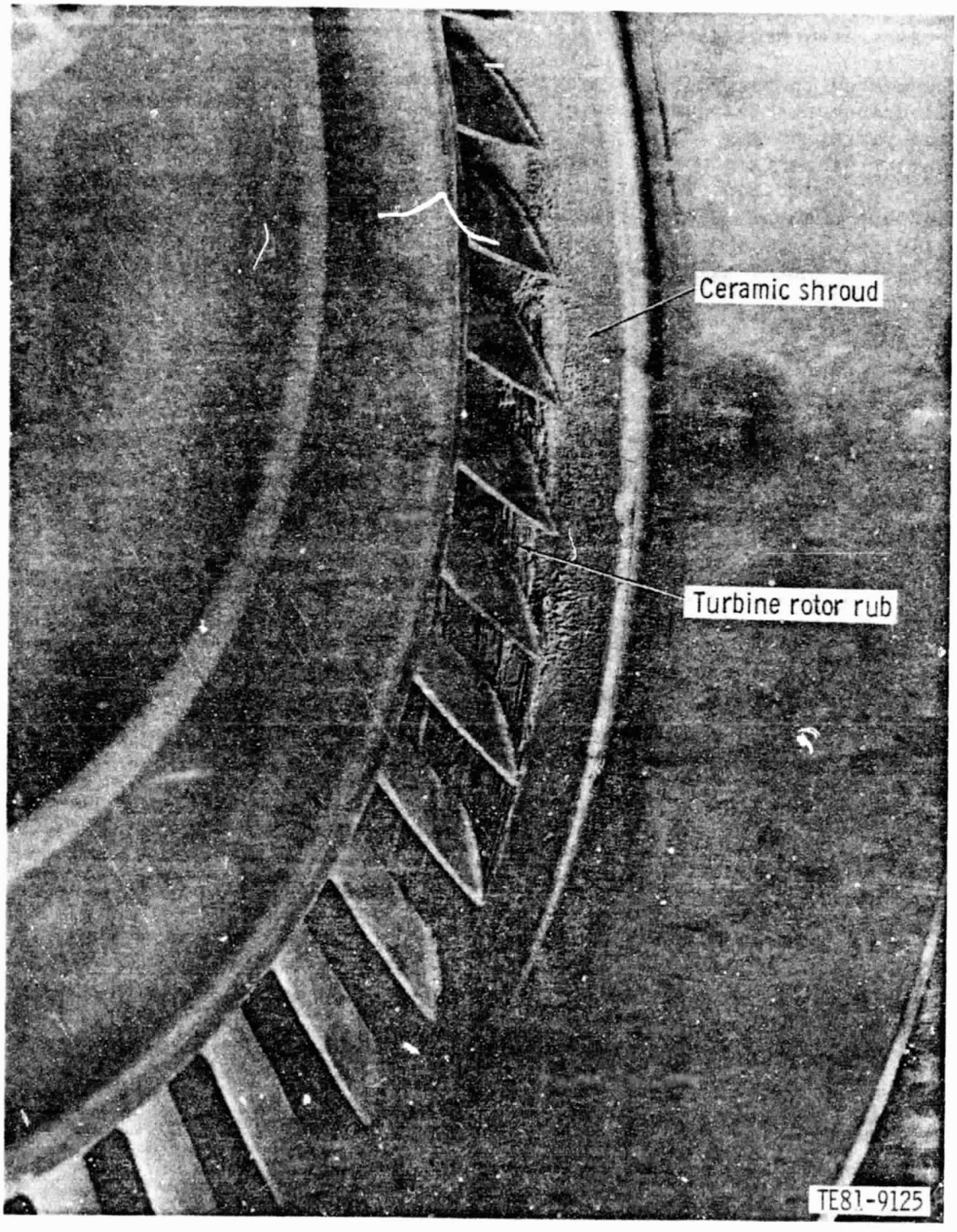

Figure 68. Ceramic turbine shroud after rotor rub (engine C-4, BU 6).

2965°F-Configuration Gasifier Turbine Nozzle Design and Analysis

Summary

The preliminary 2265°F-configuration gasifier turbine nozzle design will use the 2070°F-configuration nozzle design as a baseline. The ceramic materials thermal capabilities have been reviewed, and the gasifier vane material has been upgraded from reaction-bonded silicon carbide to alpha silicon carbide. A ceramic component probability of survival analysis for the vane and outer vane support ring was completed and reported in the last progress report. During the current reporting period, the analysis effort was completed on the inner vane support ring. It was decided that analysis of the 2265°F-configuration shroud was not required.

Objective

The objective of the preliminary design analysis of the 2265°F-configuration gasifier turbine nozzle is to calculate the probability of survival of the inner vane support ring when it is exposed to 1241°C (2265°F) transient thermal conditions. The calculated probability of survival will be compared to the development goal of $P_s = 0.9$ to determine if any component design change or material strength improvement is required.

The philosophy of the design of the 2265°F-configuration gasifier turbine nozzle is to begin with the 2070°-configuration design as a base. The 2265°F-configuration cycle temperatures will expose the nozzle assembly to a more severe thermal environment than was analyzed in the 2070°F-configuration component analysis. To compute the Weibull probability of survival for the ceramic components at 1241°F (2265°F) gas conditions, a transient heat transfer analysis was done to determine when the maximum ΔT exists in the ring. The temperatures at this time were used to determine the thermal stresses and the resultant probability of failure. This analysis used the finite element models developed in the 2070°F-configuration analysis.

Discussion

The Ref. 1 progress report defined the cycle gas temperatures and transient temperature schedules used on the inner ring analysis. Steady-state heat transfer analysis predicted a maximum ceramic inner vane ring temperature of 944°C (1731°F). This is within the 1300°C (2372°F) temperature capability of the reaction-bonded silicon carbide material used for this ring.

A transient heat transfer analysis was completed and temperatures at 24 sec into the transient heat-up and 6 sec into the transient cool-down were selected as the points in time when maximum ΔT occurs in the ring (Figures 69 and 70). These temperatures and aerodynamic loads were used to calculate the stresses for both transient conditions.

Reaction-bonded silicon carbide material strength properties of MOR = 366.80 MPa (53.2 ksi) and M = 8.0 were used in combination with the calculated stresses to predict the Weibull probability of survival. For the cool-down transient, the maximum principal stress is 141.1 MPa (20.5 ksi), with a P_s =

	°F	°C
A	1330.0	721.11
B	1280.0	693.33
C	1230.0	665.56
D	1180.0	637.78
E	1130.0	610.00
F	1080.0	582.22
G	1030.0	554.44
Max	1333.2	722.88
*Min	1003.2	539.56

*Denotes hidden

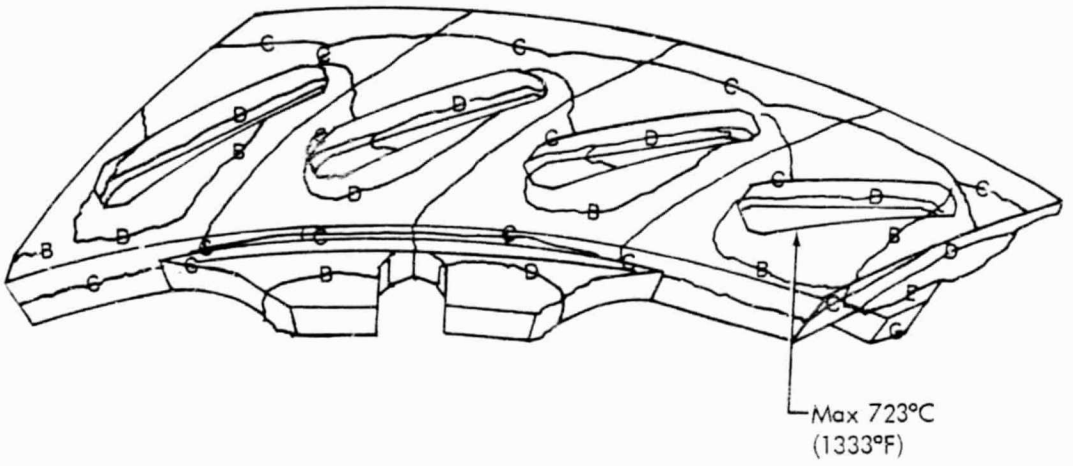

Material: Reaction-Sintered Silicon Carbide

TE81-9126

Figure 69. 2265°F-configuration inner vane support ring temperature distribution 24 sec into heat-up thermal transient.

0.99642. The heat-up transient maximum principal stress is 165.8 MPa (24.0 ksi), with a P_s = 0.98753 (Figure 71). Both of these probability of survival rates are below the design goal of P_s = 0.999757, but are above the development goal of 0.9. The inner vane support ring is thus satisfactory for use in the 2265°F-configuration CATE engine, assuming the part meets the strength requirements.

Table VII summarizes results for the outer and inner vane support rings at the 2070°F-configuration and 2265°F-configuration analysis conditions. Comparison of the two sets of results reveals the stresses and probability of survival do decrease, but because of the low number of rings to be tested in the CATE program (15-30 of each part), the number of expected failures will not be affected by the decrease in probability of survival.

	°F	°C
A	1500.0	815.56
B	1460.0	793.33
C	1420.0	771.11
D	1380.0	748.89
E	1340.0	726.67
F	1300.0	704.44
G	1260.0	662.22
*Max	1509.3	820.73
Min	1258.3	681.29

*Denotes hidden

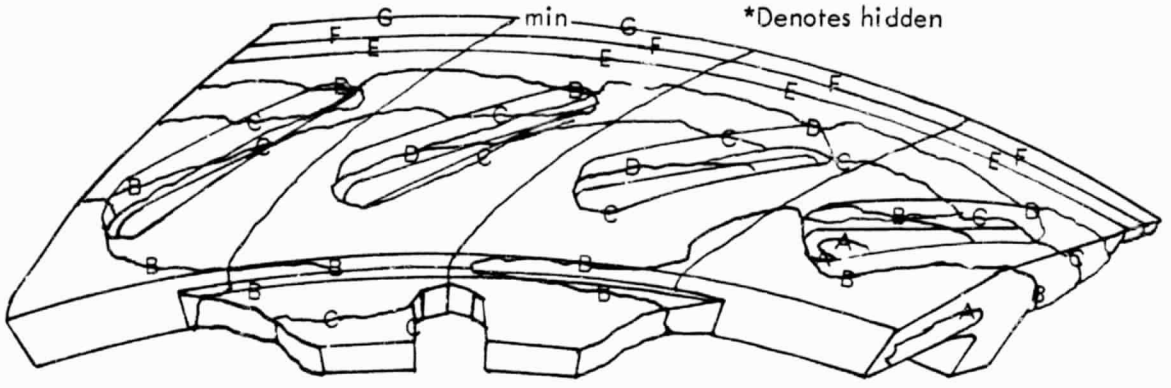

Material: Reaction-Sintered Silicon Carbide

TE81-9127

Figure 70. 2265°F-configuration inner vane support ring temperature distribution 6 sec into cool-down thermal transient.

TABLE VII. PROBABILITY OF SURVIVAL DURING THERMAL TRANSIENT FOR 2070°F- and 2265°F-CONFIGURATION CERAMIC COMPONENTS

	Analysis conditions	
	1132°C (2070°F)	1240°C (2265°F)
Outer ring		
Heat-up	P_s = 0.99994 at 20 sec 152 MPa (22.0 ksi)	P_s = 0.99795 at 14 sec 201 MPa (29.1 ksi)
Cool-down	P_s = 0.99967 at 30 sec 193 MPa (28.0 ksi)	P_s = 0.98764 at 24 sec 285 MPa (41.3 ksi)
Inner ring		
Heat-up	P_s = 0.998901 at 8 sec 114.4 MPa(16.60 ksi)	P_s = 0.987535 at 24 sec 165.7 (24.04 ksi)
Cool-down	P_s = 0.999767 at 8 sec 109 MPa (15.8 ksi)	P_s = 0.996424 at 6 sec 141.1 MPa (20.47 ksi)
Shroud ring		
Heat-up	P_s = 0.999999 at 10 sec 77.70 MPa (11.27 ksi)	Not available
Cool-down	P_s = 0.999999 at 22 sec 56.5 MPa (8.20 ksi)	Not available

	ksi	MPa
D	22 0	151.63
E	16.0	110.32
F	10.0	68.95
G	4.0	27.58
H	-2.0	-13.79
Max		
*Min	-5.3	-36.70

*Denotes hidden

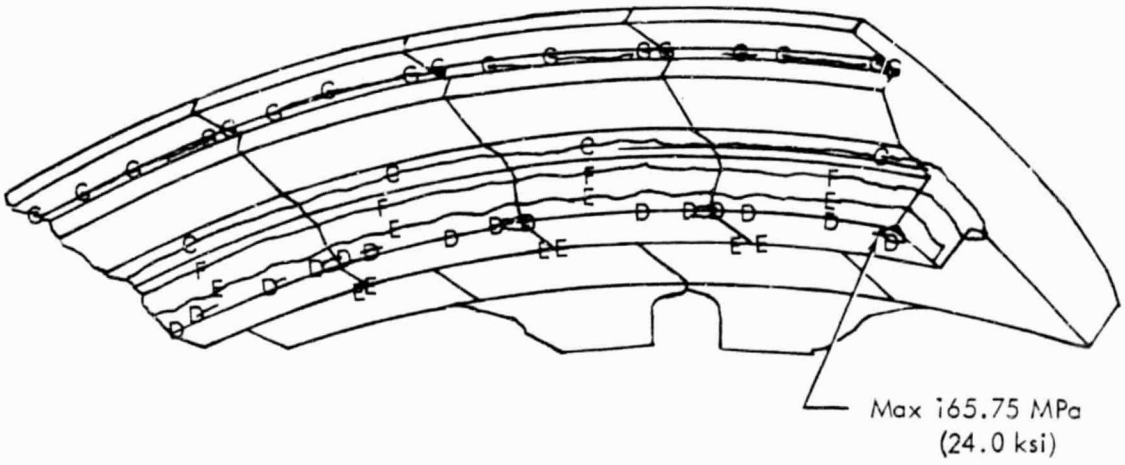

Material: Reaction-Sintered Silicon Carbide

TE81-9128

Figure 71. 2265°F-configuration inner vane support ring maximum principal stress distribution 24 sec into heat-up thermal transient.

GASIFIER TURBINE BLADE

Summary

The effort to design and develop a satisfactory ceramic turbine blade for the 2070°F-configuration engine has continued in this period with progress made in several areas.

- Extensive spin testing of individual blades and the first assembly spin test were accomplished in this period. Blades individually proof tested to 110% speed were used in the assembly, but failure of one blade occurred at 93% speed. Analysis of this failure revealed that blade stress and reliability are significantly affected by nonuniformity in blade attachment load distribution. Variations in compliant layer thickness have been discovered and may have contributed to the failure. Further, reliability of the stalk region of the blade is below predicted levels and material surface strength may be lower than anticipated in the stalk area.
- Initial blade vibration characteristics have been established by bench evaluations. Results are essentially as predicted except for observed multiple responses in the first two modes, which is considered unusual.
- Following completion of ceramic blade process optimization at Carborundum, the first significant quantity of injection-molded, sintered silicon carbide blades was produced. Because of several abnormal circumstances, the yield of acceptable parts was low, but 90 acceptable machined blades were received for testing at DDA.
- By using the simplified finite element model of the 2070°F-configuration blade, an alternate configuration proof test has been studied. An evaluation of a possible proof test with the blade mounted in a skewed position was completed. Certain of the blades were expected to be improved during proof testing; however, analyses could not substantiate this concept.
- The effort to develop an injection-molded, sintered silicon nitride blade of the 2070°F-configuration at GTE Labs, Inc., has continued, and progress has been made. Blade tooling is available, and a wax binder system has been selected for development. Parameters for compounding, molding, and sintering have been established, and a few sintered blades have been provided. A problem has been encountered in binder removal that results in internal blade cracks. Current efforts are directed toward correcting this problem.

Design and Analysis

Summary

By using the previously established coarse-mesh, finite element model, analysis of an alternate spin-test configuration has been completed. The blade mounted in a skewed position was modeled and the effectiveness of spin testing evaluated. The skewed position mounting was intended to offset airfoil tilt and increase loading of concave airfoil surfaces during proof testing, and to improve subsequent blade reliability. Analysis of results indicates the skewed proof position will not significantly improve blade reliability and further rotation in mounting does not seem practical.

Objective

The objective of this analytical effort was to determine the effectiveness of a proposed revision in spin-test blade mounting. A skewed blade mounting during spin was proposed that would increase concave airfoil surface loading in compensation for airfoil tilt, which results in low concave surface loads during spin test.

Discussion

Analysis of an alternate spin test mounting of the 2070°F-configuration blade design has been completed. The current configuration features a tilted airfoil, which minimizes stress during engine operation but does not provide an significant load or "proofing" of airfoil concave surfaces during spin test. It may be possible to improve the effectiveness of spin-proof testing by mounting the entire blade in a skewed retaining slot.

A skewed position was proposed that would increase loading on the airfoil concave surfaces during spin test and provide a proof of these surface elements. The engine disk slots would not be skewed from the normal position.

Two configurations involving this concept have been analyzed by means of the new coarse-mesh, finite element model (FEM). Analysis with the blade mounted in a normal slot orientation was accomplished with the original fine-mesh FEM. The three spin-test slot conditions are as follows:

1. Broach rotation 0, no change from the engine blade mounting configuration;
2. Broach rotation 1, a slot rotation of 9.4° toward the concave airfoil surface, as shown in Figure 72;
3. Broach rotation 2, the 9.4° slot rotation plus a 4.7° tilt of the slot that provides a radial stack of the airfoil tip and hub section centers of gravity.

The effect of spin test on blade reliability in the 3-sec acceleration condition has been established for each slot position (Table VIII). It appears that the alternate slot positions evaluated will not improve airfoil reliability by spin proof testing up to 43,250 rpm (117%), and testing above that speed will result in more than 10% loss in proof test. Further rotation or tilting of the slot does not seem practical because locally high stresses could result from abnormal contact points in the attachment.

Further study is warranted, but analysis of skewed mounting slots is being discontinued at the present time. Currently, the approach to improving overall blade reliability centers on design of a new airfoil with reduced hub setting angle and improved attachment stress distribution. If airfoil stress distribution cannot be improved in transient conditions, improved material strength will be a more significant factor in providing blade reliability.

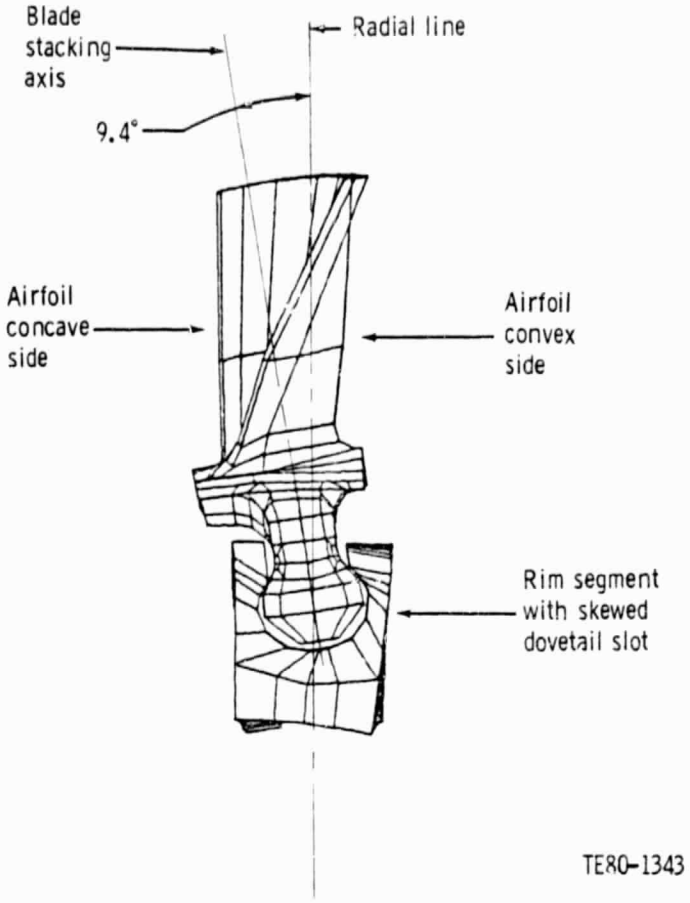

Figure 72. Slot rotation one.

TABLE VIII. PROBABILITY OF SURVIVAL AT 3-SEC ACCELERATION CONDITION AFTER ROOM-TEMPERATURE PROOF TEST OF 2070°F-CONFIGURATION TURBINE BLADE

FEM	Broach rotation	Proof rpm	Probability of survival after proof		
			Dovetail	Airfoil	Totai
Fine mesh	0	0	0.98310	0.99920	0.98231
	0	36,905	0.99718	0.99954	0.99672
	0	40,000	0.99976	0.99971	0.99947
	0	43,250	0.99998	0.99972	0.99977
Coarse mesh	1	0	0.984343	0.99949	0.99423
	1	36,905	0.98824	0.99949	0.98774
	1	40,000	0.99543	0.99953	0.99495
	1	43,250	0.99958	0.99960	0.99918
	2	36,905	0.99203	0.99981	0.99184
	2	40,000	0.99799	0.99985	0.99784
	2	43,250	0.99960	0.99989	0.99950

Spin Testing

Summary

Spin testing of sintered silicon carbide blades comprised a significant portion of the blade development effort during this 6-month period. The first group of finished 2070°F-configuration blades became available and testing of these blades included the following accomplishments:

- o An assembly procedure was established for the 40-blade rotor, including steps for retainer plate rivet installation.
- o 52 blades were individually spin proof tested to 110% speed and 42 blades survived this testing.
- o A 40-blade rotor assembly was built and subjected to a spin-proof test intended to reach 105% rpm. A blade failure occurred at 93% rpm. Failure occurred in the blade stalk and originated in the surface (nonmachined), but no flaw was found.
- o Repeat proof testing at 110% resulted in additional failures: 15% of the previously proof-tested blades failed, indicating possible variability in proof-test condition or loading.
- o A variation in L605 compliant layer thickness was discovered.
- o To improve reliability of the rotor assembly, the individual proof-test speed was increased to 117%, with L605 compliant layers selected for thickness uniformity. The failure rate at 117% rpm was 26% for blades not previously proof tested.
- o A repeat proof test at 117% rpm using IN-600 compliant layers (available with uniform thickness) produced no failures. This may indicate a significant reduction in test load variation.
- o The second rotor assembly configuration has been established and will use IN-600 compliant layers and blades twice proof tested to 117% rpm.

Objective

The objective of the spin test program, in addition to providing evaluation of the design, is to provide a reliable rotor assembly for the first hot engine simulator test. Planned testing in the simulator includes operation to 100% speed and 1038°C (1900°F) with very slow temperature acceleration rates.

Discussion

Spin testing in this period centered on evaluations of the 2070°F-configuration sintered silicon carbide blades. The blades represent the result of initial process optimization at the Carborundum Company. All blades were machined at the Crafts Company. The attachment is machined with an axial machining lay that reduces apparent MOR strength in this area. The maximum principal stress vector on the surface of the dovetail is perpendicular (radial direction) to the machining. This effect corresponds with lower MOR strengths observed on transverse ground bars compared with the strength of longitudinally ground MOR bars. In the case of transverse ground bars, the maximum principal stress vector on the surface is perpendicular to the machining as the bar is tested in bending. It has been shown that a thermal treatment consisting of 24 hr at 1250°C (2282°F) will improve transverse ground bar strength essentially to that of longitudinally ground bars. A similar effect is anticipated in the blade attachment; therefore, the finished blades were heat treated or "oxidized" prior to spin testing.

During this period, 52 blades were proof tested to 110% (40,600 rpm) in a single-slot disk. L605 compliant layers and boron nitride spray lubricant were used. Ten failures resulted, leaving 42 proof-tested blades for the first rotor assembly (40 blades required). All failures occurred on the convex or suction side of the airfoil and in one of two locations. Six failures originated on the machined surface of the dovetail and four on the as-fired surface on the side of the stalk. Two blades failed after reaching the proof-test speed of 40,600 rpm. One failed after 20 sec at speed and the second failed after 40 sec at speed during the planned 1-min hold period. This probably reflects minor speed variation during the hold period, and not a time-oriented function.

The predicted spin-test failure rate of less than 8% at 40,600 rpm is better than the 19.6% failure rate actually obtained. The prediction using the finite element model was based on pressed and sintered bar data with 343 MPa (49.7 ksi) strength and Weibull M = 7.9. Moreover, the stalk failure rate to attachment failure rate of four to six is higher than the predicted ratio of one to ten.

Many of the blades revealed large (500 μm) crystals in the fracture surfaces, which were not anticipated on the basis of testing of initial parts available on completion of the process development program. Since this condition does not exist on all blades, some variation in process (i.e., sintering temperature) is indicated. Carborundum's experience indicates that the large grains may not affect material strength adversely.

Rotor Assembly

To ensure proper cover plate rivet installations, trial installations in a "dummy" rotor were made. The trials used a partial set of prototype ceramic blades, matching cover plates, and a full scale rotor disk. Two head shapes (flat and rounded) have been made with variations in rivet length and the amount of upset. A set of parameters has been selected, and additional trials were completed to establish repeatability. This is a press-type operation that does not induce impact loads during assembly. A Plexiglas enclosure is used that protects blades from handling damage but has rivet access and allows complete visibility of the rotor.

With rivet procedures established and proof-tested blades available, the first rotor build was initiated. Blades and compliant layers mounted in the disk prior to installation of blade retaining plates are shown in Figure 73. These plates are retained with rivets installed through the holes shown. This partial assembly with blades wedged outward was made to permit measurement of blade tip radii and platform seal radii. Some variations in specified radii at the seal and tip were shown to exist on the blades, apparently as the result of errors in fixturing that produce blades of correct tip radius at the stacking axis only. The blade tip is short near the trailing edge, but long near the leading edge. Runout with a typical blade is 0.13 mm (0.005 in.) at the tip and 0.19 mm (0.0075 in.) at the platform lip seal. This condition was felt to be acceptable for initial spin testing and hot simulator testing.

C-2

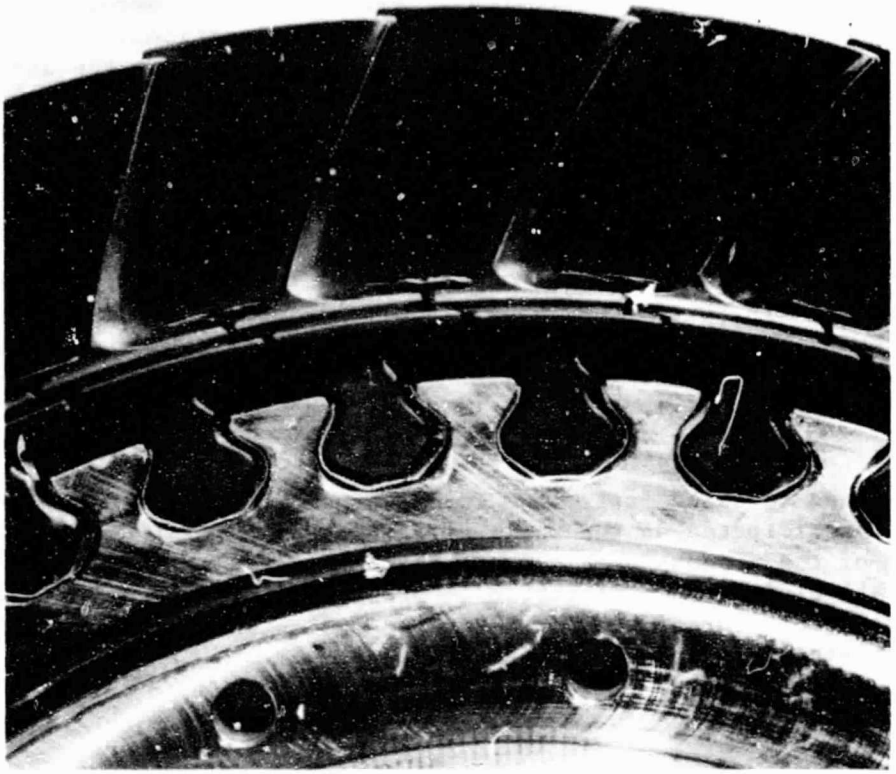

TE81-9129

Figure 73. Ceramic-blade rotor prior to coverplate installation.

Assembly was completed without difficulty. All parts fit as anticipated and rivets were successfully installed. Rivet heads required machining to obtain desired thickness, but no other problems were encountered. The completed rotor assembly ready for balance and spin test is shown in Figure 74.

Assembly Spin Test

The completed rotor assembly was balanced and subjected to ambient temperature spin testing in the evacuated spin pit. The test was intended to reach 105% speed and hold for 1 min. Rotor condition was visually unchanged after scheduled shutdown and inspection at 80% and 90% speed. Failure occurred at 93.2% speed in an attempt to reach 95% speed.

A single blade failed and only minor damage was incurred by the other 39 blades. The failed blade, lower portion, is shown in Figure 75 as installed in the rotor and after removal from the disk. The fracture originated in the stalk region above the attachment. The origin was on the surface and a flaw cannot be found with microexamination. This location corresponds to the zone of maximum calculated stress in the blade stalk and had been an initiation

TE81-9130

Figure 74. Ceramic-blade rotor--completed assembly.

site of failures in blade-proof testing at 110% speed. However, the previous lowest speed stalk failure (four occurrences) was 108% speed. Although some failures are anticipated as one approaches the previously completed 110% proof-test speed, failure at 93% speed, which only produces 72% of the stress at 110% speed, was not anticipated (centrifugal stress scales on the square of the speed).

Assembly Failure Investigation

An extensive failure investigation was initiated immediately after the assembly test and has broadened as information becomes available. This situation is particularly interesting since the failed part had been previously spin tested to 110% speed and then failed at 93% speed and a flaw is not apparent at the surface failure origin.

While some areas of investigation are incomplete, considerable knowledge has been gained and the more significant results are presented below.

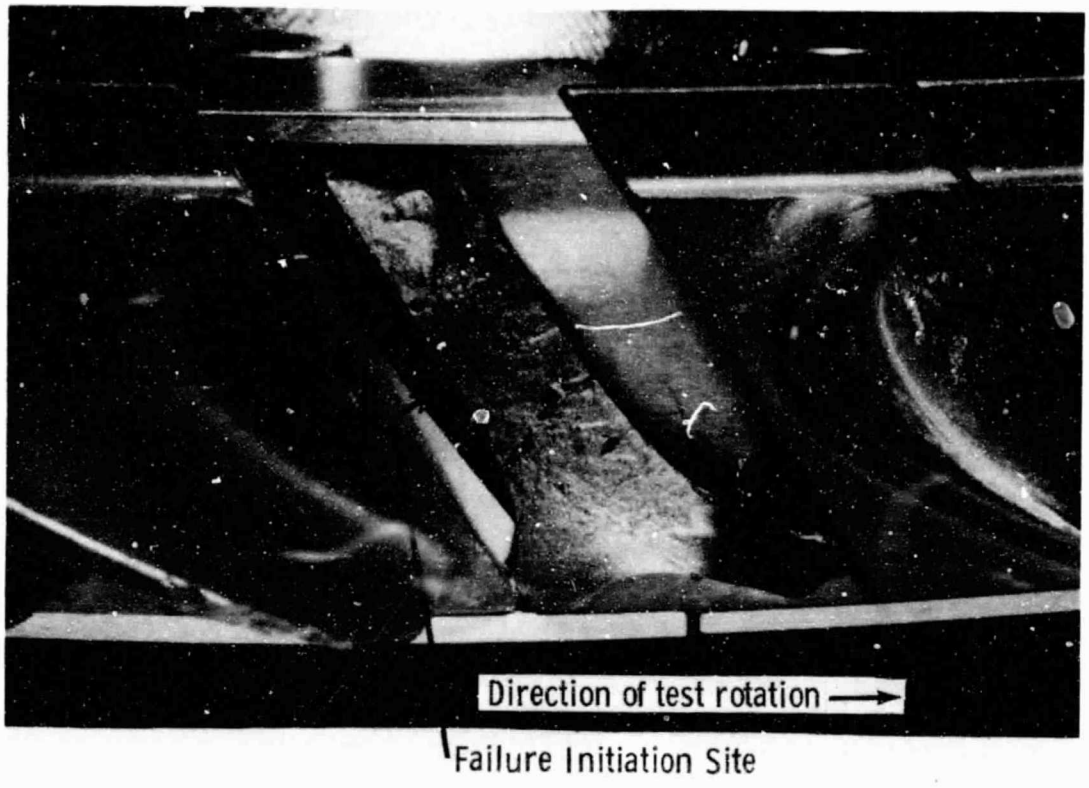

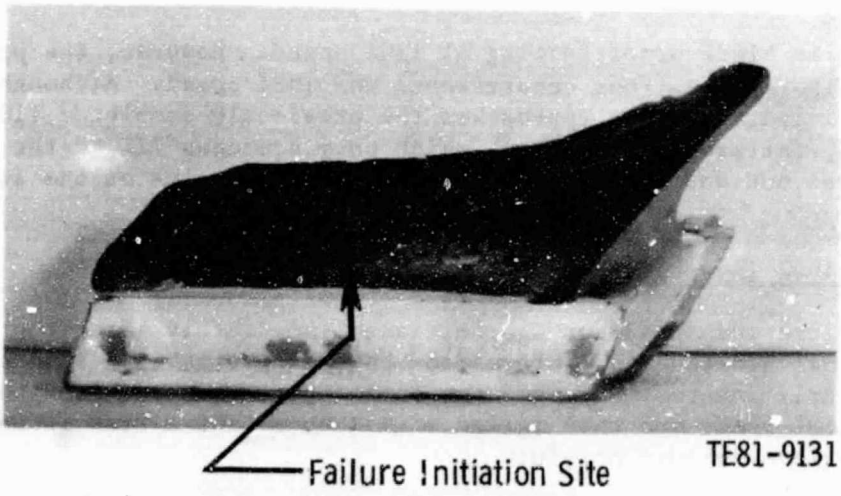

Figure 75. Ceramic blade failure, rotor assembly spin test.

Blade Quality Standard

The quality acceptance standards used prior to the assembly were reviewed along with records of defects found in the test blades. There were no recorded defects in S/N FX 24927, which failed in assembly at 93%; therefore, the acceptance criteria were not a factor in this failure.

Further review and correlation with proof-test failures revealed that detectable flaws at the injection molding gate have resulted in failures. These flaws are in a region of low stress, and several flawed blades have passed 117% rpm proof tests. However, some blades with prerecorded gate flaws failed in attempted proof testing. Except for these molding laps or voids, no other accepted flaw indications (visual, Zyglo, X-ray) are known to have resulted in blade failure.

Test Procedure

A review of test conditions and procedures indicates very little variation in test-to-test conditions. Rotational speed is controlled to within 0.07% (at 36,905 rpm). Blade rotational direction was not previously the same in individual and assembly proof testing. Rotational direction should not affect blade loading in the evaculated pit, but the procedure has been changed so that blade direction and spin direction are the same in all spin testing.

Part Shape Pertubations That Affect Blade Loading

Part shape uniformity is considered critical in the areas of blade attachment, compliant layer, and wheel slot contact surfaces. The most significant variation in part shape has been found in L605 compliant layers--thickness variations up to 0.038 mm (0.0015 in.) have been revealed. IN-600 layers were uniform in thickness to within 0.005 mm (0.0002 in.). All spin proof testing to date has been with L605 compliant layers. Variations in disk slot surface condition were found to be within 0.008 mm (0.0003 in.), including the slot involved with blade failure at 93% rpm. This meets the drawing requirements and is acceptable.

Load Variations

Load variations had a minor effect on computed blade stress, as did reliability FEM analysis of a 2° tilt in blade mounting. Attachment stress increased 2.5% and blade failure probability (P_f) increased from 1.4% to 1.7% in cold spin at 100% rpm. Analysis of nonuniform loading along the attachment contact surfaces was simulated in the finite element model (FEM), and a significant response was noted. Stress levels more than doubled in the attachment stalk and airfoil in some loading conditions, and P_f rose from 1.4% to almost 50% at 100% rpm. The coarse-mesh FEM used in these analyses is not completely adequate for the unusual loading conditions, but results indicate a trend toward high stress and low reliability if attachment loading is not uniform. New L605 compliant layers with improved thickness control are being fabricated.

Effects of Friction on Blade Stress

Testing is planned to measure the coefficient of friction at the blade attachment contact surfaces. Equipment required for this test will soon be available. In the interim, analysis has been completed using an assumed coefficient of 0.38 and probability of failure increased from 1.4% to 2.9%, which is significant but minor compared to results indicated by nonuniform loading.

Residual Stress

Residual stress measurements have been completed on three blades. The method used involves attachment of strain gages to the blade stalk region, then cutting the blade to remove structural support from the instrumented surface. Results indicate a wide variation within and between parts. Data indicating residual stresses ranging from -416 MPa (-60.3 ksi) to +58 MPa (+8.4 ksi) have been observed. The results are certainly significant, and considerably more data are required to assess the impact on part reliability.

Another method of measurement is needed to acquire data nondestructively. X-ray diffraction is being considered.

Possible Damage From Handling or Riveting

Care in handling has been observed by all concerned. Instrumented testing indicates immeasurably low blade stress response to riveting operations performed during rotor assembly. Handling or riveting impact damage during assembly is not considered a factor in the assembly failure.

Accuracy of the Analysis

A review of the FEM indicates a sufficiently fine mesh for accuracy in predicting maximum stress levels at the various failure sites observed to date. An instrumented blade spin test is planned. Strain gages located at the peak stress sites in the attachment and stalk will provide data to confirm or refute computed values.

Blade Material Strength versus Bar Strength

Blade reliability predictions are based on a MOR bar strength of 343 MPA (49.7 ksi), with one standard deviation = 51.2 MPA (7.43 ksi). Testing of 52 longitudinally ground bars molded and processed with the blades indicates MOR = 361 MPa (52.4 ksi) and s = 51.5 MPa (7.47 ksi). It appears from these data that the material strength is essentially as used in design analysis. Further, overspeed to failure testing produced an average failure speed that is essentially as predicted by analysis, again indicating strength as anticipated.

However, there are proportionately more failures in the stalk region of the blade than had been predicted. There are nearly as many stalk failures as attachment failures in proof testing, but analysis predicts only one stalk failure per ten attachment failures. These data indicate that the stalk surface material strength may be lower than assumed in the analysis. The stalk failures originate at the surface, which is as fired (nonmachined). Some data are available that indicate stalk material strength:

Companion bars molded with blades

1. As-fired surface (5 bars): Avg MOR = 361.5 MPa (52.43 ksi)
2. As-fired surface (10 bars): Avg MOR = 286.6 MPa (41.56 ksi)
3. As-fired and oxidized surface (10 bars): Avg MOR = 379.2 MPa (55.00 ksi)

Subsized bars cut from blade

1. Machined all over (11 bars): Avg MOR = 458.5 MPa (66.51 ksi)
   Corrected to standard test: Avg MOR = 315.1 MPa (45.7 ksi)
2. As-fired test surface (2 bars): Avg MOR = 404.1 MPa (58.6 ksi)
   Corrected to standard test: Avg MOR = 277.2 MPa (40.2 ksi)

Unfortunately, it is not possible to cut a test bar from the blade stalk with an as-fired surface, as there is not enough flat surface in the stalk. The as-fired surface bars tested were cut from the dovetail area in unmachined blades. In comparing blade material strength with associated test bar data, a 20% reduction in strength appears to be associated with the bar cut from the blade dovetail.

Effect of Surface Glassy Layer on Blade Strength

A glassy layer formed on the blade as-fired surfaces during the post-machining oxidation treatment of 1250°C (2282°F) for 24 hr in air. This layer formed to a significantly lesser amount on machined surfaces. It has been removed from the stalk area of all blades by polishing with diamond paste. Initial proof-test data indicate improved performance (reduced failure rate) with the polished stalk, but a failure rate similar to the attachment failure rate has resulted in continued testing.

In addition to the above areas of investigation, spin proof testing of 2070°F-configuration blades has continued. The following tests have been completed using L605 compliant layers and boron nitride lubricant:

1. Oxidized blades, initial proof test to 110% speed: 52 tested, 42 passed (19% failed), 10 failed between 100.8% and 110% speed.
   Failure origins: 6 attachment, 4 stalk.
2. Oxidized blades, second proof test to 110% speed: 40 tested, 34 passed (15% failed), 6 failed between 104.9% and 108.9% speed.
   Failure origins: 1 attachment, 3 stalk, 2 airfoil.
3. Oxidized blades with stalk surface polished to remove glassy layer, initial proof test to 110% speed: 8 tested, 7 passed (12% failed), 1 failed at 109.5% in attachment.
4. As-fired and machined blades (nonoxidized), initial proof test to 110% speed: 8 tested, 5 passed (32% failed), 3 failed between 86.4% and 96% speed (all failures in the stalk).

Because of the apparent improved performance of the oxidized blades with polished stalks (item 4 above) and the poor performance of nonoxidized blades, the oxidized and polished condition was selected for further evaluation. Also, a higher proof-test speed seemed necessary to provide increased reliability at 100% speed; therefore, 117% proof testing was initiated. The use of L605 compliant layers continued, but they were selected with maximum thickness variation = 0.015 mm (0.0006 in.). Results are as follows:

5. Oxidized and polished stalk blades, initial proof test to 117% speed, selected L605 compliant layers: 62 blades tested, 49 passed (21% failed), 13 failed between 106.3% and 117% speed.
Failure origins: 6 attachment, 6 stalk, 1 airfoil.

Twenty-three of the item 5 blades had not been previously proof tested and may be compared to predicted performance. Twenty-six percent of the 23 "virgin" blades failed, compared to a predicted 22% failure rate, indicating improved correlation with analysis and overall improved performance. This improvement was felt to be the result of stalk polishing and more uniformly thick compliant layers. A repeat 117%-speed proof test was desired using selected-thickness L605 compliant layers, but enough parts were not available and IN 600 layers with 0.0002 in maximum thickness variation were used.

6. Oxidized and polished stalk blades, second proof test to 117% speed, uniform-thickness IN-600 compliant layers: 49 blades tested, 49 blades passed.

Analysis of Spin Test Data

For ease in discussion a summary of spin test data is presented in Table IX. By using these data, the failure rates for some of the tests have been determined and are presented in Figure 76 for comparison with the computed failure rate speed. The following observations are made:

- o Six oxidized blades spun overspeed to failure have an average failure speed about equal to prediction.
- o Fifty-two oxidized blades spun to 110% speed have a P_f of nearly 20%, compared to the 8% predicted rate.
- o These two data points suggest that blade material mean strength is as anticipated, but Weibull modulus is lower than expected.
- o The second 110% proof test of oxidized blades resulted in an additional 15% blade loss that cannot be explained by blade strength variability.
- o The 23 oxidized and polished blades with selected-thickness compliant layers seem to have improved reliability at 117% proof speed. The achieved failure rate of 26% is still above the predicted 22%, but below the 32% implied by the straight line between the oxidized-only data points.

The failure of blades in a second 110% proof test can be explained by assuming variability in test conditions.

The concept of stochastic proof testing offers a possible explanation for blade failures occurring in a repeat proof condition or even at a less stressed subsequent proof. In ordinary proof testing, items are subjected to a proof test in which a fixed level of stress is applied to each item. Those that fail are discarded and the remaining sample of unfailed items are assumed able to survive additional exposures to the proof stress without failing. It is assumed throughout that proof testing does not degrade the sample of survivors.

In the case of ceramic turbine blades, it has been observed that if the surviving population is again proof tested at the same level as before, additional failures are observed:

TABLE IX. 2070°F-CONFIGURATION SiC BLADE SPIN TESTING

Pretest condition	Test	No. tested	No. passed	Percent failed	Failure site
	Initial 110% proof	52	42	19	6 attachment (101-110%) 4 stalk (108-110%)
	Rotor ass'y 105% proof	40	39	3	1 stalk (93%)
Oxidized	Second 110% proof	40	34	15	1 attachment (105%) 3 stalk (106-109%) 2 airfoil (105,107%)
	Overspeed to failure	6	0	100	5 attachment (117,122,128,129,135%) 1 stalk (116%)
Untreated	Initial 110% proof	8	5	38	3 stalk (86-96%)
	Overspeed to failure	4	0	100	3 attachment (110,122, 124%) 1 stalk (134%)
	Initial 110% proof	8	7	13	1 attachment (110%)
	Second 110% proof	7	7	0	None
Oxidized and polished	*Initial 117% proof Previous 110%, 110%	34	27	21	3 attachment (107-116%) 3 stalk (110-117%) 1 airfoil (109%)
	*Initial 117% proof Previous 110% untreated	5	5	0	None
	*Initial 117% proof	23	17	26	3 attachment (97-112%) 3 stalk (110-112%)
	Initial 117% proof totals	62	49	21	
	Second 117%	49	49	0	None

* Selected-thickness L605 compliant layers.
Uniform-thickness IN-600 compliant layers.

Original sample (before proof testing), 52 blades,
Failed first proof test, 19%,
Failed second proof test, 15%.

These results obviously do not reflect a simple proof test.

A plausible model to explain this phenomenon is that the "proof test stress level" is not constant from test to test, but is itself a random variable defined by an unknown distribution. The cumulative probability of failure of the parent population of blades is described well by a Weibull distribution in terms of rotational speed based on blade material strength data. Inasmuch as many factors could influence the value of proof-test level, it is assumed that this random variable is normally distributed about the nominal proof-test speed.

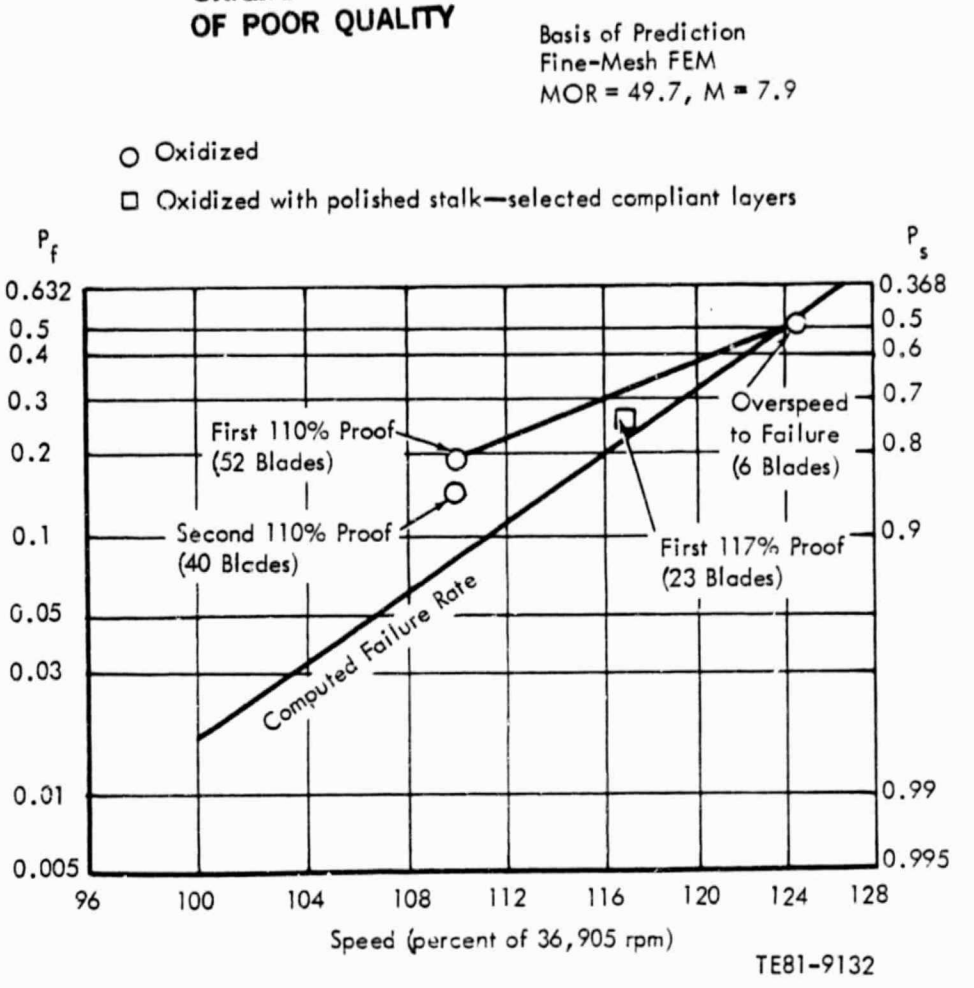

Figure 76. Reliability of 2070°F-configuration blades.

A computer program has been developed utilizing a random sampling scheme (Monte Carlo simulation) to combine groups of variables that are statistical (distributive) in nature into a resulting function. In this application, the predicted failure rate based on Weibull factors and an assumed proof-test speed variation are combined to predict the statistical nature of proof spin tests. By using this program, the following analysis has been completed:

- To match the first 110% proof results in which 19% failed, a coefficient of variation = 11.3% speed is required.
- By using the 11.3% speed coefficient of variation, a failure rate of 17.1% is predicted at 93% speed for a rotor assembly comprised of 40 blades that had previously been proofed at 110% speed.
- By using the 11.3% speed coefficient of variation, a failure rate of 14.4% is predicted in a second 110% proof test. This compares to the 15% encountered in the actual test.
- To match the first 117% proof-test results in which 26% failed, a coefficient of variation = 4.2% is required.
- By using a 4.2% speed coefficent of variation, an 11% failure rate is predicted for a second 117% proof.

- o Since no failures occurred in the second 117% proof test, the coefficient of variation is zero. This result also implies insignificant variation in the first 117% proof.
- o Test results imply a very low failure rate in subsequent testing below 117%.

It is now planned to build a second rotor assembly using 40 of the blades twice proof tested at 117% speed. New IN-600 compliant layers of uniform thickness and boron nitride lubricant will be used. Present plans include proof testing the assembly to 108% speed prior to hot engine simulator evaluations.

Blade Vibration Testing

Summary

The initial bench dynamic characterization of 2070°F-configuration blades was completed during this period. Blade frequencies in the fundamental mode were 11% lower than predicted and 5.5% higher than predicted in the first torsion mode. Coincidence of the fundamental mode and 28th engine order (vane passage frequency) is the only significant interference and will occur in engine mid-speed range as predicted. The nominal interference point will occur at 25,000 rpm, which is lower and preferred to the predicted 29,000 rpm location.

Discussion

Initial testing of ten blades to determine natural frequencies has been completed. The blades were scanned in this testing in which blades were mounted in a bench fixture. The fixture slot was formed using the engine disk broach. The compliant layer is as in the engine, and clamping is provided through a lower base loading ram. The following variables have been tested to date:

- o Various compliant layers, including L605, 347 stainless, IN-600, and platinum, have been tested.
- o Variations in base load from 1000 lb to 2600 lb (2280 lb corresponds to 100% rotor speed attachment load) have been tested.
- o Holographs at several response frequencies have been made.
- o Frequency distribution in ten blades have been recorded.

Test data were reviewed to obtain mean frequency and $\pm 3\sigma$ scatter. The frequencies agree reasonably well with the analysis, but the indicated scatter is larger than the ±5% assumed scatter, as shown below:

Mode	Calculated mean	Test mean	Percent Δ test vs. calc.	$\pm 3\sigma$ test scatter ~% mean
1	13,700	12,182	-11	± 14
2	22,750	23,994	+5.5	± 16

The data are also shown versus engine rpm in Figure 77. The frequency range shown is 3 standard deviations in measured data. Interference with mean fundamental mode and vane passage frequency is at 26,000 rpm. This is slightly lower than computed with a "fixed" blade attachment, which indicates a similar interference at 29,000 rpm in Figure 78. This reduced frequency probably indicates reduced fixity in the test case (which is felt to simulate the engine loading and structural damping). Study of the data continues and additional testing is planned, but the nominal result is essentially as anticipated.

Study of data obtained also indicates that blade frequency in the first two modes is only slightly affected by changes in base load over the range evaluated. Further, changes in compliant layer material or repeated loading and unloading of the base ram to improve compliant layer seating had minor effects on frequencies.

An unexpected result of this testing was the multiple frequencies observed in the first and second modes, i.e., a single blade responds at more than one frequency in the fundamental mode and in the second mode. This phenomenon is being studied further and more testing is planned.

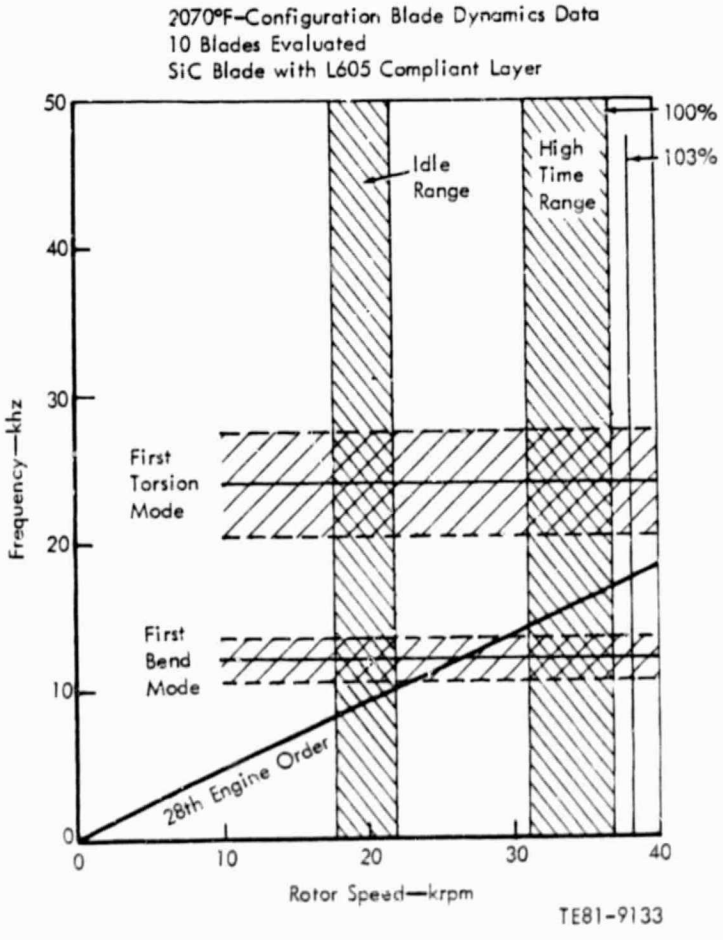

Figure 77. Measured 2070°F-configuration ceramic blade dynamic characteristics.

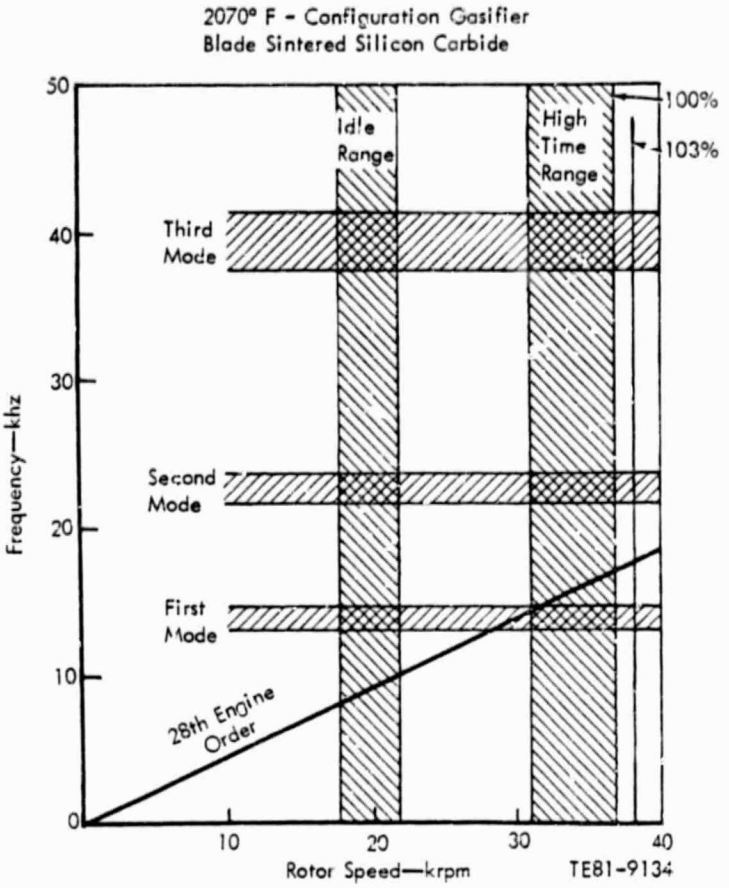

Figure 78. Predicted 2070°F-configuration ceramic blade dynamic characteristics.

Carborundum Process Development

Summary

Initial optimization of a process applicable to an injection-molded, sintered alpha silicon carbide turbine blade was previously completed. Parameters established in that program have been used to provide the first 2070°F-configuration blades for evaluation testing. At completion of process development, Carborundum injection molded 1250 blades, anticipating an adequate yield to satisfy DDA's initial requirements, which included 90 finished blades and 140 unmachined blades.

Because of several abnormal circumstances, Carborundum's yield of acceptable parts was decreased below that expected, and while 90 finished blades were delivered, only 46 unmachined blades were found acceptable. An additional 600 blades are being injection molded and will be delivered to DDA early in 1981.

Discussion

Carborundum has completed its first "production" run of molded α-SiC blades and some study of the quality yield has also been completed. To satisfy a requirement for 230 nonmachined blades, Carborundum injection molded 1250 blades and continued these in groups through the various processing steps.

The resulting yield of acceptable quality parts has been established for various process steps as follows:

- o Carborundum process yield, 230 blades desired (90 to be machined by CBO, 140 to be machined by DDA)
- o 1250 blades were injection molded, NDE yield = 1155 (96%)
- o 1150 blades were subjected to binder bake-out, NDE yield = 1040 (90%)
- o 367 (35%) baked parts cracked while awaiting sinter furnace repair
- o 647 blades were sintered, NDE yield = 431 (64%)
- o 431 blades were shipped to DDA, NDE and dimensional evaluation yield = 143 (33.2%)
- o Overall yield = 143 of 1250, 11.4% (unmachined)
- o 90 of 97 blades have been machined by Crafts Company
- o 46 blades will be machined by DDA.

The overall yield was only 11.4%, but several abnormal or correctable circumstances affected the results and the true process yield is predicted to be about 35%. The effect of three conditions on yield has been evaluated, with results as follows:

- o The first 550 molded blades were affected adversely by the gate geometry. Gate stem removal created a depression and a fissure in the dovetail end face. The addition of a fillet radius at the gate stem greatly reduced this problem in the remaining 700 blades.
- o A large quantity of blades were held for over 6 weeks after binder bake-out because of failure of the sintering furnace, and 367 blades held in this fragile stage cracked or simply fell appart. Further, those blades that were subsequently sintered and found to be of suitable NDE quality were found to be generally of unacceptable dimensions.
- o A group of about 250 blades was sintered with alternate furnace fixturing, which reduced surface carbon formation, but did not seem to affect quality or shape.

A follow-on group of blades has been started through the process. A total of 645 blades have been injection molded and processed through binder bake-out. After completion of the remaining process steps, the yield of this group will be supplied unmachined to DDA.

GTE Process Development

Summary

A 1-year development program with GTE Sylvania Laboratories began in February 1980 and has continued through the current reporting period. The program will establish processing parameters for a sintered silicon nitride (SNW 1000) turbine blade of the 2070°F-configuration. The program will yield 30 blades (20 unmachined and 10 finished) plus 100 MOR bars.

Significant progress has been made in process development. Blade tooling is available and a wax binder system has been selected for further development. Parameters for compounding, molding, and sintering have been established. Problems have been encountered in binder removal, and internal cracks in blades have resulted. Current emphasis is placed on correcting this problem. A few blades have been made, and dimensional evaluation is encouraging.

Objective

The objective in GTE's program is to establish process parameters suitable for an injection-molded, sintered silicon nitride (SNW 1000) blade in the 2070°F-configuration. This includes development of a suitable binder, injection-molding parameters, binder removal, sintering, and inspection. The current program will demonstrate the total process, culminating in the delivery of sample blades and MOR test bars. Manufacturing sizable quantities of blades for engine test will be accomplished in a follow-on program.

Discussion

Molding

Process development continued at GTE Laboratories, Inc., during this reporting period. The injection mold tooling with blade cavity and two MOR bar cavities was available to GTE in July 1980. Initial injection molding trials were completed using a wax binder system with 63% by volume ceramic. Generally, the ability to fill blade and bar cavities (including flash) was excellent. The problems encountered were as follows:

- o Negative draft in the tool at the stalk forward face resulted in blade fracture when the die was opened.
- o "Short shot" trials indicated a minor problem in filling the blade dovetail.
- o "Short shot" trials indicated poor fill conditions at both MOR bar cavities.

The tool was returned to the supplier to eliminate negative draft in the stalk, enlarge slightly the blade cavity gate, and revise the gating to the MOR bar cavities. The original gate location was at the bar end and directed at the bar side face.

Following tooling modification, injection-molding development has advanced considerably. The quality of molded parts as determined by radiography has been greatly improved by modifications in mixing and in loading mix into the injection molder. In a recent group of 40 shots, the rejection rate stood at about 10%.

Molding conditions for CATE blade fabrication have been finalized except for mold temperature. Final selection of an optimum mold temperature has been held off while a study is made of the cracking of parts in binder burnout.

Binder System Development

A wax-based binder system and process for compounding Si_3N_4 powder and binder into a material capable of producing 2070°F-configuration blades and MOR bars by injection molding are being developed. The selection of binder materials and the compounding of the binder system with Si_3N_4 powder will be described. A Battelle program for injection molding of ceramics, of which GTE is one of many sponsors, had the primary input on the selection of binder materials.

o Binder Selection

Two binder systems were chosen for evalutaion at the beginning of this program, one based on low-density polyethylene and the other on a mixture of waxes. Each has additives to lower melt viscosity and increase flow. All components were chosen to decompose completely and cleanly to facilitate removal from molded parts by a thermal process.

Both binder systems were evaluated with three goals in mind:

- o Ability to support solids loading levels of Si_3N_4 in a range that will produce sinterable parts.
- o Sufficient flow at these loadings to fill complex shapes with thin sections.
- o Complete, nondisruptive removal by a thermal process.

On the upper end of the scale of ceramics to binder loading level, both the polyethylene and wax-based binders have been compounded to a 66% by volume loading of Si_3N_4. At the lower end, test coupons with loadings as low as 60% had been carried through a molding and binder removal process and sintered to 98.8-99% of theoretical density. Therefore, a range of 60-66% was chosen for study. The flow characteristics of each binder system were studied using a spiral flow mold. The wax system exhibited greater flow and its flow was increased more readily by increasing injection temperature.

Molding trials of both binder systems were made using the blade and MOR bar mold. The wax binder has successfully filled the mold up to a solids loading level of 66% by volume ceramic. The polyethylene system has been tried only up to 62% loading of ceramic, but also filled the mold.

Complete and nondisruptive thermal removal of both binder systems has been carried out in test coupons of small cross sections. Residual carbon levels after binder removal of 0.03% can be readily obtained. Some binder removal tests of larger cross section, and faster removal cycles showed increased part disruption with the polyethylene.

As a result of these tests showing the superior flow and binder removal characteristics of the wax-based binder system, that system was selected for use in the fabrication of CATE turbine blades and MOR bars.

o Compounding

Processed ceramic powder is mixed with the heated binder in an instrumented torque rheometer that has two interchangeable mixing heads of 60- and 33-cc capacity. In this instrument, the mixing blades are driven by a dynamometer. This yields information on the torque resistance and thus on viscosity as a function of shear rate, temperature, and mixing time.

In mixing studies to date, it has become evident that compounding powder/binder mixtures in the desired working range of 60 to 66 v/o (% volume) is feasible. In one experiment Si_3N_4 powder was compounded to a uniform creamy mixture with a volume loading of 72 v/o. Several mixtures compounded in the 60 to 64 v/o range have been molded and the binder removed and sintered to acceptable densities.

The following were identified as critical parameters to be controlled during the compounding process:

Mix Homogeneity. Under microscopic examination a certain inhomogeneity can be observed in the form of small spherical areas of lighter material, especially visible in highly loaded material. These areas apparently are powder that did not completely wet with binder. Simple application of longer mix times, higher temperatures or rpm, or different blade types has not eliminated this effect. The effect has been traced to weakly bonded aggregates formed in a heating operation preceding compounding. These agglomerates were not completely broken up during compounding. By lowering the temperature of this heating cycle or by wet milling before compounding, these agglomerates were eliminated, resulting in a more homogeneous powder/binder mixture.

Entrapped Air. Entrapped air in the solidified, mixed material is a serious potential problem. The entrapped air is compressed into the molded part, later causing severe delamination and bloating during the first stage of binder removal when the part is heated above the binder flow temperature. Slow mixing of the material under vacuum removes this entrapped air. De-airing is presently being accomplished in a second mixing operation.

Entrapped Moisture. Entrapped moisture in the mixed and cooled material also causes problems in binder removal. Observations made during binder removal tests indicate reduced part disruption during the initial stages of binder removal if the powder is predried just prior to compounding.

o Binder Removal

A persistent problem of internal cracking has been observed in thermal binder removal. Radiographic analysis of molded parts indicates a uniform distribution of ceramic before burnout. After burnout, the surface of the part often shows no flaws detectable at a magnification of 10X. Radiography shows large internal cracks, generally in the dovetail, stalk, and platform zones, but sometimes extending up into the thinner blade. The effort at GTE currently centers on understanding and eliminating this program.

o Part Evaluation

GTE has successfully sintered blades and MOR bars. Two blades have been supplied to DDA for dimensional evaluation and correlation of NDE techniques. Correlation of defects found by the two companies was excellent, as determined by visual and radiographic evaluations. GTE does not have facilities for fluorescent penetrant inspection, but all parts are evaluated by this method at DDA. Dimensional evaluation of these two parts reveals that one meets drawing requirements of size and shape except for 0.5° excessive twist at the airfoil tip. The other part has excessive twist up to 1.3° at the airfoil tip.

GASIFIER TURBINE INLET PLENUM

During this report period a plenum and two inner annuli made of densified, reaction-sintered silicon carbide were received from the Norton Company in the "as cast" condition and finish machined at DDA. These parts are now ready for testing and awaiting the availability of the burner rig.

The inner annuli received from Norton, although deviating from the drawing in length and wall thickness, could be made usable by machining in some areas that were specified to remain "as cast" (Figure 79). The plenum was close

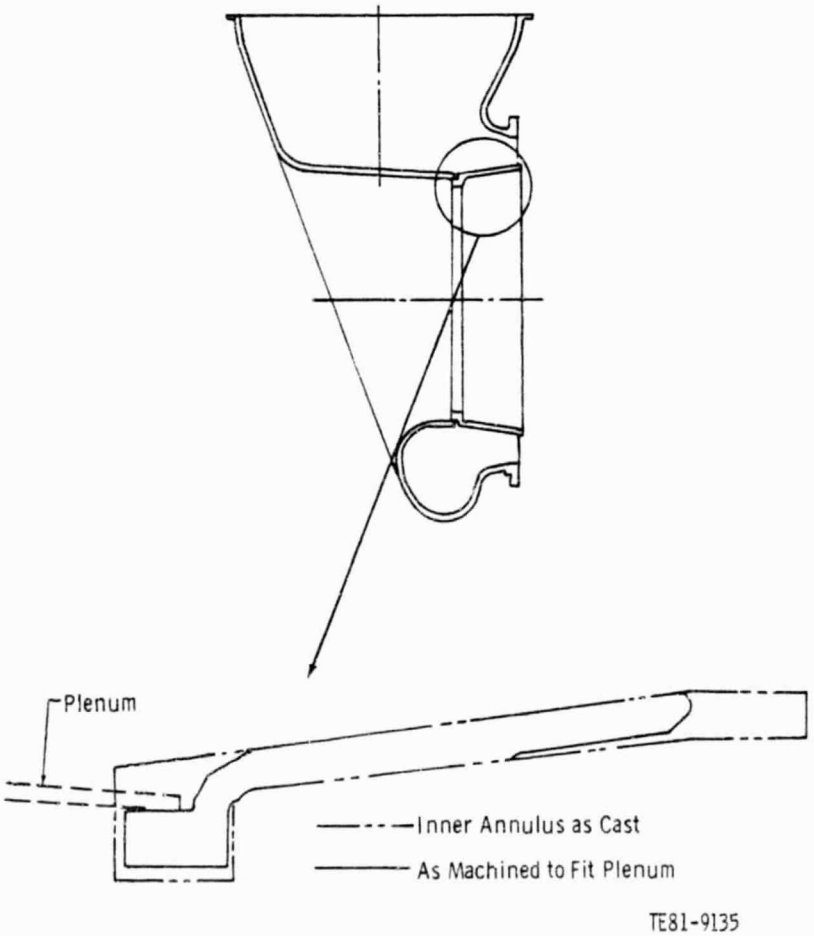

Figure 79. Location of plenum's deviation from drawing.

enough to print, with some additional machining not specified on the drawing, to be functional in all areas except the inner outlet region that pilots on the inner annulus. It was 2.8 mm (0.11 in.) under size at this pilot diameter and the wall thickness was 1.0 to 1.5 mm (0.039 to 0.059 in.) instead of 3.5 to 4.0 mm (0.138 to 0.157 in.). One of the inner annuli was machined to fit the undersize pilot of the plenum and the resulting step in the flow path was rounded off to minimize flow disturbance. Two more plenums and inner annuli have been cast and will be machined by Norton for delivery early in 1981. Conversations with Norton indicate that these plenums will deviate from print in the same region and to the same extent as the one machined at DDA.

Two plenums and inner annuli are on order from Carborundum Company and are scheduled for delivery early in 1981. These parts are to be slip cast of sintered alpha silicon carbide and machined at Carborundum. Carborundum encountered a problem in casting the mounting flange on the outlet of the plenum. It cannot easily be integrally cast with the plenum because it is thicker than the typical wall. Carborundum tried casting it separately, attaching it to the plenum in the green state, and sintering in place, but because of a difference in shrinkage of the two components, the flange ring or the plenum cracked during sintering. The present plan is to sinter each component separately, grind a pilot diameter on each, and bond after sintering.

2265°F-CONFIGURATION CERAMIC COMBUSTOR

Summary

This reporting period effort concentrated on completing the design for the initial ceramic combustion system. This design has been completed and all components (ceramic and metal) have been detailed. Heat transfer analysis of this design has been started, and preliminary results are very encouraging. Background effort has started to establish data input for calculating the probability of survival of the combustor's ceramic components.

Discussion

The design selected for initial procurement and development is shown in Figure 80. This prechamber-type combustor is similar to the 2070°F-configuration combustor. It differs from the latter in that cooling air supplied by Lamilloy wall material has been eliminated with the use of ceramic. Structurally, the combustor body is segmented to reduce stress around primary and dilution holes. This segmented assembly is supported by the prechamber assembly and four spring-loaded rods.

Figure 81 shows the air distribution for this initial design. The swirler design is identical to that in the 2070°F-configuration. The eight-hole primary and dilution configuration was selected on the basis of jet penetration, blockage, and compatibility with mechanical features. This air distribution should be compatible with satisfactory combustion performance and structural integrity.

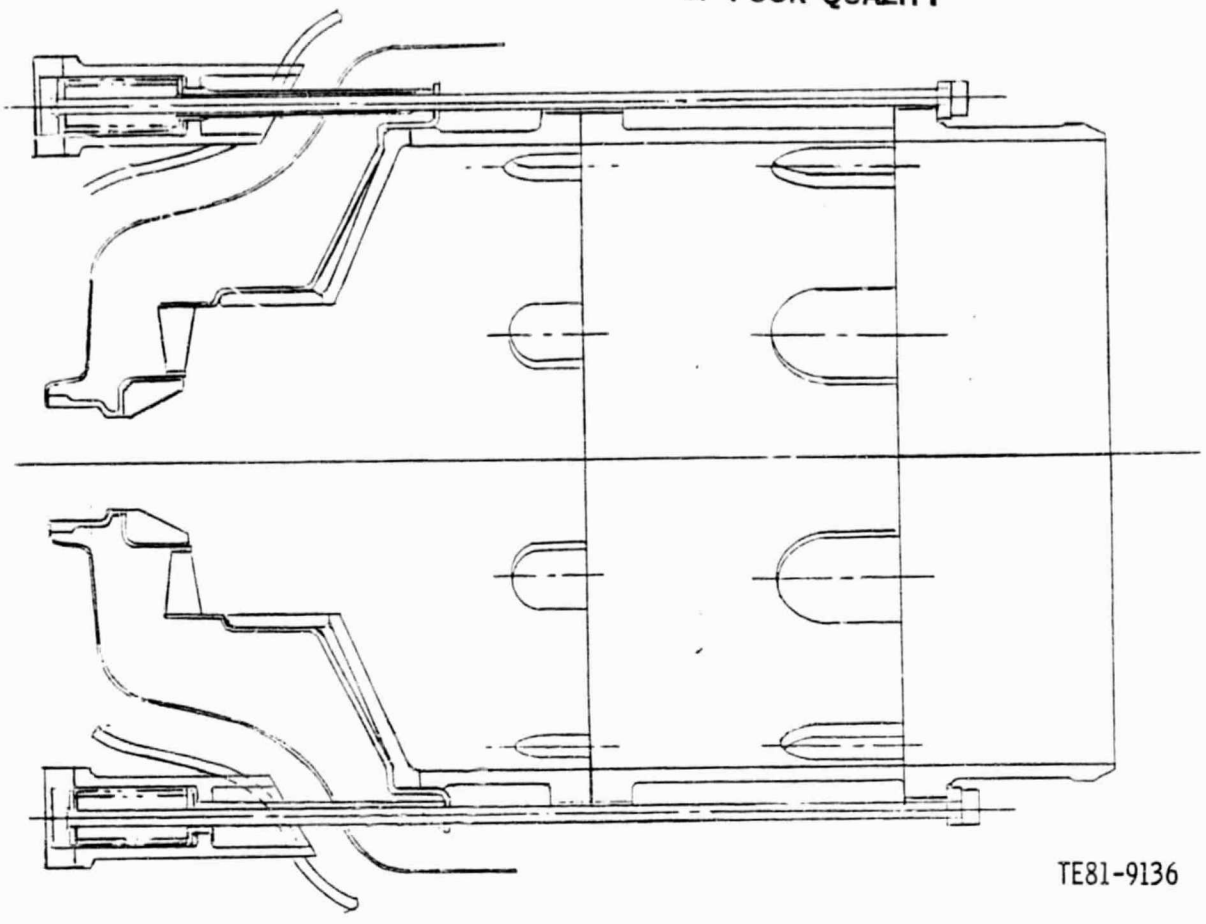

Figure 80. Ceramic combustor.

To calculate the probability of survival for the ceramic components, the input data (fuel/air ratio and combustion zone temperatures) were determined. Figure 82 shows the calculated values of flame temperatures. These values are being used by heat transfer personnel to determine wall temperatures. Probability of survival will be determined by finite element analysis.

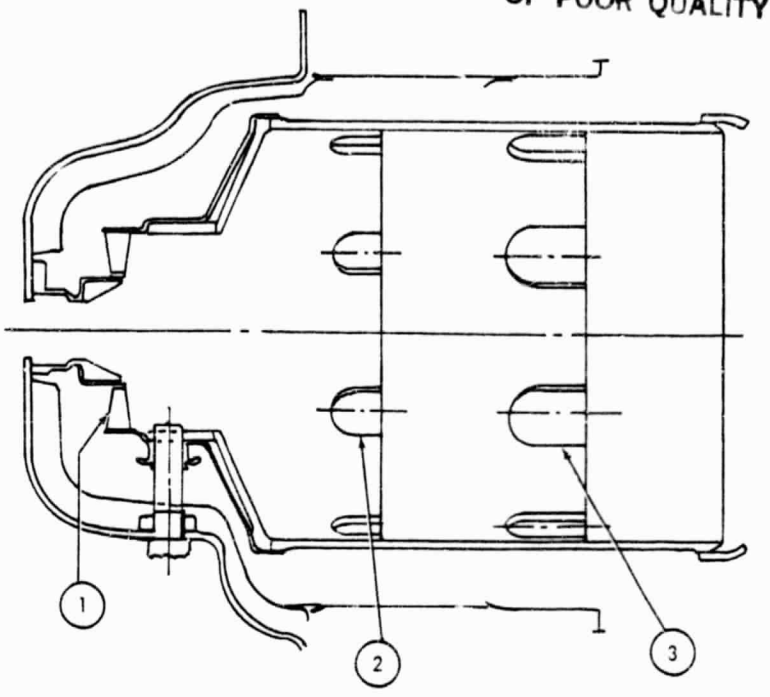

Station	Description	C_D	$A_H C_D$ ~ in.^{2}	Percent
1	Swirler	0.71	1.46	11.9
2	8 Primary slots	0.65	3.19	26.0
3	8 Dilution slots	0.65	7.63	62.1
Total			12.28	

Primary = 24.9%.

TE81-9137

Figure 81. Hole area summary--2265°F-configuration CATE combustor.

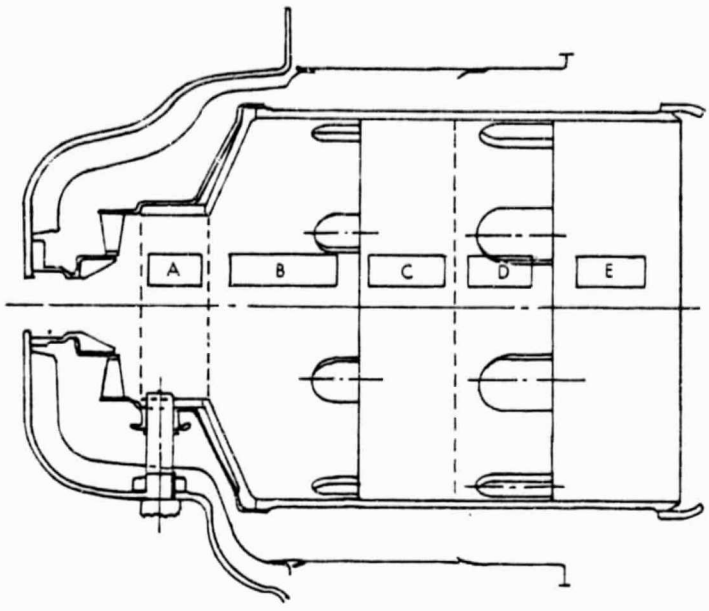

Estimated Average Flame Temperature

N_1—%	A	B	C	D	E
100	2000°F	2960°F	3400°F	2900°F	2320°F
95	2050	2980	3350	2875	2320
90	2150	3010	3300	2850	2320
85	2220	3020	3240	2820	2315
80	2320	3060	3170	2790	2315

TE81-9138

Figure 82. Flame temperatures based on CJ-2 computer program.

V. CERAMIC REGENERATOR DEVELOPMENT

REGENERATOR DISK DEVELOPMENT

Summary

The Corning audit to develop cost data for added inspections and tighter limits to prevent weak spots will be completed in March 1981. Corning reports continued progress in controlling thin separator strips. DDA was forced to abandon pressure drop as a means of detecting thin separator strips. A stronger single cement for coating and filling has been adopted. Disks with new single-piece gear adapters and gear coating are ready for test. Harrison Radiator Division is designing a new shipping container to prevent disk damage. Total engine time on 1100°C (2012°F) disks reached 2283 hr. Laboratory development of a 1200°C (2192°F) disk was completed. Testing of an NGK-Locke extruded disk resulted in hub crack-out on cool-down. A stress analysis showed high probability of radial compressive failure in the rim area due to air pressure loads. Low strength in the hot face of a used disk was attributed to high temperature peaks during engine accelerations. A sampling technique and limit for thin separator strips were established. The 1100°C (2012°F) disks were shown to be one-third stronger than 1000°C (1832°F) disks. Disk radial compressive strength was shown to be correlated with separator thickness, as tangential MOR had been previously.

Objectives

The objectives of this effort were as follows:

- To improve manufacturing and inspection processes to eliminate weak areas and provide resistance to handling damage.
- To decrease gear wear and gear attachment stresses.
- To increase temperature capability to 1200°C (2192°F) to accommodate acceleration peaks.
- To improve regenerator effectiveness, pressure drop, and strain tolerance.

Regenerator disk development objectives were to be achieved by the following steps:

- Varying disk manufacturing parameters to determine their effect on weak spots.
- Combining the most effective manufacturing parameters.
- Confirming strength improvement and repeatability.
- Proving the effectiveness of X-ray and microscopic inspection to detect weak areas.
- Tightening internal leakage and cell slant limits as indicators of weakness.
- Using stress analysis to interpret failures.
- Improving rim coating to reduce susceptibility to rim cracking and handling damage.
- Eliminating gear adapter fit and rivet retention problems by redesign.
- Improving disk constraint in shipping container.
- Providing guidance to manufacturers of extruded disks to improve performance and strain tolerance.

Discussion

Strength Improvement

Corning has continued its audit of 50 disks to develop cost data for additional disk inspection and tighter limits to screen out weak areas in disks. It expects to complete this audit in March 1981. The audit includes new X-ray and microphotographic inspection and tighter limits on internal leakage and cell slant. The audit has revealed means of controlling leakage and cell slant by holding closer tolerances within the present tolerance bands. Cell slant has typically been held to 40% of the present limit.

Corning reports continued progress in its program to develop a new process to prevent the formation of thin separator strips, which DDA has established to be the major cause of disk failures. Corning has completed five iterations in this process development with good repeatibility and is near selection of the final process.

DDA has been forced to abandon the detection of thin separator strips by pressure drop measurement. Although a statistically very significant correlation between separator thickness and pressure drop was demonstrated, dispersion in the data was too great to provide control, even when a third major variable of cell slant was included.

Rim Fill and Coating Cement

Two disks with a single cement for coating the outer diameter and filling the face rim area have completed 687 and 329 hr of engine operation, respectively, with no distress. The single cement appears to have superior strength, adhesion and coverage and has been adopted as standard. Previous use of two different cements presented processing problems in providing a good fill and in achieving a good bond where the two cements meet.

Several disks were received with the face rim area filler cement projecting above the face. This condition causes greatly accelerated seal wear. Hand sanding to remove the excess cement resulted in wall damage from the cement debris. Corning will ensure that repairs to the cement will be made prior to finish grinding of the faces.

Drive Gear Adapter and Gear Coating

The first disks with single-piece drive gear adapters and alternative gear tooth wear coating have been received for testing. The single-piece adapters prevent disk rim cracks due to poor gear adapter fit, disk damage from loose rivet spindles, and disk handling damage on an exposed corner. Plasma-sprayed Triboloy 400 gear tooth coating has been replaced with tungsten carbide to prevent chipping and wear.

Packaging

Two 1100°C (2012°F) disks were damaged in shipment on different occasions. The outer diameter cement coating and as many as three matrix wraps were pulled away, generating a circumferential crack about one third of the way around the disks under the rubber gear attachement. The first failure was attributed to loose axial and radial restraint. The second failed disk had close radial restraint, so attention was focused on axial restraint. The need for separate axial gear restraint as well as axial disk restraint to prevent transmittal of gear inertial loads to the disk was recognized. Harrison Radiator Division will design packing with full restraint. Disks are being shipped with special handling until new packing is available.

1100°C (2012°F) Disk Testing

A total of 2283 hr of engine testing have been accumulated on 1100°C (2012°F) disks, with 1137 hr on the highest time disk. These disks are rated 100°C (180°F) higher than previous Corning disks. No operating problems have been experienced.

1200°C (2192°F) Disk Development

Corning has completed laboratory development of a 1200°C (2191°F) alumina silicate disk material and firing schedule, which must now be translated to production-size facilities. A completion date cannot be predicted because of other priorities.

Alternative Disk Matrices

A second disk with extruded equilateral triangular magnesium alumina silicate (MAS) matrix supplied by NGK-Locke was tested at gas inlet temperatures up to 642°C (1186°F). This disk was a cemented mosaic of 36 rectangular pieces, as shown in Figure 83. The solid ceramic support hub cracked loose from the matrix between the cement and matrix. Since the joint was still quite tight and the crack was not observed until the disk had cooled, the crack probably occurred on cool-down. Higher expansion rates of the MAS matrix and hub make expansion match more difficult and transients more of a problem. NGK will investigate hub material and cement changes.

Performance of the NGK disk is compared to that for a standard 1000°C (1832°F) Corning thin-wall disk in Table X. The lower pressure drop and effectiveness of the NGK disk are similar to those obtained with the earlier Corning thick-wall disks. Nominal matrix parameters for the disks compared in Table X are shown in Table XI.

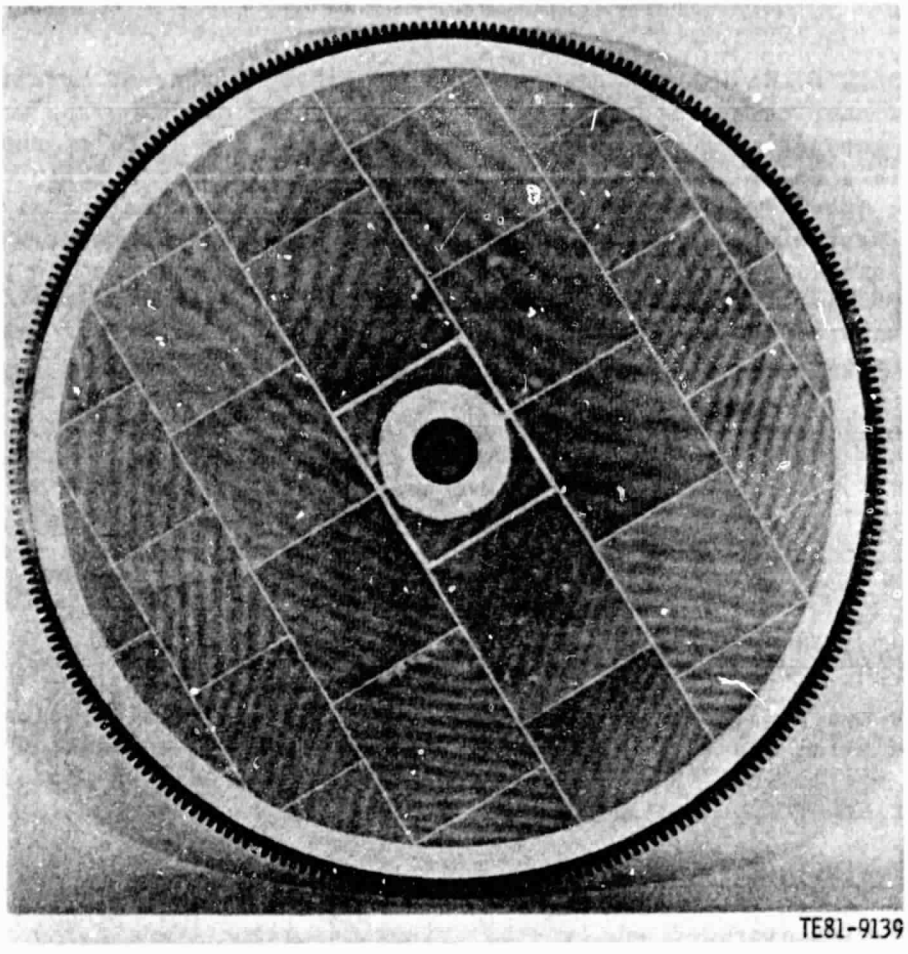

Figure 83. NGK-Locke extruded regenerator disk.

TABLE X. PERFORMANCE COMPARISON OF EXTRUDED NGK AND WRAPPED CORNING 1000°C (1823°F) THIN-WALL REGENERATOR DISKS USING IDENTICAL SEALS IN REGENERATOR RIG

Free shaft 404-4 engine speed condition--%	Hot gas inlet temp--°C(°F)	Effectiveness--%		Gas side pressure drop-- Δpress/press		Seal leakage--%	
		NGK	Corning	NGK	Corning	NGK	Corning
60	543 (1009)	95.8	98.7	0.011	0.011	9.1	7.7
70	538 (999)	93.5	95.6	0.015	0.014	6.2	6.1
80	556 (1033)	92.1	94.9	0.017	0.020	5.4	4.8
90	590 (1094)	90.6	93.6	0.023	0.028	6.2	4.0
100	642 (1186)	89.0	93.4	0.031	0.037	6.9	4.2

TABLE XI. COMPARISON OF NGK AND CORNING 1000°C (1832°F) THIN-WALL MATRIX PARAMETERS

	Holes-- cm^2 ($in.^2$)	Wall thickness-- mm (in.)	Open area --%	Hydraulic diameter-- mm (in.)	Surface area/ volume-- m^2/m^3 (ft^2/ft^3)
Extruded NGK equilateral triangle	143 (920)	0.135 (0.0053)	64.2	0.59(0.0232)	4356 (1328)
Wrapped Corning 1000°C (1832°F) thin-wall	204 (1311)	0.061 (0.0024)	78.7	0.579(0.0228)	5422 (1653)

The higher seal leakage experienced with the NGK disk using identical seals (shown in Table X) has not been explained, but may be related to the mosaic structure or higher thermal expansion of the NGK disk. The structure of the seals used is very similar to that of seals used on metal disks with much higher expansion, where leakage at the higher speed conditions is in the 4-5% range.

Stress Analysis of the Regenerator Disk with Non-axisymmetric Mechanical and Pressure Loading

A detailed stress analysis of the regenerator and ring gear drive system was made to try to interpret four rig and engine core failures. Since the failures occurred during operation at the 100% power cycle point, they were more likely due to the high pressure levels that occur at this point than to thermal stresses. The failed disks displayed circumferential cracks, which indicated either radial stress or shear stress was involved in the crack propagation.

Since two of the failures occurred within a few corrugations of the hub/matrix interface, some explanation was sought for the actual occurrence of high stress in that region. Previously, only axisymmetric pressure loading had been applied to a finite element model consisting of axisymmetric elements (Figure 84). The resulting radial and tangential normal stresses at the matrix/hub interface were small. Non-axisymmetric load distributions that had been previously applied to this model were much less concentrated and localized than mechanical load distributions occurring in the actual system.

To remedy these deficiencies, an analysis was made by summing a large number of "harmonic" solutions to obtain a reasonable simulation of the actual complex mechanical and pressure load distributions. As shown in Figure 85, non-axisymmetric pressure distributions are caused by pressure drop across the cross-arm seals. The mechanical loads are due to the pinion drive gear force, the friction drag on the seals, and the weight.

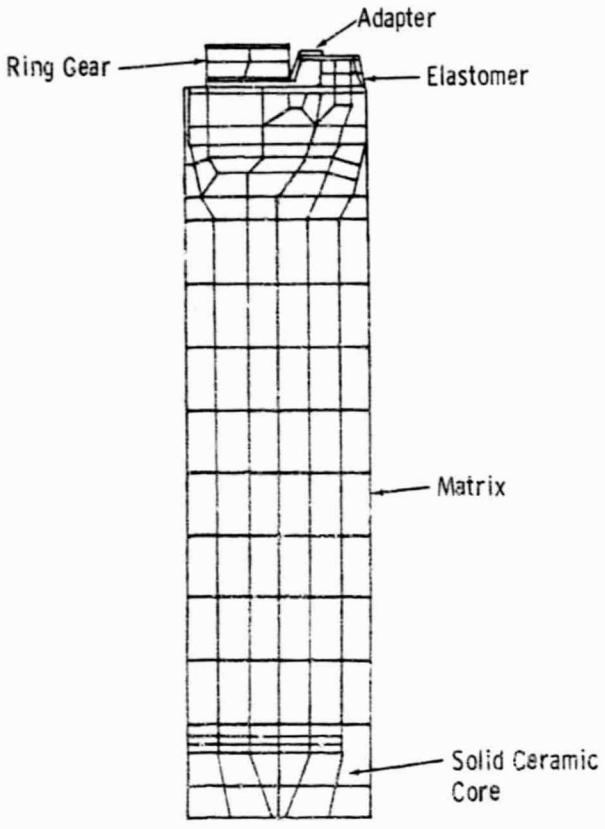

Figure 84. Finite element model.

The highest normal stresses predicted by the detailed analyses were predominately compressive, due to pressure, and primarily confined to the low-pressure rim of the core. Figure 86 shows radial and tangential isostress plots at a circumferential location in the model near where the peak values of these stresses occurred. The peak radial and tangential stresses occurred at the inboard edge of the interface between the elastomer and the matrix. The highest value of the radial stress was 492 kPa (71.2 psi), and the maximum tangential stress was 1112 kPa (161.2 psi). The circumferential variation in radial and tangential stress at the location of the maxima is shown in Figure 87.

The two core failures that occurred in the vicinity of 26.7 cm (10.5 in.) radius were in a region of relatively high radial stress. A statistical analysis of available strength data indicated that the radial stress was in a much more critical relationship to strength than the tangential stress.

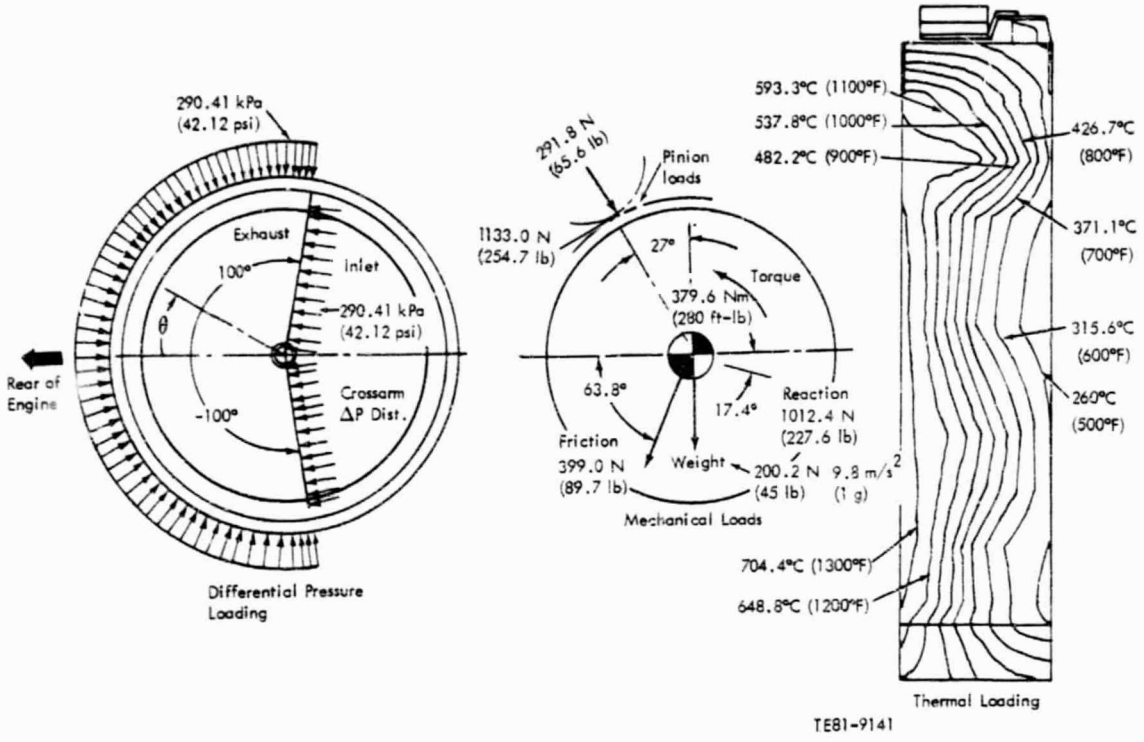

Figure 85. Differential pressure loading.

The statistical analysis of strength data indicated that specimen data from DDA's in-house testing were well correlated by a log-normal distribution for specimens from a given disk. A typical plot displaying this relationship is shown by Figure 88. Unfortunately, up to that time only tangential MOR data had been generated by the DDA in-house program. An attempt was made to predict the radial compressive strength of the DDA cores by comparing the DDA MOR_T data with MOR_R and radial compressive strength data published by the Ford Motor Co. for thin-walled alumina-silicate (AS) core matrix material specimens. This estimate was made by assuming the same ratio between MOR_T and radial compressive strength as was indicated by the Ford data.

By using this assumed strength relationship, the approximate region in which radial stress exceeded mean strength was defined for each core for which specimen strength data were available. A typical approximate region in which radial compressive stress exceeds estimated radial compressive strength is shown in Figure 89. This particular core was selected for comparison was chosen because its tangential strength was near the average for all cores tested.

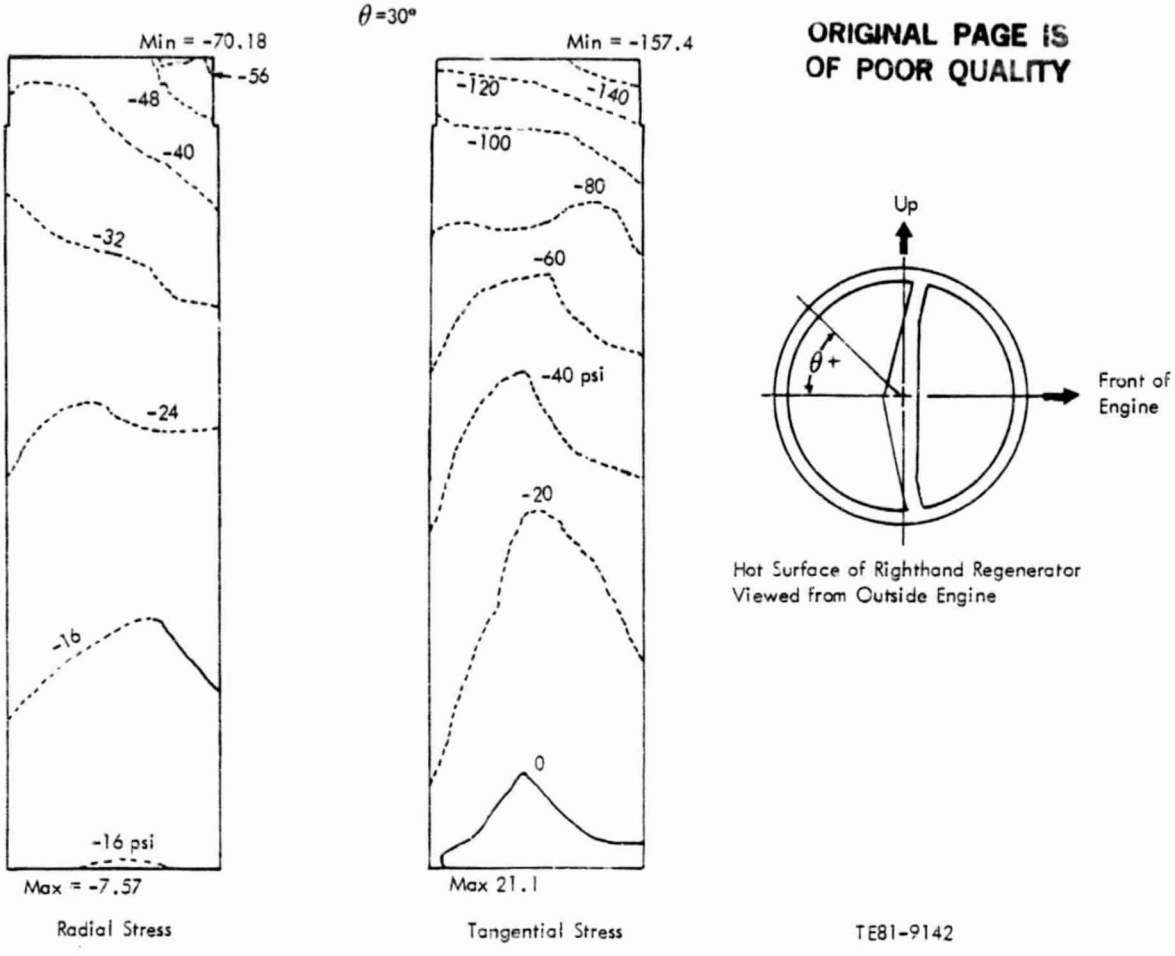

Figure 86. Matrix stresses.

The results of this study pointed up the need for more accurate characterization of material strength properties, especially radial compressive strength. Only core failures that occurred in the vicinity of the rim could be interpreted in terms of normal stresses predicted by this study. The failures that occurred near the matrix/hub interface were not predicted by the magnitude of normal stresses expected in that region of the core.

Further study will be required to explain the failures that occurred at the interface between the matrix and the solid hub. There was some indication of high shear stress at this interface. However, a much more detailed representation of the crossarm friction forces will be required to accurately calculate this shear stress.

DISK MATERIALS EVALUATION

Summary

During the past 6 months the effect of hot face seal-matrix mass transfer and corrosion on the 1000°C (1832°F) AS matrix has been shown to be statistically insignificant compared with cyclic thermal exposure (CTE) damage caused by engine acceleration-deceleration transients in engine-exposed disks.

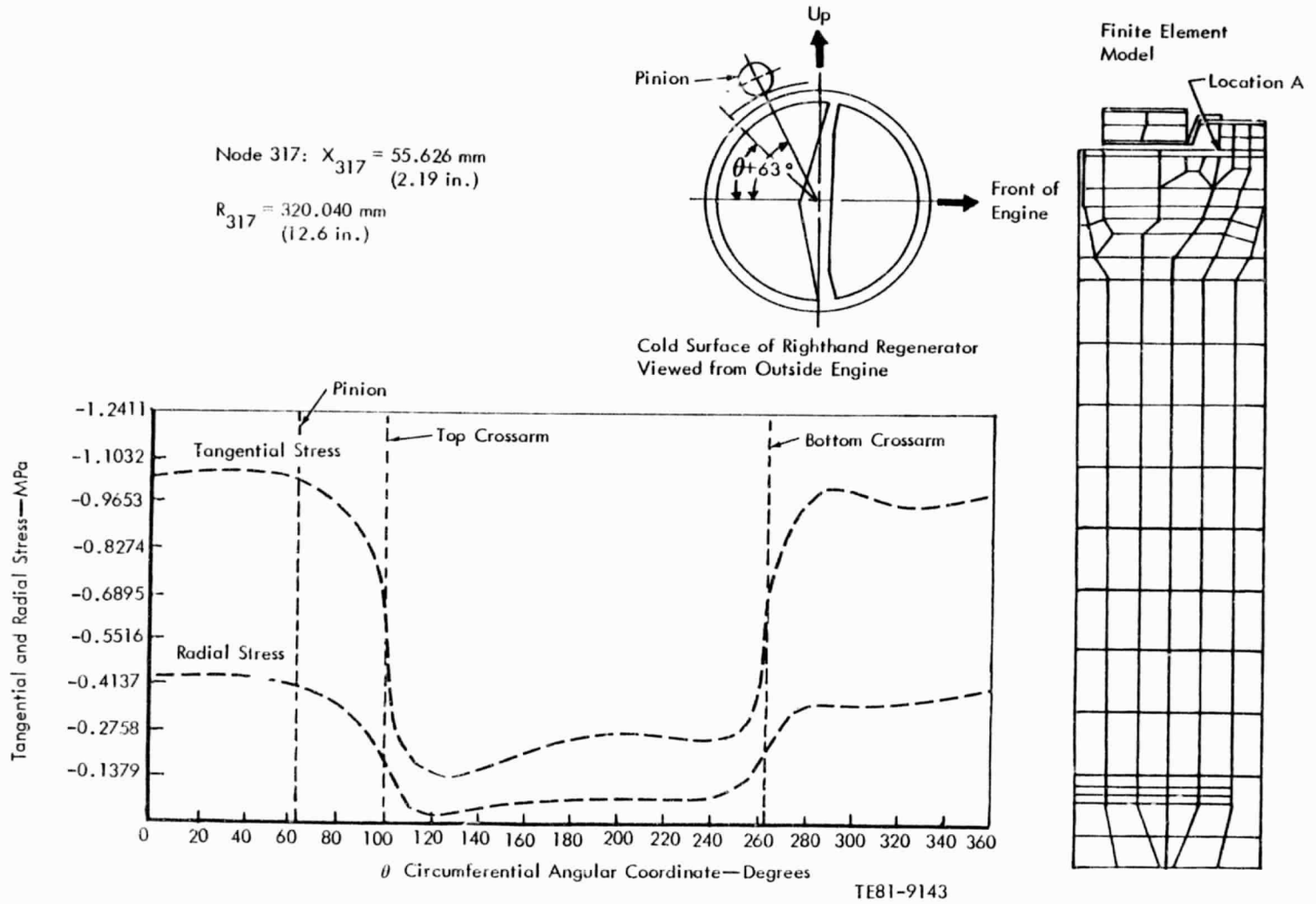

Figure 87. Circumferential variation of radial and tangential stresses at Location A.

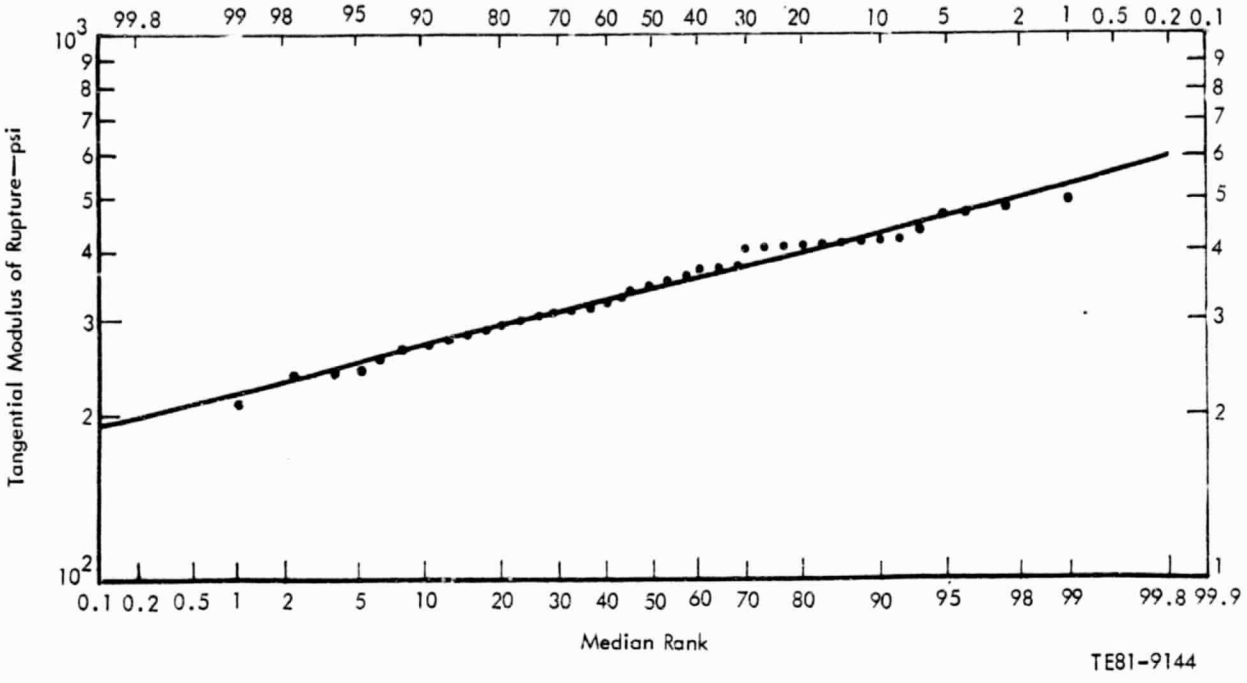

Figure 88. Strength distribution, disk 3.

It has also been shown that MOR_T is a function of separator wall thickness over the entire 1000°C (1832°F) eight-disk sample tested to date. An acceptance limit inspection system has been designed and successfully tested against the eight-disk sample.

The four-disk sample of the 1100°C (2012°F) AS disk production has been completed with the reception of disks 2, 3, and 4. Enough of the as-received testing is complete to confirm the original indication from disk 1 that the 1100°C (2012°F) material is approximately one-third stronger than the 1000°C (1832°F) AS disks at the same separator wall thickness.

Finally, an experimental design to evaluate disk radial compressive strength has been completed and enough data acquired to show that the low end of the strength distribution is critical relative to some mechanical design stresses. Further, radial compressive strength is closely correlated with separator wall thickness. A related experiment to measure the thermal coefficient of expansion and the elastic modulus of the elastomer used to bond the ring gear to the disk has been started.

Objective

There were four objectives during this period. The first was to separate and identify the effects of acceleration-deceleration transients, or CTE fatigue (CTE), and hot face seal-matrix mass transfer and corrosion in the loss in strength of the matrix hot face observed in engine-exposed disks. Second

Disk	Avg. MOR_T —psi
2	272
3	345
4	174
6	273
7	356
8	329

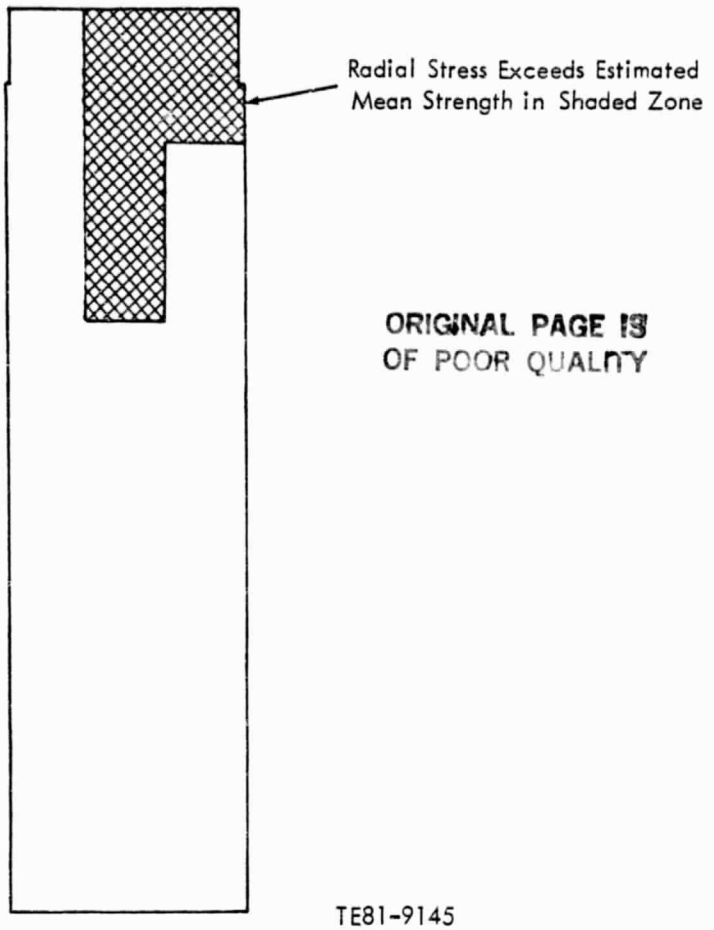

Figure 89. Radial stress/strength for disk 6.

was the design of a statistical acceptance sampling plan for matrix separator wall thickness for incoming disks. Third was the acquisition of the first "as-received" MOR data from disks 2, 3, and 4 of the 1100°C (2012°F) disk series. Fourth was the development of radial compressive strength data for a group of selected disks.

Approach

The approach to the first objective was based on exposing 1000°C (1832°F) AS matrix samples to hot gas acceleration-deceleration transients in a laboratory burner. The temperature transients were identical to those measured in engine regenerator disk inlets. The loss in hot face MOR values in these samples was then compared to the loss measured in hot face MOR for engine-exposed disk samples that had both temperature-transient exposure and seal hot face mass transfer due to normal seal-matrix friction and wear.

The second objective was approached by applying two conventional acceptance sampling plans to the data base made up of the MOR and separator wall thickness values from the eight-disk sample of 1000°C AS disks acquired during

this program. This data base included two disks that failed in regenerator rig testing. The MOR and separator wall thickness values, as close to the point of failure in these disks as possible, were used to calculate the acceptance limits in both plans. The eight-disk data base was then run through both acceptance sampling plans and a single plan was selected.

The approach to the third objective was that used in testing all previous disks: samples were taken at each of five disk radii, with three MOR test bars at each of six axial positions through the sample. The MOR data were correlated with the fracture plane separator wall thickness.

The approach to the fourth objective was a two-step procedure, the first step being a comparative test of compression strength sample configuration and bonding procedure, and the second compressive strength measurements of a four-disk group using two 1000°C (1832°F) disks and two 1100°C (2012°F) disks.

Results

CTE--Seal Material Mass Transfer

To establish a basis for comparison of the engine-exposed 1000°C (1832°F) AS matrix with the laboratory samples exposed in the burner, a number of hot face samples from the 3050-hr engine disk were prepared, electron microscope photographs were taken, and axial probe scans were made. Figure 90 shows the Ni^{+2} ion concentration gradient from the "glaze" or seal contact surface into the matrix (from left to right in the upper photomicrograph). The concentration is only approximate since the probe beam is 2-3 μm in diameter and the Ni^{+2}-bearing layer is 6-7 μm thick. The relative metal ion counts are shown in the lower frame.

Next, two samples of 1000°C (1832°F) AS matrix were thermally exposed at 1093°C (2000°F) for 5 hr under steady-state conditions and 5 hr at 1093°C (2000°F), consisting of 2 hr, 13 min at steady-state and 2 hr, 47 min of acceleration-deceleration transients peaked and held at 1093°C (2000°F) for 2.0 sec per cycle. The onset of the upshock was adjusted to 1149°C/sec (2100°F/sec) and the onset of the downshock was 343°C/sec (640°F/sec), corresponding to truck-bus turbine engine gas temperature transients. The 350-hr engine disk data are compared to the laboratory samples in Table XII.

TABLE XII. LOSS IN MOR_T IN 1000°C (1832°F) AS MATRIX IN STATIC THERMAL EXPOSURE, TRANSIENT THERMAL EXPOSURE, AND TRANSIENT EXPOSURE WITH SEAL CONTACT MASS TRANSFER

Thermal and transient exposure/hr/cycles	Mean MOR--kPa (lb/in.^{2}) Hot face (T_1--C_1)	Axial remnant (T_2--B_6)*	Sign. level of difference hot face-Rem
1093°C (2000°F)/5 hr (steady-state)	2144(311)	2161(313)	$\alpha > 0.10$
1093°C (2000°F)/5 hr/5,000 cycles	1640(238)	2138(310)	0.01 α>0.001
1010°C (1850°F)/3050 hr/ 35,000 cycles	1634(237)	2277(331)	0.01 α>0.05

*See Table XIII.

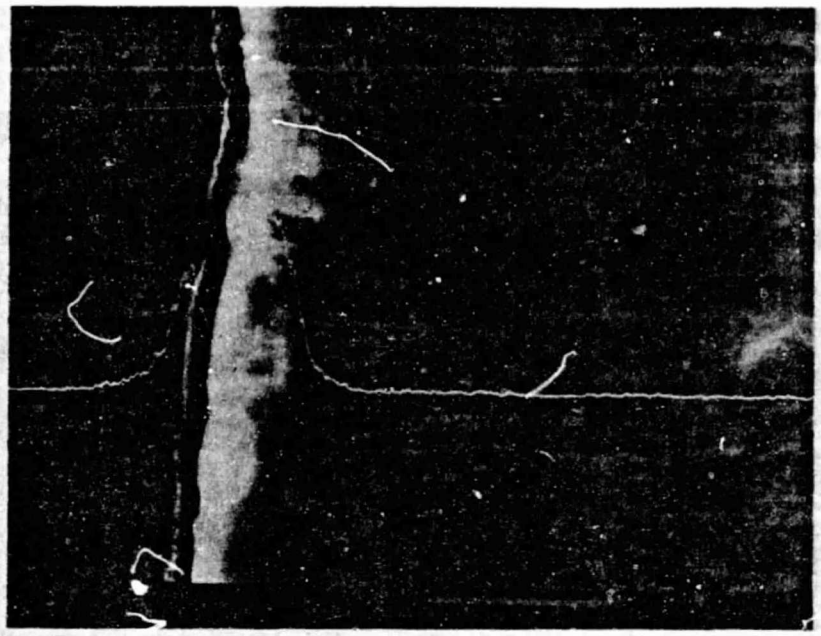

(a) Approximate Ni^{+2} concentration from the seal contact surface into the matrix.

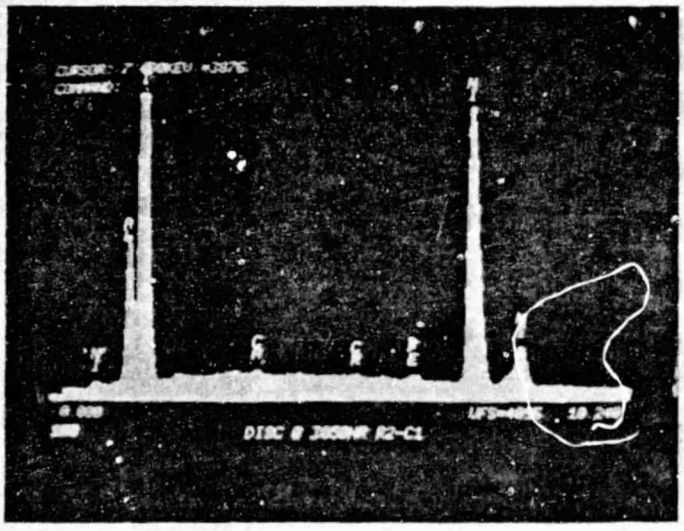

(b) Relative cation count.

TE81-9146
357747

Figure 90. Approximate Ni^{+2} concentration and relative cation count.

It is clear that the CTE loss (line 2) in strength is greater than the steady-state thermal exposure loss (line 1). Both the CTE-exposed and engine-exposed matrix sample losses in MOR are statistically significant and are very nearly equal, indicating that the transfer of Ni^{+2} to the matrix plays little or no part in the loss in hot face strength.

Finally, a sample of 1100°C (2012°F) AS matrix was exposed to the same 1093°C (2000°F)/ 5 hr/5000 cycle CTE test as the 1000°C (1832°F) matrix sample. Table XIII gives the detailed data. The trend is very similar to that for the 1000°C (1832°F) samples: MOR, T_3-B_6 T_2-B_2 T_1-B_1. The hot face T_1 through B_1 is reduced in MOR to a level significantly less than that for the remaining test bars.

TABLE XIII. CTE TEST OF 1100°C (2012°F) AS MATRIX DISK 1 SHOWING HOT FACE LOW IN MOR

Sample	Axial position-- mm (in.)	Channel skewness-- degrees	MOR_T-- psi		MOR_T-- kPa
T_1		5.0	304.0		2096
C_1	4.8(0.19)	5.0	338.2	325.1	2332
B_1		5.0	333.0		2296
T_2		5.0	379.0		2618
C_2	15.9(0.63)	5.0	412.3	343.4	2842
B_2		6.0	238.2		1642
T_3		5.0	417.2		2876
C_3		6.0	420.3		2897
B_3		6.5	405.4		2795
T_4		7.0	445.1		3069
C_4		8.0	453.9		3129
B_4	54.8(2.16)	8.0	459.8	456.9	3170
T_5		8.0	475.8		3281
C_5		9.5	470.2		3241
B_5		10.0	469.0		3234
T_6		10.0	484.4		3339
C_6		11.0	496.6		3423
V_6		12.5	485.2		3345

Acceptance Sampling Plan for Disk Separator Wall Thickness

Previous work has shown that the MOR_T is strongly dependent on the separator strip wall thickness in the AS matrix used in this program. As a consequence, two disk quality control plans, both based on the 1000°C (1832°F) material eight-disk data base, were tested for application to this problem of a received disk strength. The quality control program that best fits the requirements of the CATE project is based on a lower limit for the separator wall thickness. This lower limit is based on sampling the disk separator thickness at a number of points on the surface, calculating a mean and an estimate of the variability--the standard deviation, and using these data to calculate a "t statistic" that permits comparison of the disk mean and variability with the

t values for a normal population. The accept/reject decision that results is based on known, selected level risks. The acceptance limit was calculated using the fact that two 1000°C (1832°F) disks, 4 and 6, failed in regenerator rig testing. The lower 0.95 confidence limit MOR values for these two disks were used to establish the low tolerance limit of 0.037 mm (0.00146 in.) by the intersection of the disk 6 lower 0.95 confidence limit with the 0.95 confidence limit for the entire disk population. Figure 91 shows the regression equation line for the entire disk population, the confidence limits, and the disks 4 and 6 lower confidence limit MOR values. When the disk population was tested against the acceptance limit, adopting a risk of accepting a bad disk of 0.05 and a risk of rejecting a good disk of 0.05, a sample of seven groups of six separator walls per disk inspected resulted. Table XIV compares the mean separator wall thicknesses for the eight-disk group. Disk 4 would be rejected by the acceptance plan, but disk 6, which had a narrow band of thin separator walls near the outer periphery, would be accepted.

During this time period disks 2, 3, and 4 of the AS 1100°C (2012°F) material series were received and the "as received" MOR_T values determined for most of the radial sample locations. For comparison purposes, the mean MOR values, listed by radius, are shown in Table XV.

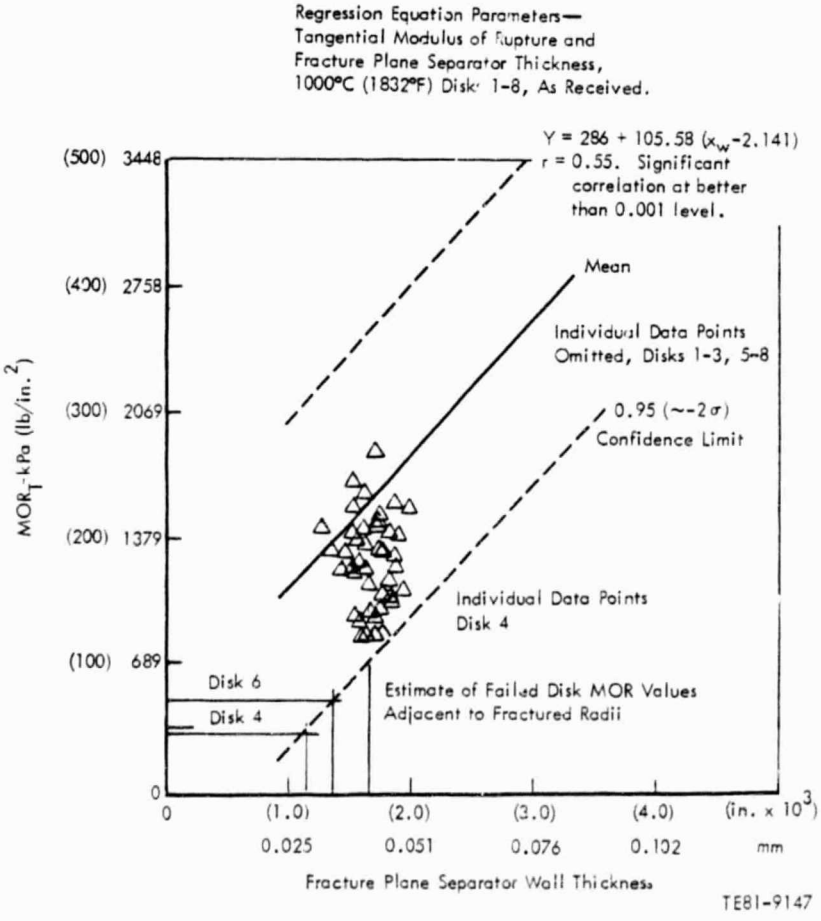

Figure 91. Base for lower tolerance acceptance limit.

TABLE XIV. MEAN SEPARATOR WALL THICKNESSES FOR 1000°C (1832°F) AS DISKS

Disk	Mean thickness--mm (in.)		Std. deviation (σ)
1	0.049	(0.00193)	0.00599 (0.000236)
2	0.047	(0.00186)	0.00546 (0.000215)
3	0.063	(0.00249)	0.00683 (0.000269)
4	0.042	(0.00167)	0.00470 (0.000185)
5	0.043	(0.00210)	0.00579 (0.000228)
6	0.062	(0.00243)	0.00998 (0.000391)
7	0.073	(0.00288)	0.00685 (0.000270)
8	0.052	(0.00203)	0.01161 (0.000471)

1100°C (2012°F) matrix disks, AS-received MOR_T values.

TABLE XV. MEAN MOR_T VALUES FOR 1100°C (2012°F) AS DISKS TO DATE

Radius-- cm (in.)	Values per disk--kPa (lb/in.^{2}) 1	2	3	4
30.5(12.0)	3156 (452)	2765 (396)	1948 (279)	2441 (350)
25.4(10.0)	3072 (440)	2737 (349)	1947 (279)	2203 (315)
20.3 (8.0)	2817 (403)	2619 (375)		2140 (308)
15.2 (6.0)	2683 (384)			2278 (326)

The mean MOR values range from 3156 kPa (452 lb/in.^{2}) to 1948 kPa (279 lb/in.^{2}), with an average of 2469 kPa (358 lb/in.^{2}) for the 1100°C (2012°F) disks to date. The corresponding mean MOR values range from 2758 kPa (400 lb/in.^{2}) to 869 kPa (162 lb/in.^{2}), with an average of 2013 kPa (292 lb/in.^{2}) for eight 1000°C (1832°F) disks. The mean MOR has increased by 23% and the variability, measured by the range, has decreased by 27% in the 1100° (2012°F) disks.

Radial Compressive Strength of AS Matrix

Calculation of mechanically induced compressive and/or shear stresses in the engine disk prompted an investigation of the radial compressive strength of the 1000°C (1832°F) matrix (where there have been four disk failures to analyze) and the 1100°C (2012°F) matrix for comparison purposes. Although the work is incomplete, some important preliminary findings are available.

The 1000°C (1832°F) matrix results were successfully correlated with the fracture plane separator wall thickness, with a low mean of 361 kPa (52.3 lb/in.^{2}) and a large regression coefficient, or slope, of

$$9284 \frac{\text{kPa}}{\text{mm}} \left(\frac{34.2 \text{ lb/in.}^2}{\text{in.} \times 10^3} \right).$$

This results in a 0.95 lower confidence limit of 69 kPa (~10 lb/in.^{2}), as seen in Figure 92. Disk 1, of the 1100°C (2012°F) series, was tested and demonstrates a mean of 704 kPa (102 lb/in.^{2}) and a lower 0.95 confidence limit of 414 kPa (60 lb/in.^{2}) (Figure 93). This indicates a correlation with the MOR_T levels observed, linked through a similar dependence on separator wall thickness, which will be investigated as more data are acquired.

Conclusions

The presence of mass transfer products at the seal/matrix interface shows no statistically significant effect on the MOR_T, beyond that caused by CTE exposure, up to 3050 in 1000°C (1832°F) rated disks. Cyclic thermal exposure caused by acceleration/deceleration cycles causes a significant loss in MOR in both the 1000°C (1832°F) and 1100°C (20120°F) matrices.

A satisfactory acceptance criteria for separator wall thickness quality control has been designed and tested against a known disk population.

Three more 1100°C (2012°F) disks have been tested in the as-received condition. To date, the 1100°C (2012°F) disks are superior to the 1000°C (1832°F) disks on both an intra- and interdisk basis.

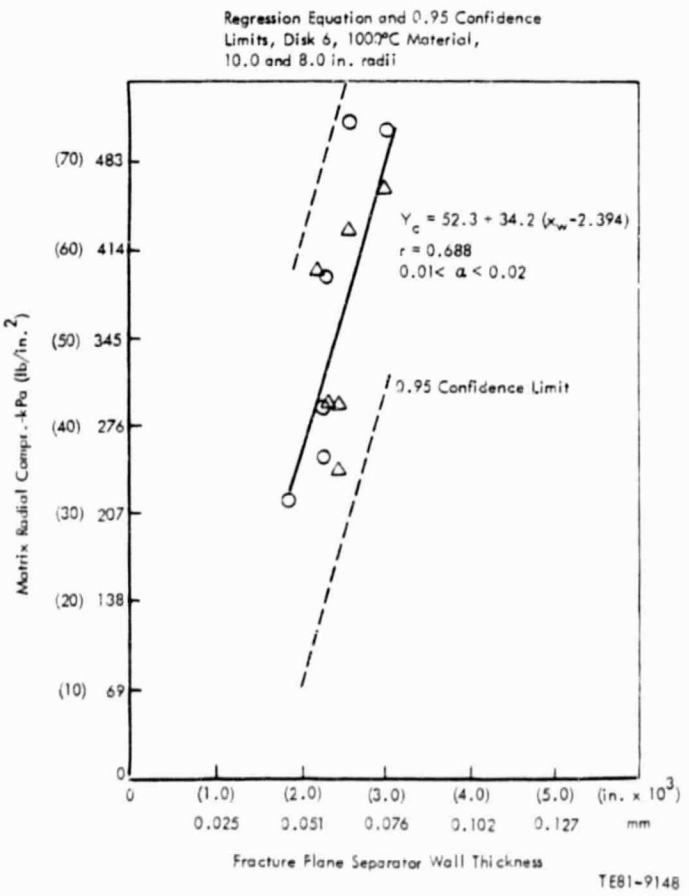

Figure 92. Radial compressive strength 1000°C (1832°F) AS matrix, disk 6.

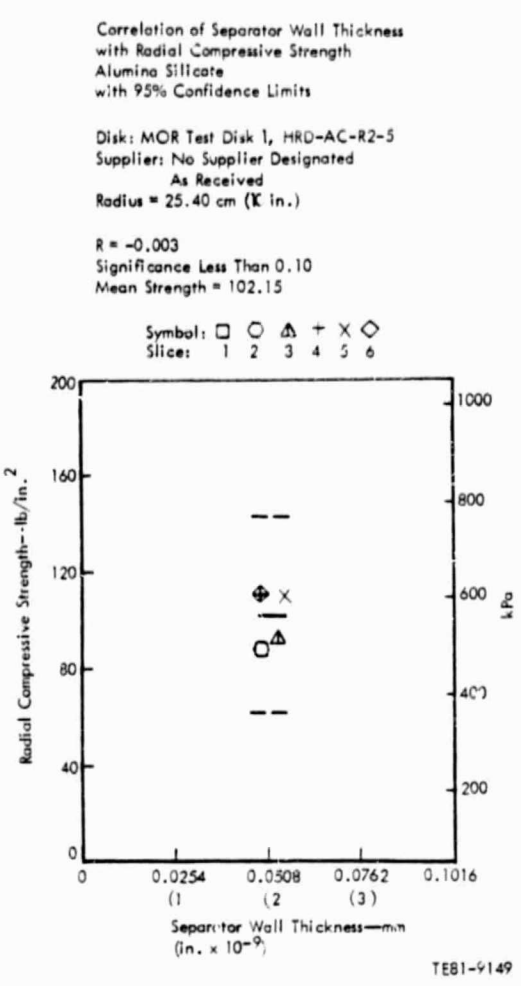

Figure 93. Radial compressive strength 1100°C (2012°F) AS matrix, disk 1.

The radial compressive strength is indicated to be a critical consideration in meeting mechanical stresses in some 1000°C (1832°F) disks. The compressive strength depends on the separator wall thickness, and the 1100°C (2012°F) matrix is significantly stronger in compression than the 1000°C (1832°F) matrix at approximately the same wall thickness.

REGENERATOR SEAL DEVELOPMENT

Summary

Development of the three-piece, high-temperature, cooled seal continued with reductions in leakage and definition of cooling flow requirements. Drawings were being prepared for a more effective alternative cooling scheme. Two new one-piece seals with 70% NiO/30% CaF_2 wearface were tested. A 50-hr regenerator rig test was run on an uncooled seal at 982°C (1800°F) and demonstrated much better stability of CaF_2 lubricant in the wearface than in laboratory tests, but disclosed a leaf corrosion problem without cooling.

Objective

The objective was to develop an inboard seal capable of low friction, wear, and leakage for operation at a regenerator inlet gas temperature of 982°C (1800°F).

Regenerator seal development objectives were to be achieved by:

- o Applying compressor discharge air to cool the inboard seal crossarm sufficiently to prevent creep without introducing thermal warpage to cause leakage.
- o Cooling the crossarm wearface to provide chemical stability.
- o Seeking a crossarm wearface compound that is more chemically stable and provides a better thermal expansion match with the substrate.
- o Alternately trying a design with a compliant isolator between wearface and substrate.
- o Counteracting thermal coning of the seal rim to reduce leakage and concentrated wear.

Discussion

Three-Piece, High-Temperature Seal Testing

Testing and development were continued on the three-piece, high-temperature, cooled-seal concept to minimize leakage and improve cooling. Two additional seals were tested. One had good initial flatness, achieved by reducing the number of spot welds attaching the lightly loaded cooling baffle and by peening the leaf and baffle weld areas to correct weld distortion. The other seal incorporated weld stress relief, which did not produce good flatness. Two additional seals, produced in this period but not tested, incorporated a thinner weld area to reduce weld distortion. Lack of crossarm flatness had previously been identified as a source of leakage in the leaf test rig.

Leakage data for all four of the three-piece, high-temperature seals tested to date are compared to those for the best one-piece seals in Table XVI. The table shows that leakage is higher for the three-piece seals. This is attributed to weld distortion in the thicker three-piece seal crossarm, which will be minimized in the next seals by milling the weld area thinner. Seal H3051 had the least distortion and showed the lowest leakage, while H3050 was the worst. Seal H3051 incorporated a peening procedure for flattening, while H3050 incorporated an unsuccessful stress relief.

The three-piece seals show excessive leakage at low speeds in the free shaft condition, which is attributed to the low operating temperatures encountered at those conditions.

TABLE XVI. INBOARD REGENERATOR SEAL--PERCENT LEAKAGE COMPARISON

Engine operating condition	One-piece seals		Three-piece, high-temperature seals			
	H3072	H3071	H3048	H3049	H3051	H3050
50% free shaft	6.5	7.4	16.5	14.2	13.7	23.7
60%	4.9	--	14.0	10.9	9.5	21.2
80%	3.3	3.9	9.8	6.7	6.7	14.2
100%	3.3	3.3	8.5	5.6	5.5	11.0
60% power transfer	4.2	3.4	--	--	3.9	--
80%	3.2	3.0	6.6	5.0	3.0	--
100%	3.4	3.2	6.3	7.1	4.1	--

Variations in the distribution of cooling airflow were tested to determine their effect on seal leakage and crossarm temperatures. Variations in cooling flow were achieved by throttling the rim and hub sources and by moving and changing the size of the exhaust port. The original arrangement of these cooling flow ports is shown in Figure 94. It was concluded that complete blockage of the rim source for cooling air provides the least leakage and best crossarm temperature distribution. Figure 95 shows crossarm temperatures with no cooling, with full internal cooling as exhibited by Figure 94, and with cooling flow supplied to the hub only from an external source. Steep temperature gradients exist between 21.6 and 28 cm (8.5 and 11 in.) radii with no cooling flow, and cooling flow from the rim source makes those gradients worse. Steep temperature gradients were believed to warp the crossarm and cause leakage. Conduction was adequate to prevent high temperatures at the uncooled edges of the crossarm. Cooling was not improved by changing the location and size of ports. Figure 95 shows that external cooling flow equivalent to 7.3% of total regenerator flow was required to cool the seal to an acceptable 816°C (1500°F). After a major allowance for nonassignable seal leakage, it was estimated that the same cooling could be supplied with only half that flow. An increase in engine fuel consumption due to the cooling flow bypassing the regenerator is expected to be less than 2% because the flow still receives about half the normally regenerated heat and is not lost to the turbines.

The cooling effectiveness for the seal structural platform can be improved by applying the cooling flow to a thin porous layer between the structural platform and the plasma-sprayed wearface instead of on the leaf side of the platform as at present (Figure 94). Seals have been run successfully with the wearface sprayed on a porous metal compliant layer, but without the addition of cooling air. The compliant layer will have the added advantage of isolating differential expansion between wearface and platform. Drawings are being prepared for this alternative cooling scheme.

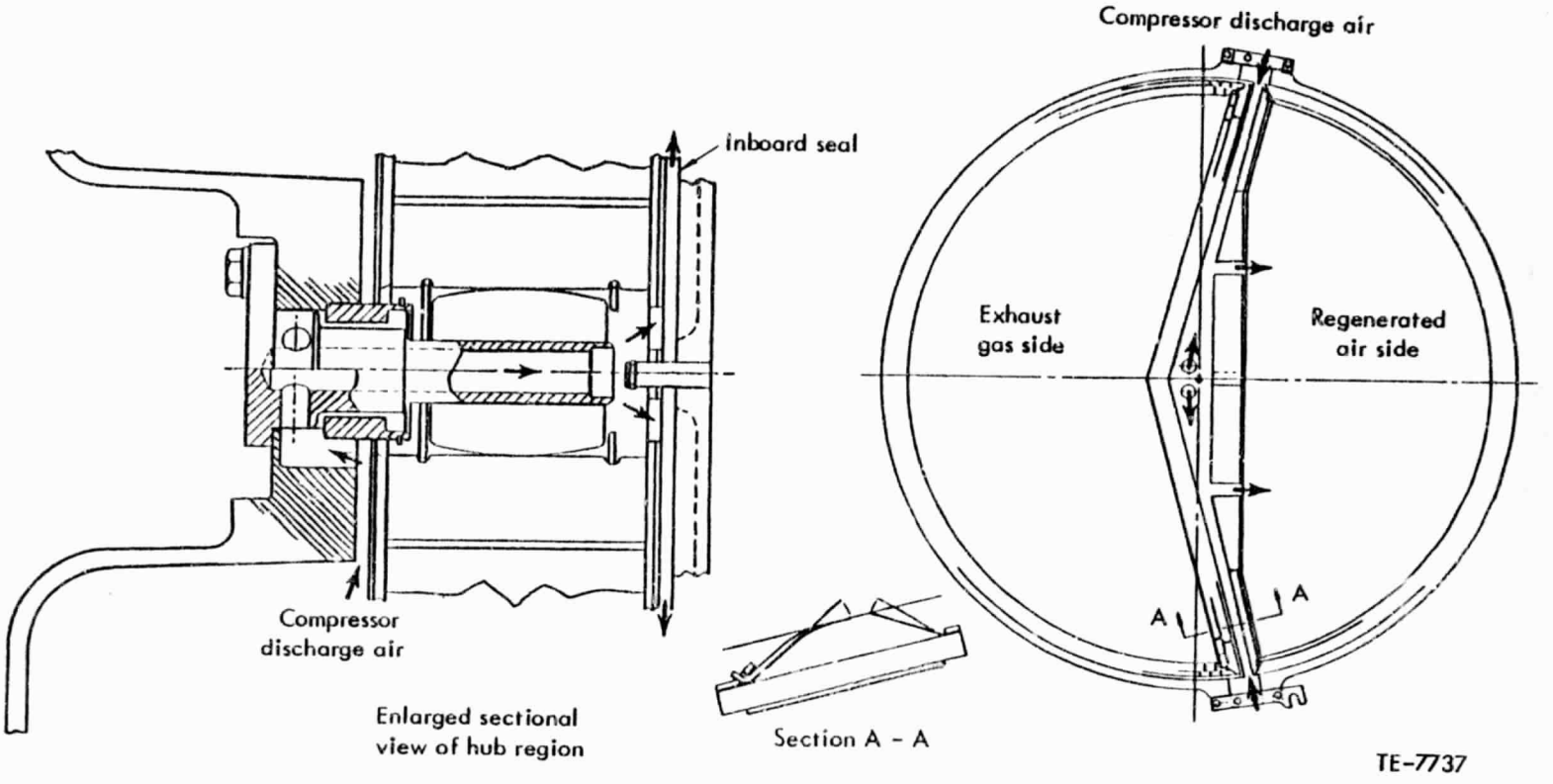

Figure 94. Regenerator inboard seal cooling air system.

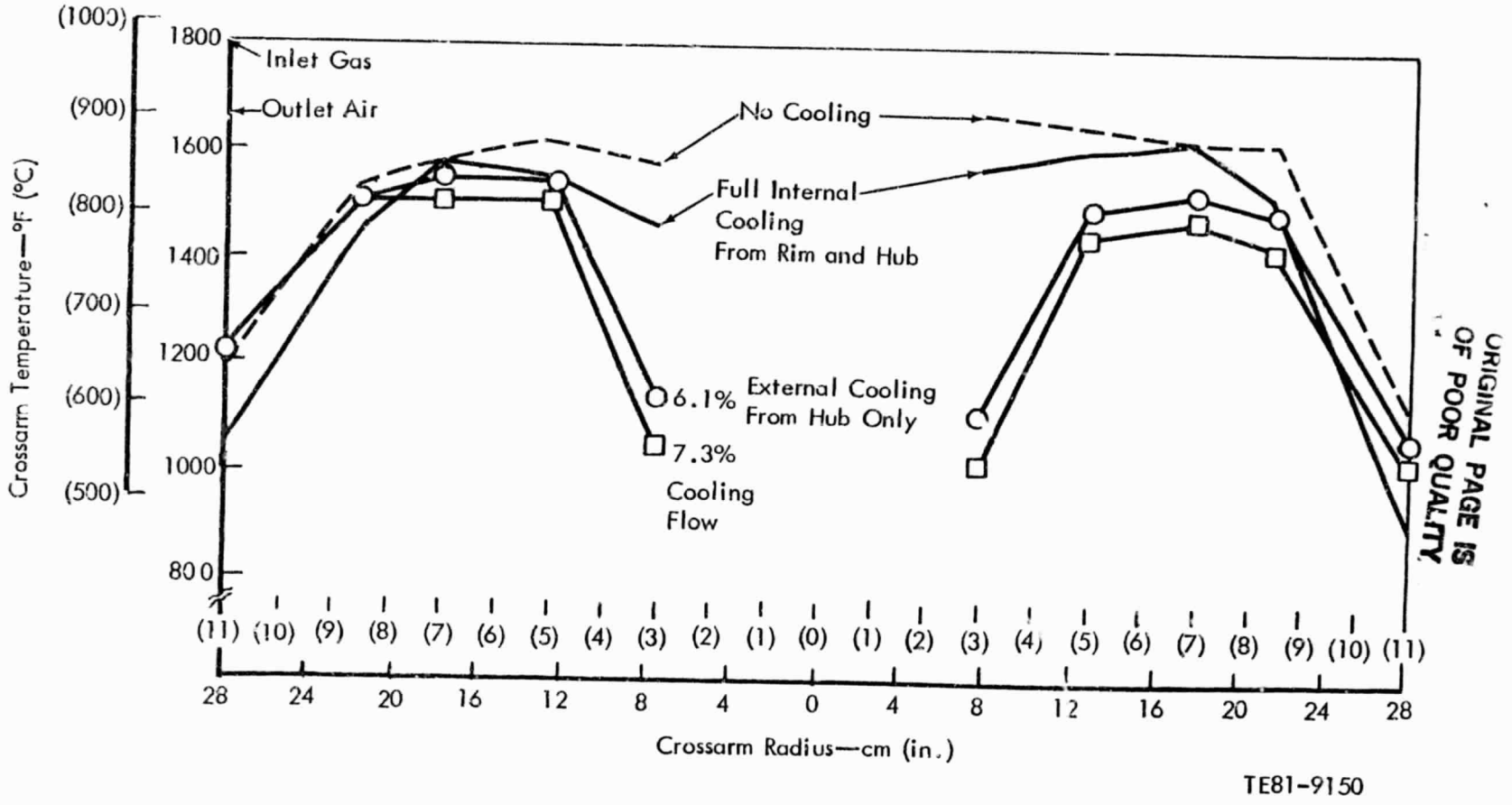

Figure 95. Three-piece, high-temperature regenerator seal crossarm temperature with and without cooling for 60% engine speed conditions.

One-Piece Seal Testing

Standard one-piece inboard seals incorporate a 85% NiO/15% CaF_2 crossarm wearface. Six seals with a 70% NiO/30% CaF_2 wearface were ordered for the CATE program because laboratory tests showed that this mix produced the best thermal expansion match with the substrate. The second pair of these seals has now been tested and shows lower leakage, as did the first pair previously reported. Table XVII compares the leakage of the second pair of 70% NiO/30% CaF_2 seals with an average for ten standard 85% NiO/15% CaF_2 seals and shows generally lower leakage for the 70% NiO/30% CaF_2 seals.

The four three-piece seals described in the previous section also incorporated the 70% NiO/30% CaF_2 wearface. Future three-piece seals will incorporate a 90% NiO/10% CaF_2 wearface, which has shown better chemical stability and lower friction and wear at temperatures above 871°C (1600°F), but poorer thermal expansion match.

TABLE XVII. INBOARD REGENERATOR SEAL--PERCENT LEAKAGE COMPARISON FOR ONE-PIECE SEALS

Engine operating condition	85% NiO/15% CaF_2 crossarm wearface (10 seals)			70% NiO/30% CaF_2 crossarm wearface	
	Avg	Max	Min	H3072	H3071
50% idle	7.0	18.0	4.0	6.6	9.6
60% power transfer	4.0	7.0	2.9	4.1	3.7
80%	3.7	4.7	2.9	3.2	2.9
100%	4.2	5.1	3.4	3.4	3.1
50% idle (after decel.)	5.6	9.1	3.7	5.0	4.6

50-Hr 982°C (1800°F) Test of NiO/CaF_2 Wearface Seal

Laboratory tests showing the chemical instability of the CaF_2 lubricant in the inboard seal crossarm wearface and severe reaction between it and the AS regenerator disk at 982°C (1800°F) were previously reported. Laboratory tests had shown very high seal and disk wear. Full-scale regenerator rig tests and engine tests showed little evidence of the laboratory reactions, probably because of the cooling and self-cleaning effects of airflow. For this reason, a 50-hr regenerator rig test was run on an uncooled seal with 85 NiO/15 CaF_2 wearface to determine the reaction rates at 982°C (1800°F) under engine operating conditions. Wear was high, 0.125 mm (0.005 in.) but not catastrophic as in the laboratory. SEM showed that conversion of CaF_2 to $Ca(OH)_2$ or chalking only extended 10 microns (0.0004 in.) deep. Cooling in the high-temperature seal should reduce this chalking, shown in Figure 96. Thermal distortion of the seal was greater than normal but still quite tolerable, and leakage was satisfactory. Friction torque was normal, and there was no evidence of rim graphite wearface oxidation, confirming predictions. Figure 97 shows severe sealing leaf corrosion concentrated at the bend line, where stress corrosion contributes. Susceptability of René 41 to oxidation at high temperatures may require replacement with Haynes 188; however, cooling of the high-temperature seals is expected to prevent leaf oxidation.

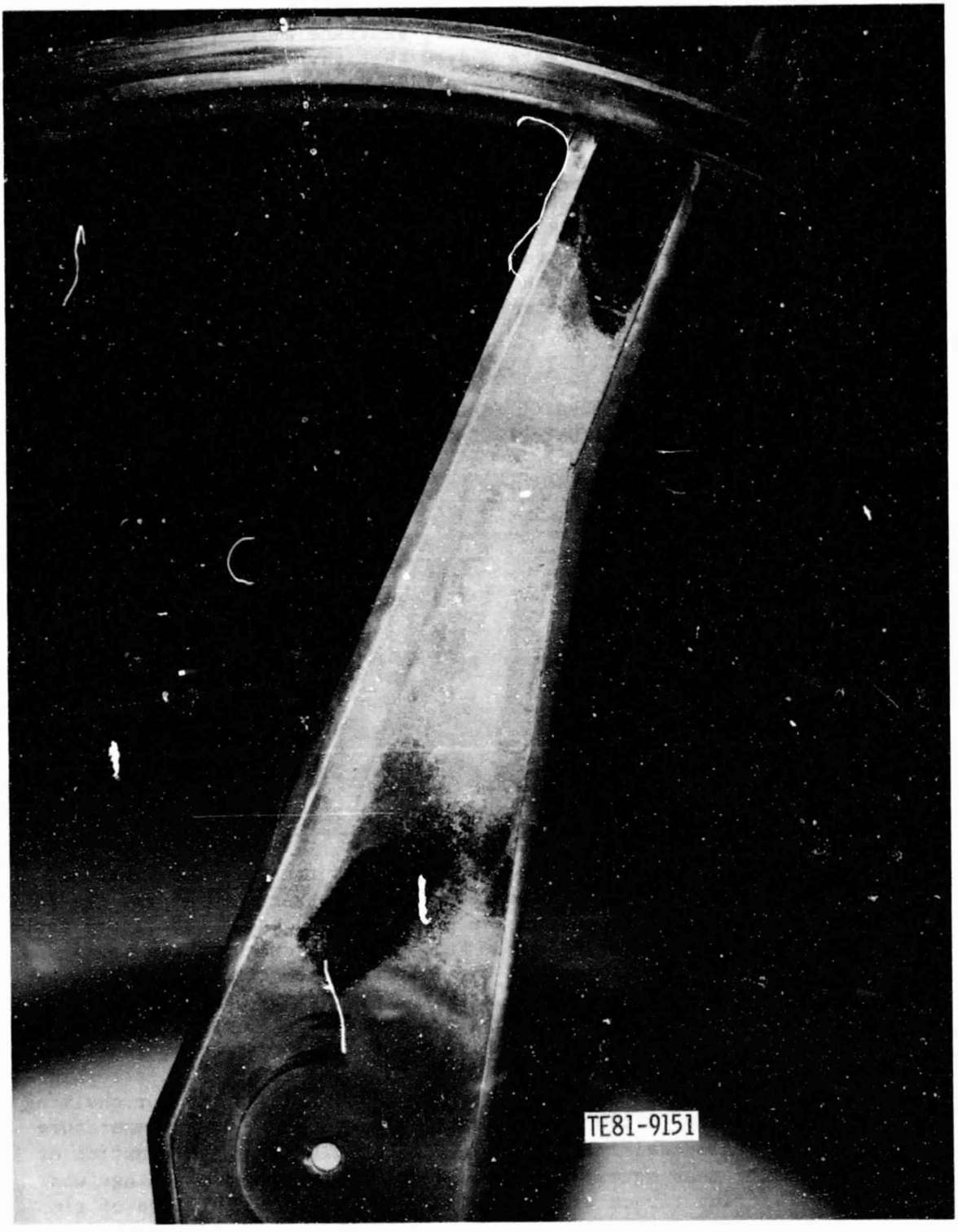

Figure 96. Wearface chalking after 50 hr of 982°C (1800°F) rig testing (negative crossarm).

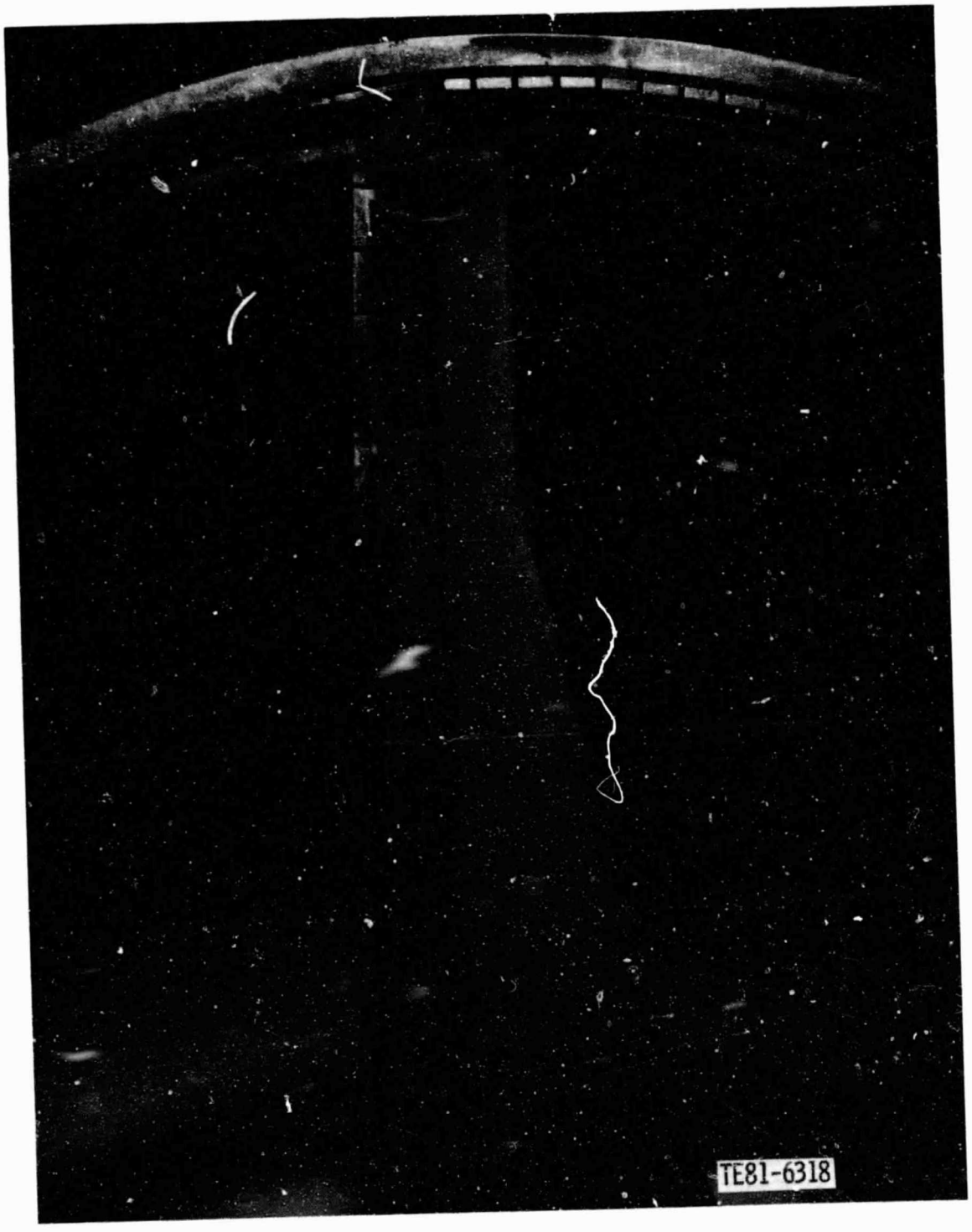

Figure 97. Leaf corrosion after 50 hr of 982°C (1800°F) rig testing.

Seal Wearface Materials

Summary

CaF_2 seems to be a stable high-temperature lubricant (up to 982°C, 1800°F). It will react, however, on the wearface and form oxide or other compounds. The glaze is primarily NiO. Its thickness is decreased with increasing CaF_2 concentration and higher running temperature.

Objective

The current effort on seal wearfaces is aimed at assessing the NiO/CaF_2 for use to temperatures of 982°C (1800°F). In this regard, a regenerator seal fabricated by plasma spraying a premixed blend of 85% NiO/15% CaF_2 powder has been run in a regenerator rig at simulated CATE engine conditions for 75 hr, including 50 hr run at 982°C (1800°F). The seal crossarm wearface was then sectioned and examined metallurgically.

Discussion

Two distinct regions could be seen on the seal wearface, a dark glaze surface forming mostly on the positive, cooler side of the crossarm and a flaky yellow-green surface on the negative, hotter side of the crossarm (Figure 96). The flaky glaze is mainly NiO, as determined by X-ray analysis. It is decorated with spots of calcium compounds (Figure 98). No fluorine was detected. Micrographs of the cross section of the seal (Figure 99) show the laminated nature of plasma-sprayed seal compounds. Clearly, CaF_2 is unchanged up to the chipped edge (surface glaze). Figure 100 shows the unglazed yellow-green surface of the seal. X-ray intensity maps indicate that the calcium concentration is higher and fluorine is only occasionally detected.

X-ray diffraction of the seal failed to reveal any significant amount of CaF_2 or other calcium compounds. However, electron diffraction of the thin-glaze specimens prepared by ion milling from the back side indicates that the glaze is probably NiO, while the rugged surface spot could be CaO or sometimes CaF_2.

To measure the glaze thickness, the seal wearface specimen was mounted at a slight angle and polished. However, no measurement could be made on this specimen because the glazed surface kept tearing off during polishing. Specimens from two seal wearfaces running at lower temperature, i.e., 760°C (1400°F), were successfully polished. The beveled glaze surfaces of H929 (85 NiO/15 CaF_2 and H947 (100 NiO) are shown in Figure 101. The thickness of the glaze is 12 and 46 μm for H929 and H947, respectively.

In summary, CaF_2 seems to be a stable high-temperature lubricant up to 982°C (1800°F). It will react, however, on the wearface and form oxides or other compounds. The glaze is primarily NiO. Its thickness decreases with increasing CaF_2 concentrations and higher running temperatures.

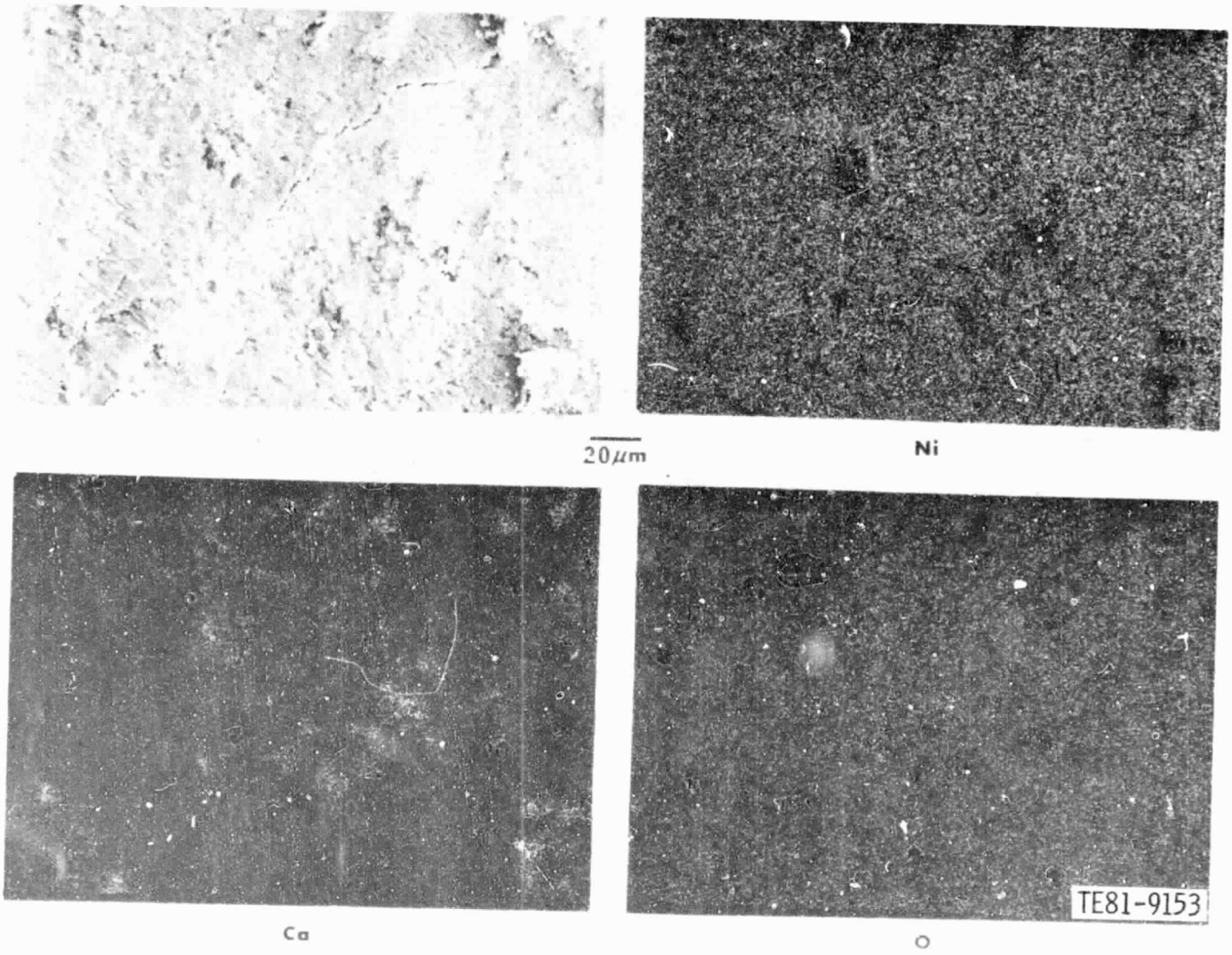

Figure 98. Photomicrograph of typical glazed wearface of 982°C (1800°F) seal and X-ray intensity maps of Ni, Ca, and O. No fluorine was detected.

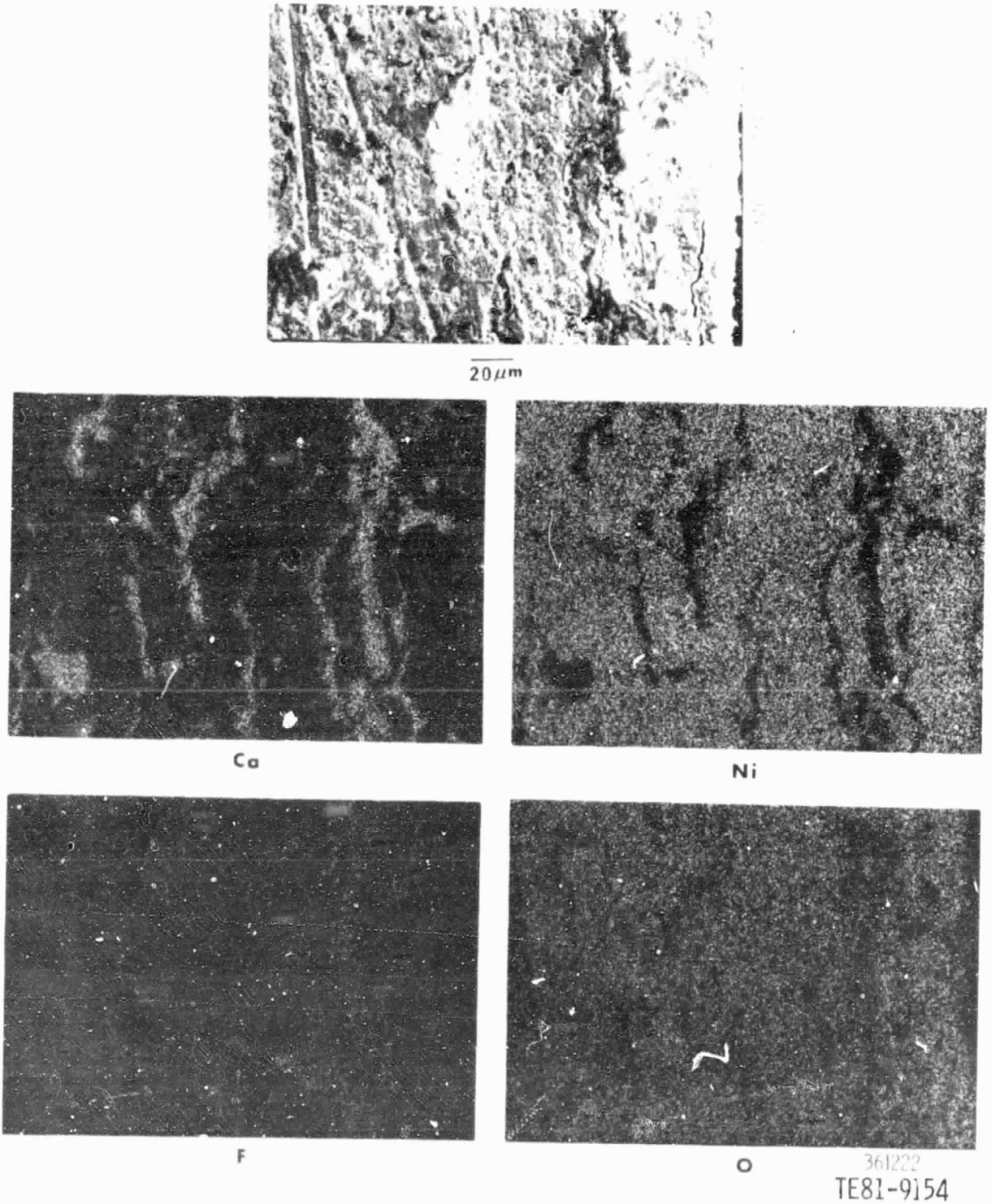

Figure 99. SEM micrograph and characteristic X-ray intensity maps of the cross section of the seal wearface. The glazed surface is at the right side.

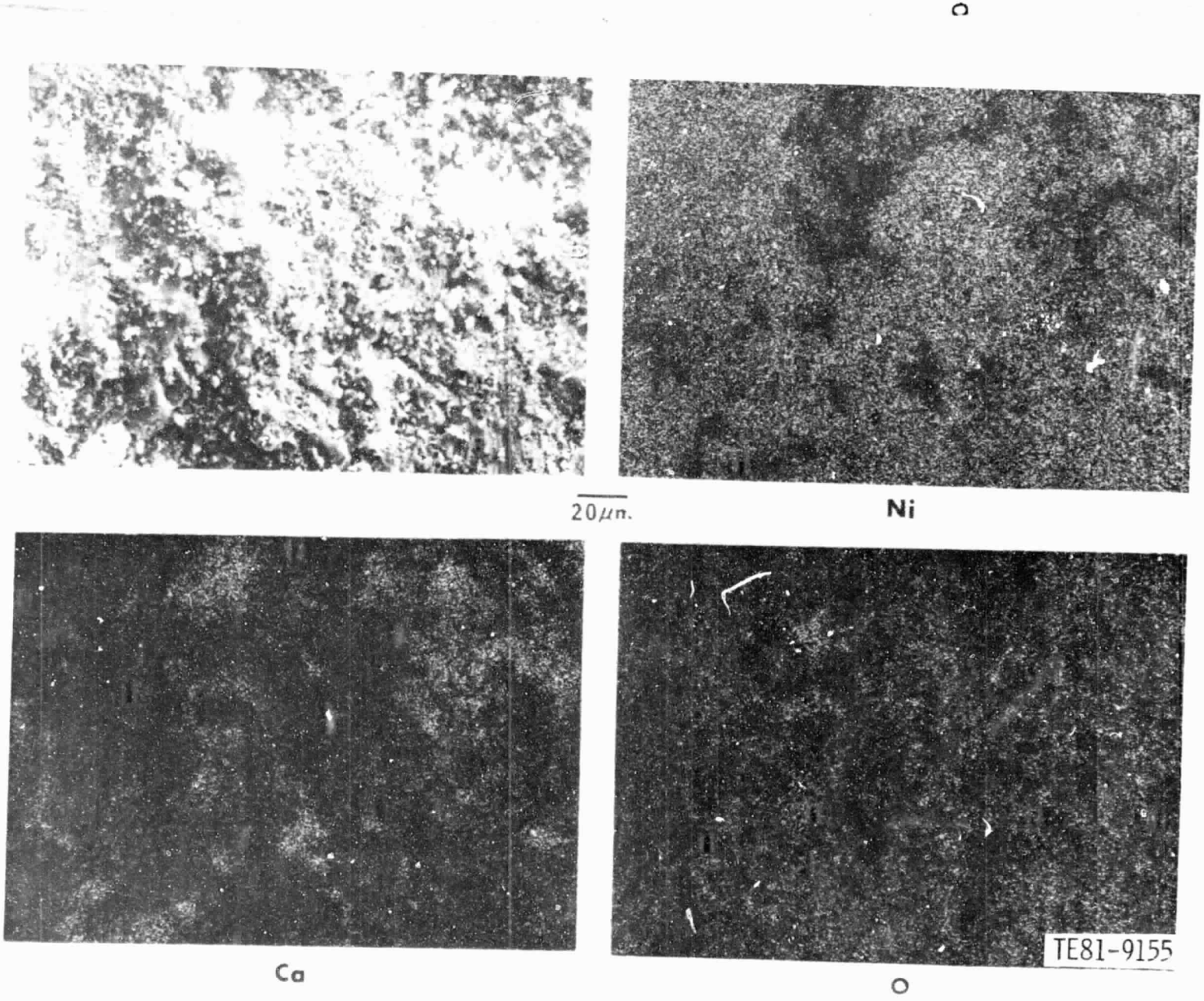

Figure 100. Typical unglazed wearface (yellow-green area) on 982°C (1800°F) seal. Fluorine was occasionally detected.

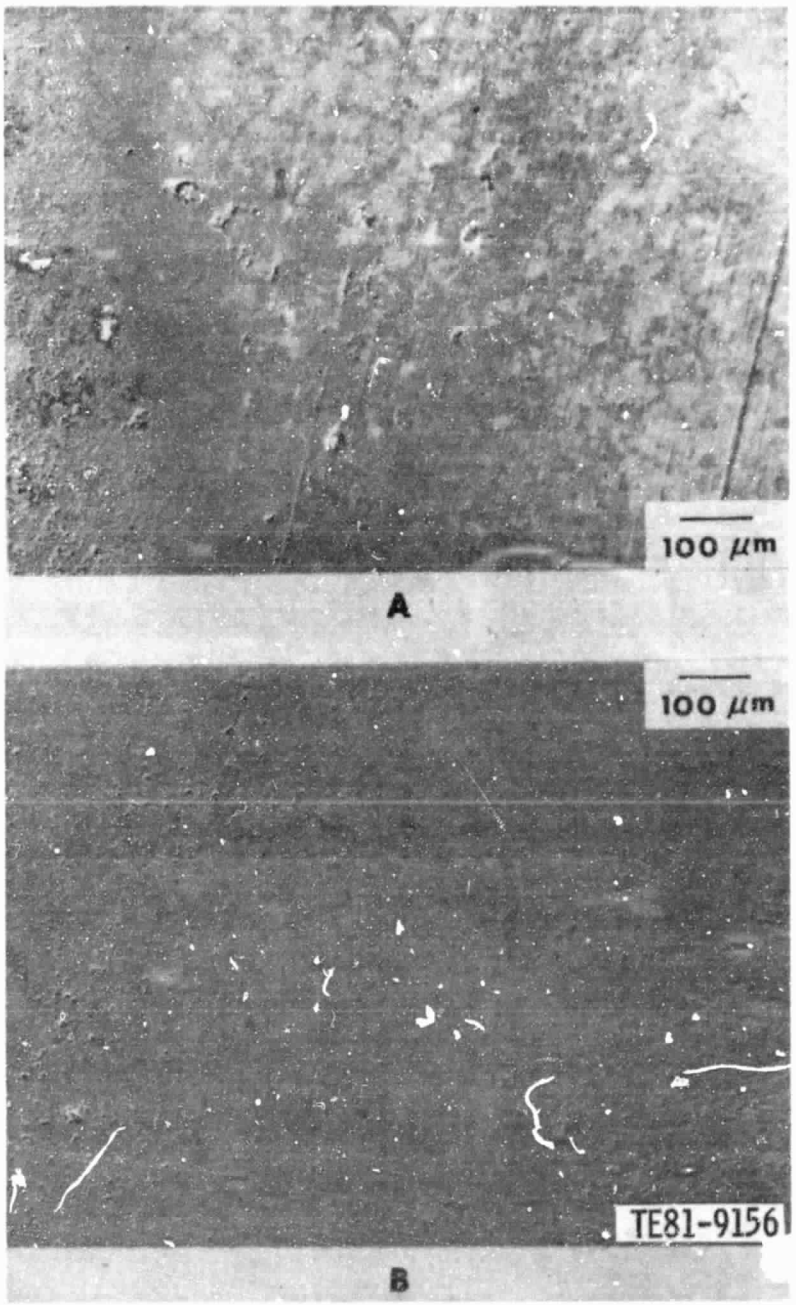

Figure 101. SEM micrographs of (A) seal H929 (85% Ni/15° CaF_2) and (B) seal H947 (100% NiO). Samples were mounted at a 6° angle and polished.

VI. GENERAL ENGINE DESIGN AND DEVELOPMENT

ENGINE BLOCK COOLING

Summary

During this 6-month period, development work continued on the ambient air-cooled block. The accomplishments were as follows:

- Tests were conducted on engine C-4 to establish the cooling airflow requirements to keep the block crossarm temperature at the desired level. The relationship of block temperature to turbine inlet temperature and cooling airflow was determined and the relationship of pressure drop to airflow through the crossarm cooling path was established. Although turbine inlet temperature was limited to 1038°C (1900°F), extrapolation of the data indicates that the proposed block cooling blower will hold the block temperature to levels required for 1132°C (2070°F) operation.
- The internal engine parts required for the ambient air cooling were run in engine C-4 for over 700 hr, 600 of which were on an endurance schedule.
- The external parts of the system--the blower, brackets, and ducting--were detailed, checked, and approved.

Objective

The objective for this report period was to further assess the feasibility of cooling the crossarm area of the engine block with ambient air delivered from an externally mounted blower and to establish the requirements for the blower.

Discussion

Engine C-4 was built with the internal modifications required for cooling the crossarm with ambient air. These modifications establish a flow path for the crossarm cooling air, sealed from the rest of the engine. This is shown schematically in Figure 102. Air is brought into the top of the block chamber adjacent to the crossarm on each side of the engine, flows along the inner surface of the crossarm, and is expelled from the bottom. Flow restrictions that previously existed at the top and bottom and especially at the horizontal centerline were reduced by removing metal from the block and by modifying internal sheet metal parts. The containment ring, gasifier nozzle support struts, and inner and outer engine flow path walls, which previously were cooled by compressor discharge air after it had been used to cool the crossarms, are by these modifications cooled by compressor discharge air supplied by a different path. Since the external blower that ultimately will supply the ambient air has not as yet been procured, shop air was used as an ambient air supply with instrumentation to control and measure the flow and pressure at the entrance to and exit from the block. Seven thermocouples were spaced along each crossarm to determine the temperature pattern.

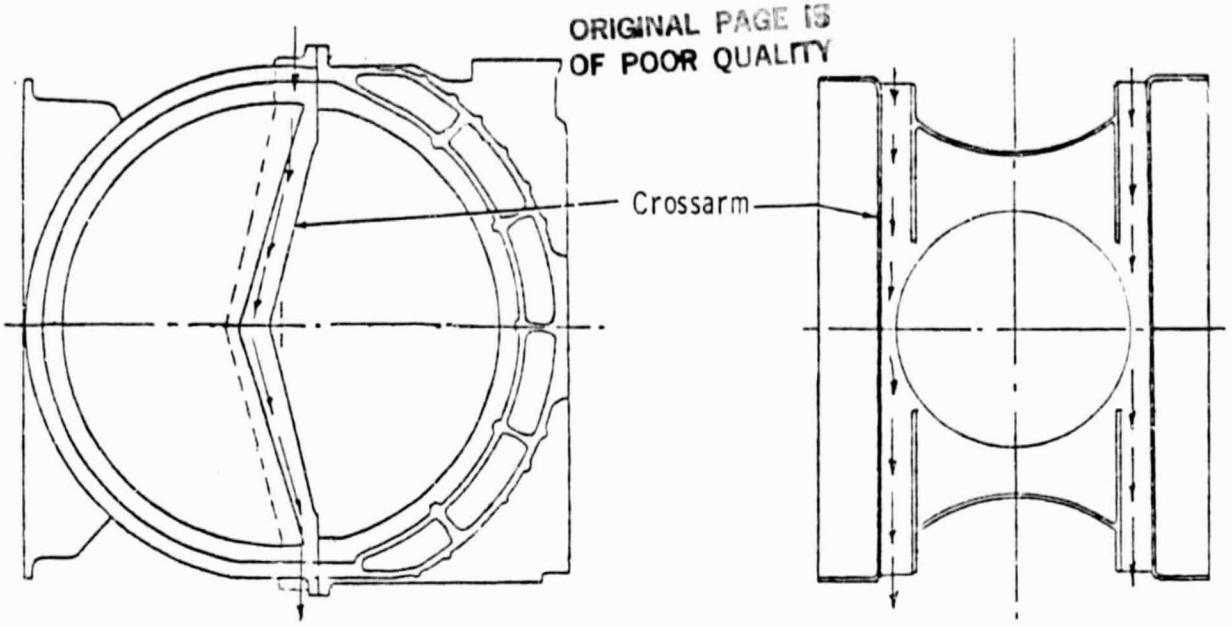

Figure 102. Schematic of ambient airflow through block.

Block temperatures were taken with 55.7 dm^3/sec (118 cfm), 42.5 dm^3/sec (90 cfm), and 37.8 dm^3/sec (80 cfm) cooling airflow with the engine running at 90%, 95%, and 100% speed. These temperatures are plotted in Figure 103 and compared with typical temperatures measured on an engine using standard crossarm cooling. The plot shows that even with only 37.8 dm^3/sec (80 cfm) airflow, the block temperature does not surpass the baseline.

The maximum block temperature at each running condition recorded with 55.7 dm /sec (118 cfm) cooling airflow was plotted against turbine inlet temperature (T_4) and found to increase linearly with T_4 (Figure 104). Since the data were limited for the other three flow rates, they are represented only by the point at 100% speed. Since it is reasonable to assume that the relationship of maximum block temperature to T_4 will be the same for any value of cooling airflow, an indication can be obtained of the maximum block temperature to be expected for the CATE (2070°F) engine, as shown by the dotted lines in the figure.

The pressure drop through the block is plotted against airflow in Figure 105 and compared with the curve that was analytically predicted and with the expected output of the proposed centrifugal blower with three different values of voltage supplied to its dc motor. With 12 v supplied, the blower can be expected to deliver 39 dm^3/sec (82.6 cfm). As shown in Figure 104, this will limit the maximum block temperature to 520°C (968°F).

Future testing will include running with cooling air in the lower flow range (within the output capabilities of the blower) and measuring block temperatures over a running range of 70% to 100% speed. The external parts of the system, blower, mounting brackets, and plenum are at the procurement stage.

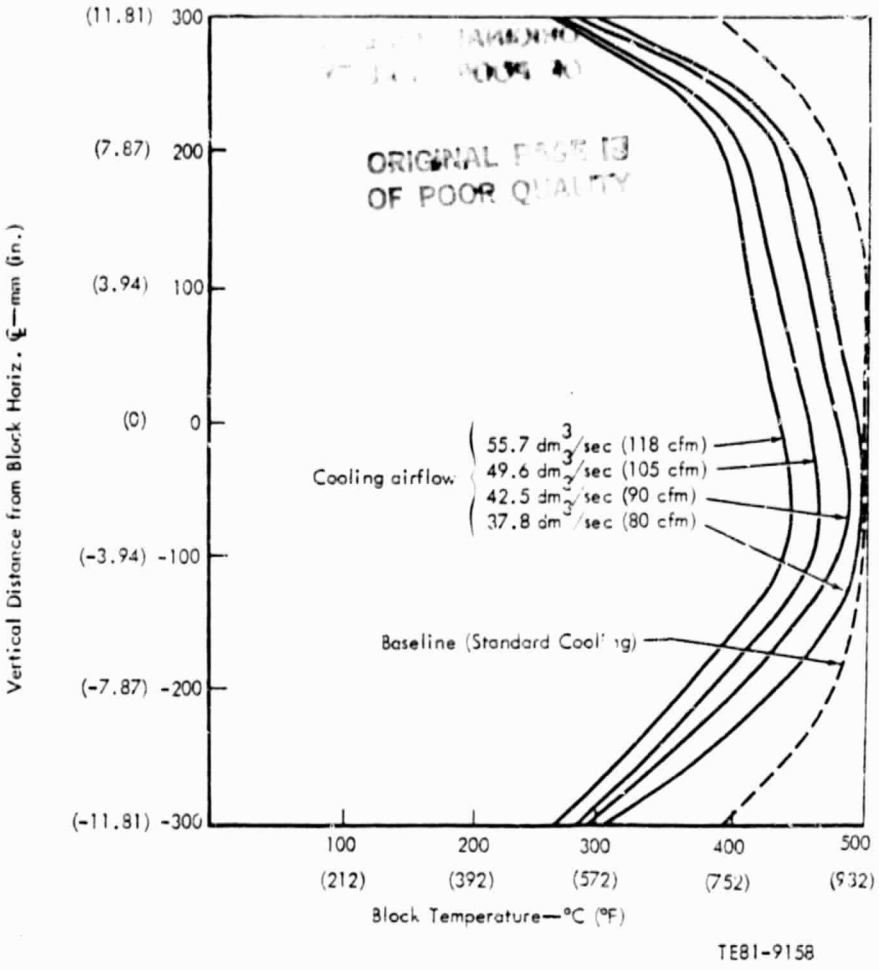

Figure 103. Comparison of air-cooled block temperatures with standard block.

2070°F-CONFIGURATION HOT ENGINE SIMULATOR RIG COMBUSTOR

Summary

The 2070°F-configuration hot-engine simulator rig combustor testing, in conjunction with the CATE fuel injector and ignition system testing, was completed on the combustor component rig. Performance aspects measured included starting characteristics, lean burning limits, low-speed efficiency and steady-state exhaust temperature pattern, and radial gradients.

The system performed satisfactorily in all aspects.

Objectives

The design objectives for the hot-engine simulator rig combustor include the following:

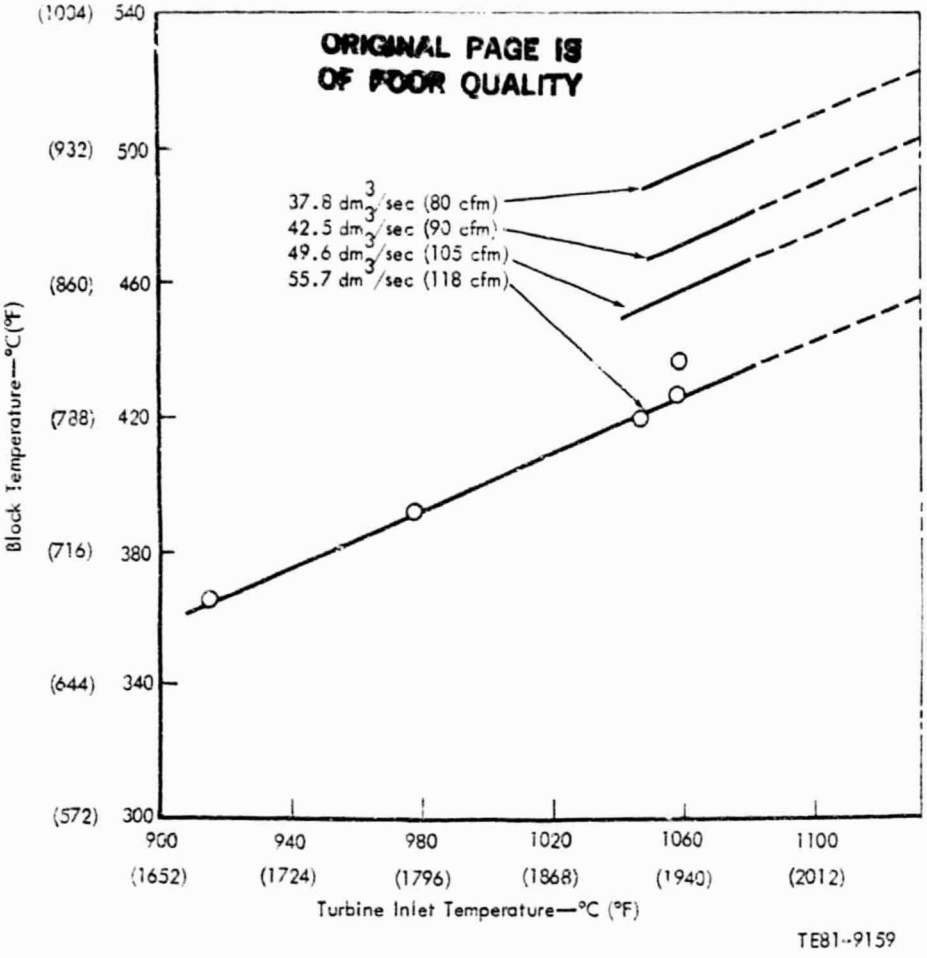

Figure 104. Maximum block crossarm temperatures versus turbine inlet temperatures.

- o Combustor temperature pattern and profile must approximate 2070°F-configuration engine design goals.
- o Combustor system must be easy to light-off and accelerate to idle.
- o Pressure loss must be compatible with simulator rig cycle.
- o Combustor must have adequate durability.

Discussion

The nonregenerative cycle for the hot-engine simulator rig affects the combustor design by lowering the inlet temperature from 738°C (1360°F) to 213°C (415°F) and increasing the temperature rise from 420°C (755°F) to 937°C (1700°F). The design changes made in the 1900°F-configuration combustor consisted of increasing the primary zone airflow, decreasing the total hole area to maintain design pressure loss, and changing combustor wall Lamilloy^{R} to lower porosity, thus providing proper cooling flow. Figure 106 is a photograph of this combustor.

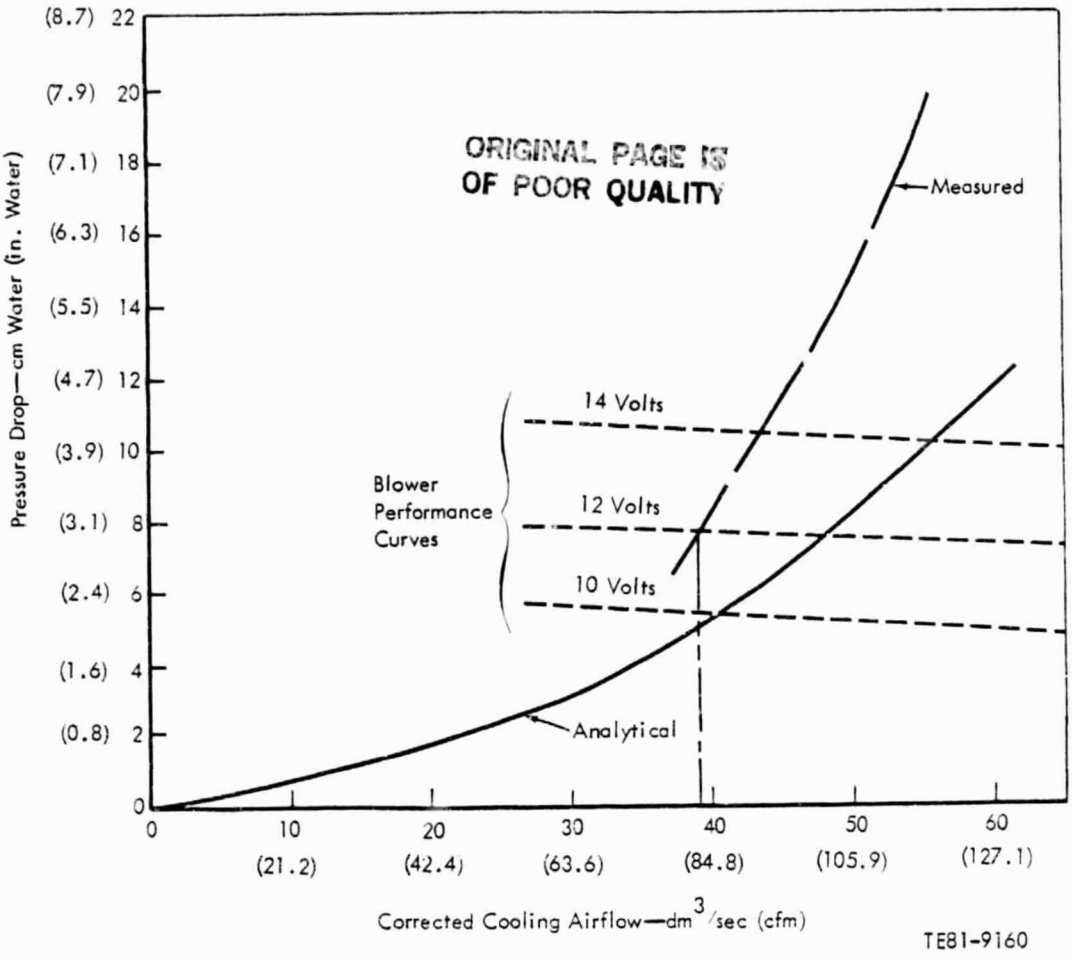

Figure 105. Cooling airflow versus pressure drop.

The test results of light-off, low-speed efficiency, and exhaust gas temperature patterns and profiles were summarized in the previous 6-month report. Testing was completed in this 6-month period, with effort applied to improving the exhaust gas temperature pattern and gradient and eliminating carbon formation on Lamilloy ^{R} walls in the primary zone.

Louvers were added to the combustor wall forward of the primary holes (Figure 106).

Component burner rig results of the simulator combustor are compared to the regenerative combustor in Table XVIII:

TE81-9161

Figure 106. Combustor design for the hot engine simulator rig.

TABLE XVIII. COMPONENT BURNER RIG RESULTS

	Regenerator combustor baseline	Simulator combustor
Pressure loss	2.4%	2.4%
$T_{max}/T°_{avg}$ K/°K(°F/°F)	1.073 (1.098)	1.089 (1.111)
Radial gradient		
Tip °K (°F)	-1.3 (-2.3)	-10.9 (-19.7)
Pitch	+11.7 (+21)	+21.3 (+38.4)
Root	-10.4(-18.7)	-32.3 (58.1)

T_6 ENGINE CONTROLS

Summary

The major accomplishment during this reporting period was the successful testing of all control operating modes on an absorption dynamometer using engines C-1 and C-4 with T_6 thermocouples (turbine exit temperature). The first control was then installed on engine C-4 to begin durability testing. The second unit was fabricated and also successfully tested on the two engines.

Objective

The objective for the period was to advance the control system development so it would be suitable for use on the 2070°F-configuration engine. This required verifying all automatic shutdowns, successful hot and cold starting, accelerations, power transfer control, clutch lockup and dump, and safe N2 overspeed protection with no dynamometer load.

Discussion

During this report period, software debugging became much more subtle and more difficult for the supplier to correct without an on-site digital development system engine. It was therefore decided that a Tektronics Microprocessor Development System similar to that used at Woodward would be rented and installed at DDA for 1 month. This program was very successful, since turnaround time was greatly reduced.

Several major software improvements were made to provide better control. The T_6 thermocouple lead, fuel control loop gain, and power transfer clutch control loop gain were given variable values depending on N1 (gasifier speed) in order to complement the varying engine dynamic responses caused by changes in mass airflow. Dynamic response of the power transfer clutch in engine C-4 continues to present operating difficulties. Even with one clutch plate removed, the characteristic gain is too high, causing the control loop to cycle. The clutch gain in engine C-1 is acceptable.

Problems with cold starting were encountered on engine C-4 and are under investigation. Additional cold-start compensation has been added to the Electronic Control Assembly (ECA) software, and the thermocouple design has been modified to allow more tip insertion into the power turbine diffuser middle flow annulus.

TWO-STAGE POWER TURBINE

Summary

In the current reporting period, the design effort on the 2265°F-configuration has produced a general arrangement with all of the major design aspects defined. The power turbine is a two-stage system with metal components except for the first-stage nozzle assembly, which is a ceramic structure made of individual vanes and rings bonded into an assembly. The major design and development tasks remaining are the development of a ceramic bonding system, analysis of the probability of survival of the ceramic nozzle, and generation of detailed part drawings for fabrication.

Objective

The objective of this effort is to provide a power turbine for operation in the CATE 2265°F-configuration engine. The turbine must suit a 1241°C (2265°F) performance cycle that provides an SFC of 200.7 mg/watt-hr (0.3616 lb/hp-hr). Following preliminary studies reported last period, design objectives have been further defined: a two-stage configuration with metal rotor will be used. Only the first-stage power nozzle will be ceramic. From a ceramic applications point of view, the design of this component is the primary objective of this task.

Discussion

Design of the two-stage power turbine for the 2265°F-configuration engine has continued. This new turbine is being designed to provide the desired performance level at a 1241°C (2265°F) gasifier rotor inlet temperature. The two-stage design was established following preliminary studies completed in the last reporting period. That study included evaluations of six possible configurations, including single- and two-stage configurations with metal or ceramic blading. The only truly adequate configuration that would provide desired performance and long life (18,000 hr in-truck application) requires ceramic blading in both stages. This approach would increase program costs, and the two-stage all-metal rotor configuration was chosen. It will allow a design that meets program performance goals and will provide adequate life for all proposed test stand and vehicle demonstrations in the CATE program. Subsequent to selection of a power turbine concept, design emphasis has been placed on further definition of component details during this period.

The two-stage turbine must fit within the current IGT 404 frame (block) and use as much of the currently developed engine (parts or concepts) as possible, including the 2070°F-configuration ceramic gasifier turbine. Normal design practices such as providing rotor containment in the event of failure, will be provided. The effective use of cooling air and minimization of seal leakage are of primary importance to meeting performance goals. The design criteria for long-life vehicular application are to be observed except for the blade stress-rupture life.

A power turbine design performance cycle has been established (Table XIX). Interstage conditions have also been calculated as required for determining component temperatures and pressure loads. These data include the effects of estimated secondary flows and leakages.

A preliminary flow path was previously established, but a review of the aerodynamic design of the power turbine revealed the need to lengthen the turbine to improve airfoil passage diffusion characteristics and thus achieve desired performance. This period's activities encompassed a complete redesign. A new flow path was generated. Airfoil chord lengths were increased, but axial vane-to-blade gaps were maintained. The longer turbine requires relocation of one main engine bearing aft by 6.4 mm (0.25 in.). The turbine general arrangement is presented in Figure 107. Completed portions of the power turbine rotor redesign include the following:

- o A new flow path has been established.
- o New blade airfoil shapes have been established and the predicted maximum power lives of 350 hr and 3000 hr for the first and second stages are unchanged from the previous design.
- o Blade frequencies have been computed. The data have been reviewed and the airfoil count at all turbine stages for the 2265°F-configuration engine have been established as follows:

Gasifier vane	28
Gasifier blade	40
Power turbine first vane	27
Power turbine first blade	44
Power turbine second vane	32
Power turbine second blade	40

TABLE XIX. POWER TURBINE DESIGN CYCLE DATA

Blade inlet total temperature	1052°C (1925°F)
Vane inlet pressure	206.8 kPa (30.0 psia)
Vane exit flow	1.31 kg/sec (2.88 lb/sec)
Rotational speed	25,133 rpm
Power	270 kw (362 hp)
Work (ΔH)	206.8 kj/kg (88.0 btu/lb)
Corrected work ($\Delta H/\theta_{cr}$)	46.3 kj/kg (19.9 btu/lbs)
Expansion ratio (total-total)	1.927
Turbine efficiency (total-total)	89.4%
Turbine type	2 axial stages

Blade frequencies and their relationship with significant engine orders are shown in Figures 108 and 109. Interference points are shown in the engine operating speed range, but predicted dynamic stress response is low.

review of the axial spacing allowance between vane and blade rows shows it s adequate, based on DDA experience.

- o Preliminary first- and second-stage disk sizing has been completed. The disks should provide desired cyclic life and overspeed burst margins. A more detailed finite-element analysis is now required.
- o Rotor system dynamics have been reviewed with the new disk sizes and revised bearing positions. The first mode frequency is decreased slightly but considered satisfactory at 48.6% speed versus 62.9% in the current engine with single-stage power turbine.

General Arrangement

With the guidance of the previously detailed design parameters, a general arrangement of the two-stage power turbine components was determined (Figure 110). In the previous progress report it was established that both power turbine rotors made from Mar-M246 would have satisfactory lives to demonstrate the CATE program goals. By necessity, both power turbine vane rows are canti-

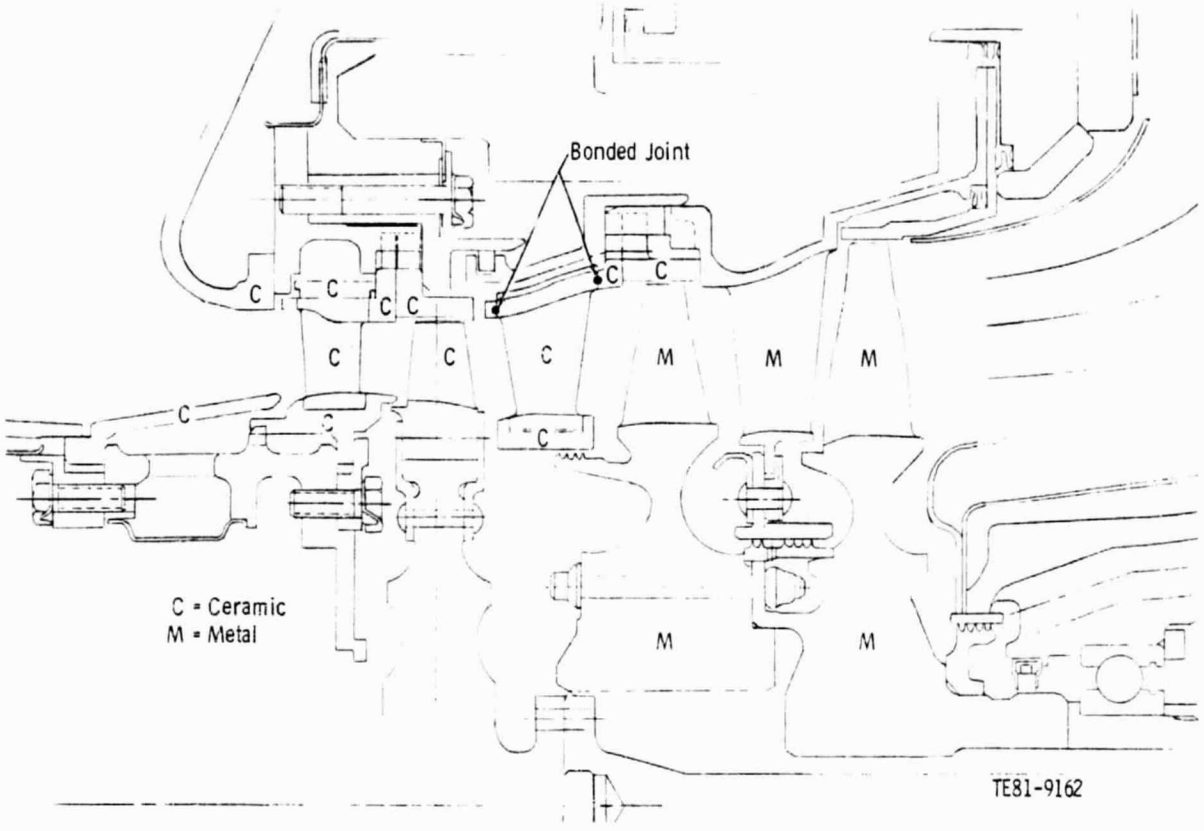

Figure 107. 2265°F-configuration turbine.

levered from the outer flow path structure and present the same technical problem of how to cantilever-mount the vane. Developing the mounting technique for both vane rows in ceramic structures would incur duplicate and parallel development costs. A review of the flow path gas temperature determined that the second-stage vane row gas temperature was low enough to permit the use of a solid-metal airfoil casting. Thus it was decided that in the 2265°F-configuration power turbine only the first-stage vane row and turbine tip shroud would be ceramic.

In Figure 110 the first power turbine rotor is piloted and bolted to the second power rotor, which is inertia-welded to a steel shaft. This power turbine rotor assembly is positioned by two antifriction bearings in the front half of the gearbox, which is aligned to the engine block. The second-stage nozzle is centered by cross keys from the engine center bulkhead. The second-stage nozzle casting also provides cross keys to center and position the first-stage ceramic nozzle vane assembly and rotor tip shroud. The two sets of cross keys provide for differential thermal expansion of the engine block, the second-stage nozzle, and the first-stage ceramic nozzle assembly. The second-stage shroud is a separate low expansion metal (NX-188) alloy casting cross-keyed

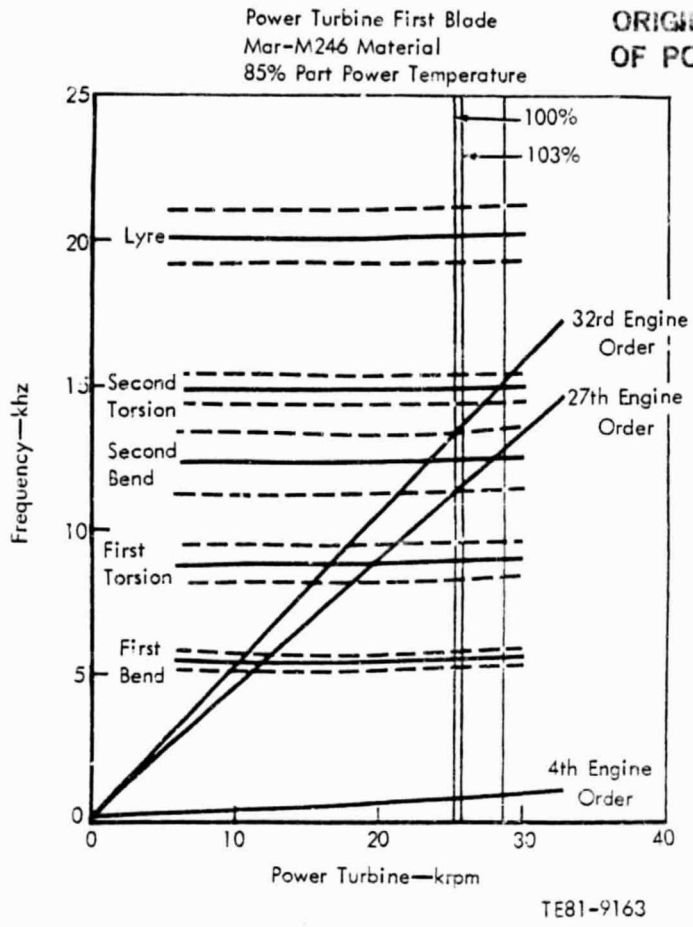

Figure 108. Dynamics analysis, power turbine, 1st blade.

with the metal nozzle to the block bulkhead. The axial load of the first-stage ceramic nozzle assembly is transmitted through the second-stage nozzle assembly to the block bulkhead, as is the axial load from the second-stage nozzle. Sealing between the turbine stages is accomplished by labyrinths on the rotors running in close radial proximity to the seal surfaces on the nozzle assembly.

The fabrication of the ceramic first-stage nozzle will draw upon experience gained in producing the 2070°F-configuration gasifier nozzle components. Individual vanes and ring structures will be fabricated by the same techniques developed on the gasifier components. The ring structures will have holes and pockets to retain the vanes. To achieve cantilever mounting, the outer platform of the vane will be bonded to the outer vane support ring (Figure 110). The vane inner platform fits into close clearance pockets in the inner ring structure, providing the radial and axial location of the ring. Development of the ceramic bond will be the primary ceramic development task on the 2265°F-configuration two-stage power turbine.

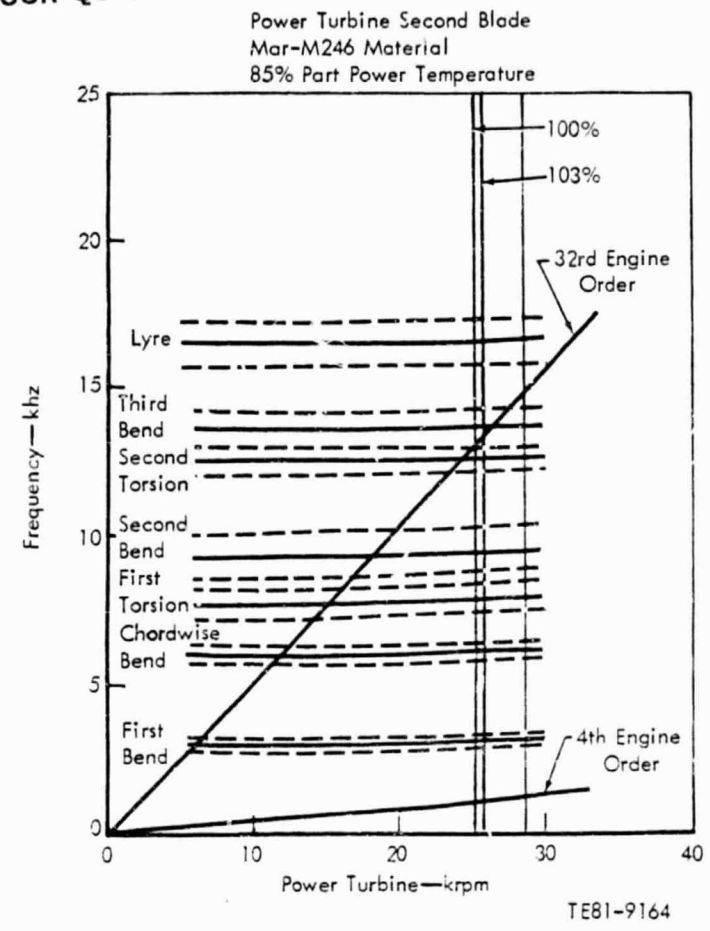

Figure 109. Dynamics analysis, power turbine, 2nd blade.

Preliminary discussions have been held with several ceramic vendors on the bonding task. Although no developed bonding system is currently available, some vendors felt enough laboratory work had been done to indicate its feasibility. This development task is within the CATE program charter to develop and advance ceramic technology.

Development of design details, ceramic component three-dimensional analysis model generation, and development of ceramic bonding technology are planned for the next reporting period.

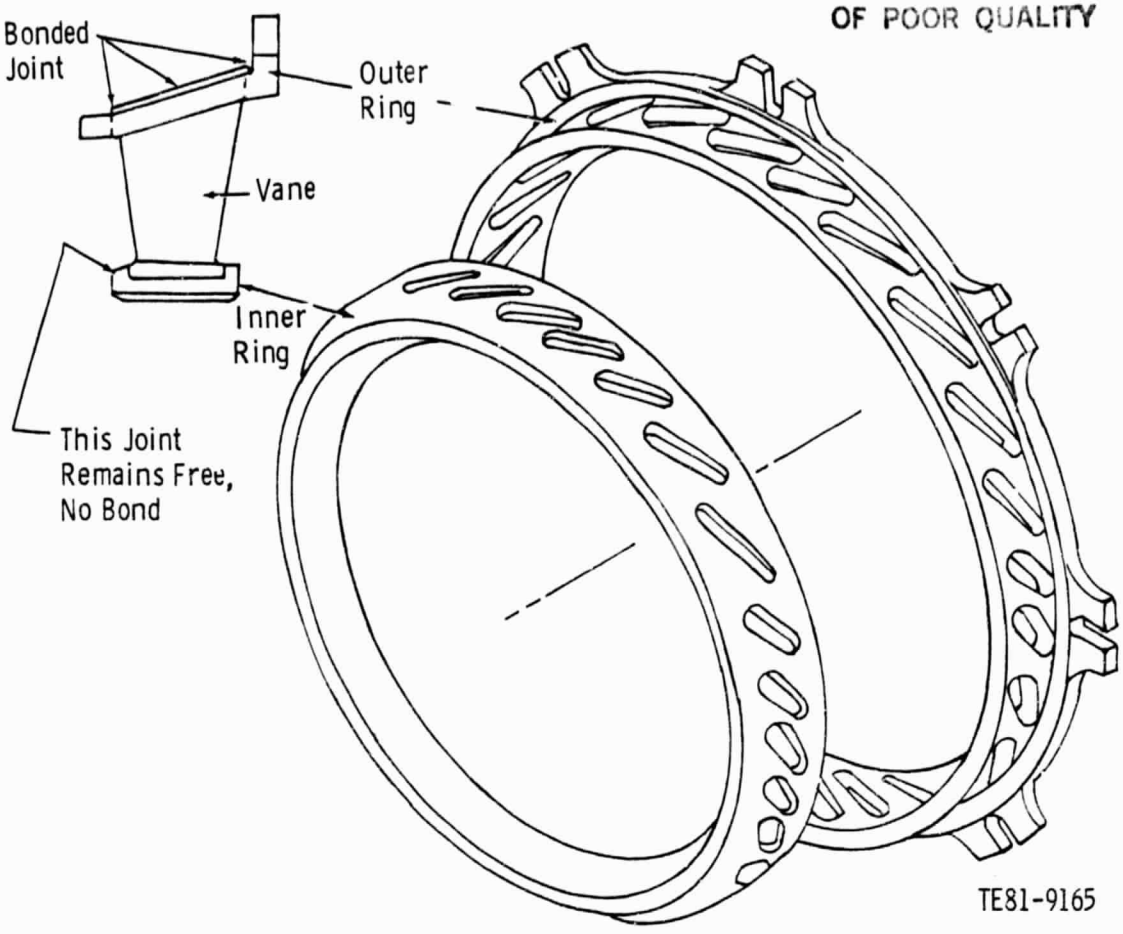

Figure 110. 2265°F-configuration 1st stage ceramic power turbine nozzle assembly.

REFERENCES

1. Joseph A. Byrd, Michael A. Janovicz, and Franklin A. Rockwood, "Ceramic Applications in Turbine Engines: Progress Report for 1 January 1980 to 30 June 1980," NASA CR-165197, Detroit Diesel Allison EDR 10383, November 1980.

2. S. Michael Hudson, Michael A. Janovicz, and Franklin A. Rockwood, "Ceramic Applications in Turbine Engines: Progress Report for 1 July 1979 to 31 December 1979," NASA CR-159865, Detroit Diesel Allison EDR 10156, May 1980.

3. Thomas P. Crowley, Frederick R. Faxvog, and David M. Roessler, "Photoacoustic Effect with Thermally Thin Solids," Applied Physics Letter, Vol. 36, No. 8, 15 April 1980, pp. 641-643.

4. R. L. Thomas, J. J. Pouch, Y. H. Wong, L. D. Favro, and P. K. Kuo, "Subsurface Flaw Detection in Metals by Photoacoustic Microscopy," Journal of Applied Physics, Vol. 15, No. 2, February 1980, pp. 1152-1156.

ACKNOWLEDGMENTS

The CATE program management acknowledges the efforts of the following personnel in contributing to the preparation of this report:

L. Davis	Regenerator Seal Design
R. Pecha	Ceramic Turbine Inlet Plenum and High-Temperature Block Design
R. Fox	Ceramic Regenerator Material Evaluation
M. French	Ceramic Regenerator Design
Dr. P. Heitman	Ceramic Materials Development and Characterization
P. Khandelwal	NDE Development of Ceramic Components
B. Schechter	Abradability Testing
T. Pacala	Regenerator Seal Material Development
P. Jablonski	Ceramic Turbine Vane and Tip Shroud Design
D. Talcott	Ceramic Machining Process Development
R. Furstnau	Engine Electronic Control System
S. Thrasher	Engine and Rig Testing
J. Wertz	Ceramic Turbine Blade Design
E. Young	2070°F High-Temperature Combustor Design
R. Quinn	Ceramic Disk Stress Analysis
Dr. J. Chang	Ceramic SEM and Failure Analysis